THE UNIVERSITY OF ALBERTA

MODELING FLUIDIZED BED JET INTERACTIONS USING COMPUTATIONAL FLUID DYNAMICS

by

JONATHAN JAMES TYLER ©

A THESIS

SUBMITTED TO THE FACULTY OF GRADUATE STUDIES AND RESEARCH IN
PARTIAL FUFILMENT OF THE REQUIREMENTS FOR THE DEGREE OF
MASTER OF SCIENCE
IN
CHEMICAL ENGINEERING

DEPARTMENT OF CHEMICAL AND MATERIALS ENGINEERING

EDMONTON, ALBERTA
SPRING, 2000

National Library
of Canada

Acquisitions and
Bibliographic Services

395 Wellington Street
Ottawa ON K1A 0N4
Canada

Bibliothèque nationale
du Canada

Acquisitions et
services bibliographiques

395, rue Wellington
Ottawa ON K1A 0N4
Canada

Your file Votre référence

Our file Notre référence

The author has granted a non-exclusive licence allowing the National Library of Canada to reproduce, loan, distribute or sell copies of this thesis in microform, paper or electronic formats.

L'auteur a accordé une licence non exclusive permettant à la Bibliothèque nationale du Canada de reproduire, prêter, distribuer ou vendre des copies de cette thèse sous la forme de microfiche/film, de reproduction sur papier ou sur format électronique.

The author retains ownership of the copyright in this thesis. Neither the thesis nor substantial extracts from it may be printed or otherwise reproduced without the author's permission.

L'auteur conserve la propriété du droit d'auteur qui protège cette thèse. Ni la thèse ni des extraits substantiels de celle-ci ne doivent être imprimés ou autrement reproduits sans son autorisation.

0-612-60190-0

Canada

THE UNIVERSITY OF ALBERTA

Library Release Form

NAME OF AUTHOR: Jonathan James Tyler

TITLE OF THESIS: Modeling Fluidized Bed Jet Interactions Using Computational Fluid Dynamics

DEGREE: Master of Science

YEAR THIS DEGREE GRANTED: 2000

Permission is hereby granted to the UNIVERSITY OF ALBERTA LIBRARY to reproduce single copies of this thesis and to lend or sell such copies for private, scholarly or scientific purposes only.

The author reserves other publication rights, and neither the thesis nor extensive extracts from it may be printed or otherwise reproduced without the author's written permission.

Jonathan Tyler

8 Hythe Ave. South
Burnaby, British Columbia
V5A 3B4

Date: January 28, 2000

THE UNIVERSITY OF ALBERTA

FACULTY OF GRADUATE STUDIES AND RESEARCH

The undersigned certify that they have read, and recommend to the Faculty of Graduate Studies and Research, for acceptance, a thesis entitled MODELING FLUIDIZED BED JET INTERACTIONS USING COMPUTATIONAL FLUID DYNAMICS submitted by Jonathan James Tyler in partial fufilment of the requirements for the degree of Master of Science in Chemical Engineering.

Dr. P.A.J. Mees, Supervisor

Dr. K. Nandakumar

Dr. J. Yokota

Date: November 26, 1999

ABSTRACT

Computational fluid dynamic (CFD) simulations were conducted using CFX 4.2 from AEA Technology in order to verify and validate the two fluid multiphase flow models against experimental results. A fully three dimensional fluidized bed simulation with a side injection gas nozzle was constructed and simulations performed at various jet velocities, aeration rates and with different model parameters.

Based on these simulations it was determined that the Superbee TVD discretization scheme should be used on a well designed discretization mesh of at least 50,000 nodes. Particular care must be taken when specifying the nozzle inlet boundary condition.

Predicted bubble behavior and jet penetration into the fluidized bed agreed well with literature and experimental results. Two large recirculation zones were predicted to form within the fluidized bed; the simulations tended to over predict these recirculation zones. The two fluid model within CFX 4.2 gives results that agree qualitatively with experiments.

P

ACKNOWLEDGEMENTS

The author would like to extend his gratitude to Dr. Philip Mees for his supervision, guidance and support throughout this project. It has been a challenging and rewarding project.

Additional support and discussion has been provided from members at Syncrude Canada Limited from Dr. Barry Bara, Dr. Larry Hackman and Dan Bulbuc. Without these people this project would not have been possible. Thanks to Dr. Berutti and Jason Cowpan from the University of Saskatchewan for sharing their experimental apparatus and for the enjoyable time that I spent in their company gathering observations from the apparatus.

Financial support was provided from Syncrude Canada Limited; without whom my experience as a graduate student and an engineer would have been much diminished. Scholarships from NSERC Canada and the University of Alberta have been greatly appreciated and contributed to the overall successes enjoyed in this project. I am very grateful for this support.

I would like to thank Bob Barton and Jacques Gibeau for maintaining and troubleshooting the computer systems. Without their help and expertise my work would not have been completed.

Finally, I would like to thank my family and friends for their support and patience throughout this project. A special thanks to Catherine for making sure that my weekends were spent in the mountains and not in front of the computer screen.

TABLE OF CONTENTS

1 INTRODUCTION 1

2 LITERATURE REVIEW 4

2.1 Flow Behavior within a Fluidized Bed 5

2.1.1 General Flow Behavior 5

2.2.2 Bubble Movement within a Fluidized Bed 10

2.2.3 Vertical Jet Behavior 16

2.2.3 Horizontal Jets in Fluidized Beds 17

3 GOVERNING EQUATIONS OF SINGLE AND MULTIPHASE FLOWS 30

3.1 Approaches to Flow Modeling 31

3.1.1 Eulerian Continuum Approach 31

3.1.2 Lagrangian Trajectory Approach 32

3.1.3 Kinetic Theory Approach 33

3.1.4 Ergun Equation and Other Empirical Approaches 34

3.1.5 Direct Numerical Simulation 35

3.2 Single Phase Flows 35

3.2.1 Derivation of the General Transport Theorem 35

3.2.2 Continuity Equation 41

3.2.3 Momentum Equation 41

3.3 Multiphase Flows 42

3.3.1 Forces Acting on Solids in a Gas-Solid Multiphase Flow System 46

3.3.2 Drag Forces 47

3.3.3 Solids Pressure 50

3.3.4 Friction 55

3.3.5 Particle Viscosity Due to Interparticle Collisions 55

3.3.6 Radial Distribution Functions 62
3.3.7 Basset Force 63
3.3.8 Magnus Force 63
3.3.9 Saffman Force 63
3.3.10 Pressure Gradient Induced Forces 64
3.3.11 Response Times 64
3.4 Modeling and Averages 66
3.4.1 Volume Averaging 67
3.4.2 Phase Average and Intrinsic Average 67
3.4.3 Minimum Control Volume Sizes for Phase Averages 68

4 COMPUTATIONAL METHODS 72
4.1 Computational Techniques 73
4.1.1 Representing Flow Fields in CFX 4.2 73
4.2 Discretizing the Governing Equations 75
4.2.1 Diffusion Terms: 77
4.2.2 Advection Terms: 78
4.2.3 Upwind Differencing (UDS): 79
4.2.4 Hybrid Differencing (HDS): 79
4.2.5 Total Variation Diminishing Schemes: 80
4.3 Constructing Finite Difference Schemes 82
4.3.1 Higher Order Non-oscillatory Schemes (SONIC and UNO) 86
4.4 Analysis of Several Different Discretization Schemes 88
4.4.1 FIRST ORDER UPWINDING (FOUW) 89
4.4.2 LAX-WENDROFF Central Differencing (LW) 90
4.4.3 WARMING-BEAM (WB) 90
4.4.4 Minmod TVD (MINMOD) 91
4.4.5 MUSCL TVD (MUSCL) 91
4.4.6 SUPERBEE 92

4.5 Source Terms 96
4.6 Coupling Difference Equations with IPSA 96
4.6.1 Semi-Implicit Method for Pressure-Linked Equations (SIMPLE) 97
4.6.2 Inter Phase Slip Algorithm (IPSA) 98
4.6.3 Volume Fraction Equations 99
4.6.4 Pressure Correction Equation 100
4.6.5 IPSA in Harwell-FLOW3D Computer Code: now CFX 4.2 102
4.6.6 Rhie-Chow Interpolation 103
4.7 Numerical Errors and Convergence 104
4.7.1 Output File Summary of CFX 4.2 Simulations 105
4.8 Summary of Computational Methods 108

5 CFX 4.2 MODEL SET-UP 109
5.1 CFX 4.2 Model Set Up 110
5.1.1 Geometry 110
5.1.2 Grid Generation 113
5.1.2 Boundary Conditions 115
5.2 Initial Conditions 117
5.3 Phase Properties 118
5.3.1 Gas Phase Properties 118
5.3.2 Solids Phase Properties 119
5.3 CFX Flow Solver Acceleration 119
5.3.1 Under Relaxation Factor Studies 120
5.3.2 Single versus Double Precision 125
5.3.3 Courant False Time Stepping 126
5.4 Summary of Simulation Set-Up 129

6 EXPERIMENTAL SECTION 130
6.1 EXPERIMENTAL SET UP 131

6.1.1 Geometry 131
6.1.2 Particle Properties 132
6.1.3 Experimental Procedure 132
6.2 Observations 135
6.2.1 Below Umf 137
6.2.2 At Umf 137
6.2.3 Above Umf 138
6.2.4 Bubble Sizes and Rise Velocities 138
6.2.5 Transient Analysis 140

7 RESULTS AND DISCUSSION 142
7.1 Part I: Numerical Considerations 143
7.1.1 Three Dimensions and Symmetry 143
7.1.2 Discretization Scheme Comparison 145
7.1.3 Grid Refinement Studies 148
7.1.4 Sensitivity Analysis: Continuous Phase Pressure Removed from Solids Momentum Equation 162
7.1.5 Solids Pressure Sensitivity Analysis 166
7.1.6 Summary of Numerical Studies 168
7.2 Part II: Physical Predictions 169
7.2.1 Tests Below Umf 169
7.2.2 Tests Above Umf 176
7.2.3 Jet Behavior and Penetration Results 180
7.2.4 Overall Flow Patterns 184
7.2.5 Particle Tracking 188
7.2.6 Bubble Shapes 194
7.2.7 Bubble Velocities 199
7.2.8 Time Averaged Data 199
7.3 Summary of Physical Predictions 208
8 CONCLUSIONS AND RECOMMENDATIONS 210

8.1 Numerical Considerations 211
8.2 Physical Predictions 212
8.3 Recommendations 212

REFERENCES 215
APPENDIX A: Mathematical Proofs 223
A.1: Total Derivative of the Jacobian 223
A.2: Gauss' or Divergence Theorem 225
A.3: Number Density 227
APPENDIX B: Computer Codes 229
B.1: Minimum Control Volume Size MATLAB File 229
B.2: C Computer Code for Comparison of Different Discretization Schemes 230
APPENDIX C: CFX 4.2 Command and FORTRAN Files 245
C.1: CFX 4.2 Command File *.fc 245
C.2: CFX 4.2 Fortran File 251

LIST OF TABLES

Table	Description	Page
2.1	Horizontal Penetration Expressions from Literature	21
3.1	Common Solids Pressure Functions in Literature	51
3.2	Solids Viscosity Correlations Available in Literature	56
5.1	User FORTRAN Geometry Variables for Simulations	112
5.2	Under Relaxation Parameter Tests	120
5.3	Courant Number Analysis for Δt=0.001 s	127
6.1	Experimental Operating Conditions and Video Reference Numbers	135
6.2	Summary of Video Capture Image Dimension Conversions from Pixels to Centimeters	136
6.3	Bubble Rise Velocity, Horizontal Velocity and Size from Experiments	141
7.1	Numerical Simulations Summary	144
7.2	CPU Demand and Discretization Scheme	148
7.3	Vorticity in the Near Jet Region	161
7.4	Physical Prediction Simulations Summary	171
7.5	Average Bubble Rise Velocities from Simulations	200

LIST OF FIGURES

Figure	Description	Page
2.1	Different fluidization flow regimes in a fluidized bed. Adapted from Chyang *et al.* (1998)	6
2.2	Gross characteristic flow regimes in a fluidized bed. Adapted from Chyang *et al.*(1998)	8
2.3	Flow patterns within voids formed in fluidized beds.	13
2.4	Horizontal jet penetration as a function of fluidization velocity. Adapted from Chyang *et al.* (1998)	25
2.5	Flow Regimes of the gas discharge mode for horizontal nozzles. Group B particles. From Chyang *et al.* (1997)	26
3.1	General control volume in curvilinear coordinates	36
3.2	Drag coefficient correlation based on Re_p=45 using the drag correlation of Schiller and Naumann (1933) for particles in gas flows	48
3.3	Solids pressure functions used in literature	52
3.4	Plot of solids viscosity versus solids volume fraction.	57
3.5	Elastic collision of two solid spherical particles of different sizes	58
3.6	Collision of a single sphere with a cloud of particles in shear flow	60
3.7	Limiting cases for solids volume averaging analysis.	69
3.8	Minimum control volume size for statistically valid multiphase averaging.	71
4.1	Control volume indices in CFX 4.2	74
4.2	Simple flow variables either side of a shock.	76
4.3	Variable locations at mesh intersections	77
4.4	Superbee TVD scheme	81

4.5 TVD half cell construction in forward direction 83

4.6 TVD half cell construction in backward direction 84

4.7 Construction of the parabolic interpolation 86

4.8 First order upwinding test. 92

4.9 Lax-Wendroff test. 93

4.10 Warming-Beam test. 93

4.11 MINMOD test. 94

4.12 MUSCL test. 94

4.13 Superbee test. 95

4.14 Total variation plots with time step for each of the discretization schemes studied. 95

4.15 Inner and outer iteration summaries in CFX 4.2 107

5.1 Photograph of experimental two dimensional bed filled with coke particles 111

5.2 Definition of geometry variables used in FORTRAN user file 111

5.3 Typical mesh used for simulations 114

5.4 Meshing algorithm 116

5.5 Boundary conditions and discretization mesh in three dimensions 117

5.6 Inner residual reduction with under relaxation tests for Run 1, Table 5.2 121

5.7 Inner residual reduction with under relaxation tests for Run 2, Table 5.2 121

5.8 Inner residual reduction with under relaxation tests for Run 3, Table 5.2 122

5.9 Inner residual reductio with under relaxation tests for Run 4, Table 5.2 122

5.10 Inner residual reduction with under relaxation tests for Run 5, Table 5.2 123

5.11 Inner residual reduction with under relaxation tests for Run 6, Table 5.2 123

5.12 Inner residual reduction with under relaxation tests for Run 7, Table 5.2 124

5.13 Inner residual reduction with under relaxation tests for Run 8, Table 5.2 124

5.14 Inner residual reduction with under relaxation tests for Run 9, Table 5.2 125

5.15 Double precision residuals comparable to Table 5.2, Run 9. 126

5.16 Gas continuity residual using Courant false time stepping 128

6.1 Diagram of the fluidized bed experimental apparatus. Modified from Jason Cowpan's MSc thesis, University of Saskatchewan, 1999. 133

6.2 Cut away diagram of the windbox. Courtesy of Jason Cowpan MSc thesis, University of Saskatchewan, 1999. 134

6.3 Definition of the bubble dimensions from digitized video observations 139

6.4 Demonstration of "fingers", round bubbles and bubbles cleaving into mushrooms. 140

7.1 Time series gas volume fraction isosurface plots. U_{jet}=150 m/s. 149

7.2 Time series gas volume fraction isosurface plots. U_{jet}=250 m/s. 150

7.3 Time series gas volume fraction isosurface plots. U_{jet}=300 m/s. 151

7.4 Nozzle inlet boundary control volume specification and jet velocity 155

7.5 Gas mass residuals versus iteration count for run DA01 156

7.6 Gas mass residuals versus iteration count for run DA02 157

7.7 Gas mass residuals versus iteration count for run DA04 157

7.8 Gas mass residuals versus iteration count for run DA05 158

7.9 Gas mass residuals versus iteration count for run DB01 158

7.10 Gas mass residuals versus iteration count for run DB02 159

7.11 Gas mass residuals versus iteration count for run DC01 159

7.12 Gas mass residuals versus iteration count for run DC02 160

7.13 Generalized sense of vorticity in the near jet region 161

7.14 Additional vortex structures predicted in the near jet region with a dense computational mesh 162

7.15 Comparison of hydrodynamic model B (left) and model A (right). Gas volume fraction contours 164

7.16 Bed surface height over time for run CA01 173

7.17 Bed surface height over time for run CB01 173

7.18 Predicted solids streamlines and bed surface at minimum fluidization 175

7.19 Predicted solids streamlines and bed surface below minimum fluidization 175

7.20 Predicted solids streamlines and bed surface with zero aeration; packed bed condition. 176

7.21 Transient bed behavior with a step change in fluidization velocity 178

7.22 Jet regime phase diagram of Chyang *et al.*(1997) for all simulations 180

7.23 Maximum jet penetration defined on a gas iso-contour of 0.8 from tip of nozzle. 182

7.24 Penetration results form simulations compared with the expression of Merry (1971). 185

7.25 BA02 solids flow pattern vectors in the fluidized bed. 186

7.26 BA03 solids flow pattern vectors in the fluidized bed 186

7.27 Recirculation zone beneath the nozzle inlet pipe close the low X wall of the simulation 187

7.28 Solids wake region behind nozzle pipe and entrainment into jet. 187

7.29 Instantaneous solids flow patterns for seeding above the jet plume run BA02. 189

7.30 Instantaneous solids flow patterns for seeding below the jet plume run BA02 190

7.31 Predicted gas and solids instantaneous streamlines. 191

7.32 Predicted bubble in a fluidized bed at start up. 197

7.33 Predicted bubble in a fluidized bed at less than minimum fluidization. 197

7.34 Predicted bubble in a fluidized bed at greater than minimum fluidization 198

7.35 Predicted bubble in a packed bed or zero fluidization 198

7.36 Predicted time averaged gas volume fraction data for run CA01 across the width of the bed. $0.5U_{mf}$ U_{jet}=150 m/s 202

7.37 Predicted time averaged gas volume fraction data for run CB01 across the width of the bed. $0.5U_{mf}$ U_{jet}=250 m/s 203

7.38 Predicted time averaged gas volume fraction data for run CC01 across the width of the bed. $0.5U_{mf}$ U_{jet}=300m/s 203

7.39 Predicted time averaged gas volume fraction data for run FB01 across the width of the bed. $2U_{mf}$ U_{jet}=250 m/s 204

7.40 Predicted time averaged gas volume fraction data for run FC01 across the width of the bed. $2U_{mf}$ U_{jet}=300m/s 204

7.41 Predicted time averaged gas volume fraction data for run FB02 across the width of the bed. $3U_{mf}$ U_{jet}=250 m/s 205

7.42 Predicted time averaged gas volume fraction data for run FC02 across the width of the bed. $3U_{mf}$ U_{jet}=300 m/s 205

7.43 Predicted time averaged gas volume fraction data for run GB01 across the width of the bed. $2U_{mf}$ U_{jet}=150 m/s 206

7.44 Predicted time averaged gas volume fraction data for run GB03 across the width of the bed. $2U_{mf}$ U_{jet}=300m/s 206

7.45 Predicted time averaged gas volume fraction data for run GC01 across the width of the bed. $3U_{mf}$ U_{jet}=150m/s 207

7.46 Predicted time averaged gas volume fraction data for run GC03 across the width of the bed. $3U_{mf}$ U_{jet}=300m/s 207

NOMENCLATURE

Arabic Letters

Symbol	Description
$\bar{r}$	Position vector
$\hat{e}_i$	Unit direction basis vector
$\bar{\bar{J}}$	Jacobian
$\bar{v}$	Velocity vector
$\hat{n}$	Unit normal vector
$\bar{\bar{I}}$	Identity matrix
$\bar{f}_b$	Body force vector
$\bar{\bar{A}}$	General matrix
$\bar{F} = (F_1, F_2, F_3)$	Continuous vector function
$\hat{i}, \hat{j}, \hat{k}$	Unit basis vectors in Cartesian coordinates
$\dot{m}_{\alpha\beta}$	Thermodynamic phase change from phase α to β
$\bar{U}$	Velocity vector
$\dot{M}$	General mass flux (used in Rhie-Chow interpolation)
$\bar{B}$	Cell average of other terms in momentum equation over point P
ΔU	System relative velocity
Δx, Δy, Δz	Mesh spacing in X, Y and Z directions
(X_1, X_2, X_3)	Particle origin point
(x_1, x_2, x_3)	Current position
A	Bounding area
a_i	Particle radii in a specific group

A_i	Area of control volume face at position i=N,E,S,W
a_i	Advection and transient coefficients for phase i
a_{ij}	General *ij* element of matrix $\overset{=}{A}$
A_{ij}	Cofactor of matrix $\overset{=}{A}$
$A_{O,C}$	Orifice area in simulation
$A_{O,E}$	Orifice area in experiment
b_i	Interphase transfer coefficient for phase *I*
B_P	Other terms in momentum equation at node P
c	Local characteristic velocity
$c_{\alpha\beta}$	Drag coefficient of phase β on phase α
C_D	Drag coefficient
C_i	Convection coefficient at node i
c_i	Source linearization term for phase *i*
Cn	Courant number
D	Denominator
D	Nozzle orifice diameter in simulation
D_0	Nozzle orifice diameter
D_{32}	Sauter mean diameter
D_i	Diffusion coefficient at position i
D_p	Particle diameter (μm)
d_p	Particle diameter (μm)
ds	Cell miss-match
dV	Change of volume in curvilinear coordinate system.

dV_0	Change of volume in Cartesian coordinate system
e	Restitution coefficient
f	Transported quantity
$F(t)$	Integrated quantity, f, over a volume
$f(x,t)$	Integrable function representing conserved quantity
$f_1 f_2$	Bounding surface functions
f_{12}	Collisional force between particles 1 and 2
f_i	Mapping function from x to ξ coordinate system
f_i	Transport quantity at node i
Fr^*	Modified Froude number
$G(\varepsilon)$	Solids pressure function
G_0	Solids compaction modulus
g_0	Radial distribution function
G_s	Solids stress
h,P,k	Parameters defining the fit of parabola Q_i
h_i	Magnitude of curvilinear transform
i,j,k	Control volume indices
ilen	Total length of 1-D discretization mesh
k	Empirical parameter
k	Gidaspow dense-phase drag correction multiplicative factor
l	Average interparticle spacing (m)
M	Particle laden jet parameter from Guedon *et al.* (1994)
m^*	System relative mass

m_i	Individual particle mass
n	Number density
n	Iterate count or time step
N	Numerator
N,E,S,W	Relative position of neighboring nodes to central node P
n,e,s,w	Control volume interfaces
P	Particle, general
P	Pressure
p	Gidaspow drag correction exponent
p^*	Pseudo-pressure
p'	Pressure correction
P_i	Pressure at node i
P_s	Solids pressure
Q_i	Parabola built off of point i
r	Radius
r	Flux limiter ratio
R	Residual
Re_P	Particle Reynolds number
R_{min}	Minimum control volume radius (m)
S	Entropy
S	Volumetric source term
S_C, S_P	Linearized source terms
S_{ij}	Velocity strain rate tensor

t	Time (s)
T	Absolute temperature
U	Internal energy of a powder
u^*, v^*, w^*	Pseudo-velocities in pressure correction method
U_b	Bubble rise velocity
U_{mf}	Minimum fluidization velocity
U_p	Particle approach velocity
$v(t)$	Volume at time t in n-space
V_b	Specific volume, volume weighted specific bulk volume
v_k	Volume occupied by phase k.
v_p	Volume of one particle
X	Value at node X

Greek Letters

$\bar{\xi} = (\xi_1, \xi_2, \xi_3)$	Curvilinear coordinate system
$\overset{=}{\tau}$	Shear stress tensor
ε_p^C	Calculated volume fraction based on a volume average
ψ	Diffusional flux vector of f
Φ	Volumetric rate of production of f
ρ	Density (kg/m^3)
μ	Molecular (fluid) viscosity
ζ	Bulk viscosity
δ	Error bound on CV

β	Drag force exerted on a single sphere
Γ	Diffusivity
ψ	Flux limiter
$\phi()$	Lagrangian position function
ε^*	Compaction volume fraction
α,β,γ	Direction cosine angles
δ_{ij}	Kronecker delta
ε_{mf}	Volume fraction at minimum fluidization
λ_{mfp}	Mean free path between particle collisions
ε_p	Phase average volume fraction (true value)
ϕ_s	Sphericity
Θ_s	Granular temperature

Superscripts

*	Pseudo value
C,PARABOLIC	Central differencing using parabolic interpolation
CENTRAL	Lax-Wendroff central differencing
n	Time step
n+1/2	Half time step or pseudo time step
UP	Upwinding
UP2	Second order upwinding

Subscripts

i+1/2, i-1/2	Half cell values

Abbreviations

CV	Control Volume
DNS	Direct numerical simulation
FCC	Fine cracking catalyst
FD	Flow domain
FOUW	First order upwinding
IPSA	Interphase Slip Algorithm
LW	Lax-Wendroff Central Differencing
PEA	Partial Elimination Algorithm
SIMPLE	Semi-Implicit Method for Pressure Linked Equations
WB	Warming-Beam Differencing

Chapter 1

Introduction

This project studied the use of a two-fluid multiphase computational fluid dynamics model for simulating the interaction of a horizontal gas feed jet on the hydrodynamics of a gas/solid fluidized bed. Two of the largest fluidized bed reactors are located in Fort McMurray, north Alberta to hydrocrack the oil from the rich oil sands reserves. Design modifications to these units or construction of an additional reactor is a very costly undertaking and requires the best available design tools. The main aim of this project was to provide a review of the current state of the art multiphase flow modeling software from AEA Technology to model a two phase gas fluidized bed and provide information about model limitations, requirements and predicted flow behavior in a much smaller pseudo-two dimensional fluidized bed. These studies will be used to continue the modeling work with a reacting gas/solid/liquid fluidized bed system. Work from this study will provide a theoretical basis from which to continue.

Theoretical work requires comparison against experimental observations for validation. It also requires internal model verification to ensure that the model assumptions and solution methods are reliable under different operating conditions. Both model verification and validation has been carried out in this work to provide a basis on which to continue multiphase flow modeling.

A fully three dimensional, transient incompressible two fluid simulation model was set up and solved using the CFX 4.2 solver from AEA Technologies. The solids phase was assumed to consist of completely spherical, monosized particles of constant density. The gas phase was assumed to be incompressible and behave as a laminar air flow. No turbulence model was used for these simulations.

A single phase gas jet was discharged into a rectangular computational domain representing an incipently fluidized two-phase bed. The nozzle was modeled to be at the end of a length of solid pipe with an orifice of comparable area to that used in the experimental apparatus at the University of Saskatchewan. Fluidization gas was injected through the distributor at the bottom of the bed providing aeration for the solids phase. Only gas was allowed to pass out of the top section of the bed thereby ensuring a constant mass of solids within the fluidized bed. All geometric parameters of the fluidized bed simulation were adjustable through use FORTRAN routines.

Simulation data was recorded every 0.05 seconds for analysis. The analysis of multiphase flow simulations can be very complicated and several different techniques to observe the data were used. One of the most useful ways to study the data was in the form of animated movies that provided flow information about the formation of the jet plume and bubble formation within the fluidized bed. Instantaneous streamlines for the solids and gas phase were also plotted to determine how the flow field might look at an instant in time. Time averaged volume fraction data over the width of the bed provided information about the transient behavior of gas and solids voidage.

This thesis is broken into three main parts concerning theoretical background and derivations, experimental observations and computational results. Chapter 2 deals with an introduction to fluidization technology and the related flow phenomena that have been observed. In Chapter 3, rigorous derivations of single phase hydrodynamic equations are discussed and their extension to multiphase flow systems are outlined. Chapter 4 touches on numerical methods available for solving the partial differential equations derived in Chapter 3 and goes on to discuss the merits and weaknesses of the current state-of-the-art computational methods. Chapter 5 details the set up and assumptions used when performing the fluidized bed simulations in this study. Chapter 6 describes the experimental facilities and the results that were obtained for validating the simulation results. Chapter 7 focuses on validation and verification of the computational results against those listed in Chapter 6. Chapter 8 provides a conclusion and recommendations for future work.

Chapter 2

Literature Review

This thesis focuses on the application of computational fluid dynamics to multiphase flow modeling with the specific intention of verifying and validating the application of such models to the interaction of a horizontal gas jet within a gas-solid fluidized bed. Fundamental governing equations for single-phase flow models are reviewed and extended for multiphase flow systems. Current state-of-the-art numerical methods for solving the resulting transient, three-dimensional partial differential equations are presented and contrasted. Experimental results are used to compare against the simulation studies for validation of the solution and modeling methods. This chapter provides a brief overview of the rich body of research that has been conducted concerning fluidization technology and some of the approaches available for simulation.

2.1 Flow Behavior within a Fluidized Bed

2.1.1 General Flow Behavior

The understanding of the overall flow patterns within fluidized beds has been given great attention over the past decade due to the use of this technology in a wide range of industries. In the petroleum industry the development of more active catalysts for the production of gasoline requires the replacement of older bubbling fluidized beds with circulating fluidized beds. Fluidized bed nuclear fission reactors are even being investigated as an alternative to traditional designs (Rots *et al.*, 1996). New emissions standards are forcing the electric power industry to burn coal with much lower emissions of sulfur and nitrogen oxides (Miller and Gidaspow, 1992; Lyczkowski *et al.*, 1993). Erosion of internal fluidized bed surfaces, and even of the particulate phase itself (Werther and Xi, 1993), remains a challenge and needs to be addressed in more detail for continued widespread commercial application of this technology (Lyczkowski *et al.*, 1993; Bouillard *et al.*, 1989). Berruti *et al.* (1995) present a good review of the hydrodynamics of circulating fluidized beds and some of the current research requirements. Many studies have focussed on the gas-particle flow in vertical pipes (Sinclair and Jackson, 1989; Nakamura and Capes, 1973). It has been suggested that the overall flow patterns within multiphase flow systems, including gas in liquid and solid in gas flows, might be more dependent upon coherent structures present in the flow field. An excellent review of these coherent structures present in multiphase flows is presented by Van Den Akker (1998).

Fluidized beds operate over a wide range of flow regimes which are set by both the fluidization gas velocity and the nature of the particles being fluidized (Fan and Zhu, 1998). A general overview of these flow regimes and their dependence on fluidization velocity is shown in Figure 2.1.

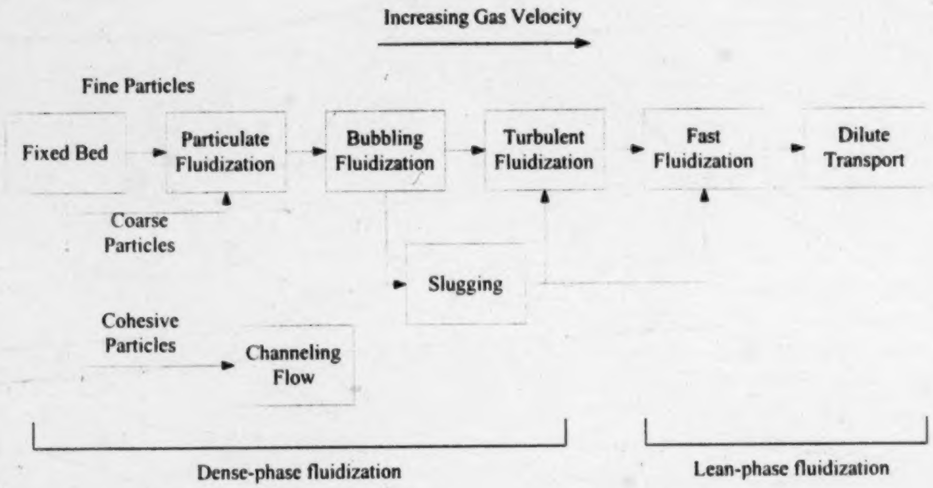
Increasing Gas Velocity
Fine Particles
Fixed Bed
Particulate Fluidization
Bubbling Fluidization
Turbulent Fluidization
Fast Fluidization
Dilute Transport
Coarse Particles
Slugging
Cohesive Particles
Channeling Flow
Dense-phase fluidization
Lean-phase fluidization

Figure 2.1 – Different fluidization flow regimes in a fluidized bed. Adapted from Chyang *et al.* (1998).

Dense-phase fluidization encompasses particulate fluidization, bubbling fluidization and turbulent fluidization. Above these gas flow velocities the behavior of the bed changes to a more dilute system and can be classified as being lean-phase fluidization. Fixed beds represent a percolating flow through a packed bed of particles. At higher fluidization velocities between minimum fluidization and minimum bubbling fluidization the bed is said to behave in the particulate fluidization regime. The bed appears homogeneous and the gas flows through the interstitial spacing between particles. This regime only exists for Geldart Type A particles (Geldart 1973) under a narrow operating range of gas velocities. Increasing the fluidization velocity above the minimum bubbling velocity leads to the formation of bubbles within the fluidized bed or the so called bubbling fluidization regime. In the bubbling fluidization regime bubbles are readily observed within the dense phase of the bed. Higher fluidization velocities lead to the turbulent fluidization regime where there is vigorous movement of the particles within the bed but distinct bubbles are not discernible. The surface of the bed becomes more diffuse due to the increased entrainment of solid particles into the freeboard section of the reactor (Figure 2.2 c).

Vessel geometry can also lead to a change in the fluidization behavior observed with increased fluidization velocity. Slugging refers to the regime where bubble sizes comparable to the width of the vessel are present (Figure 2.2 d). This behavior is most noticeable when the ratio of bed width to height is quite low. In this case particles are moved up through the bed as slugs. Increasing fluidization velocity in the slugging regime can lead directly to turbulent fluidization or fast fluidization.

In addition to fluidization gas velocity dependencies, the method of delivery of aeration gas will affect the fluidized bed flow behavior. Spouting fluidization occurs when a central jet is introduced into a fluidized bed. Solids are entrained in the central core region and accelerated upwards along the axis of the reactor forming a dilute core flow region. Entrained solids fall on to the top of the bed where they recirculate back down along the dense annular region forming a solids circulatory pattern (Figure 2.2 e).

Channeling within a fluidized bed is usually due to the cohesive nature of particles. Particle shape, size and density can also have effect on the channeling effects. Channeling can also occur in a bed when the fluidization gas is not evenly distributed across the distributor plate (Figure 2.2 f).

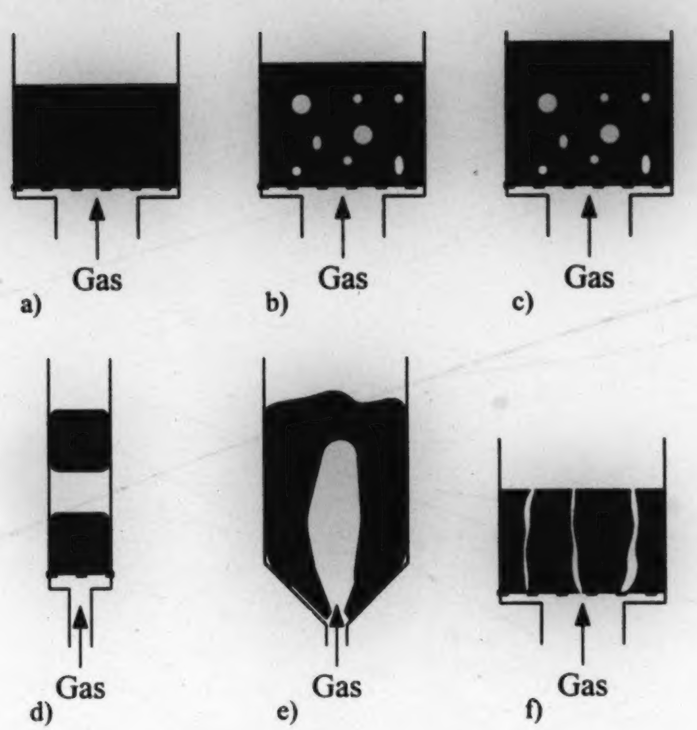

Figure 2.2 – Gross characteristic flow regimes in a fluidized bed. Adapted from Chyang *et al.* (1998)

Circulating fluidized beds represent one of the most versatile types of industrial fluidized beds and find application in coal combustion, incineration and petroleum upgrading. Solids are taken from the freeboard section of the reactor and recycled (or recirculated) back to the dense phase region of the reactor using a nonmechanical or L-valve. Tsuo and Gidaspow (1990) report that experimental observations by several authors (Weinstein *et al.*, 1986; Hartge *et al.*, 1986) show a nonhomogeneous radial distribution of solids volume fraction that increases monotonically with radius. A core-annulus type of flow pattern in circulating fluidized beds has been shown to exist in several experimental reports (Capes and Nakamura, 1973; Gajdos and Bierl, 1978; Bader *et al.*, 1988; Miller and Gidaspow, 1992). Solids radial fluxes are measured in a fluidized bed using a probe which is inserted into the flow with the collection port facing upwards (to measure downwards flux) or downwards to measure upwards flux. Since the fluidized bed is a transient system, measurements must be time averaged and the upwards and downwards fluxes subtracted to get the total flux and direction. Many early attempts at mathematically modeling two phase flow behavior have used one dimensional formulations; however, care must be taken when observing early one dimensional attempts (Yerushalmi *et al.*, 1976) since the flow was assumed to be unidirectional and this has been shown to be an incorrect assumption. Sinclair and Jackson (1989) further cite that a one dimensional analysis can be inappropriate when the single dimension is not at right angles (90° or 180°) to the gravity vector in which case particles will tend to be distributed nonuniformly over the cross section as a result of gravitational sedimentation.

Gidaspow *et al.* (1989) have carried out an experimental study of the formation and descent of solids clusters within a circulating fluidized bed apparatus. This work was complemented by a later study (Tsuo and Gidaspow, 1990) using a two dimensional computational fluid dynamics model studying the flow patterns within a circulating fluidized bed. With these numerical studies they observed cluster formation along the walls of the vessel measuring approximately 2 to 3 cm in size and traveling downwards at 1.1 m/s. Clusters were observed to combine and grow in size. From this study they have concluded that for the dilute circulating fluidized bed regime their two dimensional model can predict the formation of clusters in agreement with observations. For dense phase fluidization regimes the flow system behaves as a core annulus type of system with solids down flow along the vessel walls. This too was in agreement with experimental observations.

2.2.2 Bubble Movement within a Fluidized Bed

Considerable effort has been concentrated on formulating the hydrodynamic models describing multiphase flows in industrial equipment such as fluidized beds and pneumatic transport riser systems. Davidson (1961) first formulated multiphase flow hydrodynamics by constructing two continuity equations (one each for the gas and solids phases) and expressed the relative velocity between the two phases in terms of Darcy's law for flow in porous media. He also assumed that the solids flow around bubbles was irrotational ($\nabla \times \bar{v} = 0$); this assumption can be justified based on the mixture momentum balance (Gidaspow and Solbrig, 1976; Lyczkowski *et al.*, 1982). Bubbles within the fluidized bed play a significant role in the dispersion, mixing and contact between the gas and solids phases. Jackson (1963) carried out perturbation analyses of his governing equations and showed that a small perturbation in voidage will grow without bound. Davidson and Harrison (1963) analyzed bubble formation on the assumption that there must be some stable bubble size that will form within the fluidized bed. This stability was defined in terms of bubble size that had to be greater than the terminal velocity of the particles for the formation of a stable bubble. Rietema and Mutsers (1973) used a small perturbation analysis, reviewed in detail by Jackson (1985), to obtain a criterion for bubbling. Rietema and Mutsers' work has been continued by Mutsers and Rietema (1977), Piepers *et al.* (1984) and Rietema (1984). The analysis of bubbles as shocks, or flow instabilities, within the fluidized bed domain is in addition to the question of stability of the governing hydrodynamic equations as analyzed by Lyczkowski *et al.* (1978).

The question of the formation of bubbles within a fluidized bed has been studied by many people (Fanucci *et al.*, 1979; El-Kaissy and Homsy, 1976; Jackson, 1963; Pigford and Baron, 1965; Garg and Pritchett, 1975). However, as pointed out by Jackson (1963) most stability studies have used linear stability theory to predict the onset of bubbles. There is no guarantee that a small perturbation will grow when the nonlinearities of the governing equations can no longer be neglected. Verloop and Heertjes (1970) were the first to show that shock waves will form within a fluidized bed when porosity waves rise faster than an equilibrium disturbance. Foscolo and Gibilaro (1984) determined an expression for this velocity based on particle properties and the gravitational constant by neglecting inertial effects. This work was extended by Rowe (1986) for Geldart Type A and B powders (Geldart, 1973).

Fanucci *et al.* (1979) presented a rigorous characteristic analysis of the governing partial differential equations. Assuming a sinusoidal particle velocity variation with time at the distributor plate they determined that the characteristic paths intersected and shocks formed. This type of analysis was repeated by Rasouli (1981) using the relative velocity equations; similar intersecting characteristic paths were also observed. Each of these analyses have used the somewhat unrealistic formulation where the inlet velocity has varied sinusoidally with time. Harris and Crighton (1994) have considered the evolution of an initially small voidage disturbance in a gas fluidized bed; their analysis resulted in the prediction of gas slugs which are common in flow systems where the ratio of the height of the vessel is large when compared to its diameter. Gidaspow (1994) dedicates a chapter to the formation of bubbles and their treatment as shocks within a fluidized bed for a one dimensional analysis using a slip velocity formulation of the void propagation equation. He starts by defining a one dimensional continuity equation for both the solids and gas phases; these equations are linked by the definition of the void fraction which must sum to one in order to satisfy continuity. The gradient of the relative velocity between the two phases is expressed in terms of the relative velocity model of Gidaspow (1994) which includes terms for gravity, drag, vessel wall friction and solids normal stress. A limiting case of a fluidized bed at minimum fluidization is assumed so that the Ergun equation can be applied for the drag relationship. Gidaspow also assumed that the flow was fully developed and that the relative velocity was based on a balance between the buoyant and drag forces within the bed. Based on these assumptions a characteristic void propagation can be determined and compared with the convective void propagation velocity in the bed. If this characteristic velocity is greater than that of the bed, then shocks, hence bubbles, will form. However if this velocity is less, then the bubble will dissipate into the bed and bubbles will not form.

Much experimental work has been carried out to study single bubbles within gas fluidized beds at minimum fluidization. Single bubble dynamics within a fluidized bed are similar to those in a liquid medium (Clift and Grace, 1985; Fan and Tsuchiya, 1990; Krishna, 1993). Most bubbles within a fluidized bed are either of spherical cap or elliptical cap shape. Two basic types of bubbles have been observed, the fast bubble and the slow bubble, each is shown in Figure 2.3 a and b, respectively.

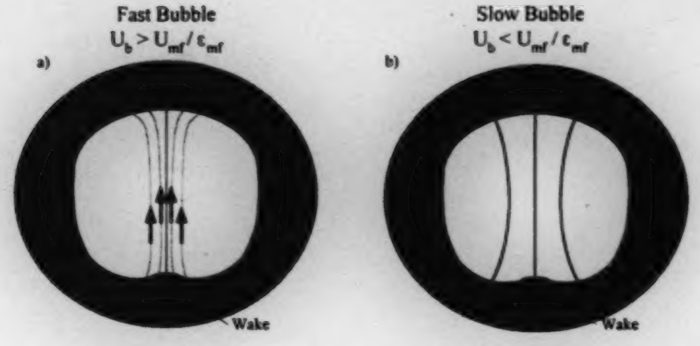
Fast Bubble
$U_b > U_{mf}/\varepsilon_{mf}$
a)
Wake
Slow Bubble
$U_b < U_{mf}/\varepsilon_{mf}$
b)
Wake

Figure 2.3 – Flow patterns within voids formed in fluidized beds. a) fast bubble, b) slow bubble.

A cloud region is formed around the periphery of the bubble and circulates in a closed loop between the bubble and the fluidized bed. Rowe (1971) visualized this cloud by injecting a coloured NO_2 tracer gas near the periphery of the bubble. When the bubble propagation rise velocity, U_b, is greater than that of the interstitial fluid, a "clouded" fast bubble forms and the gas recirculates up through the centre of the bubble and out of the top of the void. As the gas rise velocity increases significantly higher than the interstitial fluid velocity the cloud becomes very thin and internal recirculation of the gases within the bubble takes place. However, when the gas rise velocity is less than the interstitial fluid velocity, a cloud does not form around the bubble. Instead the interstitial gas flows through the bubble (Fan and Zhu, 1998). Gabor (1972) reported experimental observations of the bubble movement within a freely bubbling fluidized bed and how this movement affected a horizontal line of coloured tracer particles within the bed. As the bubble moves up through the bed the particles did not pulse upward during bubble formation on the distributor plate. The particles remained at rest until a rising bubble came into their vicinity. Particles near the bubble but not along the axis of bubble rise were initially moved upward and then followed a curved trajectory downward.

Therefore, actual bubble rise in a fluidized bed causes particles to move with a net downward displacement unless the particles fall through the bubble roof and get carried upwards in the bubble wake.

Bubbles play a significant role in the solids movement throughout fluidized bed reactors and for the contact of solids with the gas phase; it has been suggested that the solids transport in the wakes of rising voids is *the* essential mixing mechanism (Kunii and Levenspiel, 1991). The importance of locating feed materials within the bubble zone has been stressed by Guedon *et al.* (1994) for the proper mixing of prepolymer materials within fluidized beds and for the avoidance of hot spots within the reactor. The rising voids within the fluidized bed causes some lateral drift of solids within the fluidized bed (Grace *et al.*, 1997; Valenzuela and Glicksman, 1984; Eames and Duursma, 1997) as solids particles are displaced radially with void passage. Eames and Duursma (1997) carried out theoretical calculations and report that it is the ratio of initial bubble distance from the bed surface to vessel width and not the ratio of bubble diameter to vessel width that has a marked effect mixing. Bubble wakes in single-phase flow are defined as the streamline enclosing the region beneath the bubble base (Fan and Zhu, 1998). In a gas-fluidized bed this single phase can be considered to be the emulsion phase, a combination of the gas and solids phases within the fluidized bed. Hence, a bubble wake is defined as the area enclosed by a streamline at the base of the bubble. Littman and Homolka (1973) made pressure measurements around a bubble moving through a fluidized bed and concluded that the pressure wake is also closed and can trail as much as twelve bubble radii. As the bubble rises through the bed the solids in the wake are entrained and carried up the bed. This provides a mechanism for the overall mixing of the solids within the bed. Bubble formation within small laboratory apparatus typically form slugs with solids trickling through the top of the bubble (Figure 2.2 d); however, in larger industrial units bubbles are often formed away from the walls and will proceed rapidly up the reactor thereby decreasing residence time (Behie *et al.*, 1970).

Two different views can be applied when studying bubble wakes within a fluidized bed. The first view, attributed to Clift (1986), is based on analogy to gas bubbles in liquids. The bubble Reynolds number Re_b is of the order of 100. At this flow regime it would be expected that the bubble rise through the fluidized bed would lead to a vortical motion of particles and gas within its wake. The second view indicates that the wake is produced by gas and solids entering the wake from the outer boundary, flowing radially inward toward the bubble center and vertically downward out of the wake (Kozanoglu and Levy, 1991). At this time more thorough experiments are needed to clarify either of these views. It has been reported (Rowe and Partridge, 1965; Rowe, 1971) that vortex shedding may occur in gas fluidized beds in the wake region of a bubble.

Models have been proposed to solve the governing equations of multiphase flows to predict bubble behavior within the fluidized bed. Two-fluid models have been formulated by many researchers (Kuipers *et al.*, 1992; Gidaspow, 1986; Tsuo and Gidaspow, 1990; Bouillard *et al.*, 1991; Ding and Gidaspow, 1990; Gidaspow and Ettehadieh, 1983); this particular approach to modeling is described in detail in Chapter 2. Lagrangian approaches have also been attempted whereby each particle within the fluidized bed is tracked according to Newtonian physics and the interstitial gas flow field is calculated based on Eulerian field mechanics. Hoomans *et al.* (1995) have carried out such simulations using 40,000 particles and compared these results with experimental results for bubble formation and rise times. Their model involved a hard sphere approach with the input of a restitution and friction coefficients. Other exotic forms of solving the governing equations have been attempted with varying degrees of success. Andrews and O'Rourke (1996) have implemented a Multiphase Particle in Cell (MP-PIC) method employing both a two fluid model but with a clumping of solids particles in a Lagrangian sense.

2.2.3 Vertical Jet Behavior

Much research has focussed on the penetration of vertical jets into fluidized beds (Merry, 1975; Gidaspow *et al.*, 1983; Filla *et al.*, 1983). The high speed impingement of particulate on vessel internals can lead to attrition and eventual wear of the structures. For beds with fast chemical reactions much of the conversion may occur in the jetting zone near the distributor plate (Behie and Kehoe, 1973; Behie *et al.*, 1975). Merry (1975) analyzed data for vertical jet penetration into fluidized beds from several sources (Markhevka *et al.*, 1971; Basov *et al.*, 1969; Zenz, 1968; Shakhova, 1968; Yang and Kearns, 1970) and proposed an expression that correlates a wide range of data.

$$\frac{L}{d_0} = 5.2\left(\frac{\rho_f d_0}{\rho_p d_p}\right)^{0.3}\left[1.3\left(\frac{u_0^2}{g d_0}\right)^{0.2} - 1\right] \tag{2.1}$$

Expression (2.1) is quite general and correlates a wide range of data for gas and liquid fluidized beds, with nozzles up to 35 mm diameter and jets of up to 0.5 m in length. All of the data used were for beds of effectively uniform particle size and for Merry's correlation it was not clear at present exactly how the mean particle size D_p in the correlation should be specified for a bed with a very wide range of particle sizes. Wen *et al.* (1981) have stated that it is important to set up experiments whereby wall effects are minimized and a more realistic interaction of several jets is studied. In some situations the physical implementation of this is very difficult. Computer simulations have been shown to be effective for predicting the overall behavior and pressure distributions within circulating fluidized bed reactors fluidized with a central vertical jet (Benyahia *et al.*, 1996).

2.2.3 Horizontal Jets in Fluidized Beds

One of the most common ways of introducing feed into a fluidized bed is the use of nozzles which are inserted into the vessel; this approach is common for petroleum upgrading. Lummi and Baskakov (1967) injected a CO_2 tracer with an air jet to measure tracer concentrations within the bed. Zenz (1968) presented a curve to predict horizontal penetration depth. Shakhova (1968) derived an expression for horizontal jet penetration based on a simple momentum balance. Kozin and Baskakov (1967) proposed a correlation for horizontal jet penetration based on specific air distributor designs. Two of the earliest reports for predicting the penetration of a horizontal gas jet into fluidized beds were conducted by Shakhova (1968) and Merry (1971). Early investigations by Merry (1971) used a series of pseudo-two dimensional fluidized beds with transparent face plates to visually measure the penetration of a horizontal gas feed jet into the fluidized bed. Merry investigated using beds of sand, kale seed and steel shot under atmospheric conditions. Nozzle diameters of 2.54 to 14.3 mm were used with jet exit velocities of between 40 and 300 m/s. He found maximum penetrations of 30 cm and proposed a semi-theoretical expression for predicting maximum jet penetration into the bed based on fluid properties (viscosity, density), nozzle diameter, inlet jet velocity and bed properties (density, particle diameter and void fraction). This expression has been applied to a wide range of data reasonably well and predicts horizontal penetrations to within ±30%.

A horizontal gas jet injected into a fluidized bed essentially becomes a two-phase jet of gas and entrained solid particles. Solids particles from the jet are entrained in the jet and accelerated in the gas jet stream. Abramovich (1963) analyzed a two-phase jet in air by assuming that the motion of the admixture particles approximated the local air velocity and that the transverse cross-section of the jet was similar to the temperature profiles observed in jets of non-uniform temperature. His analysis only applies to tiny liquid droplets and dust in a jet which are said to be one way coupled and have an insignificant impact on the jet flow field. In a fluidized bed there are often considerable relative velocity differences between the gas and solid phases and this dilute jet analysis is not appropriate. The situation is complicated by the fact that the relative velocity will vary both along the length of the jet and also across the jet. Merry presented a well thought out approach for modeling jet discharge into a fluidized bed as follows: treat the two-phase jet as if it were a homogeneous jet in which the density varies only along the axis (this variation is due to the change in relative velocity between particle and gas as the particle travels through the jet region). This expression is then modified to account for the fact that particles of different size will be accelerated from rest at different rates. This simplification is justified by the fact that the pressure gradient along the jet axis in a fluidized bed is small.

Bubbles are assumed to form only at the end of the jet region and an insignificant number of bubbles actually come off of the jet plume. The jet acts as a sink with particles becoming entrained and then accelerated to the jet velocity. These high-speed particles will bump into slower moving particles that have just been entrained into the jet and as such the slower moving particles will rebound back out into the boundary of the jet. Merry contends that this is the mechanism by which the top surface of the jet void is supported within the fluidized bed. By balancing the drag force with the weight that is exerted on the particle Merry determined that the jet boundary is in a state of stable equilibrium with the local gas velocity.

Three zones can be defined for the particle movement within the fluidized bed region adjacent to the jet/bed boundary. Region A is where the jet acts like a sink and the particles are entrained into the jet. Region B is the path of the particles within the jet which either travel downwards towards the bottom of the jet or get rebounded back into the jet boundary. Where momentum transfer to the entrained particles is greater, deceleration of the gas stream is greater and jet penetration is less. Merry reported that particles in the region near the nozzle orifice at the inception of the jet actually appear to migrate in a direction opposite to that of the flow of the gas jet; this has been confirmed by Xuereb *et al.* (1991).

An approximate solution for the discharge of a turbulent jet into a fluidized bed was presented by Shakhova (1968). He assumed that the jet plume and the fluidized bed are separated by a two-phase boundary layer consisting of plume gas (the jet) and the fluidized bed emulsion phase. This boundary layer between the jet plume and the fluidized bed is divided into two zones and showed the validity of this model with experimental results. Based on his calculations, as the thickness of this two phase zone increases the mean density of the jet plume also increases. Due to boundary layer growth, the transverse jet density changes with increasing jet penetration into the bed. Shakhova assumed that Schlichting's equation governs the jet cross sectional velocity profile and used expressions for boundary layer thickness and an integral momentum balance to determine the axial velocity distribution. As the axial velocity decreases, the fluidized bed density exerts an ever-increasing influence on the jet surface and the plume begins to collapse. Based upon these relationships, he developed an expression for the horizontal jet penetration into the bed. Unfortunately, Shakhova chose to neglect the observed hydrodynamic effect of bubble formation and fluidization velocity. Fluidization gas velocity has an effect on the overall bed porosity, which would impact on the average bed density and hence the two-phase boundary layer in his model. His final working equation was based upon a simple turbulence model and required an empirical parameter for turbulence values.

A summary of several expressions for horizontal jet penetration is listed in Table 2.1. Not all of the expressions were developed for horizontal gas jets being discharged into a fluidized bed. The study by Hong *et al.* (1997) investigated the penetration from an inclined nozzle but their expression treats the horizontal penetration as a special case. Guedon *et al.* (1994) investigated the penetration depth of inclined solids laden jets into fluidized beds and their relationship listed is also a special case of their more general expression. Only the expressions of Merry, Shakhova and Zenz were used to compare against simulation results.

Table 2.1

Horizontal Penetration Expressions from Literature

Expression	Author
$\frac{L_{\max} - L_{\min}}{2d_0} = 7.8\left[\frac{\rho_g}{\rho_p}\frac{U_0}{(gd_0)^{1/2}}\right]$	Shakhova (1968)
$0.044\frac{L_{\max}}{d_0} + 1.57 = 0.5\log\left(\rho_g u_0^2\right)$	Zenz (1968)
$\frac{L_{\max}}{d_0} = \left[5.25\left(\frac{\rho_0 u_0{}^2}{(1-\varepsilon)\rho_p g d_p}\right)^{0.4}\left(\frac{\rho_f}{\rho_p}\right)^{0.2}\left(\frac{d_p}{d_0}\right)^{0.2} - 4.5\right]$	Merry (1971)
$L_{\max} = 9.7\times10^{14} M^{1.83} U_j^{2.82} \rho_b^{-6.23}$	Guedon *et al.* (1994) (from a solids laden jet)
$\frac{L_{\max}}{d_0} + 3.80 = 1.89\times10^{6}\left[\frac{\rho_j U_j^2}{(1-\varepsilon_g)\rho_s g d_p}\right]^{0.327}\left(\frac{\rho_g}{\rho_s}\right)^{1.974}\left(\frac{d_p}{d_0}\right)^{-0.040}$	Hong *et al.* (1997) (horizontal jet special case)

More recent investigations by Xuereb *et al.* (1991) have included detailed observations about the formation of bubbles from the tip of the jet region and particle migration along the surface of the jet plume boundary. These experiments were carried out in a two-dimensional bed with a transparent face plate in order to study the behavior of horizontal or inclined jets in a gas-solids fluidized system. The use of cinematographic techniques has enabled them to point out the interactions between the jet and the bubbles resulting from the fluidization, as well as the inherent fluctuations of the jet. Values of morphological parameters which characterize the jet were found from pictures and movies: penetration length and expansion angle, corresponding to three positions of the nozzle: inclined upwards, inclined downwards, or horizontal. The effect of the fluidization velocity, the gas injection velocity and the particle diameter was studied in these configurations. The existence of a dragging zone, previously reported by Merry (1971), of particles from the dense phase into the jet, close to the injection point, was confirmed.

Xuereb *et al.* (1991) defined three zones along the length of the horizontal jet into a fluidized bed: i) the particle entrainment zone, ii) the linear jet expansion zone and iii) the bubble zone. Jet penetration fluctuations were caused by the natural formation of bubbles within the fluidized bed and were reported to occur at frequencies between 2 and 5 Hz. As shown by their experimental photographs, it was very difficult to get a good idea of the bubble shape, size, etc… They also observed that naturally occurring bubbles within the fluidized bed will cause the jet to move towards the bubble even if it has to bend downwards.

The late nineties have seen a renewed interest in studying the size and shape of the void formed within a fluidized bed created by the use of a horizontal gas jet. Chen and Weinstein (1993) employed an X-ray technique to measure instantaneous solids void fractions through the depth of a fluidized bed. This method gave a chord (or depth) averaged view of the solids volume fraction and is used for identifying the location and size of the jet plume. Nozzle orifice diameters of 0.64 and 1.27 cm were investigated at jet velocities of 23, 46 and 69 m/s. Maps of the mean solid fraction and of statistical properties of the fluctuating component show that there are three discernible regions in the jet influenced area of the bed: coherent void, bubble trains and a surrounding compaction zone.

Chen and Weinstein (1997) conducted measurements of jet penetration into a fluidized bed using a heated horizontal gas jet and correlating temperature with gas voidage. These data provided a comparison of the picture of the jet structure obtained from the spread of the jet momentum (Chen and Weinstein, 1993) to that of the spread of the heated gas. Gas temperatures were measured in a vertical plane containing the axis of the nozzle jet. Also, the effect of the superficial velocity through the bed distributor was studied. Measurements were made with the thermocouple traverses providing the temperature field in a vertical plane containing the jet axis. Even with a jet velocity of over 30 m/s, the jet was observed to bend upwards a few centimeters from the nozzle. Their data show that there is a bubble train leaving the upper surface of the jet at about 2 cm from the jet entry wall and that bubbles do not typically leave from the tip of the jet plume. This observation is somewhat inconsistent with other studies. Solids were observed to remain stagnant within a zone below the jet. This zone below the jet was inferred from a relatively high temperature zone which is consistent with the existence of a stagnant compaction zone below the jet which is formed by the gas entrained through the zone into the jet. One of the main conclusions of this paper is that Merry's (1971) correlation gives reasonable estimates of horizontal jet penetration over a wide range of fluidized bed operating conditions. Fluidization gas was varied from 0.03m/s to 0.21 m/s and the fluidized particles were FCC with ρ=1450 kg/m^3 and D_p=60 μm.

Chyang *et al.* (1997) continued studies of the gas discharge modes including bubbling and jetting formed at a single horizontal nozzle into a two-dimensional gas fluidized bed by visual observation. Nozzles of diameter 3.0, 4.5, 6.0, 7.5 and 9.0 mm were investigated. Jet velocities were varied from 1 to 130 m/s. Gas discharge modes were determined for different jet flow velocity ranges as follows: For high velocities a permanent flame-like cavity stands in front of the orifice and is called a jet. However, when the jet velocity is low, bubbles are formed at the nozzle orifice and proceed up along the reactor wall. When particles are light and small or the nozzle diameter is large, the gas discharge mode at the orifice will be unstable. These authors call this the "transition state". However, the behavior of a two dimensional system is expected to be quite different from that of a three dimensional system (Chen and Weinstein, 1993; Guedon *et al.*, 1994; Tyler and Mees, 1999) because in the latter case, there is a path by which the gas and solid can move around the sides of the jet. This prevents the jet ceiling from becoming a stagnant zone as it does in the 2D geometry where the jet and the bubble track isolate the ceiling from the rest of the bed. This observation is of significance when using computational fluid dynamics to predict fluidized bed and horizontal gas jet interactions.

Chyang *et al.* (1997) observed that fluidization gas velocity has an effect on the maximum penetration of the jet and are shown in Figure 2.4. At U_f / U_{mf} equal to 0.6-1.0 there was a maximum observed in the jet penetration. Based on this result they decided to continue all tests at minimum fluidization. Jet penetration increased with increased nozzle diameter for a fixed velocity. This result is not surprising as the jet momentum flux increases with increasing orifice size at constant jet velocity. Most authors tend to use the dimensionless number L/D_o as a measure of jet penetration length.

Penetration decreased with increased particle size within the fluidized bed. The literature correlations under estimated the penetration that was measured in this study. Chyang *et al.* (1997) attribute this to the various definitions used for penetration length for the correlations. Some experimentalists use maximum penetration while others use jet curvature or "pinch points" to define the end of the jet plume.

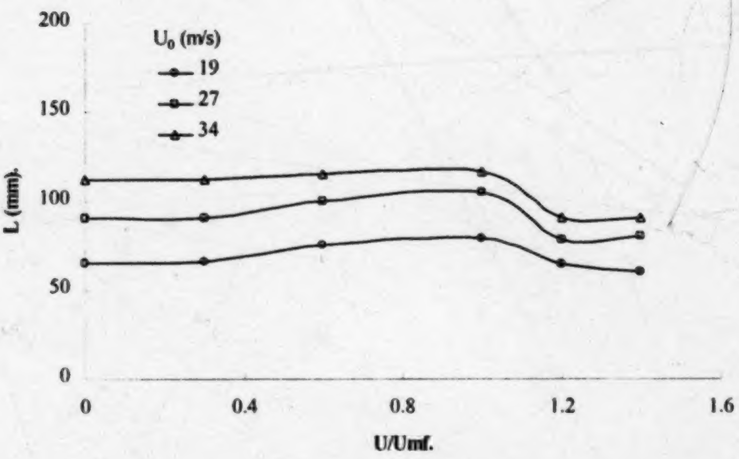

Figure 2.4 – Horizontal jet penetration as a function of fluidization velocity. Adapted from Chyang *et al.* (1997)

Two nondimensional numbers were used to classify the nozzles. The modified Froude number: $Fr^{*} = \frac{2\rho_g D_0^2 U_0^2}{3\rho_p D_p^3 g}$ which is the ratio of gas inertial force at the jet to the gravity force acting on the particles, and the ratio of the nozzle diameter to the particle diameter. Based on these dimensionless numbers and their test runs they determined a nozzle flow regime phase diagram consisting of bubble, jet and transition regimes; see Figure 2.5.

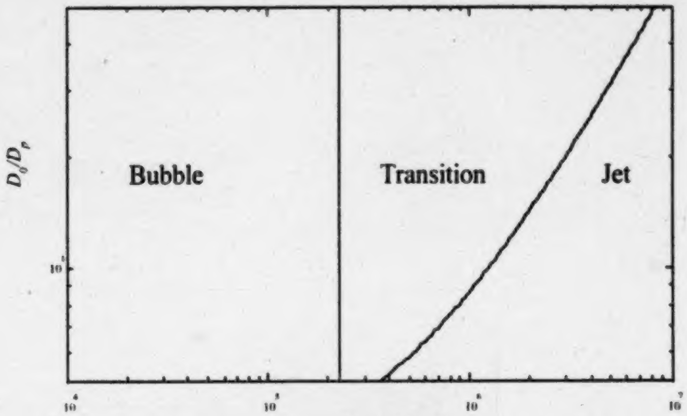

$$Fr^* = \frac{2\rho_g D_0^2 U_0^2}{3\rho_p D_p^3 g}$$

Figure 2.5 - Flow regimes of the gas discharge mode for horizontal nozzles. Group B particles. From Chyang *et al.* (1997) Figure 23.

At high Fr* numbers a jet is readily observed while at low Fr* numbers a bubbling regime is encountered on the phase diagram. From the experiments of Chyang *et al.* (1997) it can be concluded that the gas discharge mode will be changed from bubbling to jetting while as the gas velocity (inertia force / moment) is increased. The dominating factor for gas discharge mode from a horizontal nozzle is the inertial force of the gas flow through the nozzle.

An in depth study of horizontal gas jet penetration was conducted by Hong *et al.* (1997) using a small experimental apparatus of 314x25 mm two-dimensional gas-solid fluidized bed with a vertical jet in the center and an inclined jet at the side of the bed. Millet and two kinds of silica sand were used as the bed material. These particles are quite large, on the order of 1 to 2 mm in diameter, and have a density ranging between 808 and 878 kg/m^3. These researchers also developed a computer code for predicting the penetration depth of the horizontal gas jet into a fluidized bed. First order upwind (FOUW) was used to discretize advection terms (see Chapter 3 for a discussion of numerical methods). Their formulation of the governing multiphase hydrodynamic equations is similar to that used in the software package CFX 4.2.

Hong *et al.* (1997) state that there are two processes occurring near the nozzle. The first being the formation of a torch-like vacant space, which is the jet. This is due to the gas phase drag force being exerted on the solids and creating a volume for the gas. Concurrently, particles are entrained into the jet due to the high gas velocity and the low gas pressure at the bottom of the jet. Therefore, the bottom of the jet is compressed by the entrainment process and to some degree further compression leads to the detachment of the jet from the nozzle and the subsequent formation of bubbles.

Gross bed properties predicted with their computer code, such as horizontal gas jet penetration, agreed well with their experimental results. They also note that at lower jet velocities there is a greater difference between the predicted and measured penetration lengths. One major drawback when using CFD to model the fluidized bed with a horizontal nozzle is discretization of the nozzle inlet. As the nozzle orifice becomes smaller, a finer mesh is required to properly define the orifice. A finer mesh leads to an increase in mesh density and increased computational demands. There are merits to both the empirical correlation and the CFD simulations.

By decreasing the submergence of the nozzle within the bed, Hong *et al.* (1997) observed a slight increase in gas jet penetration with both their experiments and simulations. Unfortunately simulation results regarding only the jet penetration were reported and not overall predicted flow patterns or solids volume fraction distributions.

One of the main conclusions of their study was that simulations take a long time and produced penetration results that agreed well with experiment and literature correlation. So the question is: why do CFD for a nozzle penetration length when a simple correlation will give a value to within 25%?

Fluidized beds are also used in the exothermic production of base polymers. The formation of "hot spots" within the reactor can lead to product degradation, internal fouling and run away reactions. Obviously the understanding and control of the injection of feed material into these reactors has a significant impact on the overall operation. Guedon *et al.* (1994) conducted tests to see how the intermittent injection of solid particles into a fluidized bed affected bed performance and mixing parameters. Most of the injected particles ended up at the tip of the jet plume and were mixed into the bed only through the motion of the bubbles within the fluidized bed. In such a case it is very important to ensure that the jet penetrates into the bubbling part of the fluidized bed. Although visual observations are invaluable, the 2D nature of a bed required to take such observations can have significant wall effects which are not present in a true three dimensional industrial reactor. Guedon *et al.* (1994) decided to use a semi-cylindrical column made of steel with a Perspex face plate. Experiments were conducted at 25 bars. Polyurethane particles with a density of 650 kg/m^3 and a Sauter mean diameter, D_{32}, of 754 μm. Superficial velocity was varied from 0.4 to 0.6 m/s. Injected pre-polymer particles had a similar density to the particles already present in the bed; D_{32}=628 μm. Injected particles were colored for easier visual observations.

Particles were injected into the fluidized bed from a pressurized holding vessel with a pneumatic valve and traveled along a 1.1 m 0.0127 m ID line and into the bed through 0.0127 m ID nozzle. The nozzle injection system was modeled using a force balance on the particle slug as it moved along the injection line. From this model an injection velocity could be calculated and subsequent penetration results correlated to this velocity and the holding vessel pressure.

Guedon *et al.* (1994) concluded that using an intermittent feed jet to feed solids into the fluidized bed can be used to good effect to deliver feed particles to specific areas within a fluidized bed. Injected particles tended to end up near the tip of the jet and could only be dispersed through the bed by gas bubbles. Therefore the tip of the jet should be positioned within the bubbling part of the fluidized bed. The injection system was successfully modeled and the injected particles were shot into the bed as a solid slug of particles. The length of the injection line should be kept below a certain critical value. An empirical correlation was derived to predict the penetration depth of the injected solids into a dense fluidized bed.

Chapter 3

Governing Equations of Single and Multiphase Flows

For years the flow of fluids in, around and over objects has been the fascination of many researchers. This chapter deals with the general conservation equation(s) and its (their) application to single and multiphase flow systems. Extensions and constitutive relationships required for modeling system closure are presented and the different approaches are discussed. The perception and approaches used to average these continuous equations are described and some of the limitations involved with the assumptions are described.

3.1 Approaches to Flow Modeling

There are several different approaches for modeling flow scenarios. Each method has its set of strengths and weaknesses but may find favor for application in specific areas.

3.1.1 Eulerian Continuum Approach

Most engineers are comfortable with using the Eulerian approach for observing data. Process equipment performance typically requires field data, such as velocity fields, pressure fields and the distribution of basic flow properties such as mass concentrations, temperatures and mass fluxes. The Eulerian approach is typically the most suitable approach when information of this kind is required. Flow variables at discrete points within the domain are reported. This is probably the easiest to grasp presentation of flow data. Experiments typically report certain measured values at points within the flow being studied.

Multiphase Eulerian models are formulated by regarding both the continuous (gas) and dispersed (solids) phases as interpenetrating continua. A momentum balance for the solids phase is determined by some form of averaging method. Single-phase flow equations describing the continuous phase are coupled with the solids momentum equation using additional source and interaction terms within the model equations. Although each phase is not explicitly continuous for multiphase models, assumptions are made so that the equations can be applied to multiple phases. Transport quantities of each of the pseudo-continuous phases have to be determined and applied in a continuum approach.

Important to the application of a continuum model is the definition of an infinitesimal control volume (CV) within the flow domain (FD). The CV must be small enough compared to a characteristic length to accurately represent the small scale flow phenomena. From a macroscopic point of view the CV must be small enough so that the concept of a continuous phase can be adopted. Additionally this CV must be large enough so that a statistically valid number of particles within the CV are present to represent the continuous properties of pressure, temperature, density and velocity for both the continuous (usually the gas phase) and the dispersed phases (solid particles). Too small a CV and an insufficient number of particles can be captured within the model; this is explored in more detail in a following section.

3.1.2 Lagrangian Trajectory Approach

The Lagrangian approach treats each particle within the flow domain as an individual entity whose path is explicitly tracked throughout. Particle motion is governed by ordinary differential equations describing the motion of the particle in a Lagrangian coordinate system. As such, the particle velocity and corresponding path can be determined by integrating these equations. This approach is suitable when it is required to predict the motion of individual particles and how their flow patterns are affected by transient effects. Simulations of this type can be applied to follow tracer particles, such as radioactive tracers, deposition studies and erosion impact studies. Currently these types of simulations are extremely computationally demanding and realistic results are only possible for very dilute solids flows with simplifying assumptions.

Particles are labeled and set to occupy an initial position within the flow domain under study. The particle *P* can be considered to have an origin point (X_1, X_2, X_3) and at times $t>0$ the particle P occupies a new position (x_1,x_2,x_3). Therefore the new position x_i is a function of the original position and time $\bar{x} = \phi(\overline{X},t)$. All of the particles are assumed to be distinct and to remain distinct by not agglomerating. A continuous inverse transformation must also be defined to map the current particle location and time back to the original particle position.

Two general approaches are applied to the Lagrangian simulation of multiphase flows, stochastic and deterministic models. The deterministic Lagrangian trajectory model neglects the effect of the instantaneous fluctuating velocity field of the carrier phase turbulence and its effects on the transport processes of the particle phase. Stochastic models take this instantaneous gas turbulence into account and formulate the instantaneous gas velocity in the formulation of the motion of the particles. Statistical methods are applied in the stochastic approach.

In order to be able to solve the individual particle trajectories the carrier gas flow field must be calculated a priori. Eulerian computations are usually applied to calculate the flow field under study. Velocity field results are then coupled with the Lagrangian prediction of the particle movement within the flow and the affects of particle to particle and particle to carrier phase are calculated. In order to achieve convergence many iterations are required to obtain solutions for each of the phases.

The Lagrangian approach is extremely computationally intensive and requires large computing facilities for simulations that model reasonable physical situations.

3.1.3 Kinetic Theory Approach

In dense gas/solids flows the approach of the kinetic theory of gases can be applied. It is assumed that most, if not all, of the transfer of energy within the flow domain occurs due to particle to particle interaction in the form of collisions. Each particle is likened to a "molecule" and the collisional properties of these particles are used to predict the flow behavior.

Certain constitutive relationships have to be included with the model to account for properties analogous to those of the gas molecular kinetic theory approach. Some of these properties include the restitution coefficient, solids viscosity terms and a granular temperature which appears as a new transported quantity.

The frequency distribution of particles within the flow domain are assumed to obey a Maxwellian distribution and to be a function of time, position and instantaneous velocity. The Maxwellian distribution for particles in three dimensions can be determined and the treatment of particle collisions and transport coefficients can be included. The Boltzmann integral-differential equation can be determined using the Reynolds Transport theorem and equates the rate of change of f for a system of a number of particles to the rate at which f is altered by encounters. A transport equation can be determined from this Boltzmann integral-differential equation resulting in Maxwell's transport equation. The latest version of CFX 5.0 will include a kinetic theory model of multiphase flows. It will not be discussed further in this thesis work.

3.1.4 Ergun Equation and Other Empirical Approaches

The classic Ergun equation gives a relationship between the pressure drop in a packed bed to the flow rate and the properties of particle and gas. This equation has been very successfully applied to predict pressure drops and required flow rates for many industrial fluidized bed applications and still finds relevance in all areas of fluidized bed work. Other empirical results predict jet penetrations, bed expansion heights and voidage distribution functions for a number of different geometries. Empirical results are very important to get a feel for how a flow system will behave and should be used to gain an insight into the flow domain in question by using well established and verified relationships.

3.1.5 Direct Numerical Simulation

Direct numerical simulation (DNS) involves solving the entire set of Navier Stokes equations on a very fine grid to model all of the nonlinear interaction terms. In the case of multiphase flows each particle is tracked and advanced through the flow domain by calculating all of the interaction forces around the particle including particle-particle interactions, particle-fluid interactions and fluid-particle interactions. DNS is extremely computationally intensive and has not found wide spread application. It is hoped that large DNS runs will provide correlations that can be used in other less demanding methods such as the Eulerian two-fluid models.

3.2 Single Phase Flows

3.2.1 Derivation of the General Transport Theorem

To describe fluid flow phenomena, governing equations based on the conservation of mass, momentum and energy must be constructed for single phase flow (Aris, 1962) and then generalized to multiphase flow systems. Each of these three conserved quantities can be expressed in the more general transport theorem governing conservation. For these discussions the conservation of angular momentum will not be elaborated on. An infinitesimally small fluid element is considered within the flow domain. All conservation equations in continuum mechanics can be derived from the general transport theorem. A variable *F(t)* is defined as a volume integral over an arbitrary volume element *v(t)* in an n-space as shown in Equation 3.1.

$$F(t) = \iiint_{v(t)} f(\bar{x},t)\,dv \tag{3.1}$$

where $f(\bar{x},t)$ is an integrable function representing a parameter such as mass, momentum or energy; t is the time; and $\bar{x}$ is a position vector. In three dimensions the vector $\bar{x} = (x_1, x_2, x_3)$. In order to be able to calculate the total rate of change of *F(t)* it is necessary to introduce an ξ-space where the volume of *F(t)* is fixed with respect to time so that the interchange of differentiation and integration is possible for the total derivative of F. In order to be able to do this we define the relationship of the change of volume with time to that of a new coordinate system $\bar{\xi}$ such that this new coordinate system has no volume change associated with it. Figure 3.1 defines the control volume in this new curvilinear coordinate system.

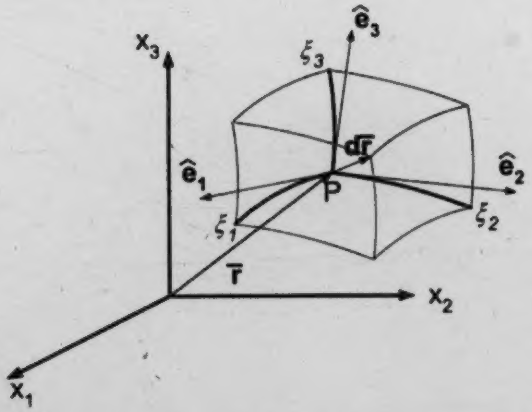

Figure 3.1 – General control volume in curvilinear coordinates.

The point P can be located in coordinate systems as Cartesian (x_1,x_2,x_3) and also as curvilinear (ξ_1, ξ_2, ξ_3). Subsequently the point (x_1,x_2,x_3) can be described as $x_1=f_1(\xi_1, \xi_2, \xi_3)$, $x_2= f_2(\xi_1, \xi_2, \xi_3)$ and $x_3= f_3(\xi_1, \xi_2, \xi_3)$ where it is assumed that f_i are continuous functions with continuous partial derivatives.

If ξ_2 and ξ_3 are held constant, then as ξ_1 varies the position vector **r** traces a curve called the ξ_1 coordinate curve; this treatment can be applied for both ξ_2 and ξ_3. Therefore:

$$d\bar{r} = \frac{\partial \bar{r}}{\partial \xi_1} d\xi_1 + \frac{\partial \bar{r}}{\partial \xi_2} d\xi_2 + \frac{\partial \bar{r}}{\partial \xi_3} d\xi_3 \tag{3.2}$$

The vector $\partial\bar{r}/\partial\xi_1$ defines a tangent at the point P which can be assigned a directional unit vector of $h_1\hat{e}_1$ with $h_1 = |\partial\bar{r}/\partial\xi_1|$; similar expressions can be determined for $\hat{e}_2$ and $\hat{e}_3$. Therefore the previous expression can be written as:

$$d\bar{r} = h_1 d\xi_1 \hat{e}_1 + h_2 d\xi_2 \hat{e}_2 + h_3 d\xi_3 \hat{e}_3 \tag{3.3}$$

If the orthogonal basis vectors $\hat{e}_1$, $\hat{e}_2$ and $\hat{e}_3$ are mutually perpendicular at any point P, then the curvilinear coordinates are orthogonal. In this case the volume of the parallelepiped formed by the infinitesimal position vector $d\bar{r}$ is given by:

$$dV = \left| \frac{\partial \bar{r}}{\partial \xi_1} \cdot \frac{\partial \bar{r}}{\partial \xi_2} \times \frac{\partial \bar{r}}{\partial \xi_3} \right| d\xi_1 d\xi_2 d\xi_3 = \left| \frac{\partial (x,y,z)}{\partial (\xi_1,\xi_2,\xi_3)} \right| d\xi_1 d\xi_2 d\xi_3 \tag{3.4}$$

In which case,

$$dV = \bar{\bar{J}} dV_0 \tag{3.5}$$

Where the Jacobian is defined as:

$$\bar{\bar{J}} = \begin{vmatrix} \frac{\partial x_1}{\partial \xi_1} & \frac{\partial x_1}{\partial \xi_2} & \frac{\partial x_1}{\partial \xi_3} \\ \frac{\partial x_1}{\partial \xi_1} & \frac{\partial x_1}{\partial \xi_2} & \frac{\partial x_1}{\partial \xi_3} \\ \frac{\partial x_1}{\partial \xi_1} & \frac{\partial x_1}{\partial \xi_2} & \frac{\partial x_1}{\partial \xi_3} \end{vmatrix} \tag{3.6}$$

and represents the change in volume of an element when transforming from one coordinate system to another.

We now have an expression to transform the initial deforming coordinate system to one where the volume element is not dependent on time.

$$F(t) = \iiint_{v(t)} f(\bar{x},t) dv = \iiint_{v_0} f(\bar{\xi},t) \bar{J} dv_0 \tag{3.7}$$

The total derivative of *F(t)* can now be calculated by bringing the differentiation with respect to time into the integrand which is now being calculated over constant volume, v_0. It can be shown that $\frac{d\bar{\bar{J}}}{dt} = \left(\nabla \cdot \bar{v}\right)\bar{\bar{J}}$ where $\bar{v} = \frac{d\bar{x}}{dt}$, please see *Appendix A.1*. Therefore, the expression of the total derivative now becomes:

$$\frac{dF}{dt} = \frac{d}{dt}\iiint_{v(t)} f\left(\bar{x},t\right)dv = \frac{d}{dt}\iiint_{v_0} f\left[\bar{x}\left(\bar{\xi},t\right)\right]\bar{\bar{J}}dv_0$$

$$\begin{aligned}
&= \iiint_{v_0}\left(\frac{df}{dt}\bar{\bar{J}} + f\frac{d\bar{\bar{J}}}{dt}\right)dv_0 \\
&= \iiint_{v_0}\left(\frac{df}{dt} + f\left(\nabla\cdot\bar{v}\right)\right)\bar{\bar{J}}dv_0 \qquad (3.8) \\
&= \iiint_{v(t)}\left(\frac{df}{dt} + f\left(\nabla\cdot\bar{v}\right)\right)dv
\end{aligned}$$

Note that the full derivative df/dt can be expressed as

$$\frac{df}{dt} = \frac{\partial f}{\partial t} + \bar{v}\cdot\nabla f \qquad (3.9)$$

And substituting into the general transport theorem (3.8)

$$\frac{dF}{dt} = \iiint_{v(t)}\left(\frac{\partial f}{\partial t} + \nabla\cdot f\bar{v}\right)dv \qquad (3.10)$$

The rate of change of *F* can be found from the net flow of *f* across the closed surface of *v(t)* and the generation of *f* within *v(t)*. Defining ψ as the (diffusional) flux vector of *f* across the closed surface of *v(t)* and *Φ* as the volumetric rate of production of *f*, the rate of change of *F* can be specified as:

$$\frac{dF}{dt} = -\iint_{A} \hat{n} \cdot \psi dA + \iiint_{v(t)} \Phi dv \tag{3.11}$$

Where $\hat{n}$ is the outward facing normal to the closed surface, *A*, bounding the volume *v(t)*. Gauss' theorem can be applied to this surface integral to change it into a volume integral, please see *Appendix A.2: Gauss' Theorem*. The general transport theorem can now be combined with the volumetric production and convective flux terms to obtain:

$$\iiint_{v(t)} \left(\frac{\partial f}{\partial t} + \nabla \cdot f\bar{v} + \nabla \cdot \psi - \Phi \right) dv = 0 \tag{3.12}$$

Since this derivation has been for an arbitrary volume, the integration operator can be removed and the general conservation equation in a single phase of fluid can be written as follows:

$$\frac{\partial f}{\partial t} + \nabla \cdot \left(f\bar{v} \right) + \nabla \cdot \psi - \Phi = 0 \tag{3.13}$$

There are four different behavior to address in the general conservation equation: i) discretization in time, ii) advection terms, iii) diffusion based terms and iv) source terms. Each of these terms will be dealt with in Chapter 3 Computational Techniques.

3.2.2 Continuity Equation

Based on the general conservation equation, an expression for the conservation of mass can be formulated by setting *f* equal to the fluid density ρ, there is no diffusive mass flux, *ψ=0*, and there is no volumetric mass production, *Φ=0*.

$$\frac{\partial \rho}{\partial t} + \nabla \cdot \left(\rho \bar{v} \right) = 0 \tag{3.14}$$

3.2.3 Momentum Equation

To derive the momentum equation, *f* is set to the momentum per unit volume, $\rho \bar{v}$. Diffusive momentum flux is due to shear stresses within the fluid. This term is generally lumped with the static pressure of the fluid, *P* and is expressed as $\psi = \left(P\bar{\bar{I}} - \bar{\bar{\tau}} \right)$. Source term is the action of body and other forces acting on the fluid (including gravitational and magnetic fields); this is a force per unit mass and is expressed as $\Phi = -\rho \bar{f}_b$.

$$\frac{\partial \left(\rho \bar{v} \right)}{\partial t} + \nabla \cdot \left(\rho \bar{v}\bar{v} \right) = \rho \bar{f}_b - \nabla P + \nabla \cdot \bar{\bar{\tau}} \tag{3.15}$$

Different expressions for the stress tensor, $\overset{=}{\tau}$, refer to fluids with different properties. Many fluids can be characterized as Newtonian where the shear stress within the fluid is only proportional to the gradient of velocity. For this discussion a Newtonian fluid will be assumed and the stress tensor will simply be stated and not derived:

$$\overset{=}{\tau} = \mu\left(2S_{ij} - \frac{2}{3}\delta_{ij}S_{ll}\right) + \zeta\delta_{ij}S_{ll} \tag{3.16}$$

S_{ij} is the velocity strain rate tensor, μ is the fluid viscosity and ζ is the bulk viscosity coefficient, which is usually assumed to be insignificant.

3.3 Multiphase Flows

Multiphase flows are characterized from single phase flows in that there is interaction between different thermodynamic phases present within the flow system. Multiphase flows include gas-solids flows (fluidized beds, pneumatic transport, granular and chute flows), gas-liquid (bubble columns, atmospheric flows, application of sprays, etc…), liquid-solid flows and gas-liquid-solid flows (three phase biological contact units, three phase fluidized beds, etc…). Multicomponent flows are flows in which there are different chemical species interacting. Multicomponent flows can also be multiphase flows such as the pneumatic transport of benzoic acid in solid form – in this case the benzoic acid is present as solid particles and as a sublimated gas phase within the carrier gas phase for transport. Multiphase flow is a very common phenomenon and is the topic of this study. Gas-solids flows within a fluidized bed reactor has been the focus of this research.

Much work has been carried out to formulate the correct equations governing two-phase flows within fluidized beds. Sinclair (1997) has done an extensive review of the many different formulations and presents a list of the most important governing equations used by different authors. Only the two-fluid models will be discussed in this report. Early attempts at modeling fluidized bed hydrodynamics are attributed to Davidson (1961) for assuming that the particulate phase behaves as an incompressible fluid with a constant porosity outside of bubbles. The gas was assumed ideal and pressure drop was calculated using Darcy's law for flow in a porous medium. Original formulations of the two-fluid model (Anderson and Jackson, 1967) formulate the equation of motion for the center of mass of a single particle agreeing with the control volume size as already discussed. This averaging procedure leads to terms that describe the interactions associated with the velocity fields of the two phases. One of the most confusing aspects of multiphase flow modeling is that there still exist differences in the *fundamental* governing equations used by different investigators in the literature. Some of the earliest investigations using a two fluid formulation were carried out by Arastoopour and Gidaspow (1979) and Arastoopour *et al.* (1982). Gidaspow and co-workers have done extensive work with computer simulations of circulating fluidized beds and bubbling beds using two fluid models. However, over the years Gidaspow has used several different formulations for the momentum equations. Hydrodynamic model A (Bouillard *et al.*, 1989) contained gas-phase pressure drops in both the gas and solids momentum equations. Hydrodynamic model B (Lyczkowski *et al.*, 1978) retained the entire pressure drop only in the gas momentum equation and Gidaspow's relative velocity model (Gidaspow, 1994; Arastoopour and Gidaspow, 1979) uses a formulation based on the slip velocity between the two phases. It was recognized that with Hydrodynamic model A the inclusion of the continuous phase pressure in the solids momentum equation leads to an initial value problem that is ill-posed (Fanucci *et al.*, 1979). In order to overcome this problem a normal component of solids stress based on a solids shear stress modulus was added to stabilize numerical solution.

The equations governing multiphase flow systems such as those studied in this report can be derived from first principles; however, in the previous section a detailed derivation of the single phase general conservation equations have been presented. Extension to multiphase fluid dynamics is straightforward but requires the inclusion of additional transfer terms between the momentum equations for each phase. The governing equations will be stated without derivation.

Gas Continuity:

$$\frac{\partial}{\partial t}\left(\varepsilon_g \rho_g\right)+\nabla\cdot\left(\varepsilon_g \rho_g \overline{U}_g\right)=\left(\dot{m}_{gs}-\dot{m}_{sg}\right)=0 \qquad (3.17)$$

The gas continuity is similar to that of the single phase continuity equation; however, the gas volume fraction is now included as an unknown within the equation and must be taken into account. The thermodynamic mass transfer terms (the last term on the right hand side of the continuity equation) from one phase to another is included but is not used for this work.

Gas Momentum:

$$\frac{\partial}{\partial t}\left(\varepsilon_g \rho_g \overline{U}_g\right) + \nabla \cdot \left(\varepsilon_g \left(\rho_g \overline{U}_g \otimes \overline{U}_g - \mu_g \left(\nabla \overline{U}_g + \left(\nabla \overline{U}_g\right)^T\right)\right)\right)$$

$$= \varepsilon_g\left(\overline{B} - \nabla p_g\right) + c_{gs}{}^{(d)}\left(\overline{U}_g - \overline{U}_s\right) + \overline{F}_g + \dot{m}_{gs}\overline{U}_s - \dot{m}_{sg}\overline{U}_g \qquad (3.18)$$

Coupling of the two sets of equations is carried out by the use of momentum transfer in the form of drag on one phase exerted by the other. Momentum transfer due to phase change is listed in the last two terms; however, this was not considered in this study.

Solids Continuity:

$$\frac{\partial}{\partial t}\left(\varepsilon_s \rho_s\right) + \nabla \cdot \left(\varepsilon_s \rho_s \overline{U}_s\right) = \left(\dot{m}_{sg} - \dot{m}_{gs}\right) = 0 \qquad (3.19)$$

Solids Momentum:

$$\frac{\partial}{\partial t}\left(\varepsilon_s \rho_s \overline{U}_s\right) + \nabla \cdot \left(\varepsilon_s \left(\rho_s \overline{U}_s \otimes \overline{U}_s - \mu_s \left(\nabla \overline{U}_s + \left(\nabla \overline{U}_s\right)^T\right)\right)\right)$$

$$= \varepsilon_s\left(\overline{B} - \nabla p_g\right) + c_{sg}{}^{(d)}\left(\overline{U}_s - \overline{U}_g\right) + \overline{F}_s + \dot{m}_{sg}\overline{U}_g - \dot{m}_{gs}\overline{U}_s + \nabla p_s \qquad (3.20)$$

The solids momentum equation (3.20) has several additional terms which are not found in the gas phase momentum equation (3.18). Simulations were conducted with the gas phase pressure shared between the two momentum equations thereby making these equations conform to Gidaspow's Hyrodynamic model A. Several comparison simulations were also conducted with the gas pressure removed from the solids momentum equation agreeing with Gidaspow's Hydrodynamic model B. In order to make this initial value problem well posed a solids pressure term was included in the solids momentum equation. The form of this expression is described subsequently.

There are a total of nine unknowns (three velocity components for each of the solids and gas phases, two volume fractions and the continuous, or thermodynamic, pressure) and eight equations available for solution (six momentum and two continuity equations). Since the flow is assumed to be incompressible, there is not an equation of state for the pressure and it must be solved iteratively using a pressure correction method. The pressure correction method used in CFX is described in Chapter 3 Computational Methods. Constitutive relationships for the solids viscosity, drag coefficient and solids pressure are required. These and other more general factors are discussed below.

3.3.1 Forces Acting on Solids in a Gas-Solid Multiphase Flow System

Influences affecting the flow of a single phase flow system can be broken into those forces resulting from body forces (gravitational, magnetic, etc...) and internal forces resulting from viscous interaction of the flow "particles" and pressure. Multiphase flow systems have an added influence due to the interaction of the phases with one another and also upon themselves (much as viscous shears affect single phase flows). The following is a brief description of those forces influencing multiphase flows. Not all of these forces have been explicitly modeled in this study but are included here for completeness.

3.3.2 Drag Forces

In a fluidized bed the solids particles are kept in suspension by the action of the fluidization gas passing up through the reactor and counteracting the force of gravity. One of the ways in which the gas and solids interact is through the transfer of momentum between the phases. This leads to a two way coupling of the momentum equations. Drag forces for single spheres falling in a stationary liquid (similar to sedimentation) have been studied and very good correlations have been found for the drag factor over a sphere over a wide range of Reynolds numbers (Bird, Stewart and Lightfoot, 1960).

Figure 3.2 shows some commonly used drag models for multiphase flow systems including the correlation used for this study. For this study the drag model of Gidaspow (1994) was chosen. This model was chosen based on the work done by Witt and his colleagues (Witt, Perry and Schwarz, 1998; Witt and Perry, 1995a; Witt and Perry, 1995b) at CSIRO, Australia. Witt *et al.* have used CFX and produced good comparison between fluidized bed experiments and simulation results. Other modern simulation studies have also used this correlation to good effect, see Hong *et al.* (1997). For solids volume fractions less than 0.2 the correlation of Wen and Yu (1966) is followed. Above this volume fraction the Ergun equation is used to calculate the drag factor. As pointed out by van Wechem *et al.* (1999) the rationale for this model is unclear especially as there is a discontinuity at the solids volume fraction of 0.2. This particular drag model was used for these simulations based on the drag models used in the work of Witt *et al.* More importantly the correlation of Wen and Yu (1965) was based on data that spanned the entire operating conditions.

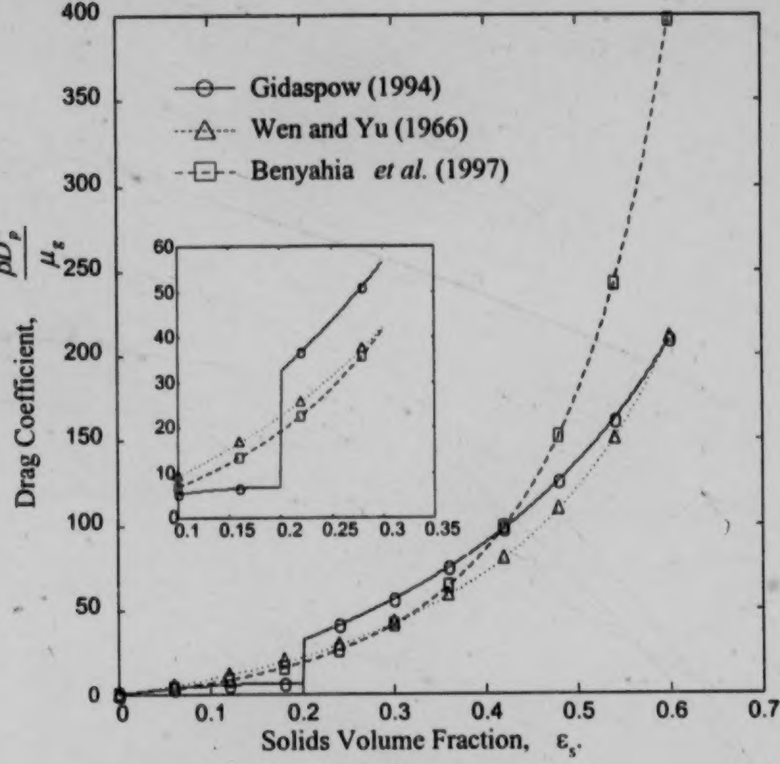

Figure 3.2 - Drag coefficient correlation based on $Re_p=45$ using the drag correlation of Schiller and Nauman (1933) for particles in gas flows.

The equations used to describe the drag correlation used for this work are obtained from a modified form (Richardson and Zaki, 1954) of the drag force exerted on a single particle and is given by:

$$\beta_v = 150\frac{(1-\varepsilon)^2}{\varepsilon(d_p\phi_s)^2} + 1.75\frac{\rho_g|V_g - V_s|(1-\varepsilon)}{\phi_s d_p} \qquad \text{for } \varepsilon_s>0.2 \qquad (3.21)$$

$$\beta = \frac{3}{4} C_d \frac{\varepsilon_g \rho_g \left| u_g - u_s \right| \left(1 - \varepsilon_g\right)}{D_p} G\left(\varepsilon_g\right) \qquad \text{for } \varepsilon_s \leq 0.2 \qquad (3.22)$$

where the drag coefficent C_d is defined based on the particle Reynolds number, Re_p, and corelations for the drag coefficient of a single sphere falling through a quiescent fluid as follows:

$$C_D = \frac{24}{\text{Re}} \qquad 0 \leq \text{Re} \leq 0.2 \qquad (3.23)$$

$$C_D = \frac{24}{\text{Re}}\left(1 + 0.1\,\text{Re}^{0.75}\right) \qquad 0 \leq \text{Re} \leq 500\text{-}1000$$

(Schiller and Nauman, 1933) (3.24)

$$C_D = 0.44 \qquad 500\text{-}1000 \leq \text{Re} \leq 1\text{-}2 \times 10^5 \qquad (3.25)$$

$$\text{Re}_p = \frac{D_p \left| U_s - U_g \right| \rho_g}{\mu_g} \qquad (3.26)$$

Since these relationships are for a single sphere drag coefficient, they have to be corrected to take the interaction of other particles into account. These expressions are corrected for the interaction of particles based on the multiplicative factor given by Gidaspow (1994):

$$k = (1 - \varepsilon_s)^p \qquad (3.27)$$

where p = -1.65. When the gas volume fraction falls below 0.8, this Gidaspow modification to the drag factor becomes inadequate. In this case the drag is calculated based on the Ergun equation (3.21).

3.3.3 Solids Pressure

Solids particles within fluidized beds come into intimate contact with one another and these interactions have to be taken into account. It was realized that in order to solve the equations governing dense multiphase gas-solids flows, terms must be included in the solids momentum equation to ensure that the solids do not reach physically unrealizable volume fractions. Coulombic stress, also known as solids pressure and/or the normal component of solids stress, has been introduced as a source term in the solids momentum equation. This coulombic stress acts as a repulsive force that increases with particle volume fraction.

The solids pressure gradient in equation (3.20) is considered to be a function of local volume fraction and is expressed as

$$-\nabla P_S = G(\varepsilon_g)\nabla\varepsilon_g \tag{3.28}$$

G is commonly referred to as the solids elastic bulk modulus and can be shown to be a thermodynamic property of powders. Several attempts at measuring G have been reported. Gough (1979) and more recently Bouillard *et al.* (1989) have determined a convenient form for the modulus G as:

$$G = G_0 e^{-k\left(\varepsilon_g - \varepsilon^*\right)} \tag{3.29}$$

with typical values of k=600, G_0=1.0 Pa and ε^*=0.376. This form is similar to that used in the CFX package.

Figure 3.3 is a plot of some commonly used approximations of G versus gas volume fraction. The correlation G_1 of Bouillard *et al.* (1989) was used for the simulations in this study. Some sensitivity studies were conducted using the relationship of Ettehadieh *et al.* (1984) and is discussed in Chapter 5; this function is very similar in value to Benyahia *et al.* (1997) shown in Figure 3.3. Values for the specific functions are listed in Table 3.1. For each solids pressure function there exists a point where the repulsive force increases exponentially. This occurs near the minimum solids packing fraction and prevents solids from reaching volume fractions that are physically unreasonable.

Table 3.1

Common Solids Pressure Functions in Literature

Expression	Reference
$G\left(\varepsilon_g\right) = 10^{-8.76\varepsilon_g + 5.43}$	Ettehadieh *et al.* (1984)
$G_1\left(\varepsilon_g\right) = e^{-600\left(\varepsilon_g - 0.376\right)}$	Bouillard *et al.* (1989)
$G_2\left(\varepsilon_g\right) = e^{-500\left(\varepsilon_g - 0.422\right)}$	
$G_3\left(\varepsilon_g\right) = e^{-20\left(\varepsilon_g - 0.62\right)}$	
$G\left(\varepsilon_g\right) = e^{-100\left(\varepsilon_g - 0.45\right)}$	Kuipers *et al.* (1992)
$G\left(\varepsilon_g\right) = e^{-600\left(\varepsilon_g - 0.39\right)}$	Lyczkowski *et al.* (1993)
$G\left(\varepsilon_g\right) = 10^{-8.5\varepsilon_g + 5.43}$	Benyahia *et al.* (1997)

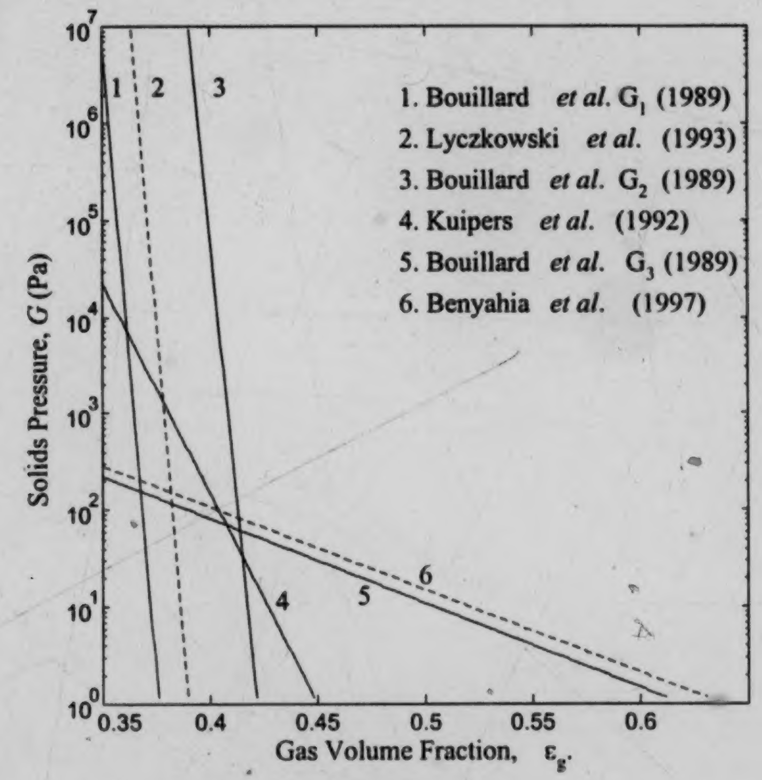

Figure 3.3 – Solids pressure functions used in literature.

Thermodynamic variables that define the state of a powder can include: specific entropy, bulk specific volume, composition and possibly several other variables that must account for the strains in a solid in more than one direction. The internal energy of a powder can be defined as:

$$U = U(S, v_B) \tag{3.30}$$

where

$$v_B = 1/\rho_s\varepsilon_s \tag{3.31}$$

Which is the volume weighted specific bulk volume of the solids. The solids stress, σ_s, can be defined like the pressure for a fluid:

$$\sigma_s = -\frac{\partial U}{\partial v_B} \tag{3.32}$$

Assuming a constant particle density of the solid, ρ_s, at constant entropy this equation can be rewritten as:

$$dU = \frac{\sigma_s}{\rho_s}\frac{d\varepsilon_s}{\varepsilon_s^2} \tag{3.33}$$

Therefore, the internal energy of the solids phase (powder) decreases with expansion. Since the only new variable that has been introduced is the bulk powder specific volume, the temperature of the powder is still given by:

$$T = \left(\frac{\partial U}{\partial S}\right)_{v_B} \tag{3.34}$$

Using thermodynamic stability, see Smith, Van Ness and Abbott (1949):

$$d^2U > 0 \tag{3.35}$$

which leads to the well known relation for fluids:

$$\left(\frac{\partial \sigma_s}{\partial v_B}\right)_{T\_or\_S} < 0 \quad or \quad \left(\frac{\partial \sigma_s}{\partial \rho_B}\right)_{T\_or\_S} > 0 \tag{3.36}$$

Since at constant temperature or entropy,

$$\sigma_s = \sigma_s(\varepsilon_s), \left(\frac{\partial \sigma_s}{\partial \rho_B}\right) = \frac{1}{\rho_s}\left(\frac{\partial \sigma_s}{\partial \varepsilon_s}\right) \tag{3.37}$$

The elastic bulk modulus *G*, similar to the Young's modulus for solids, is defined to be:

$$G = \left(\frac{\partial \sigma_s}{\partial \varepsilon_s}\right)_{T\_or\_S} \tag{3.38}$$

Based upon this analysis it is seen that *G* is a thermodynamic property of the powder.

3.3.4 Friction

Interaction of solids particles with one another also leads to the transfer of kinetic to thermal energy within the fluidized bed. This transfer of energy will be considered to be a loss of kinetic energy as the simulations in this study do not include a mechanism for the transfer of that thermal energy back to kinetic energy. Frictional forces between the solids particles have taken the form of a solids viscosity term that is similar to the gas viscosity as defined by the kinetic theory of gases.

3.3.5 Particle Viscosity Due to Interparticle Collisions

At high solids concentrations the shear motion of particles can lead to a large number of collisions between particles. These collisions lead to the transfer of momentum and can be described in terms of a solids shear stress (based on the continuum and not internal solids shear stress as experienced when studying solids deformations). Constitutive relationships for these stresses were first put forth by Lun *et al.* (1984) based on a gas kinetic theory approach allowing for the inelastic collision of particles. Gidaspow (1994) presents a solids viscosity relationship which varies little from that of Lun *et al.* (1984). Hrenya and Sinclair (1997) follow the treatment of Lun *et al.* (1984) but add a modification that sets the particle viscosity to zero at zero solids volume fraction. The original work of Lun *et al.* (1984) was derived for particles in an infinite medium. As the particles move further apart their mean free path becomes infinite and the solids viscosity at zero solids volume fraction takes on a finite value. The solids viscosity relationship of Syamlal *et al.* (1993) neglects the kinetic or streaming effect of the particles on the solids viscosity which is dominant at low solids volume fractions. As this is so, this treatment departs markedly from other models available in the literature. Since Syamlal *et al.* (1993) chose to neglect these low solids volume fraction effects, their model does correctly reduce to zero solids viscosity at zero solids volume fraction. All models coincide at higher solids volume fractions where the flow is collision dominated. The available correlations are listed in Table 3.2 and a plot of the different viscosity functions is shown in Figure 3.4.

Table 3.2

Solids Viscosity Correlations Available in Literature

$\mu_s = \frac{4}{5}\varepsilon_s^2 \rho_s D_p g_0 (1+e)\sqrt{\frac{\Theta_s}{\pi}} + \frac{10}{96}\sqrt{\Theta\pi}\frac{\rho_s D_p}{(1+e)\left(\frac{3}{2}-\frac{1}{2}e\right)\left(1+\frac{\lambda_{mfp}}{R}\right)g_0} + \frac{1}{6}\sqrt{\Theta\pi}\frac{\rho_s D_p \varepsilon_s \left(\frac{1}{2}\left(1+\frac{\lambda_{mfp}}{R}\right)+\frac{3}{4}e-\frac{1}{4}\right)}{\left(\frac{3}{2}-\frac{1}{2}e\right)\left(1+\frac{\lambda_{mfp}}{R}\right)} + \frac{1}{15}\sqrt{\Theta\pi}\frac{\rho_s D_p g_0 (1+e)\left(\frac{3}{2}e-\frac{1}{2}\right)\varepsilon_s^2}{\left(\frac{3}{2}-\frac{1}{2}e\right)}$	Hrenya and Sinclair (1997)
$\mu_s = \frac{4}{5}\varepsilon_s^2 \rho_s D_p g_0 (1+e)\sqrt{\frac{\Theta_s}{\pi}} + \frac{10}{96}\sqrt{\Theta\pi}\frac{\rho_s D_p}{(1+e)g_0} + \frac{1}{6}\sqrt{\Theta\pi}\rho_s D_p \varepsilon_s + \frac{1}{15}\sqrt{\Theta\pi}\rho_s D_p g_0 (1+e)\varepsilon_s^2$	Gidaspow (1994)
$\mu_s = \frac{4}{5}\varepsilon_s^2 \rho_s D_p g_0 (1+e)\sqrt{\frac{\Theta_s}{\pi}} + \frac{\varepsilon_s D_p \rho_s \sqrt{\pi\Theta}}{6(3-e)} + \frac{1}{15}\sqrt{\Theta\pi}\rho_s D_p g_0 \varepsilon_s^2 \frac{(1+e)\left(\frac{3}{2}e-\frac{1}{2}\right)}{\left(\frac{3}{2}-\frac{e}{2}\right)}$	Syamlal *et al.* (1993)
$\mu_s = \frac{4}{5}\varepsilon_s^2 \rho_s D_p g_0 (1+e)\sqrt{\frac{\Theta_s}{\pi}} + \frac{10}{96}\sqrt{\Theta\pi}\frac{\rho_s D_p}{(1+e)\left(\frac{3}{2}-\frac{1}{2}e\right)g_0} + \frac{1}{6}\sqrt{\Theta\pi}\frac{\rho_s D_p \varepsilon_s \left(\frac{3}{4}e+\frac{1}{4}\right)}{\left(\frac{3}{2}-\frac{1}{2}e\right)} + \frac{1}{15}\sqrt{\Theta\pi}\frac{\rho_s D_p g_0 (1+e)\left(\frac{3}{2}e-\frac{1}{2}\right)\varepsilon_s^2}{\left(\frac{3}{2}-\frac{1}{2}e\right)}$	Lun *et al.* (1984)

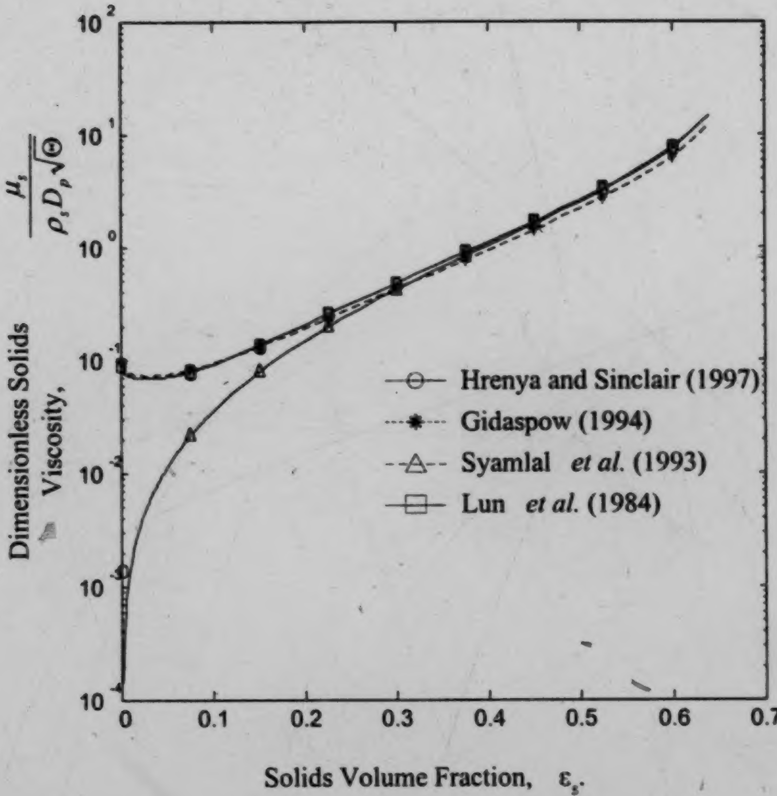

Figure 3.4 - Plot of solids viscosity versus solids volume fraction for different correlations available in the literature. Restitution coefficient set equal to 0.9. Sinclair (1997) radial distribution function used.

Consider the elastic collision of two particles of different sizes in a two dimensional *rx*-plane (Arastoopour *et al.* 1982) as shown in Figure 3.5.

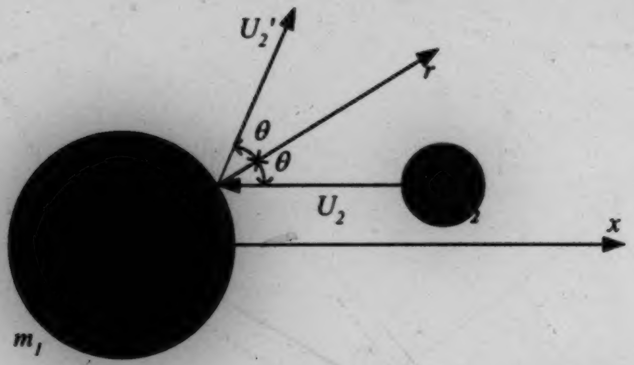

Figure 3.5 – Elastic collision of two solid spherical particles of different sizes.

Particle 2 with mass m_2 initially has momentum in the negative x direction and impacts on the stationary particle 1 with mass m_1 from which it undergoes an elastic collision resulting in specular reflection about the axis r and its subsequent velocity is in the rx plane. The rate of change of the x-component of the momentum between the two particles is given by:

$$m_2U_2 - [m_2U_2\cos(\pi - 2\theta)] = 2m_2U_2\cos^2\theta \tag{3.39}$$

with θ the contact angle in the rx-plane. Next consider a collision between two particles 1 and 2 with masses m_1 and m_2 and velocities U_1 and U_2. From Newton's law

$$m_1\frac{dU_1}{dt} = f_{12} \qquad\qquad m_2\frac{dU_2}{dt} = -f_{12} \tag{3.40}$$

with f_{12} being the collisional force. For such a system a relative mass, m^*, can be defined as $\frac{1}{m^*} = \frac{1}{m_1} + \frac{1}{m_2}$ and a relative velocity as $\Delta U = U_1 - U_2$, simplifying to the following expression for the completely elastic collision between two particles.

$$m^* \frac{d\Delta U}{dt} = f_{12} \tag{3.41}$$

Therefore, the collision of two particles moving with independent velocities can be likened to the collision of a particle colliding with a fixed particle with the same relative mass and relative velocity. This result will be important when relating the collision of a single particle with a cloud of particles in shear flow.

Now consider the collision of a single particle with a cloud of particles as shown in the Figure 3.6. A representative particle of radius *r* is shown traveling to the left and is subjected to a shear flow within a particle cloud with a velocity gradient $\partial U_p / \partial y$. The particle number density is *n*, and the mass of this particle is *m*. For analysis the velocity U_p is set to zero in the center plane of the sphere and the previous conclusions can be applied. The relative velocity (based on the shear velocity gradient and the distance, *y*, above the zero line) can be estimated as

$$\Delta U_p = \frac{\partial U_p}{\partial y} y = \frac{\partial U_p}{\partial y} r \sin\theta \cos\phi \tag{3.42}$$

with the angles defined as shown in the diagram.

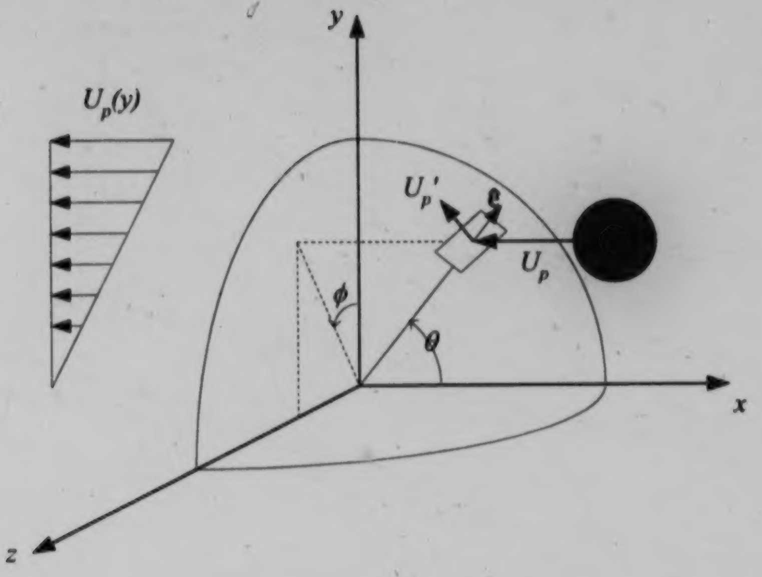

Figure 3.6 – Collision of a single particle with a cloud of particles in shear flow.

The differential area of impact of this particle on the solids cloud shown by the shaded patch is $r^2 \sin\theta d\theta d\phi$. The projected area normal to the incoming velocity U_p is $r^2 \sin\theta \cos\theta d\theta d\phi$. It has been previously shown that the momentum change from impact of two particles moving with different velocities can be expressed in terms of the relative mass and the relative velocity of the system. Based on this proof, the rate of change of x-momentum for a particle can be expressed as $2m\Delta U_p \cos^2\theta$ assuming single scattering and specular reflection. The total force acting upon the quarter sphere can be expressed in terms of the total impact of particles on the bounding area; this being a function of particle number density, approach velocity and mass.

$$F = 4\int_0^{\pi/2}\int_0^{\pi/2} n\left(\Delta U_p\right)^2 mr^2 \sin\theta\cos\theta d\theta d\phi \tag{3.43}$$

This expression for the force is made up of the change in *x*-momentum of the particles of mass *m* impacting on the semisphere (i.e. a quarter sphere, since U_p is zero at $y=0$) multiplied by the velocity. The number density *n* is required to take into account all of the particles impacting on the surface. Integrating this expression gives

$$F = \frac{\pi}{12} nm\left(\frac{\partial U_p}{\partial y}\right)^2 r^4 \tag{3.44}$$

With this expression for the force acting on the semisphere consider a mixture of two groups of particles with radii a_1 and a_2 and corresponding number densities of n_1 and n_2. Particles in group 1 are subjected to a shear flow of particles in group 2. The *x*-component of the collision force between particles 1 and 2 can be obtained as

$$F_{12} = \frac{\pi^2}{18} n_1 n_2 m^* \left(\frac{\partial U_p}{\partial y}\right)^2 (a_1 + a_2)^7 \tag{3.45}$$

This force can be projected onto an area normal to the *y*-axis and a shear stress for the solids phase can be defined as

$$\left(\tau_{xy}\right)_{12} = \frac{2F_{12}}{\pi\left(a_1 + a_2\right)^2} = \frac{\pi}{9} n_1 n_2 m^* \left(\frac{\partial U_p}{\partial y}\right)^2 (a_1 + a_2)^5 \tag{3.46}$$

Soo (1989) generalized this expression to the following

$$\tau_{12} = -\frac{\pi}{9}\frac{n_1 n_2 m_1 m_2}{(m_1 + m_2)}(a_1 + a_2)^5 (\Delta_{p2} : \Delta_{p2})^{1/2} \Delta_{p2} = -\mu_{p12}\Delta_{p2} \tag{3.47}$$

where Δ_p has the Cartesian components of

$$\Delta_{pij} = \frac{\partial U_{pi}}{\partial x_j} + \frac{\partial U_{pj}}{\partial x_i} \tag{3.48}$$

and the : operator refers to the dyadic product. The viscosity due to the particle collision is defined from the expression for the solids shear stress and for the special case of identical particles reduces to

$$\mu_p = \frac{1}{3}\varepsilon_p \rho_p D_p^2 (\Delta_p : \Delta_p)^{1/2} \tag{3.49}$$

3.3.6 Radial Distribution Functions

Expressions for the solids viscosity all depend upon a radial distribution function g_0 at contact. A brief summary of the review given by van Wachem *et al.* (1999) is presented here for completeness. Several investigators have proposed solids distribution functions for use with the determination of the solids viscosity. Early models by

Carnahan and Starling (1969) did not tend to the correct limit as solids volume fraction approached the solids packing limit. Alternate expressions have been proposed by other authors such as Gidaspow (1994), Lun and Savage (1986), and Sinclair and Jackson (1989). Van Wachem *et al.* (1999) report that Gidaspow's expression most closely follows the experimental data of Alder and Wainright (1960); however, the impact of using these different expressions in calculating the solids viscosity is at most a factor of two, excluding the model of Syamlal *et al.* (1993).

3.3.7 Basset Force

The original form of the Basset force was derived in 1888 (Basset, 1888). The Basset force occurs when a particle is accelerated in a fluid and has importance with respect to Stokes drag. The Basset force can be substantial when particles are accelerated at a high rate as is the case at the boundary of the gas jet being discharged into a fluidized bed.

3.3.8 Magnus Force

Particle rotation in low Reynolds flow leads to fluid entrainment resulting in an increase in the velocity on one side of the particle and a decrease in velocity on the other side. Due to the velocity imbalance a net lift force is exerted on the particle causing it to move towards the higher flow velocity (Magnus, 1852).

3.3.9 Saffman Force

The Saffman force falls into a category of forces exerted on particles present in a gradient such as temperature, velocity and pressure gradients. In such cases these gradient effects can have as much an importance as drag forces. Velocity gradients lead to the Saffman lift force (Saffman 1965) being exerted on a particle travelling with constant velocity.

Other gradient related forces include: Radiometric force as a result of a temperature gradient in a gas (thermophoresis) or nonuniform radiation (photophoresis). At room conditions these forces are typically only important for submicrometer particles (Fan and Zhu, 1999).

3.3.10 Pressure Gradient Induced Forces

Pressure gradients may have an impact on a force being exerted on a particle (Tchen, 1947). The significance of this force is evident when a shock wave propagates through a fluidized bed.

3.3.11 Response Times

The response time of a particle to changes in flow field variables are important for determining dimensionless numbers to characterize the flow. The momentum response time relates the time required by a particle to respond to changes in velocity. Crowe *et al.* (1998) give a detailed analysis of particle response times as follows. Consider the equation of motion for a particle in a gas phase

$$m\frac{dU_s}{dt} = \frac{1}{2}C_D\frac{\pi D_p^2}{4}\rho_g\left(U_g - U_s\right)\left|U_g - U_s\right| \qquad (3.50)$$

Using the definition of the particle Reynolds number and dividing equation (3.50) by the particle mass gives

$$\frac{dU_s}{dt}=\frac{18\mu_g}{\rho_g D_p^2}\frac{C_D \operatorname{Re}_p}{24}\left(U_g-U_s\right) \tag{3.51}$$

In Stokes flow the drag factor $\frac{C_D \operatorname{Re}_p}{24}$ approaches unity leaving the Stokes relaxation time

$$\tau_S=\frac{\rho_g D_p^2}{18\mu_g} \tag{3.52}$$

and the original formulation of the equation of motion for a particle in gas flow can be written as:

$$\frac{dU_s}{dt}=\frac{1}{\tau_S}\left(U_g-U_s\right) \tag{3.53}$$

This first order differential equation can be solved by assuming an initial condition of zero particle velocity, giving:

$$U_s=U_g\left(1-e^{-t/\tau_S}\right) \tag{3.54}$$

The Stokes relaxation time is the time required for a particle released from rest to reach 63% $\left(\frac{e-1}{e}\right)$ of the free stream velocity. For simulations in this report the Stokes relaxation time was calculated to be 0.0005 seconds.

3.4 Modeling and Averages

Basic assumptions governing the equations describing fluid flow within an infinitesimal volume element are subject to certain restraints. The general conservation equation is a balance of transported quantities over a definable, although infinitesimal, volume element within the flow domain. This continuum approach is applicable for situations where continuum mechanics can be applied. Continuum approaches might not be applicable for rarefied gas flows where the flow is dominated by interparticle spacing and not by the continuous distribution of the particles. In such cases another type of fundamental approach must be taken to formulate the governing equations using some type of statistical or kinetic theory approach. With this consideration it is also necessary to study the effect of the size of the averaging volume used to solve and model the equations. Three different averages will be discussed: temporal averaging, ensemble averaging (phase lock averaging) and volume averaging. Volume averaging was used for the work in this thesis and the emphasis of this discussion will be on that method.

Multiphase flows usually occur within a confined volume such as a reactor, pipe, tributary, etc… or some sort of bounded domain. A mathematical description of this domain is desired and as such the Eulerian approach is an ideal method. In single phase flows the transported quantities are considered to be continuous throughout the entire domain. However, for multiphase flows there is a dispersed and a continuous phase. Averaging techniques must be applied to construct a continuum description of each of the phases involved so that single phase flow models can be extended to multiphase flow models.

3.4.1 Volume Averaging

Multiphase flows consist of different phases each interacting at different length and time scales. The continuum approach can be constructed either using a temporal average such as a fractional residence time or by using a volume average technique where the phase properties are distributed using a volume fraction variable. Thermodynamic properties such as pressure, temperature and density are cumulative with volume fraction but not so with fractional residence times. Volume averaging is intuitive and linked with the control volume approach used when deriving the general conservation equation.

3.4.2 Phase Average and Intrinsic Average

Fan and Zhu (1998) define two volume averages for transport quantities within a continuum model. For a given transported quantity *f* within a specific control volume of size *v* a phase average quantity can be defined as:

$$\langle f_k \rangle = \frac{1}{v} \iiint_{v_k} f_k \, dv \tag{3.55}$$

where v_k is the volume occupied by phase *k* within the control volume *v*. An intrinsic average can be defined as the quantity of *f* within the volume v_k.

$$^{i}\langle f_k \rangle = \frac{1}{v_k} \iiint_{v_k} f_k \, dv \tag{3.56}$$

Intrinsic volume averages refer to the control volume independent value of the transport quantity such as density and velocity. Phase averages are dependent upon the size of the control volume.

Volume averages can only be applied to quantities per unit volume and other flow properties must be constructed based on ratios of these averages. The intrinsic average velocity of the phase *k* can be defined as (see Appendix A.3)

$$^{i}\left\langle \bar{v}_k \right\rangle = \frac{1}{^{i}\left\langle \rho_k \right\rangle}\left[\frac{1}{v_k}\iiint\limits_{v_k}\rho_k \bar{v}_k \, dv\right] = \frac{\left\langle \rho_k \bar{v}_k \right\rangle}{\left\langle \rho_k \right\rangle} \tag{3.57}$$

3.4.3 Minimum Control Volume Sizes for Phase Averages

Multiphase continuum models must be set up so that the volume averages are small enough when compared to the overall gross characteristic length that they can safely be neglected and not interfere with the overall macroscopic behavior of the flow. At the same time, the control volume must be large enough to capture a statistically significant number of particles. Therefore, to have a statistically meaningful phase average there exists a minimum averaging volume. This information runs contrary to the accepted view that in order to get "better" results from a computational fluid dynamics simulation it is necessary to increase the grid resolution, i.e. by increasing the number of nodes and shrinking the control volume size. This is true for a completely continuous fluid such as a single phase continuum model; however, with the addition of particles to these volume averaged continuum models a certain size limit must be observed.

Consider a simple repeating pattern of monosized spherical particles as shown in Figure 3.7.

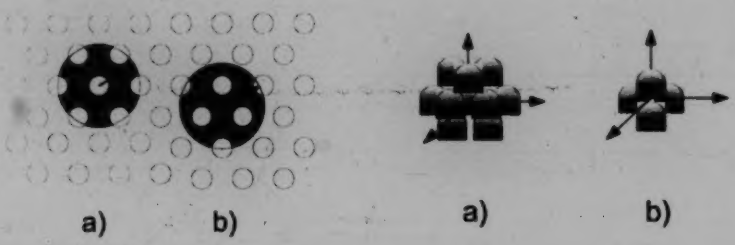

Figure 3.7 – Limiting cases for solids volume averaging analysis. Plan view on left, three dimensional view on right.

The center of the spherical control volume can be placed arbitrarily within the monosized particles; however, two limiting cases can be identified by locating the centroid of the control volume at a) the center of a particle, or b) at the symmetric center of four neighboring particles (three particles in plane and another particle to the top of these three).

The computed volume fraction of particles within a control volume invariably includes particles completely within the bounding surface and some particles which are only partially enclosed. With increasing control volume size, the number of particles within the control volume will increase and the calculated volume fraction will asymptotically approach the bulk volume fraction ε_p within the domain. Calculation of this volume fraction is based upon three geometric parameters including the diameter of the particles, inter-particle spacing and the radius of the control volume. An error margin can be defined based on this asymptotic value and the value calculated using a specified control volume size as $\delta = \left|\varepsilon_p^c - \varepsilon_p\right| / \varepsilon_p$. Average inter-particle spacing can be estimated from the particle number density, *n*, using:

$$l \approx n^{-1/3} = \left(\frac{\pi}{6}\frac{D_p^3}{\varepsilon_p}\right)^{\frac{1}{3}} \tag{3.58}$$

The ratio of l/D_p must only be a function of $f(\varepsilon_p)$. The relationship of the control volume radius can be expressed as a functional relationship of $R/D_p = f(\varepsilon_p)g(\varepsilon_p)$. The minimum control volume radius R_{min} is only a function of ε_p for a given δ. Celmins (1988) has formulated a quantitative relationship between minimum control volume radius for a given tolerance δ as

$$\frac{R_{\min}}{D_p} = \frac{\varepsilon_p^{-\frac{1}{3}}}{\sqrt{2\delta}}\left(1 - \varepsilon_p\right) \tag{3.59}$$

For a tolerance of δ=1% a three dimensional plot of the minimum volume fraction can be plotted against the particle diameter D_p and solid volume fraction ε_p, see Figure 3.8. As can be seen from this diagram there is a minimum volume fraction below which the continuum assumption for gas particle flows is not applicable. A short MATLAB routine was written to create this plot and is included in *Appendix B.1*.

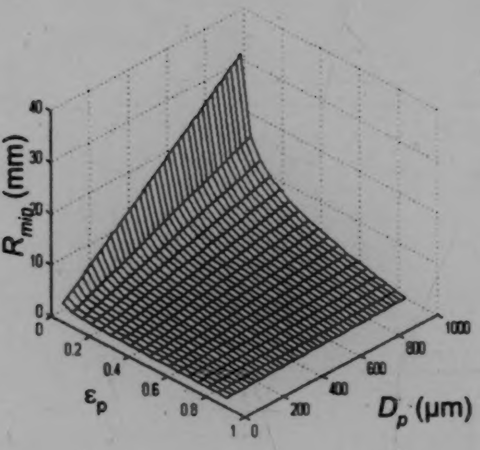

Figure 3.8 – Minimum control volume size for statistically valid multiphase averaging.

For the simulations that were carried out for this study a minimum control volume size can be calculated based on the particles size of 370 µm with a 1, 2 and 5% tolerance on the asymptotic volume fraction, assumed to be 0.42. The resulting minimum CV sizes are $2.64\mathrm{x}10^{-5}$, $1.26\mathrm{x}10^{-5}$ and $5.31\mathrm{x}10^{-6}$ m^3 respectively. Each of these minimum CV sizes is much smaller than those used in the simulations for this study, so the CV formulation can be considered acceptable in this case.

Chapter 4

Computational Methods

Governing equations of fluid mechanics are transient, three dimensional partial differential equations linked through inter-phase transfer terms. Solution of these systems of equations for geometries of engineering interest requires the use of numerical methods. This chapter deals with the discretization, organization and solution of these governing equations. General discretization schemes are described and their relative strengths and weaknesses are compared. Pressure correction methods, linked equation acceleration schemes and Rhie-Chow interpolation techniques are discussed.

4.1 Computational Techniques

Solution of the equations governing multiphase flows cannot be done analytically and the use of numerical methods has to be employed. Computational Fluid Dynamics (CFD) refers to the use of some sort of numerical solution method of the governing hydrodynamic equations to predict flow patterns within a given flow geometry. In addition to the question of the physics to be modeled with the governing equations and the simplifying assumptions and approximations that have to be included, choice of the numerical solution scheme can have a significant impact on the overall accuracy, solution time and stability of the simulation. Discussion in this section will deal explicitly with the conventions used in the CFX 4.2 simulation package from AEA Technology.

4.1.1 Representing Flow Fields in CFX 4.2

Governing equations of multiphase fluid dynamics (see Chapter 2) are partial differential equations representing a continuous flow phenomena and the solution of which will result in a continuous description of the flow field. These equations are coupled, highly nonlinear and involve several dimensions; analytical solution is not possible and solutions must be obtained using numerical methods. As previously shown in Chapter 2 the equations governing the multiphase flow in this study are:

Gas Continuity:

$$\frac{\partial}{\partial t}\left(\varepsilon_g \rho_g\right)+\nabla\cdot\left(\varepsilon_g \rho_g \overline{U}_g\right)=\left(\dot{m}_{gs}-\dot{m}_{sg}\right)=0 \qquad (2.17)$$

Gas Momentum:

$$\frac{\partial}{\partial t}\left(\varepsilon_g \rho_g \overline{U}_g\right)+\nabla\cdot\left(\varepsilon_g\left(\rho_g \overline{U}_g \otimes \overline{U}_g-\mu_g\left(\nabla \overline{U}_g+\left(\nabla \overline{U}_g\right)^T\right)\right)\right)$$

$$=\varepsilon_g\left(\overline{B}-\nabla p_g\right)+c_{\alpha\beta}{}^{(d)}\left(\overline{U}_\beta-\overline{U}_\alpha\right)+\overline{F}_g+\dot{m}_{gs}\overline{U}_s-\dot{m}_{sg}\overline{U}_g \qquad (2.18)$$

Solids Continuity:

$$\frac{\partial}{\partial t}\left(\varepsilon_s \rho_s\right)+\nabla\cdot\left(\varepsilon_s \rho_s \overline{U}_s\right)=\left(\dot{m}_{sg}-\dot{m}_{gs}\right)=0 \qquad (2.19)$$

Solids Momentum:

$$\frac{\partial}{\partial t}\left(\varepsilon_s \rho_s \overline{U}_s\right)+\nabla\cdot\left(\varepsilon_s\left(\rho_s \overline{U}_s \otimes \overline{U}_s-\mu_s\left(\nabla \overline{U}_s+\left(\nabla \overline{U}_s\right)^T\right)\right)\right)$$

$$=\varepsilon_s\left(\overline{B}-\nabla p_g\right)+c_{sg}{}^{(d)}\left(\overline{U}_s-\overline{U}_g\right)+\overline{F}_s+\dot{m}_{sg}\overline{U}_g-\dot{m}_{gs}\overline{U}_s+\nabla p_s \qquad (2.20)$$

These eight equations cannot be solved analytically and must be solved using numerical techniques. The continuous flow field is broken up into a discrete number of points at which solutions to the governing equations are found. The continuous derivatives are approximated using field variables at neighboring nodes.

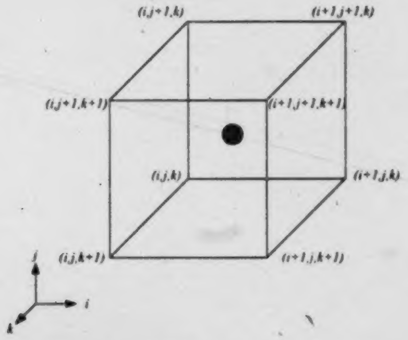

Figure 4.1 – Control volume indices in CFX 4.2

Control volumes within the CFX solver code are located by the lower, back vertex of a quadrilateral shape (in this case a cube) by the coordinates *(i,j,k)* see Figure 4.1. Control volume centers are not explicitly specified but are calculated based on the arithmetic mean of all eight vertices as defined by the discretization mesh. All variables are located at the centroids of the control volumes and represent an average value over the entire control volume. Flux properties, which have to be calculated at the surfaces of control volumes, need to be determined based on surrounding control volume averages. This has a significant impact on the overall solution accuracy and involves the use of interpolation between the centroids of control volumes.

4.2 Discretizing the Governing Equations

The basis of the CFX 4.2 Solver code (CFX 4.2 Solver manual. AEA Technology, UK) is a conservative finite-difference, or finite volume, method with all of the variables defined at the centroid of the control volumes. Conservative variables use combinations of the simple flow variables (ρ, u, v, etc…) to express quantities in terms of fluxes across boundaries. This formulation is required when solving the discretized equations across shocks or other discontinuities in the flow. For example, consider the one dimensional nonconservative form of the momentum equation:

$$\rho\frac{Du}{Dt}=\rho\left(\frac{\partial u}{\partial t}+u\frac{\partial u}{\partial x}\right)=-\frac{\partial P}{\partial x}+\left(\frac{\partial F_v}{\partial x}+S\right) \qquad (4.1)$$

In flows containing shocks the simple variables are not continuous over shock boundaries. In this case $\rho_1 \neq \rho_2$, $u_1 \neq u_2$ and $P_1 \neq P_2$, Figure 4.2.

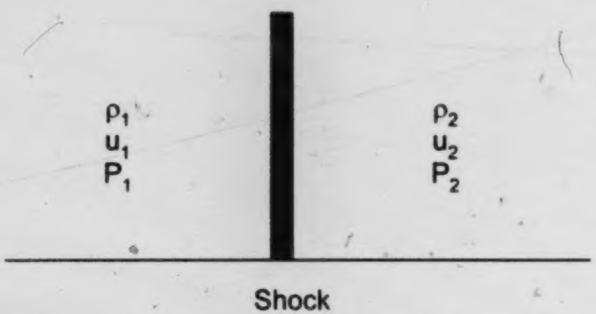

Figure 4.2 – Simple flow variables either side of a shock.

Discretization of the derivative $\rho u \frac{\partial u}{\partial x} \approx \rho u \left(\frac{u_2 - u_1}{\Delta x} \right)$ leads to an incorrect solution. What value should be taken for ρu? Values on either side of the shock over which the derivative is formed are not continuous and will cause convergence problems. By reformulating the one dimensional momentum equation in conservative form by bringing the density into the total derivative the derivative can be recast as follows:

$$\frac{\partial F}{\partial x} \approx \frac{F_r - F_l}{\Delta x} = \frac{F_2 - F_1}{\Delta x} = \frac{\left(\rho_2 u_2^2 + P_2\right) - \left(\rho_1 u_1^2 + P_1\right)}{\Delta x} \tag{4.2}$$

This formulation will give the correct physical answer in this flow situation and not result in discontinuous flux variables.

Control volumes are formed over the entire flow domain in question and the governing equations (derived in Chapter 3) are integrated and solved for the flow variables. In CFX, all spatial terms are discretized using second order central differencing but the advection terms (those involving a velocity gradient) have several different schemes available for discretization both for convenience and solution speed. Convection coefficients are obtained using Rhie-Chow interpolation formulae (discussed below).

4.2.1 Diffusion Terms:

Terms involving gradient diffusion and advection can be explained with reference to Figure 4.3. Capital letters represent the actual position of the flow variable node at the intersection of the solid mesh lines. Lower case letters represent the position of the boundaries between the actual control volumes with the dashed line representing the control volume centered on node P. For this discussion the diagonal arrow represents the two dimensional flow velocity.

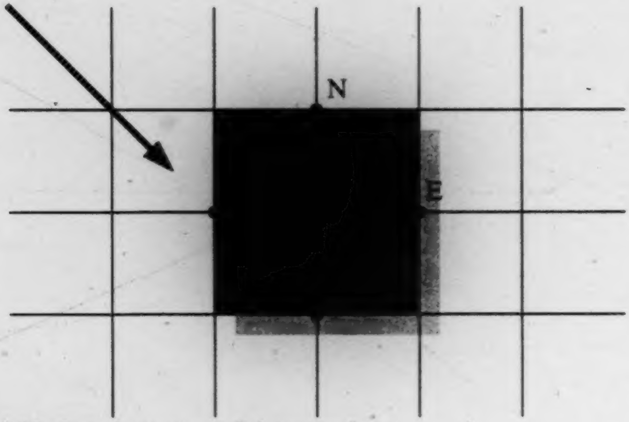

Figure 4.3 – Variable locations at mesh intersections.

Control volume centroids are represented by the solid circles where the flow variables in question are stored. The CV of interest is located at point P and has surrounding interphases with its neighbours at *n*, *e*, *s* and *w*. Consider the diffusional terms at the west face, *w*, of the control volume and discretize them as follows:

$$\iint_{A_w} \Gamma \nabla f \cdot \hat{n} dA = \frac{\Gamma A_w}{\Delta x}(f_P - f_W) \equiv D_w(f_P - f_W) \tag{4.3}$$

Here A_w is the area of the west face, Δx is the distance between the west (W) and central (P) nodes and D_w is the west diffusion coefficient. Similar expressions can be derived for the remaining three faces and when summed form the diffusive contribution to the governing equation as follows:

$$D_w(f_P - f_W) + D_e(f_E - f_P) + D_n(f_P - f_N) + D_s(f_S - f_P) + other\_terms = 0 \tag{4.4}$$

4.2.2 Advection Terms:

Discretization of the advection terms determines the overall accuracy of the solutions of the model equations used in the CFX solver. For the work presented in this thesis the HYBRID and higher order SUPERBEE schemes were used. Advection terms, which describe the convective flux of the conserved variable across the phase boundary, are required at the interfaces between control volumes; however, since the flow variables are stored at the centroids of control volumes, there has to be some sort of interpolation to determine the interface flux values. Many different schemes have been proposed over the years to deal with this issue and some of the methods available in CFX are discussed below.

4.2.3 Upwind Differencing (UDS):

When the flow is from left to right (i.e. from *W* to *E*), the advected value of the variable *f* at the west face of the control volume (f_w) is taken to be f_W, so that, at the west face:

$$\int \rho f \overline{U} \cdot \hat{n} dA = \rho U_w A_w f_W \equiv C_W f_W \qquad (4.5)$$

Here C_W is the convection coefficient at the west face. As can be seen from the discussion on diffusion, all factors involving f_W can be collected together and a matrix coefficient for the west node can be determined

$$A_W = MAX(C_W, 0) + D_W \qquad (4.6)$$

This scheme is first order accurate. Convection coefficients for the other faces (in the case of three dimensional flow this would include top, bottom, east, west, front and back faces, Figure 4.1) can be constructed in the same manner and a summation of the terms carried out to form the set of matrix equations governing the flow phenomena.

4.2.4 Hybrid Differencing (HDS):

This is a modification to the first order upwind differencing in which central differencing is used if the mesh Peclet number (C/D) (ratio of convection to diffusion) is less than 2, and upwind differencing, but ignoring diffusion, is used if the mesh Peclet number is greater than 2. In this case, the west matrix coefficient is:

$$A_W = MAX\left(\frac{1}{2}C_W, D_W\right) + \frac{1}{2}C_W \tag{4.7}$$

This scheme is also first order accurate, but is slightly better than upwind differencing because second order central differencing will be used across streams and in regions of low flow. This is the default discretization scheme used in CFX 4.2.

4.2.5 Total Variation Diminishing Schemes:

Total variation diminishing (TVD) schemes are modifications to the higher order upwind schemes in CFX with flux limiters to ensure the boundedness of the solution. The Superbee TVD scheme was chosen for these studies due to its properties of compression, shock sharpening and low asymmetry. These properties are demonstrated in the following section and have a significant impact on the overall simulation results (also please see Chapter 7 Results and Discussion).

In TVD schemes f_w is given by:

$$f_w = \left(1 + \frac{1}{2}\psi\right)f_W - \frac{1}{2}\psi f_{WW} \tag{4.8}$$

Where the flux limiter, ψ, which is given in terms of the ratio $r=\frac{f_P - f_W}{f_W - f_{WW}}$ for Superbee is:

$$\psi = \max\left(0, \min(2r,1), \min(r,2)\right) \tag{4.9}$$

In fact, any scheme which falls within the regions to the right of the dashed line outlined in the Figure 4.4 is guaranteed to be TVD and subsequently non-oscillatory. Half cell values, those involving indices with $_{i+1/2}$ have to be constructed.

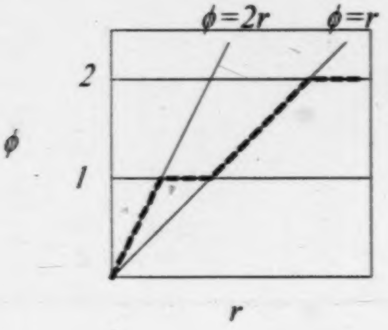

$\phi=0 \rightarrow f_{i+1/2}=f_i$

$\phi=1 \rightarrow f_{i+1/2}=f_{i+1/2}^{Central}$

$\phi=r \rightarrow f_{i+1/2}=f_{i+1/2}^{Up}$

$\phi=2 \rightarrow f_{i+1/2}=f_{i+1}$

$\phi=2r \rightarrow f_{i+1/2}=f_{i+1/2}^{Up2}$

$f_{i+1/2}=median(f_i,f_{i+1/2}^{Central},f_{i+1},f_{i+1/2}^{Up},f_{i+1/2}^{Up2})$

Figure 4.4 – Superbee TVD scheme.

Each of the terms present in this expression have to be constructed based on finite difference approximations. These are outlined next.

4.3 Constructing Finite Difference Schemes

Important in the use of CFD is the formulation of the difference equations that are used to represent the continuous differential equations governing the flow field. As a simple example, a 1D wave equation was discretized in space and time to study the characteristics of the differencing equations that have been proposed and some that are implemented in CFX.

Uniform second order accurate non-oscillatory schemes are attributed to Harten and Osher. The methods of Lax-Wendroff (LW) related to upwind methods which lead to the total variation diminishing (TVD) schemes (Van Leer and Roe). Sweby found flux limited TVD-LW methods that lead to improved TVD-LW schemes. A brief discussion of this progression is given below.

Consider the one dimensional wave equation

$$\frac{\partial u}{\partial t} + c\frac{\partial u}{\partial x} = 0 \tag{4.10}$$

and approximate the derivatives using the midpoint rule in both space and time; however, discretization of the spatial terms is expressed using half cell or intermediary values:

$$\frac{f_i^{n+1} + f_i^{n}}{\Delta t} + c\frac{\left[f_{i+1/2}^{n+1/2} - f_{i-1/2}^{n+1/2}\right]}{\Delta x} = 0 \tag{4.11}$$

It is necessary to construct values for the half cells $f_{i+1/2}^{n+1/2}$ and $f_{i-1/2}^{n+1/2}$. Consider Figure 4.5 showing nodes at time *n* and *n+1* and at positions *i-1*, *i*, and *i+1*. Half cell values can be determined at *n+1/2* and at *i+1/2*.

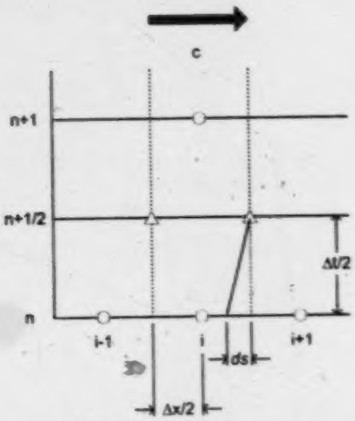

Figure 4.5 – TVD half cell construction in forward direction.

$$ds = c\frac{\Delta t}{2} \qquad (4.12)$$

The data at the base of the interpolation between locations $_i$ and $_{i+1/2}$ must come from some interpolation as follows:

$$f_{i+1/2}^{n+1/2} = f_{i+1/2}^{n} - (slope)ds \qquad (4.13)$$

where

$$slope = \frac{f_{i+1/2}^{n} - f_{i}^{n}}{\Delta x/2} \qquad (4.14)$$

simplifying:

$$f_{i+1/2}^{n+1/2} = f_{i+1/2}^{n} - \left[\frac{f_{i+1/2}^{n} - f_i^n}{\Delta x/2}\right]\left[c\frac{\Delta t}{2}\right] = f_{i+1/2}^{n} - \frac{c\Delta t}{\Delta x}\left[f_{i+1/2}^{n} - f_i^n\right] \tag{4.15}$$

In a similar manner the $f_{i-1/2}^{n+1/2}$ half cell value can be calculated as shown in Figure 4.6:

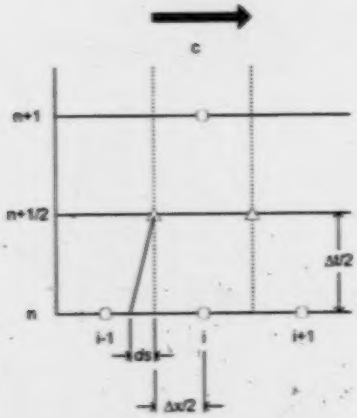

Figure 4.6 - TVD half cell construction in backward direction.

$$ds = c\frac{\Delta t}{2} \tag{4.16}$$

$$f_{i-1/2}^{n+1/2} = f_{i-1/2}^{n} - (slope)ds \tag{4.17}$$

$$slope = \frac{f_{i-1/2}^{n} - f_{i-1}^{n}}{\Delta x/2} \tag{4.18}$$

after substitution this gives:

$$f_{i-1/2}^{n+1/2} = f_{i-1/2}^{n} - \left[\frac{f_{i-1/2}^{n} - f_{i-1}^{n}}{\Delta x/2}\right]\left[c\frac{\Delta t}{2}\right] = f_{i-1/2}^{n} - \frac{c\Delta t}{\Delta x}\left[f_{i-1/2}^{n} - f_{i-1}^{n}\right] \tag{4.19}$$

These interpolations for the half cell values are substituted back into equation (4.11) to give the new expression for f_i^{n+1}.

$$f_i^{n+1} = f_i^n - \frac{c\Delta t}{\Delta x}\left[\left(f_{i+1/2}^n - \frac{c\Delta t}{\Delta x}\left[f_{i+1/2}^n - f_i^n\right]\right) - \left(f_{i-1/2}^n - \frac{c\Delta t}{\Delta x}\left[f_{i-1/2}^n - f_{i-1}^n\right]\right)\right] \tag{4.20}$$

$$f_i^{n+1} = f_i^n - \frac{c\Delta t}{\Delta x}\left[f_{i+1/2}^n - f_{i-1/2}^n\right] + \left(\frac{c\Delta t}{\Delta x}\right)^2\left[f_{i+1/2}^n - f_i^n - f_{i-1/2}^n + f_{i-1}^n\right] \tag{4.21}$$

It is necessary to define the $f_{i+1/2}^n$ and $f_{i-1/2}^n$ terms. Calculation of these half cell values determines the accuracy of the numerical scheme.

Several different methods have been proposed for constructing the half cell values in the discretization scheme just described. Schemes listed below are used for the implementation of SUPERBEE and MINMOD TVD Schemes.

Lax-Wendroff Central Difference

$$f_{i+1/2}^n = f_{i+1/2}^{n,Central} = \frac{1}{2}\left(f_i^n + f_{i+1}^n\right)$$

$$f_{i-1/2}^n = f_{i-1/2}^{n,Central} = \frac{1}{2}\left(f_{i-1}^n + f_i^n\right) \tag{4.22}$$

Warming-Beam Upwind

$$f_{i+1/2}^n = f_{i+1/2}^{n,Up} = f_i^n + \left(f_i^n - f_{i-1/2}^{n,Central}\right)$$

$$f_{i-1/n}^2 = f_{i-1/2}^{n,Up} = f_{i-1}^n + \left(f_{i-1}^n - f_{i-3/2}^{n,Central}\right) \tag{4.23}$$

Second Order Upwind

$$f_{i+1/2}^{n} = f_{i+1/2}^{n,Up2} = f_{i}^{n} + \left(f_{i}^{n} - f_{i-1}^{n}\right)$$

$$f_{i-1/2}^{n} = f_{i-1/2}^{n,Up2} = f_{i-1}^{n} + \left(f_{i-1}^{n} - f_{i-2}^{n}\right) \qquad (4.24)$$

The TVD schemes can be reconstructed based on the formulations using the half cell values as follows:

MINMOD: $f_{i+1/2}^{n} = median(f_{i}^{n}, f_{i+1/2}^{n,Central}, f_{i+1/2}^{n,Up})$ (4.25)

SUPERBEE: $f_{i+1/2}^{n} = median(f_{i}^{n}, f_{i+1/2}^{n,Central}, f_{i+1/2}^{n,Up}, f_{i+1}^{n}, f_{i+1/2}^{n,Up2})$ (4.26)

4.3.1 Higher Order Non-oscillatory Schemes (SONIC and UNO)

Harten and Osher are credited with formulating the higher order schemes by realizing that the problems associated with the TVD schemes are caused by the Lax-Wendroff central differences approximation (see equation 4.22). To alleviate these problems, they introduced a quadratic interpolation scheme based on fitting parabolas between node values and then interpolating the half cell values, Figure 4.7.

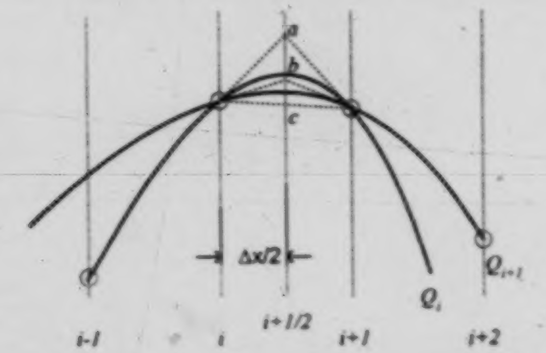

Figure 4.7 – Construction of the parabolic interpolation.

$$f_{i+1/2}^{c,parabolic} = median(a,b,c) \tag{4.27}$$

Q_i and Q_{i+1} are parabolas fitting points $({}_{i-1},\ {}_{i},\ {}_{i+1})$ and $({}_{i},\ {}_{i+1},\ {}_{i+2})$, respectively. Points a, b, c, which will define the half cell values, are at the intersection of the tangents of the parabolas directly at ${}_{i+1/2}$ half cell. The parabola is defined as $(x-h)^2 = 4P(y-k)$ and it is necessary to find *h, P, k*. Calculations for parabola Q_i :

$$\begin{aligned} X_{i+1}^2 - 2hX_{i+1} + h^2 &= 4P(f_{i+1} - k) \\ X_i^2 - 2hX_i + h^2 &= 4P(f_i - k) \\ X_{i-1}^2 - 2hX_{i-1} + h^2 &= 4P(f_{i-1} - k) \end{aligned} \tag{4.28}$$

Subtracting equation 2 from 1 and 3 from 2 results in:

$$\begin{aligned} X_{i+1}^2 - X_i^2 - 2h(X_{i+1} - X_i) &= 4P(f_{i+1} - f_i) \\ X_i^2 - X_{i-1}^2 - 2h(X_i - X_{i-1}) &= 4P(f_i - f_{i-1}) \end{aligned} \tag{4.29}$$

For a uniform grid the distance between neighboring grid points is ΔX and the off index ${}_i$ can be substituted as follows:

$$\begin{aligned} (X_i + \Delta X)^2 - X_i^2 - 2h(X_i + \Delta X - X_i) &= 4P(f_{i+1} - f_i) \\ X_i^2 - (X_i - \Delta X) - 2h(X_i - (X_i - \Delta X)) &= 4P(f_i - f_{i-1}) \end{aligned} \tag{4.30}$$

These equations simplify to:

$$\begin{aligned} \Delta X(2X_i + \Delta X) - 2h\Delta X &= 4P(f_{i+1} - f_i) \\ \Delta X(2X_i - \Delta X) - 2h\Delta X &= 4P(f_i - f_{i-1}) \end{aligned} \tag{4.31}$$

Two such higher order nonoscillatory schemes have been devised. UNO2 and SONIC both use quadratic interpolation of the Law-Wendroff central differences approximation; however, UNO2 implements Van Leer's MINMOD scheme and replaces the $f_{i+1/2}^{C}$ expression with the quadratic interpolation. The SONIC scheme uses Roe's SUPERBEE scheme in the same manner and replaces the $f_{i+1/2}^{Central}$ with the quadratic interpolation. These two methods are not implemented in the current version of CFX4.2. Having been introduced to the methods used to construct the difference approximations it is necessary to observe the effect that the different schemes have on simulation results.

4.4 Analysis of Several Different Discretization Schemes

With the various choices available for discretizing the governing equations it is necessary to study the behavior of these different schemes. A Flux-Limited Lax-Wendroff scheme was constructed for the 1D linear wave equation:

$$\frac{\partial f}{\partial t} + c\frac{\partial f}{\partial x} = 0 \tag{4.32}$$

on a grid of 900 mesh cells of size $\Delta x = 1.0$. The performance of First Order Upwinding, Lax Wendroff Central Differencing, Warming-Beam Upwinding, Minmod, MUSCL and SUPERBEE schemes were compared by convecting a simple initial wave form consisting of a parabola, spike and shock at time equal to zero along the mesh for 500 time steps. The results of the final wave form were compared with the initial waveform for each of the different schemes.

TVD is representative of the changes in total wave form height as the simulation progresses. TVD ensures no creation of any oscillations and no growth of the amplitude of the wave form. Nonoscillatory (or essentially nonoscillatory) schemes do not allow any creation of oscillations and allow some growth of the amplitude. The total variation is defined as:

$$TV(f)=\sum_{i=1}^{ilen}\left|f_{i+1}-f_i\right| \tag{4.33}$$

Numerical schemes are said to be Total Variation Diminishing (TVD) if the total variations satisfy the inequality $TV(f^{n+1})\leq TV(f^{n})$ for all time. Satisfying this conditions also ensures that there will be no oscillations produced in the solution. For conditions contrary to this inequality, oscillations will be present. Oscillations can lead to nonphysical values produced by the discretization scheme. This can be a problem when predicting values that are bounded (such as the volume fraction ε) - it is not reasonable to expect a volume fraction less than zero or greater than one. TVD schemes can be guaranteed to be present if the flux limiter is limited to lie within the area to the right of the *2r* line on the Superbee diagram, Figure 4.4. All of the TVD schemes can be constructed by choosing the correct flux limiter expression.

4.4.1 FIRST ORDER UPWINDING (FOUW)

Figure 4.8 is an overlay plot of the initial wave train given by the initial conditions in the assignment and that same wave train after being convected for n=500 time steps using

FOUW. As can be seen from the Figure, this method is highly dissipative and leads to a smearing of the three distinct shapes that were initially present. Characteristic of a first order scheme, there are no oscillations in the numerical solution.

The final normalized total variation for n=800 of FOUW at C_N=0.75 is 0.29947. Although this scheme satisfies the TVD criterion, it performs poorly due to the dissipative effects (Figure 4.14).

4.4.2 LAX-WENDROFF Central Differencing (LW)

Figure 4.9 is also an overlay plot showing the initial wave train and the wave train after being convected for n=500 time steps using LW. Most notable of this scheme are the oscillations that are present. The convected wave train also shows a slight asymmetry to the right.

The final normalized total variation for n=800 of LW at C_N=0.75 is 1.24. Since this value is greater than 1.0, the LW scheme does not satisfy the TVD criterion and is not a TVD scheme (Figure 4.14).

4.4.3 WARMING-BEAM (WB)

Figure 4.10 shows that the WB scheme leads to oscillations in the convected solution. Asymmetries are not as apparent as in the LW scheme. Sharp edges (such as those shown for the n=1 plot in Figure 4.10 on the top hat) show that oscillations using WB are most pronounced at abrupt edges (such as shocks or phase boundaries that would be present in multiphase flow simulations).

The final normalized total variation for n=800 of LW at C_N=0.75 is 1.46. Since this value is greater than 1.0, the WB scheme does not satisfy the TVD criterion and is not a TVD scheme (Figure 4.14).

4.4.4 Minmod TVD (MINMOD)

Figure 4.11 is the MINMOD solution to the convection equation at n=1 and n=500 time steps. This scheme is somewhat dissipative as shown by the longer trailing edges between the three different pulses. Due to this dissipation the pulses tend to merge into each other; however, this is not as pronounced as in the FOUW scheme.

The final normalized total variation for n=800 of LW at C_N=0.75 is 0.77. Since this value is less than 1.0, the MINMOD scheme does satisfy the TVD criterion and is a TVD scheme (Figure 4.14).

4.4.5 MUSCL TVD (MUSCL)

Figure 4.12 shows the fairly good results obtained using the MUSCL scheme. Each pulse is preserved and there is very little dissipation between them at n=600. All of the pulses are symmetric and the method is not overly compressive. Characteristic of the TVD schemes, there are no oscillations in the solution.

The final normalized total variation for n=800 of LW at C_N=0.75 is 0.89. Since this value is less than 1.0, the MUSCL scheme does satisfy the TVD criterion and is a TVD scheme (see Figure 4.14).

4.4.6 SUPERBEE

Figure 4.13 for the SUPERBEE scheme shows that all of the pulses are very well preserved; however, this method is over compressive and tends to turn all of the pulses into a "top hat" sort of shape. There is very little dispersion and the three pulses are easy to distinguish. This method has been selected for the multiphase flow modeling as the higher order discretization because it tends to sharpen shocks which are present within the flow domain.

The final normalized total variation for n=800 of LW at C_N=0.75 is 0.944. Since this value is less than 1.0, the SUPERBEE scheme does satisfy the TVD criterion and is a TVD scheme (see Figure 4.14).

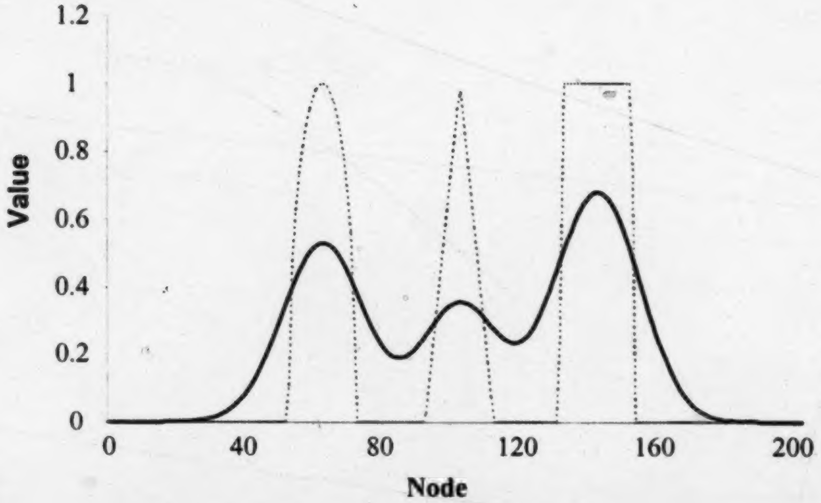

Figure 4.8 – First order upwinding test. Dashed line represents the initial wave form and the solid line represents the wave form after convecting for 500 time steps.

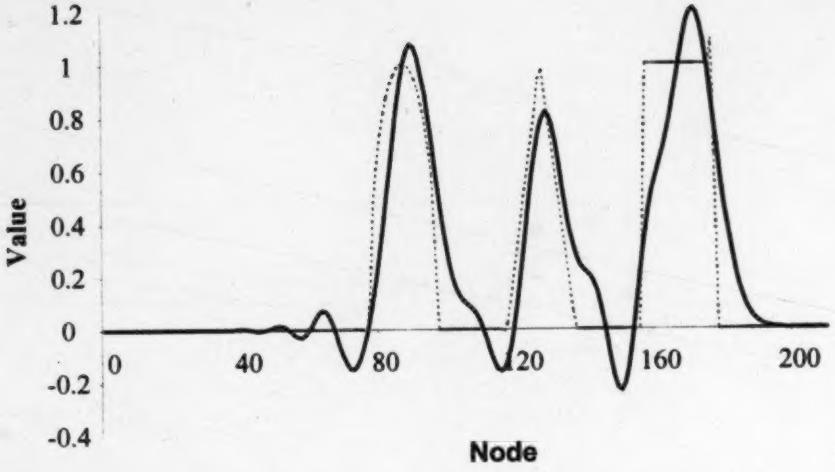

Figure 4.9 – Lax-Wendroff Test. Dashed line represents the initial wave form and the solid line represents the wave form after convecting for 500 time steps.

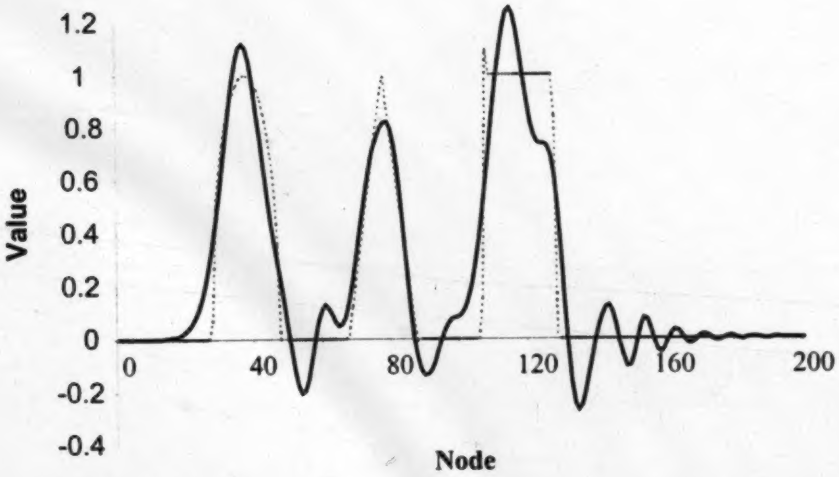

Figure 4.10 – Warming-Beam upwinding test. Dashed line represents the initial wave form and the solid line represents the wave form after convecting for 500 time steps.

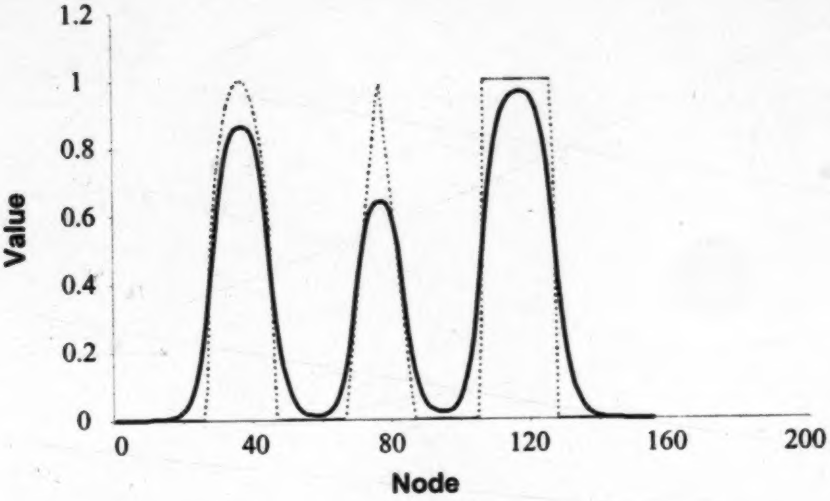

Figure 4.11 – MINMOD test. Dashed line represents the initial wave form and the solid line represents the wave form after convecting for 500 time steps.

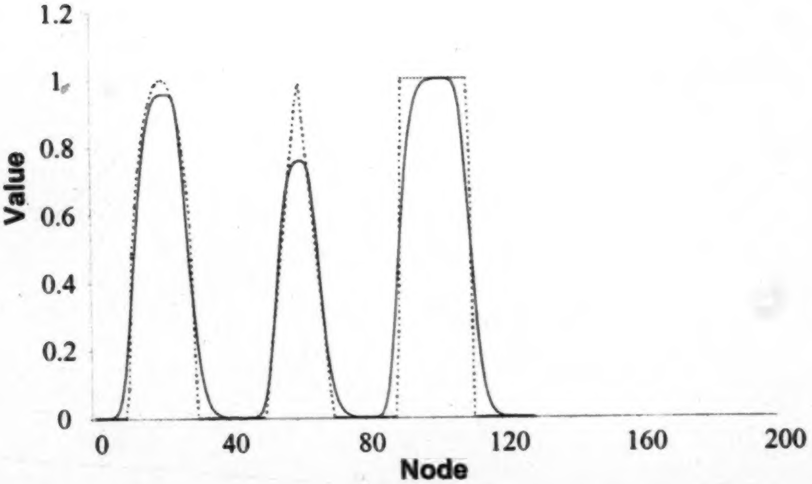

Figure 4.12 – MUSCL TVD test. Dashed line represents the initial wave form and the solid line represents the wave form after convecting for 500 time steps.

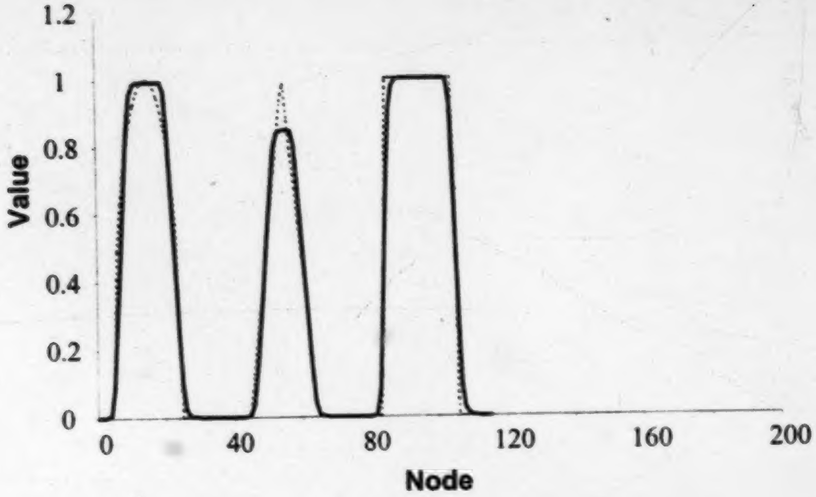

Figure 4.13 – SUPERBEE TVD test. Dashed line represents the initial wave form and the solid line represents the wave form after convecting for 500 time steps.

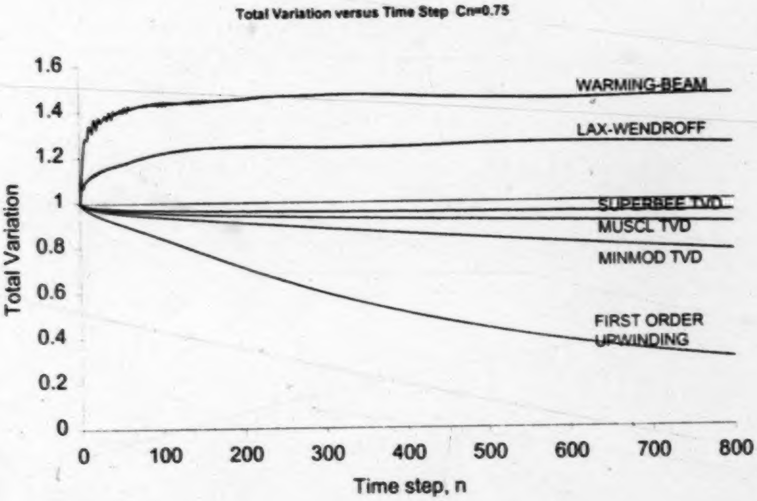

Figure 4.14 – Total variation plots with time step for each of the discretization schemes studied.

Figure 4.14 showing the total variation with time step indicates that the schemes introducing oscillations into the advected wave form had normalized total varizations that were greater than one. Dissipative schemes (such as FOUW and MINMOD) appear to have TVDs which are much lower than one. SUPERBEE and MUSCL schemes with TVDs of approximately one retained the original wave form structure the best.

4.5 Source Terms

The terms appearing as sources in the general conservation equation are split into two parts when integrated over the control volume.

$$\iiint_{v} \Phi dv = S_C + S_P f_P \tag{4.34}$$

The S_P term must be negative to ensure that the source term does not grow and create convergence problems (Patankar, 1980). This term tends to enhance the diagonal of the matrix resulting in diagonal dominance and a faster solution procedure. Source terms, including solids pressure, have been discussed in Chapter 3.

4.6 Coupling Difference Equations with IPSA

Momentum equations for the gas and solids phases must be linked through momentum transfer terms. The numerical solution of these two sets of equations requires an algorithm for solution. This section describes some of the numerical procedures used in CFX 4.2 to solve the multiphase flow equations.

4.6.1 Semi-Implicit Method for Pressure-Linked Equations (SIMPLE)

The numerical solution of the multiphase flow equations used in the CFX 4.2 solver is that of the InterPhase Slip Algorithm (IPSA) which is an extension of the SIMPLE (Semi-Implicit Method for Pressure-Linked Equations) of Patankar and Spalding (1972) which was developed for single-phase flow problems. The SIMPLE method was devised to solve for the pressure terms appearing in the momentum equations. For incompressible flow there is no equation of state for pressure and so the pressure field has to be solved iteratively. If the pressure field is given, there is no difficulty in constructing and solving the momentum equations. However, if the pressure field is not known (as is usually the case), then a pressure correction algorithm must be employed.

In the SIMPLE method, an estimated pressure field is created and a pseudo velocity field is created based upon relating the pressure in the momentum equations to reducing the continuity error. The pressure is then recalculated using a pressure correction equation and the scheme is iterated as follows:

1. Guess p^* (the estimated pressure field);
2. Solve the momentum equations to get u^*, v^*, w^*;
3. Solve the pressure correction equation;
4. Correct the pressure and velocities;
5. Solve for any other flow variables which might influence the flow field;
6. Return to step 2 with the corrected pressure as the new p^* field. Repeat until convergence.

4.6.2 Inter Phase Slip Algorithm (IPSA)

IPSA also employs an iterative solution scheme in which the pressure-correction method is used to satisfy the conservation at each iteration. In general the transport equations are coupled via the interphase transfer terms (in this case through the drag terms in the momentum equations). Accordingly, convergence could be very slow when the coupling terms are very large. For two-phase flows the Partial Elimination Algorithm (PEA) by Spalding can be employed. For the sake of argument and build up of the methods used for multiphase flows with more than two phases the development of PEA will be demonstrated.

For a particular computational cell within the solution domain, the transport equations (momentum and energy) can be simplified as (Lo, 1989):

$$\begin{aligned} a_1\phi_1 &= b(\phi_2 - \phi_1) + c_1 \\ a_2\phi_2 &= b(\phi_1 - \phi_2) + c_2 \end{aligned} \tag{4.35}$$

where a contains the advection and transient coefficients; b is the interphase transfer coefficient and c represents all other terms not yet accounted for (i.e. source terms, etc...), subscripts 1 and 2 represent each of the phases. These equations can be rearranged to give the following:

$$\begin{aligned} (a_1 + b)\phi_1 &= b\phi_2 + c_1 \\ (a_2 + b)\phi_2 &= b\phi_1 + c_2 \end{aligned} \tag{4.36}$$

When the interphase transfer coefficient, b, is large, then the value of ϕ_1 is very close or equal to ϕ_2. Also, the values of the variables have changed little from their starting values; therefore, the rate of convergence would be quite slow. PEA minimizes this slow rate of convergence by eliminating ϕ_2 from the first equation and ϕ_1 from the second equation to give:

$$\begin{aligned}\left[a_1+\frac{b}{a_2}(a_1+a_2)\right]\phi_1&=\frac{b}{a_2}(c_1+c_2)+c_1\\ \left[a_2+\frac{b}{a_1}(a_1+a_2)\right]\phi_2&=\frac{b}{a_1}(c_1+c_2)+c_2\end{aligned} \tag{4.37}$$

Taking the limit as the interphase transfer coefficient becomes large, both of the variables tend to:

$$\phi_1=\phi_2=\frac{c_1+c_2}{a_1+a_2} \tag{4.38}$$

The two phases have the same value but are not necessarily maintained at their initial points.

4.6.3 Volume Fraction Equations

Volume fraction equations can simply be written as the ratio of the denominator over the numerator:

$$\varepsilon_1 = \frac{N_1}{D_1}$$
$$\varepsilon_2 = \frac{N_2}{D_2} \tag{4.39}$$

To ensure that the sum of the volume fractions always equals one, the two equations can be rewritten as:

$$\varepsilon_1 = \frac{N_1 D_2}{N_1 D_2 + N_2 D_1}$$
$$\varepsilon_2 = \frac{N_2 D_1}{N_1 D_2 + N_2 D_1} \tag{4.40}$$

With further manipulation the above equation can be rearranged to the following:

$$\varepsilon_1 = \frac{N_1}{D_1 + \left[(N_1 - \varepsilon_1 D_1) + \frac{D_1}{D_2}(N_2 - \varepsilon_2 D_2)\right]} \tag{4.41}$$

The terms within the square brackets represent the continuity error of the two phases in question.

4.6.4 Pressure Correction Equation

The IPSA solution method makes use of a single pressure-correction equation for correcting the pressure field based on satisfying the continuity and momentum equations.

Therefore, this method yields a single pressure field that is shared between the two phases.

The momentum equations are first solved based upon an initial pressure field estimate. As a result of this, the computed velocities may not satisfy continuity. Pressure-correction is carried out to adjust the velocity and pressure fields to correct the continuity imbalance. The phase one continuity equation can be simplified to:

$$a_{1,P}\varepsilon_{a,P}-\left[\sum_{i}\left(a_{1,i}\varepsilon_{a,i}\right)+\dot{m}_{i}\right]=0 \tag{4.42}$$

Where subscript *p* refers to the computational cell under consideration and *i* refers to the neighbouring points; *a*(=ρ*Au*) is the convection coefficient; *A* is the mass flow area and *m* is the mass source term. The transient term is not considered in this discussion. Corrections are introduced into the equations by expressing the velocity as:

$$u_{1}=u_{1}^{*}+\frac{\partial u_{1}}{\partial p}p' \tag{4.43}$$

where the superscript * denotes values before the correction step and p' ($=p-p^{*}$) is the pressure correction. Substituting the pressure corrected velocity component into the above simplified continuity equation gives:

$$a_{1,P}^{*}\varepsilon_{1,P}-\left[\left(\sum_{i}a_{1,i}^{*}\varepsilon_{1,i}\right)+m_{i}\right]+a_{1,P}^{'}P_{P}^{'}\varepsilon_{1,P}-\sum_{i}a_{1,P}^{'}P_{P}^{'} \tag{4.44}$$

where $a' = \rho A \frac{\partial u}{\partial P}$. A similar expression can be formulated for the second phase. By adding together the phase-1 and 2 equations a joint-continuity equation is obtained in terms of the pressure correction.

4.6.5 IPSA in Harwell-FLOW3D Computer Code: now CFX 4.2

The IPSA method previously described has been incorporated into the FLOW3D code and the solution sequence is as follows (Lo, 1989):

1. Guess field values;
2. Solve momentum equations (using PEA if necessary);
3. Calculate convection coefficients using Rhie-Chow algorithm;
4. Solve one volume fraction equation using the implicit formulation;
5. Obtain the second volume fraction;
6. Set up the pressure-correction using the joint-continuity;
7. Solve the pressure-correction equation and apply the correction to velocities, pressures and convection coefficients
8. Check convergence and repeat from 2 if necessary.

In this form, the IPSA solution method is formulated for a two phase flow and can easily be extended to multiphase flows with little difficulty. For example, the PEA solution technique only applies to two phase flows and is not general enough

4.6.6 Rhie-Chow Interpolation

All variables in the CFX code are stored at the centroid of control volumes using a non-staggered grid. The pressure correction method used for incompressible flows requires the calculation of the pressure derivative to the second order which can lead to an oscillatory pressure field which satisfies continuity but makes no physical sense (Patankar, 1980). Rhie-Chow interpolation is used to overcome this problem with non-staggered gridding. A brief description of this method is included below based on the original formulation by Rhie and Chow (1983). With reference to Figure 4.3 the flow variables are all stored at nodes with the control volume boundaries defined by the dashed lines. Consider the steady one dimensional continuity equation over the control volume centered at P

$$\rho_g u A_e - \rho_g u A_w = 0 \tag{4.45}$$

The momentum equation now uses a central difference formulation to discretize the pressure gradient. Please note that in equation (4.46) the convective mass flux term has been expressed as $\dot{M}$ and not explicitly as a combination of nodal values. The convective mass flux can be calculated using any of the aforementioned methods in this chapter, B_P represents all other terms including friction, body forces and sources.

$$\dot{M}\left(u_P - u_W\right) = \frac{1}{2}\left(P_W - P_E\right)A_P + B_P \tag{4.46}$$

The velocity at node P can be more conveniently written as

$$u_P = -\frac{A_P}{\dot{M}}\left.\frac{dp}{dx}\right|_P \Delta x + B_P \tag{4.47}$$

The velocity at the east face, e, is the average of the u_P and u_E nodes

$$u_e = \frac{u_P + u_E}{2} = -\frac{A_e}{\dot{M}}\frac{1}{2}\left(\left.\frac{dp}{dx}\right|_P + \left.\frac{dp}{dx}\right|_E\right)\Delta x + \overline{B} \tag{4.48}$$

Substituting expressions from (4.48) into the continuity equation (4.45) can result in an oscillatory pressure field. Rhie and Chow (1983) recognized this problem and suggested formulating the pressure gradient on the control volume boundaries using first order approximations so that the first order pressure variations can be detected.

$$u_e + \frac{A_e}{\dot{M}}\left(P_E - P_P\right) = \frac{u_P + u_E}{2} + \frac{A_e}{\dot{M}}\frac{1}{2}\left(\left.\frac{dP}{dx}\right|_P + \left.\frac{dP}{dx}\right|_E\right)\Delta x \tag{4.49}$$

Expansion of the pressure derivatives using central differences and collection of like terms results in a scheme that can detect first order pressure variations on a non-staggered mesh.

4.7 Numerical Errors and Convergence

The CFX solver solves linearized transport equations. As shown previously these equations are derived by integrating the transport equations over control volumes (cells), thus each equation may be regarded as 'belonging' to a particular variable and to a particular cell. These equations describe the influence on that particular variable in that particular cell of:

a) other variables in the same cell;

b) values of the same variable in neighboring cells; and

c) values of the other variables in neighboring cells.

Iteration is used to solve for the variables within each cell that are governed by these equations. An inner iteration solves for the spatial coupling for each variable and an outer iteration is used to solve for the coupling between variables. Thus each variable is taken in sequence, regarding all other variables as fixed, a discrete transport equation is formed for every cell in the flow domain and the problem is handed over to a linear equation solver which returns the updated values of the variable. The non-linearity of the original differential equations is simulated by reforming the diffusion and convection coefficients of the discrete equations, using the most recently calculated values of the variables, before each outer iteration.

4.7.1 Output File Summary of CFX 4.2 Simulations

There are several ways to specify control of the outer iteration. A maximum number of iterations can be specified for the outer iteration. For transient calculations the maximum number of iterations might be between 5 and 50 whereas for a steady state calculation the number of outer iterations might be up to several tens of thousands depending upon the desired accuracy.

A second criterion determining whether the solution procedure has converged is the satisfaction of a tolerance on some residual. The default convergence criterion is based upon the satisfaction of a mass source residual. The mass source residual is not dimensionless but is the sum of the absolute values of the net mass fluxes into or out of every cell in the flow domain and has units of mass/time. An example of the calculation of the mass source residual is as follows:

$$R = \sum_i \left| \rho A_i \hat{u}_i \right| \text{ with i cycling through all of the control volumes} \tag{4.50}$$

A reasonable non-dimensionalization of this residual would be to divide R by the total sum of the mass flow rates through all of the inlets.

With each simulation an output file is created summarizing the residual reduction for the inner iterations and outer iterations (time step). A sample from one of these output files is shown in Figure 4.15; labels have been added to this figure to show items of interest. Included in this file is a summary of the flow variables at a monitoring point. The values at the monitoring point should converge to constants with increasing numbers of inner iterations.

For each inner iteration the absolute residuals for each of the flow variables is listed. These values should decrease with progressing inner iterations to ensure that convergence is being achieved. All data for the grid refinement studies in section 7.1.3 have used these inner iteration absolute residuals for comparison purposes. Also provided in this output file is a list of the flow variables at a monitoring point within the flow domain.

Once the convergence criteria has been achieved for the inner iteration, in this study reduction of the gas mass continuity residual to 5 x 10^{-6} was chosen as the convergence criterion, statistics for the outer iteration are presented. The average reduction factor achieved by the linear solvers presents the ratio of the last inner iteration residual to that of the first inner iteration residual. These ratios must be less than one for convergence. Maximum absolute time derivatives are also summarized.

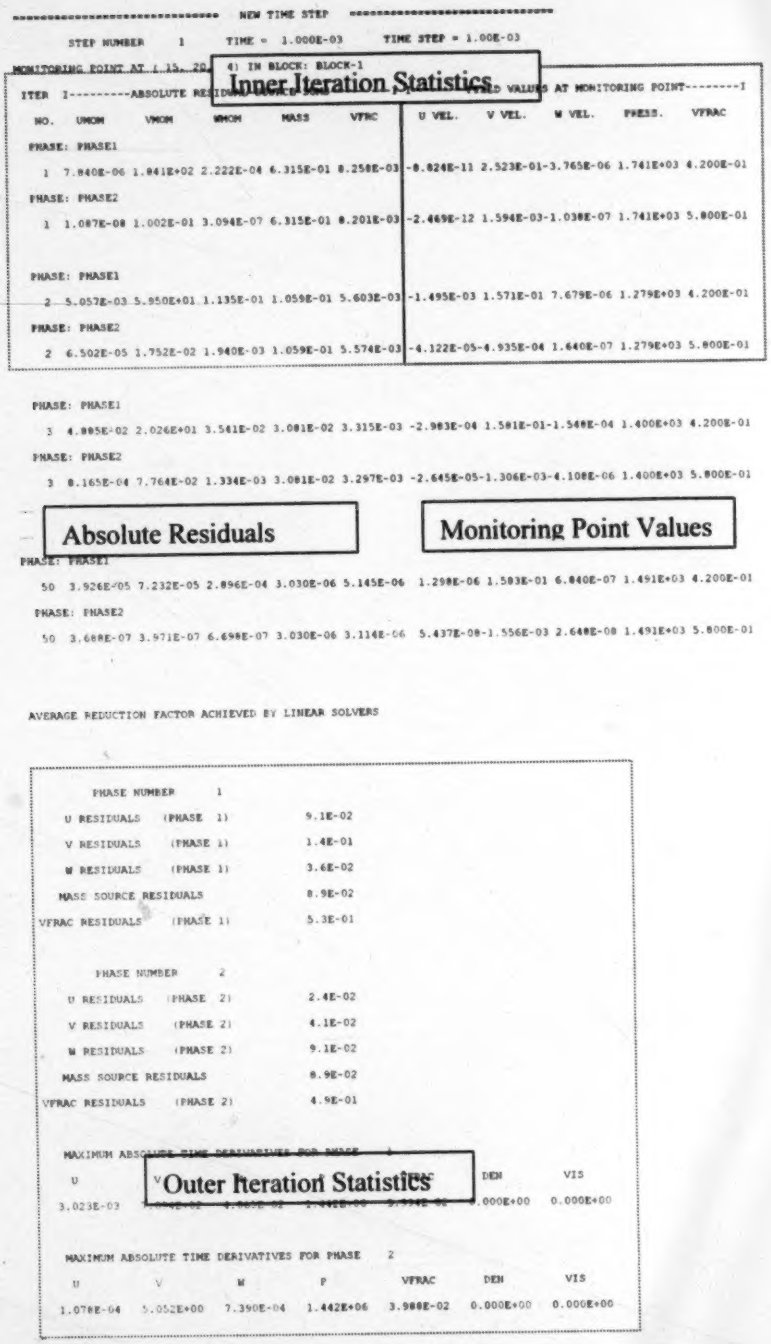

```
==============================  NEW TIME STEP  ==============================

      STEP NUMBER     1      TIME =  1.000E-03     TIME STEP = 1.00E-03

MONITORING POINT AT ( 15, 20,  4) IN BLOCK: BLOCK-1
 ITER  I---------ABSOLUTE RES                          D VALUES AT MONITORING POINT--------I
  NO.   UMOM      VMOM      WMOM      MASS      VFRC    U VEL.    V VEL.    W VEL.    PRESS.    VFRAC
 PHASE: PHASE1
    1  7.840E-06 1.841E+02 2.222E-04 6.315E-01 8.250E-03 -8.824E-11 2.523E-01-3.765E-06 1.741E+03 4.200E-01
 PHASE: PHASE2
    1  1.087E-08 1.002E-01 3.094E-07 6.315E-01 8.201E-03 -2.469E-12 1.594E-03-1.038E-07 1.741E+03 5.800E-01


 PHASE: PHASE1
    2  5.057E-03 5.950E+01 1.135E-01 1.059E-01 5.603E-03 -1.495E-03 1.571E-01 7.679E-06 1.279E+03 4.200E-01
 PHASE: PHASE2
    2  6.502E-05 1.752E-02 1.940E-03 1.059E-01 5.574E-03 -4.122E-05-4.935E-04 1.640E-07 1.279E+03 5.800E-01

 PHASE: PHASE1
    3  4.805E-02 2.026E+01 3.541E-02 3.081E-02 3.315E-03 -2.983E-04 1.581E-01-1.548E-04 1.400E+03 4.200E-01
 PHASE: PHASE2
    3  8.165E-04 7.764E-02 1.334E-03 3.081E-02 3.297E-03 -2.645E-05-1.306E-03-4.108E-06 1.400E+03 5.800E-01

PHASE: PHASE1
   50  3.926E-05 7.232E-05 2.896E-04 3.030E-06 5.145E-06  1.298E-06 1.503E-01 6.840E-07 1.491E+03 4.200E-01
 PHASE: PHASE2
   50  3.688E-07 3.971E-07 6.698E-07 3.030E-06 3.114E-06  5.437E-08-1.556E-03 2.648E-08 1.491E+03 5.800E-01


 AVERAGE REDUCTION FACTOR ACHIEVED BY LINEAR SOLVERS


       PHASE NUMBER       1
    U RESIDUALS    (PHASE  1)           9.1E-02
    V RESIDUALS     (PHASE 1)           1.4E-01
    W RESIDUALS     (PHASE 1)           3.6E-02
   MASS SOURCE RESIDUALS                8.9E-02
 VFRAC RESIDUALS     (PHASE 1)          5.3E-01

       PHASE NUMBER       2
    U RESIDUALS    (PHASE  2)           2.4E-02
    V RESIDUALS     (PHASE 2)           4.1E-02
    W RESIDUALS     (PHASE 2)           9.1E-02
   MASS SOURCE RESIDUALS                8.9E-02
 VFRAC RESIDUALS     (PHASE 2)          4.9E-01

   MAXIMUM ABSO
    U          V                                          DEN         VIS
  3.023E-03                                            .000E+00    0.000E+00

   MAXIMUM ABSOLUTE TIME DERIVATIVES FOR PHASE     2
    U           V           W           P          VFRAC       DEN         VIS
  1.078E-04   5.052E+00   7.390E-04   1.442E+06   3.988E-02   0.000E+00   0.000E+00
```

Figure 4.15 – Inner and outer iteration error summaries in CFX 4.2

Summary of Computational Methods

This chapter has shown the approach to solving the governing hydrodynamic equations of fluid mechanics for multiphase flows. Theoretical considerations of discretization scheme comparison were presented and the different schemes were compared and contrasted. Limitations of the schemes were also explored and the interpretation of numerical performance in terms of residual reduction and monitoring point values were discussed. Strengths of using the conservative formation for numerical modeling were briefly discussed and the problems associated with interpolating continuous flow field variables at points other than control volumes were elaborated on.

Chapter 5

CFX 4.2 Model Set-Up

This chapter describes the use and set-up of AEA Technology's CFX 4.2 computational fluid dynamics package. The command file and FORTRAN subroutines used for the simulations are discussed. Boundary, initial and other assumptions and conditions are described in detail. Adjustable parameters used for accelerating the simulations are discussed (Courant false time stepping, relaxation factors, double versus single precision calculations, Algebraic Multigrid acceleration, etc…).

5.1 CFX 4.2 Model Set Up

Running simulations with the CFX 4.2 flow solver requires writing a user FORTRAN file for special routines and also writing a command file to set up the desired simulation type and other solver settings. A general copy of both of the fortran (.f) and command (.fc) files are included in Appendix C. Specific details requiring explanation are elaborated in this chapter.

All simulations were of a gas-solid two-phase, three dimensional transient laminar flow situation in a rectangular fluidized bed geometry. Both phases were assumed to be incompressible and maintain constant hydrodynamic properties, such as viscosity, density and particle size. A time step of 0.001 seconds was used in all of the simulations with full flow field data output every 0.05 seconds. Convergence tolerance was set to a mass tolerance of 5.0×10^{-6} kg/s on the gas phase. This value represents the residual on the continuity equation after the outer (nonlinear) iteration.

5.1.1 Geometry

Geometry was chosen to reflect that of the experimental two dimensional bed used at the University of Saskatchewan under the direction of Dr. Berruti and operated by Jason Cowpan. A photograph of the experimental apparatus is shown in Figure 5.1; a more detailed description of the experimental apparatus is included in Chapter 6. Simulations were carried out in a Cartesian or rectangular coordinate system. The geometry was 1.2 m x 1.2 m x 0.10 m in the X, Y and Z directions corresponding with the experimental set up. The nozzle was placed on the left hand side of the fluidized bed domain and the orifice exit gas was shot towards the right. All dimensions of the simulation geometry could be changed: orifice size, nozzle insertion, nozzle submergence and also the overall bed size. Figure 5.2 shows the location and all geometry variables that could be altered for simulations.

Figure 5.1 - Photograph of the experimental two dimensional bed filled with coke particles.

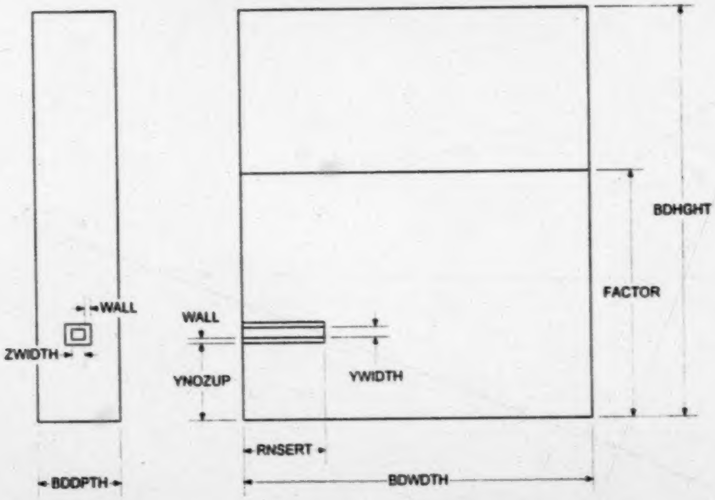
WALL
ZWIDTH
BDDPTH
WALL
YNOZUP
YWIDTH
RNSERT
BDWDTH
FACTOR
BDHGHT

Figure 5.2 – Definition of geometry variables used in the FORTRAN user file.

Each of the variables specified in the diagram are used in the user FORTRAN routines which automatically generate the mesh. Changing the variables in the COMMON /UCBLOK/ section at the head of the user FORTRAN file sets the geometry to be used in the simulations; these variables are summarized in Table 5.1.

Table 5.1:

User FORTRAN Geometry Variables for Simulations

Variable Name	**Type**	**Description**
BDDPTH	Float	Physical depth (Z direction) of reactor.
BDHGT	Float	Physical height (Y direction) of reactor.
BDWDTH	Float	Physical width (X direction) of reactor.
DIAM	Float	Particle diameter.
FACTOR	Float	Desired initial fluidized bed height. This value is overwritten by user FORTRAN.
FINES	Float	Mesh parameter, must be set equal to YNOZUP.
NTOP	Integer	Mesh parameter. This value determines the overall number of mesh points in the entire domain. Usually set to 30 or 40.
NUMZ	Integer	Mesh parameter. Odd number of mesh points in Z direction.
RNSERT	Float	Nozzle insertion into bed. Distance from left wall to tip of nozzle.
WALL	Float	Nozzle pipe wall thickness.
YNOZUP	Float	Distance from bottom of nozzle to distributor.
YWIDTH	Float	Physical size of square orifice in Y direction.
ZWIDTH	Float	Physical size of square orifice in Z direction.

Particular care was taken to generate a reasonable representation of the nozzle pipe and orifice used in the simulations. The rectangular section representing the pipe is a solid block defined in the simulation through which no flow could pass. Inclusion of this pipe has lead to certain recirculatory flow patterns beneath the nozzle due to the down flowing nature of the solids along the wall.

Since a rectangular coordinate system was chosen, the nozzle orifice could not be made round in shape. It was necessary to match the square orifice area with that of a round area used in the experimental apparatus. The correct orifice size to use in the simulations was defined as follows:

$$A_{0,E} = \pi r^2 = \frac{\pi}{4} D_0^2 \qquad A_{0,C} = D^2 \tag{5.1}$$

The area of the square orifice in the simulations, $A_{O,C}$, must be the same as the area of the round orifice, $A_{O,E}$, used in the experiments to ensure the correct momentum transfer and gas mass flow rate.

$$A_{0,C} = A_{0,E} \Rightarrow D = \frac{\sqrt{\pi}}{2} D_0 \tag{5.2}$$

Problems involving the meshing of this small dimension, D_0, within the simulation were encountered and tests were conducted to investigate this.

5.1.2 Grid Generation

Analytical solution of the governing equations of multiphase fluid mechanics is not possible so the continuous domain has to be split into a discrete mesh where approximate solutions are obtained at the intersections of the mesh lines. As pointed out by Anderson (1995), "the determination of a proper grid for the flow over or through a given geometric shape is a serious matter-one that is by no means trivial…the type of grid you choose for a given problem can make or break the numerical solution." The discretization mesh must be formulated to ensure numerical stability of the numerical solution technique while at the same time it must be structured such that mesh density is concentrated in regions of flow interest. Poor choice of mesh density can lead to incorrect solutions or solutions that are too coarse to resolve fine scale flow features. Too dense a mesh will lead to wasted computing resources.

In consideration of these facts a gridding routine was programmed in user FORTRAN as part of the CFX code to make a fine grid around the nozzle area. Figure 5.3 is a diagram of a typical discretization mesh generated with this code.

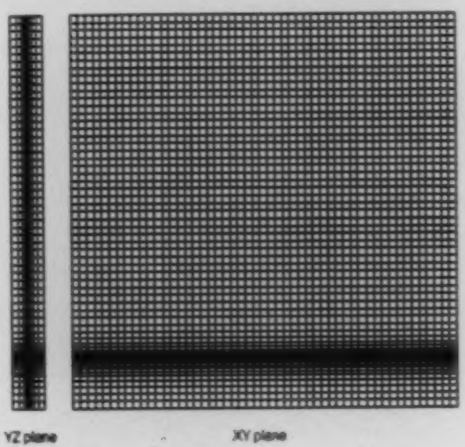

Figure 5.3 – Typical mesh used for simulations.

A geometric gridding scheme was used to mesh above and below the orifice location (typically the smallest division in the vertical direction). Two subroutines were created in the USRGRD user FORTRAN routines to facilitate meshing; these subroutines would automatically determine the number of mesh nodes and node spacing required to ensure a smooth grid progression. Specific details of these routines are included as comments in the FORTRAN listing in Appendix C.

The mesh is generated automatically based upon the dimensions that are input to specify the location and size of the nozzle orifice. Some control is afforded for selecting the overall number of mesh points by specifying the desired number of linear mesh points in the freeboard area of the domain; see Table 5.1 NTOP variable.

The general approach to creating the discretization mesh is shown in Figure 5.4. The Y direction mesh is created first by determining the largest node spacing based on a linear step in the freeboard section of the bed. A subroutine then determines a mesh spacing above and below the nozzle orifice to ensure a gradual progression from the smallest node size (usually YWIDTH) to the linear step size in the freeboard. The linear step size in the freeboard is then recalculated based on the geometric progression above the nozzle orifice. This is to ensure that the total height of the reactor is kept at the value specified by BDHGT. The same approach is applied to calculate the mesh spacing in the X direction based on linearizing the nozzle insertion (RNSERT) and then following a linear step size to the right of the nozzle pipe. This general algorithm has been applied to the generation of all grids for the fluidized bed simulations.

5.1.2 Boundary Conditions

Boundary conditions were specified both in the command file and also in user FORTRAN. It was necessary to set some boundary conditions in user FORTRAN to allow for the flexibility of specifying the positions for the pipe boundary and nozzle orifice. An isometric view of the various boundary conditions and computational geometry are shown in Figure 5.5.

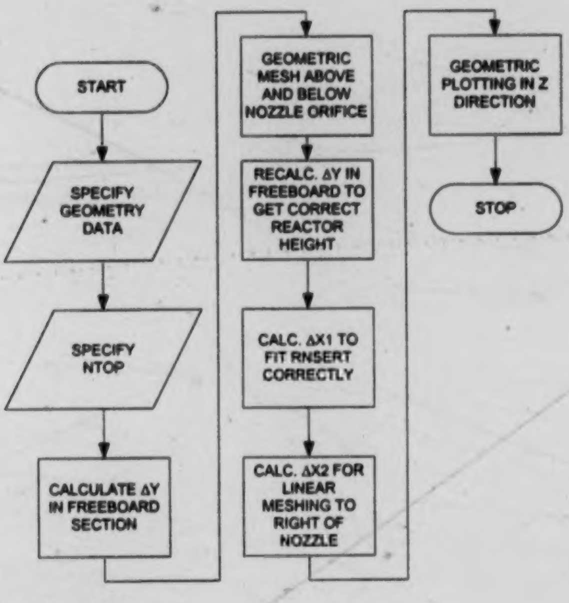
START
SPECIFY GEOMETRY DATA
SPECIFY NTOP
CALCULATE ΔY IN FREEBOARD SECTION
GEOMETRIC MESH ABOVE AND BELOW NOZZLE ORIFICE
RECALC. ΔY IN FREEBOARD TO GET CORRECT REACTOR HEIGHT
CALC. ΔX1 TO FIT RNSERT CORRECTLY
CALC. ΔX2 FOR LINEAR MESHING TO RIGHT OF NOZZLE
GEOMETRIC PLOTTING IN Z DIRECTION
STOP

Figure 5.4 – Meshing algorithm.

The simulation domain is bounded by walls that have zero momentum flux through them. It is assumed that there is a slip boundary condition for the solids at the wall and a no slip boundary condition for the gas phase at the walls. The solids slip boundary condition is required so that when a solid particle 'strikes' the wall it does not 'stick' and cause numerical problems.

Two inlets were specified for the simulations: the nozzle inlet at the tip of the nozzle pipe and the distributor plate at the bottom of the computational domain. For both of these boundary conditions the gas normal velocity was specified. Only the gas phase was fed in through the inlets as the jet was not laden with solid particles.

The top of the fluidized bed domain consisted of a pressure boundary condition which was not specified with an absolute pressure as this was an incompressible simulation. There was no solids carry over out of the domain and the gas flow into the simulation was exactly balanced by that flowing out through the pressure boundary face.

The rectangular pipe leading to the nozzle orifice was specified as a solid boundary with no flow present at the nodes where this solid exists. It was necessary to make the solid inlet pipe at least 3 by 3 control volumes in cross section due to the way in which CFX implements a solid boundary within the flow domain. More information can be found in the CFX Solver Manual.

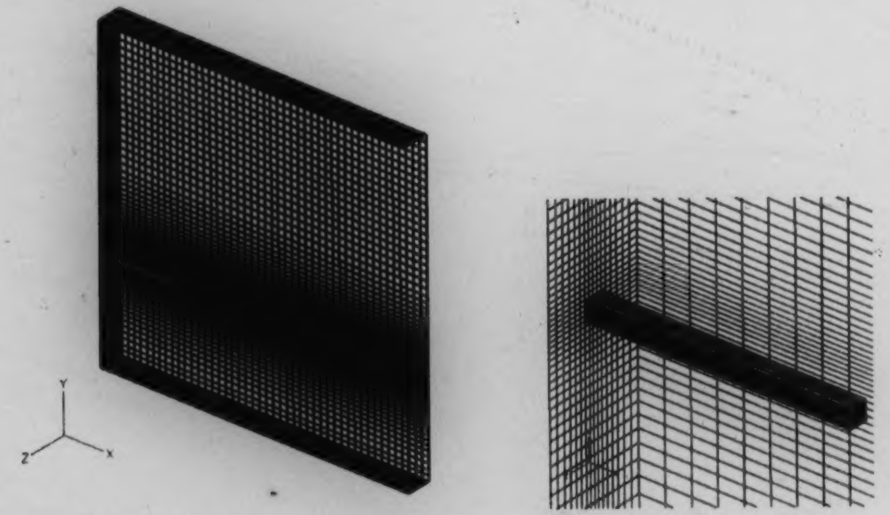

Figure 5.5 – Boundary conditions and discretization mesh in three dimensions.

5.2 Initial Conditions

Initial conditions were required to start the simulation. For all of these simulations the initial conditions were set with the user FORTRAN routine USRINT. All nodes within the computational domain were first filled completely with a gas volume fraction of 1. Next the height of the fluidized bed was determined by finding the node in the Y direction that was closest in height to that specified in the UCCOMMON block under the FRACTION variable. In all cases a desired bed height of 0.71m was set; however, due to the automatic gridding routines this height actually varied to within ±0.01 m. This was not considered to be a problem. All nodes within this height were set to have an initial solids volume fraction of 0.42.

The bed was assumed to be incipently fluidized by setting the gas phase Y velocity to that of minimum fluidization using the same equation which determines the fluidization gas velocity for the distributor plate boundary condition. The solids velocity in all directions was set to zero. McCabe, Thiele and Smith (1989) give an expression for predicting the minimum fluidization velocity as:

$$U_{mf} = \frac{0.091(\rho_s - \rho_g)gD_p^2}{150\mu_g} \tag{5.3}$$

At t=0 the gas jet was initiated at the specified normal velocity for the required simulation.

5.3 Phase Properties

5.3.1 Gas Phase Properties

The continuous phase in these simulations was assumed to be air with a density, ρ_g, equal to 1.2 kg/m^3 and viscosity, μ_g, equal to 1.8 x 10^{-5} Pa·s.

5.3.2 Solids Phase Properties

The dispersed solids phase was set to have a density, ρ_s, of either 1450 or 950 kg/m^3 depending upon the simulations that were being carried out (see Chapter 7; Tables 7.1 and 7.4). The solids viscosity, μ_s, was kept constant at 1.0 x 10^{-12} Pas. This value was chosen based on the example fluidized bed simulation in the CFX 4.2 examples directory, example 28. Solids were assumed to be monosized spherical particles of diameter, D_p, of 370 μm.

The solids compaction modulus was set to –600 with a compaction volume fraction of 0.376 agreeing with the parameters used by Bouillard *et al.*(1989) equation G_1. To avoid numerical overflow errors a solids volume cut off was set to 0.0001 in the solids momentum equation. Any control volumes with solids volume fractions less than this were considered to have only the gas phase present. No significant loss of solids mass from the simulation domain was observed by using this numerical adjustment. The drag model relationships and solids volume fraction cut off values have been discussed in Chapter 3.

5.3 CFX Flow Solver Acceleration

All simulations were implemented using algebraic multi-grid acceleration as implemented in the CFX solver code. The set up parameters are included in the command file listed in Appendix C.

5.3.1 Under Relaxation Factor Studies

Under relaxation parameters can be specified in the control file so that certain terms within the momentum equations are relaxed relative to the other terms. Relaxing certain terms can lead to an improvement in convergence rates. Some tests were conducted after choosing a suitable discretization scheme (see Chapter 7: Results and Discussion) and mesh density to accelerate the convergence of inner iterations. Using single precision it appeared that the gas continuity residual would stabilize at approximately 3×10^{-5} kg/s. Based on this value the "best" combination of relaxation factors would be those which decrease the gas continuity residual with the least number of iterations. For all simulations each of the momentum equation terms were set with a relaxation factor of 0.6; this seemed to be the most appropriate relaxation factor to use when compared with the other relaxation factor combinations tested. Figures 5.6 to 5.14 show the residual reductions for a single outer iteration when different combinations of relaxation factors are used. An outline of the relaxation factor tests is listed in Table 5.2.

Table 5.2

Under Relaxation Parameter Tests

Run	X Momentum Relaxation	Y Momentum Relaxation	Z Momentum Relaxation
1	0.6	0.6	0.6
2	0.3	0.3	0.3
3	0.3	0.7	0.7
4	0.7	0.3	0.7
5	0.7	0.7	0.3
6	0.3	0.7	0.3
7*	0.3	0.7	0.3
8	0.8	0.8	0.8
9	0.9	0.9	0.9

*Courant false time stepping implemented

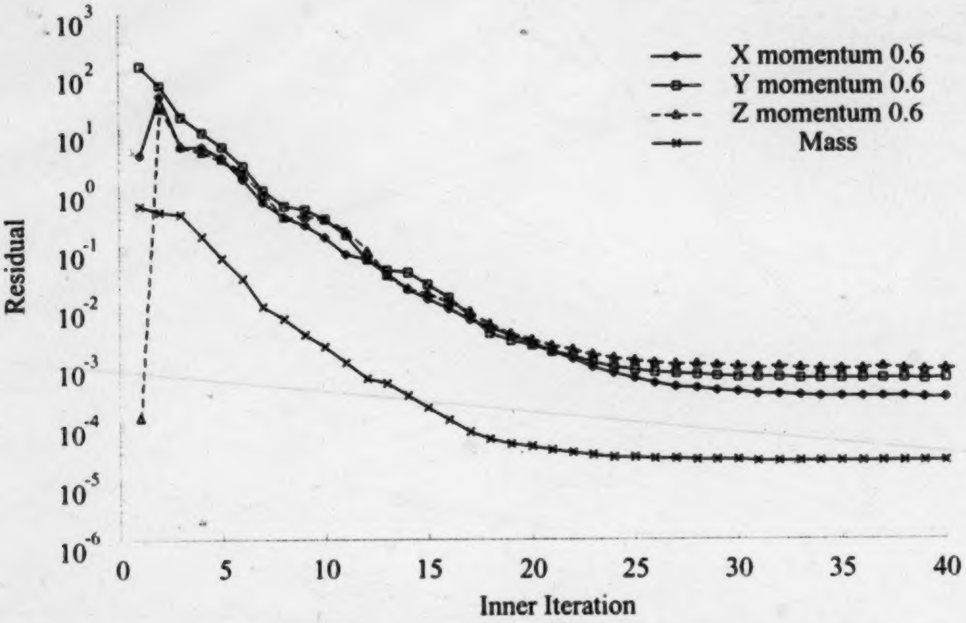

Figure 5.6 – Inner residual reduction with under relaxation test for Run 1, Table 5.2.

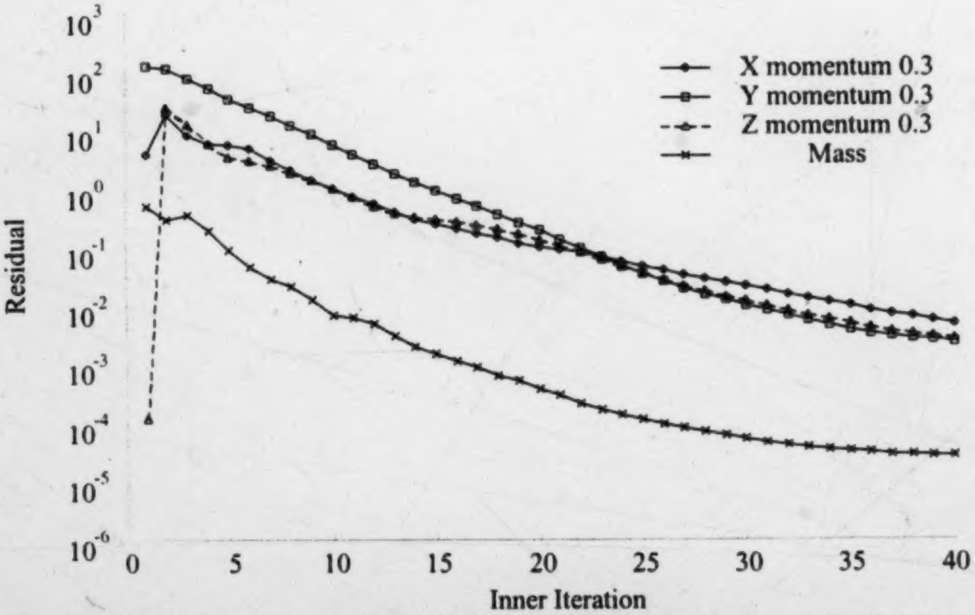

Figure 5.7 – Inner residual reduction with under relaxation tests for Run 2, Table 5.2.

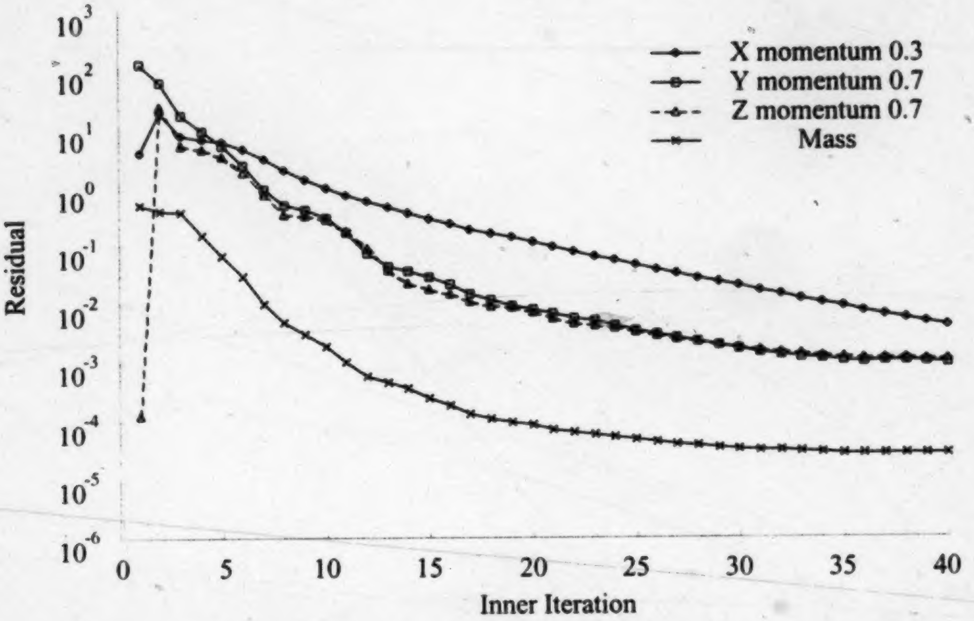

Figure 5.8 – Inner residual reduction with under relaxation tests for Run 3, Table 5.2.

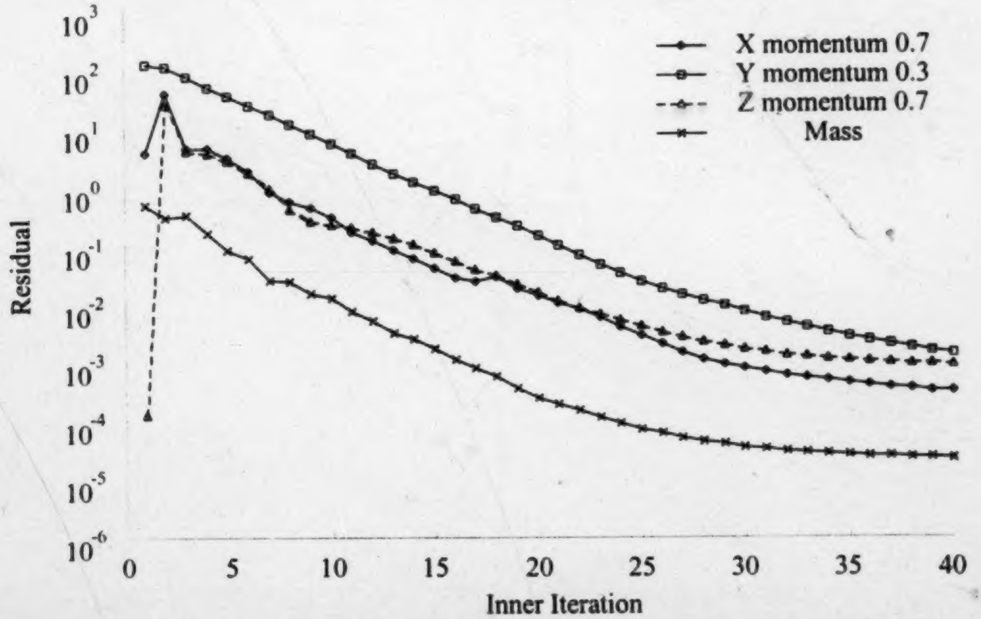

Figure 5.9 – Inner residual reduction with under relaxation tests for Run 4, Table 5.2.

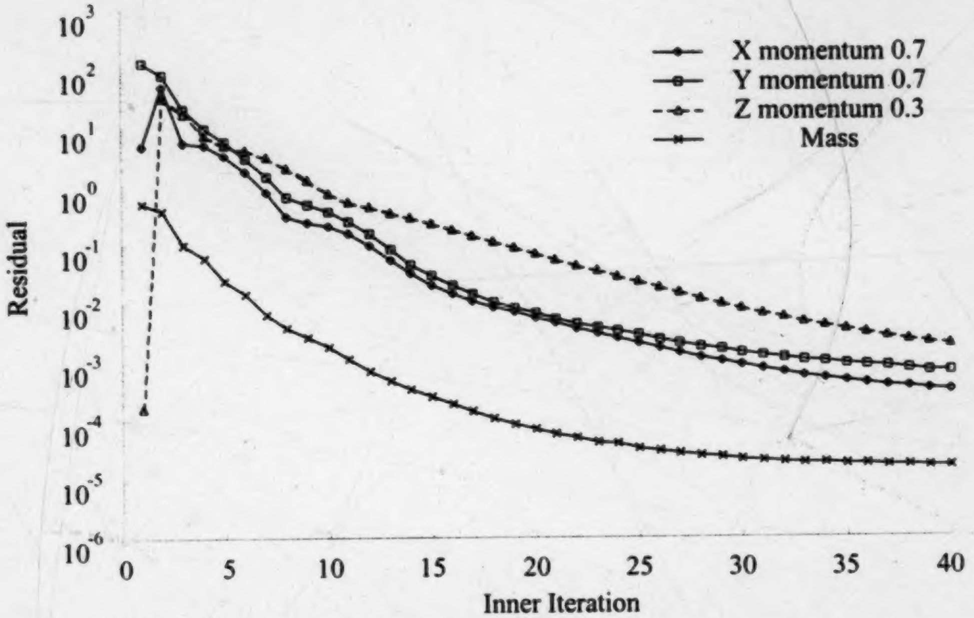

Figure 5.10 – Inner residual reduction with under relaxation tests for Run 5, Table 5.2.

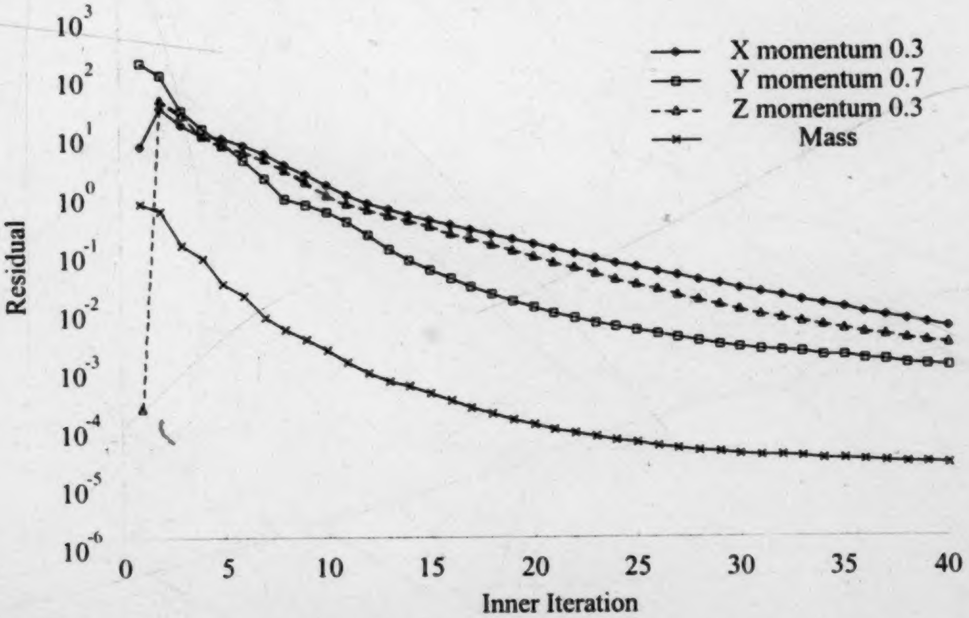

Figure 5.11 – Inner residual reduction with under relaxation tests for Run 6, Table 5.2.

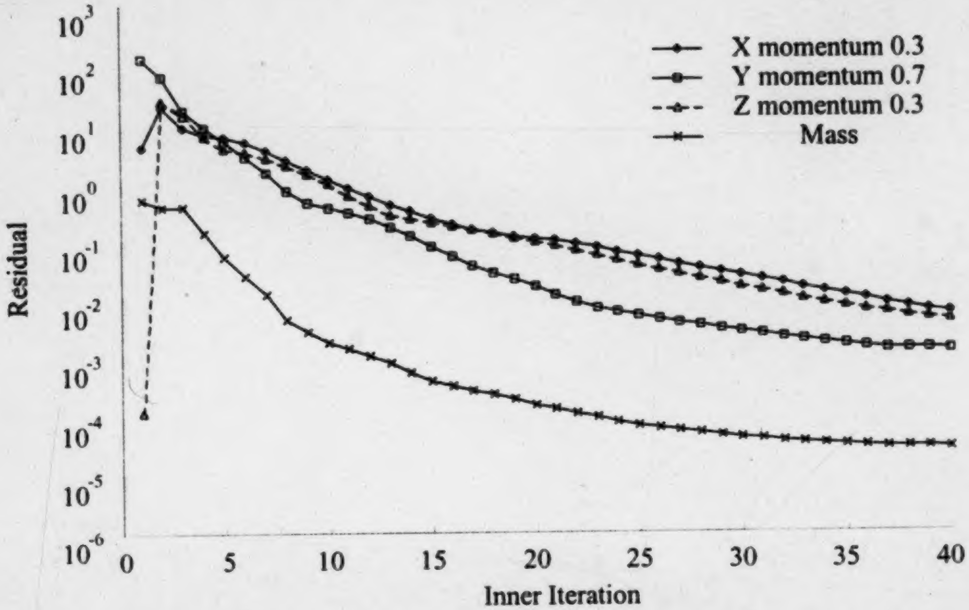

Figure 5.12 – Inner residual reduction with under relaxation tests for Run 7, Table 5.2.

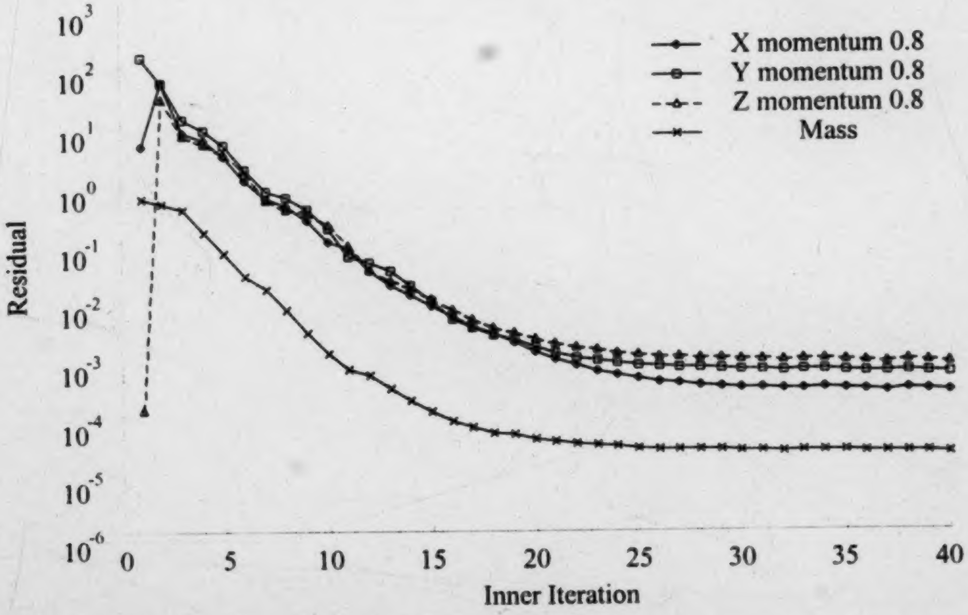

Figure 5.13 – Inner residual reduction with under relaxation tests for Run 8, Table 5.2.

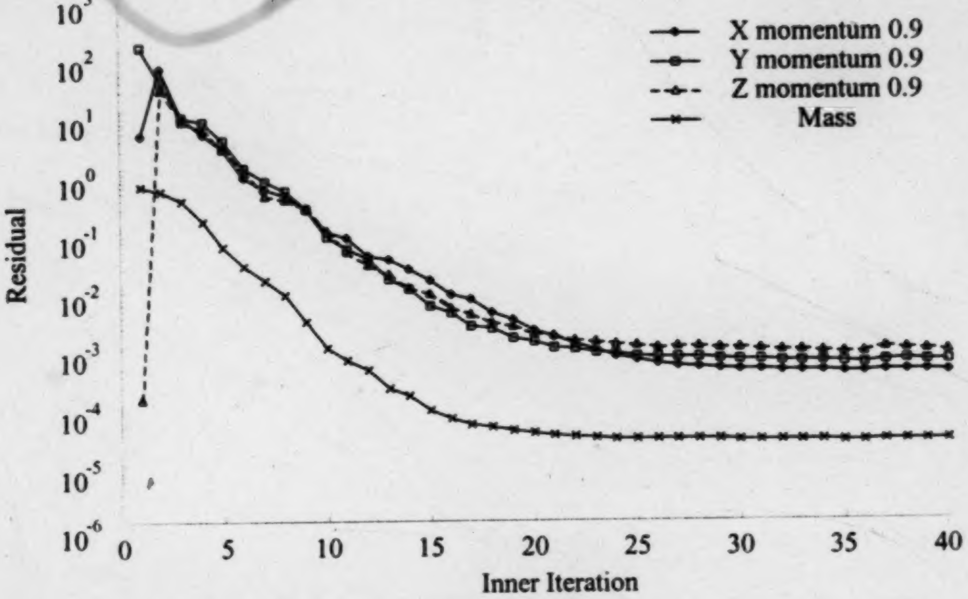

Figure 5.14 – Inner residual reduction with under relaxation tests for Run 9, Table 5.2.

5.3.2 Single versus Double Precision

The choice of single or double precision has an effect on both the solution time and numerical accuracy associated with the flow field variable representation. All runs in this report have used single precision because of the very long run times required to get substantial data from the simulations. Figure 5.15 shows the residuals from an identical run to that of run 9 Table 5.2 but using double precision. In this case the gas continuity residual is reduced by six orders of magnitude over 65 iterations. Conversely there is only a four order of magnitude reduction after 30 iterations which is slightly worse than the 15 iterations required for the same residual reduction using single precision; compare with Figure 5.14. A reduction of the gas continuity residual by four orders of magnitude is approximately equal to a 0.1 % error on the overall gas mass inlet flows within the computational domain. In this case the use of double precision numerics could lead to improved residual reduction; however, at the expense of increased iteration counts with more involved computational and memory demands. Single precision calculations should be sufficient for the desired accuracy for these simulations.

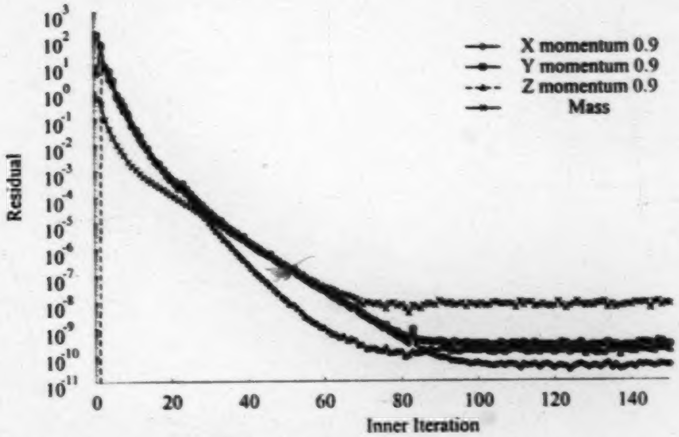

Figure 5.15 – Double precision residuals comparable to Table 5.2 Run 9.

5.3.3 Courant False Time Stepping

As previously mentioned in Chapter 3, there exists a minimum control volume size below which the continuum assumptions are not statistically valid for multiphase flows. All control volumes in these simulations were created so as to be larger than the minimum control volume size. In addition to checking for the valid control volume size, a Courant number analysis was carried out. The Courant number can be thought of as an indication of how far a flow particle (general sense of an infinitesimal control volume) has moved between nodes in a single time step. It is a dimensionless number based upon a characteristic flow velocity, mesh spacing and time step. For three dimensions, three local Courant numbers can be defined for each unit direction.

$$Cn = v\frac{\Delta t}{\Delta x_i} \qquad (5.4)$$
$$i = 1,2,3$$

Ideally the Courant number should be equal to one, in which case the information at a node has traveled exactly the same distance as the grid spacing. However, for stability with most discretization schemes it is necessary to have a Courant number less than one.

Courant numbers for simulations on two different mesh sizes are reported in Table 5.3. The characteristic Y velocity is based upon the characteristic velocities found from analyzing the experimental results. The characteristic X velocity has been assumed to be the same as the jet velocity at the nozzle orifice.

Table 5.3

Courant Number Analysis for Δt = 0.001 s

	Cn_y^{*}		Cn_x^{**}	
Grid	Maximum	Minimum	Maximum	Minimum
56 x 117 x 21	0.500005	0.0623438	15.83336	15.55543
44 x 96 x 9	0.609366	0.0494302	15.55566	1.46249

*based on a characteristic y velocity of 1.0 m/s

**based on a characteristic maximum x velocity of 250 m/s

From Table 5.3 it is seen that the Cn_x values were as high as 15. Ideally this value should be less than or equal to one. Tests were conducted using the automatic Courant false time stepping routines that are available in the CFX solver. This option analyzes the local velocity and mesh spacing and determines the "best" pseudo-time step to use between the outer iterations to satisfy the Courant number requirement. In effect, this method does more false time steps between each real time step to arrive at the converged solution. Unfortunately using Courant false time stepping increases the amount of time required to do simulations. Figure 5.16 shows the gas continuity residual reductions when the Courant false time stepping was enabled. With no additional modifications to the solver settings a reduction of about four orders of magnitude in the gas continuity residual was realized after 25 outer iterations. This residual reduction is of the same order as that using the solver with Courant false time stepping. Based on this observation Courant false time stepping was not used for simulations.

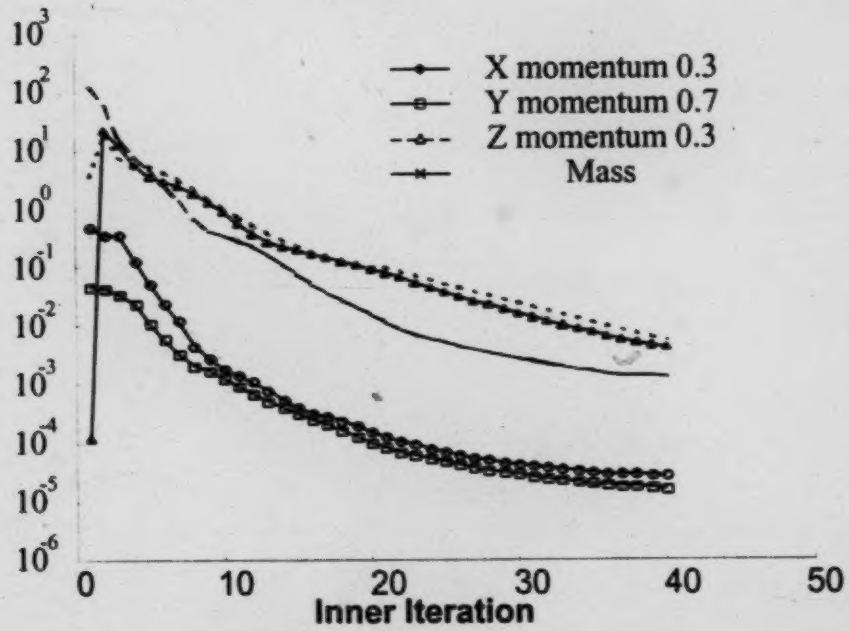

Figure 5.16 – Gas continuity residual using Courant false time stepping.

5.4 SUMMARY OF SIMULATION SET-UP

A summary of the CFX 4.2 solver set up was described in this chapter. Preliminary results from the under relaxation studies have shown that all under relaxation factors should be set to 0.6. Courant false time stepping was not shown to be useful for these simulations and will not be implemented. For efficient use of computer time, all simulations will be run using single precision. Boundary and initial conditions were described.

Chapter 6

Experimental Section

Experiments were conducted at the University of Saskatchewan to compare with some of the results from the simulation studies in this report. This chapter describes the two-dimensional fluidized bed, the methods used to record observations and descriptions of the general flow patterns observed with this apparatus.

6.1 EXPERIMENTAL SET UP

6.1.1 Geometry

The two dimensional fluidized bed was fabricated and operated at the University of Saskatchewan under the direction of Dr. Berutti. The fluid bed was rectangular in cross-section with length and depth dimensions of 1.2 m x 0.1 m, respectively, and a height of 1.2 m, see Figure 6.1. Both the front and rear faces of the bed were constructed of clear acrylic sheets to facilitate visual observations of the jet and use of a high-speed video camera. The sides of the bed were constructed of aluminum and a port was located on the left side to accommodate a horizontal injection nozzle for experiments. The axis of the nozzle was located 0.39 m above the top of the distributor plate, and 0.0117 m from the acrylic front sheet. The nozzle port allowed easy adjustment of the nozzle insertion into the fluidized bed. For all experiments carried out for this study, the nozzle insertion was held constant at 0.070 m. The cyclone return dipleg entered the bed on the left side above the nozzle at a 45° angle and extended 0.08 m horizontally into the bed.

All fluidization air and horizontal feed jet gas for these experiments was provided from an oil free compressor. The windbox below the distributor plate was split to allow for different aeration rates to be set for both the left and right sides of the distributor plate, see Figure 6.2. To provide even distribution of the fluidization gas, deflector caps were placed over the fluidization gas inlets. The right and left aeration rates were kept equal for the experiments in this study. The distributor plate had a felt covering attached to prevent particles from falling through the aeration holes and to enhance flow distribution across the distributor.

The nozzle was attached onto the end of a steel pipe and inserted into the fluidized bed. The nozzle orifice was round with an internal diameter of 3.81mm. Jet air was provided from the compressor and a mass flow controller was used to meter the jet air supply. Construction and design details of this nozzle can be requested from Dr. Berruti at the University of Saskatchewan and will not be described further here.

6.1.2 Particle Properties

The solid particles used for the experiments were medium density polyethylene particles supplied by NOVA Chemicals (Calgary, Alberta). The particles were white in colour with a density of 930 kg/m^3. Mean particle diameter was determined to be 370 μm. Minimum fluidization velocity was reported to occur at about 4.4 cm/s. Based on mass measurements for a given volume of particles, assuming negligible particle porosity, the minimum fluidization voidage was found to be 0.5.

To facilitate visualization of the particle flow patterns within the fluidized bed, a portion of the particles were coloured with paint. To colour the particles, a thin layer of particles was laid out on a large sheet and a light layer of spray paint was applied to the particles. Several coats of paint were required to completely colour these particles. It is not known if this painting changed the particle size and/or density.

6.1.3 Experimental Procedure

A NAC High Speed System Model HSV-100 camera was used for filming the experiments. The camera was able to capture colour images at 500 frames per second on super VHS videotapes. These images were then digitized and analyzed on a computer. Video observations were taken of the overall flow patterns within the fluidized bed and

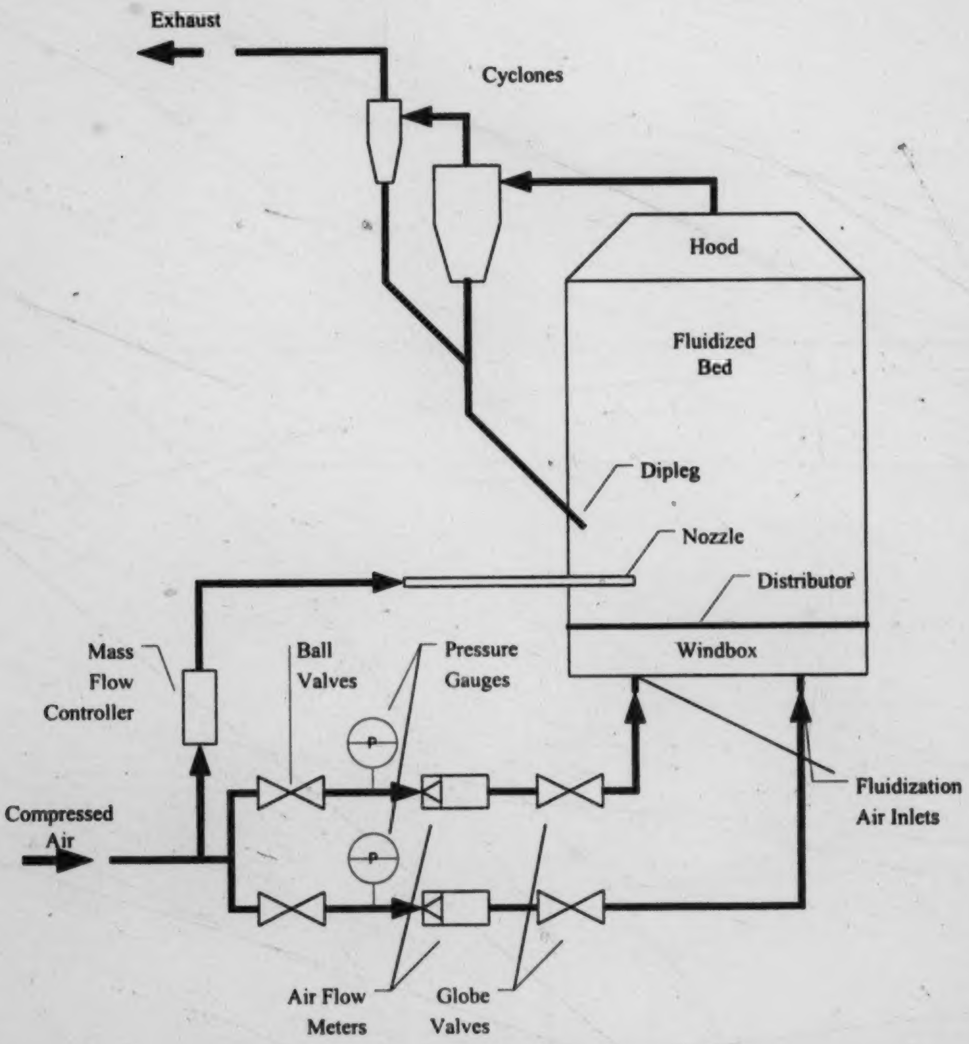
Exhaust
Cyclones
Hood
Fluidized Bed
Dipleg
Nozzle
Distributor
Windbox
Mass Flow Controller
Ball Valves
Pressure Gauges
P
P
Compressed Air
Fluidization Air Inlets
Air Flow Meters
Globe Valves

Figure 6.1 – Diagram of the fluidized bed experimental apparatus. Modified from Jason Cowpan's M.Sc. thesis, University of Saskatchewan, 1999.

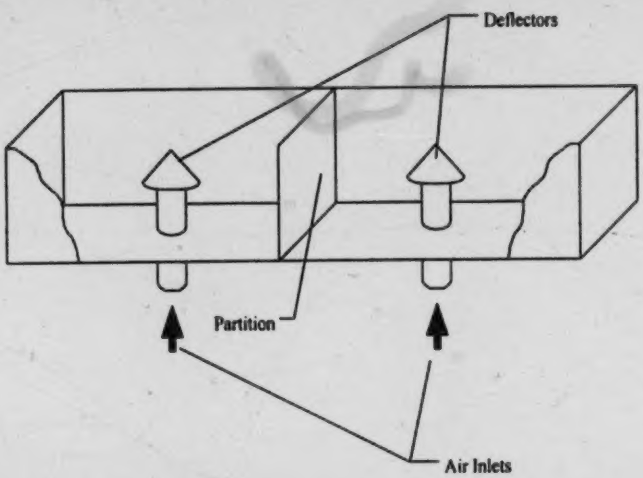

Figure 6.2 – Cut away diagram of the windbox. Courtesy Jason Cowpan M.Sc. thesis, University of Saskatchewan, 1999.

more detailed recordings were taken by zooming in on the horizontal jet region within the fluidized bed. For each of the runs approximately 10 seconds of footage was taken; this length of time was adequate to capture important jetting phenomena.

For each set of experiments the fluid bed was assembled, filled with particles to a height of 0.85 m above the distributor and all flow lines were connected. The compressor was started and the buffer tank filled. Fluidization gas was then set using the globe and ball valves to adjust and control the pressure and flow rate to the windbox. Once the fluidization gas was set, the air supply to the nozzle was adjusted using the mass flow controller. The only variables adjusted for these runs were the fluidization gas flow rate and the gas flow rate to the horizontal nozzle. The experimental operating conditions that were investigated are listed in Table 6.1 and reflect the conditions which were used in the CFD simulations. The numbers listed in the table refer to the digital time stamp in the upper right corner of the video recording.

Table 6.1:

Experimental Operating Conditions and Video Reference Numbers

	U_j (m/s)				
U_0 (cm/s)	**229.2**	**327.5**	**425.7**	**524**	**589.5**
0	301	302	303	304	305
	318C	319C	320C		
3.1	314	315	316	317	
	323C	322C	321C		
4.4	306	307	308	309	
	324C	325C	326C		
5.7	310	311	312	313	
	327C	328C	329C		

U_{mf} = 4.4 cm/s
C refers to video recording at the tip of the jet plume in the near field

Data can be extracted from the images recorded on the video tape by digitizing the images and then processing the images on a computer. Distinguishing markers with a set distance were always recorded on the video. These markers allowed the distance per pixel to calculated for each of the images analyzed. It is assumed that the aspect ratio of the pixels in the Y and X directions is the same when the video was converted to digital format. Pixel measurements with respect to distances in centimeters are listed in Table 6.2. These values were used to determine the average bubble size and rise velocity discussed in section 6.2.4.

6.2 Observations

The general flow patterns within the experimental fluidized bed could be broken into three main types: those below U_{mf}, those at U_{mf} and those at fluidization velocities much above U_{mf}. Observations of the fluidized bed were taken with a high speed video camera recording 500 frames per second. Video tapings were taken at a far field to observe the entire fluidized bed in operation and also zoomed to observe the end of the jet plume. Four high power white lights were shone onto the face of the fluidized bed to provide lighting for the recordings. Without these lights there was not enough ambient lighting to make any meaningful recordings. Attempts were also made to shine the light through the bed to illuminate individual bubbles within the fluidized bed. This attempt didn't work very well as the bed was too dense and didn't allow enough light to penetrate.

Table 6.2:

Summary of Video Capture Image Dimension Conversions from Pixels to Centimeters

Image Data Name:	Xstart (pixel)	Xend (pixel)	dx (pixel)	Measure (m)	Conversion (m/pixel)
311.09	298	441	143	0.1	0.000699
312.06	302	442	140	0.1	0.000714
313.06	298	440	142	0.1	0.000704
314.08	255	412	157	0.1	0.000637
315.08	252	413	161	0.1	0.000621
316.06	252	411	159	0.1	0.000629
317.09	253	413	160	0.1	0.000625
318.07	224	779	555	0.1	0.000180
319.05	224	780	556	0.1	0.000180
320.09	110	674	564	0.1	0.000177
323.07	165	681	516	0.1	0.000194
322.08	274	846	572	0.1	0.000175
321.10	184	705	521	0.1	0.000192
324.06	130	697	567	0.1	0.000176
325.08	114	680	566	0.1	0.000177
326.05	103	620	517	0.1	0.000193
327.07	240	754	514	0.1	0.000195
328.09	136	641	505	0.1	0.000198
329.05	113	630	517	0.1	0.000193

6.2.1 Below U_{mf}

With zero fluidization gas the bed acted as a packed bed and the jet was discharged into the medium. With increasing fluidization gas velocity (below U_{mf}) the bed would slowly start to expand and the solids particles started to make very small movements in place. No overall flow patterns within the fluidized bed were observed. The bulk bed particles seemed to remain at a fixed position but tended to vibrate with increasing fluidization gas velocity.

At fluidization velocities below minimum fluidization the particle entrainment into the jet was from above the jet plume. No particle entrainment was observed below the jet. With zero fluidization gas the bed acted as a packed bed and the jet would discharge into the bed and "carve" the region above the jet plume and bubbles would form once the roof of this carving zone collapsed back on the jet. This intermittent carving and roof collapse lead to a periodic extension and then decrease in the jet penetration length into the bed.

6.2.2 At U_{mf}

As soon as the fluidization gas was increased to U_{mf} the bed height increased and bubbles were seen to occur on the top surface of the bed. An overall slight recirculating bed pattern was observed with the particles descending along the center of the bed and then moving towards the sides (along the X axis direction). Small triangular shaped mounds of particles appeared to form at two positions on the distributor plate. These stagnant zones were not expected to form and are thought to have formed because of poor flow distribution through the distributor. Since the distributor was split to allow for a weakly recirculating bed to be set up, a deflector plate had to be placed over both of the fluidization air inlet jets to ensure that the flow would not exit at the location directly above these nozzles, see Figure 6.2. These plates might have lead to the flow patterns being observed on top of the distributor.

Particles were entrained from above and below the jet plume at U_{mf}. The flow appeared to be a line sink starting on the left at the approximate location of the tip of the nozzle and continuing to where the gas jet impinged on the front face of the reactor.

6.2.3 Above U_{mf}

At fluidization velocities much greater than U_{mf} the bed operated in the bubbling or turbulent fluidization regime. The overall recirculating pattern within the fluidized bed was still observed; however, due to the increase in the bubbles forming from the distributor and progressing up through the bed it was very difficult to ascertain any particular flow patterns.

Particles were still entrained from above and below the jet plume and then accelerated into the fluidized bed. Bubbles from the distributor moved up from below the jet and might have had some impact on entraining particles into the jet zone.

6.2.4 Bubble Sizes and Rise Velocities

From the experimental video tapes the behavior of the bubbles can be determined by using a simple geometric argument as follows. Bubble boundaries are located based on the width and height of each bubble. Since the bubbles being tracked are the same coordinate system for each run, a geometric bubble center can be identified based on the maximum width and height positions of the bubbles. Tracking this centroid over a fixed period of time will give the bubble rise velocity. By using the center of the bubble and not the bubble boundary this should negate (somewhat) the effects of bubble shape distortion. These concepts are shown in the following figure. Identical analyses were carried out on the simulation results. The perimeter points are labeled as X_1, X_2, Y_1 and Y_2; the approximate center is shown with a cross. Selected video recordings of the operating fluidized bed were digitized and then broken into individual frames as 24-bit grayscale bitmaps and the bubble information was extracted.

Figure 6.3 – Definition of the bubble dimensions from digitized video observations.

Bubbles would form at the tip of the jet and then wrap slightly back to the left (over the jet plume). Figure 6.4 shows this particular bubble behavior. Just above the tip of the jet plume a long tongue would progress vertically upwards creating a slender void. Once the roof of the jet collapsed in on itself this void would form into a more spherical bubble shape and progress up towards the top of the bed. Occasionally the jet would catch up to the bubble and cleave it through the center forming a mushroom shaped void. Internal recirculation of solids through the bubbles was observed from the center to the top of the bed.

Figure 6.4 - Demonstration of "fingers", round bubbles and bubbles cleaving into mushrooms.

Results from the average bubble rise velocity, horizontal velocity and bubble size are listed in Table 6.3. From the results presented in this table it can be seen that a characteristic rise velocity of the order of 1 m/s can be defined for bubbles, which can be considered to be flow disturbances. Likewise a characteristic horizontal velocity of approximately 0.1 m/s can be defined. These velocities can be used to determine the correct mesh spacing in the numerical simulation outside of the gas jet zone adjacent to the nozzle inlet based on Courant number.

6.2.5 Transient Analysis

The flow within the fluidized bed is highly transient showing flow behavior over a wide range of characteristic times. Bubble movement occurs on time scales larger than the behavior of the jet while the behavior of individual particles within the jetting zone have much shorter time scales associated with them. The particle Stokes relaxation time, assuming a very low slip velocity between the gas and solids phase, is calculated to be 0.4014 seconds.

Table 6.3:

Bubble Rise Velocity, Horizontal Velocity and Size from Experiments

Run	Rise Velocity (m/s)*	Horizontal Velocity (m/s)**	Bubble Area (m^2)+
306	1.38	-0.034	0.010
307	1.25	-0.072	0.017
308	0.80	-0.194	0.024
309	0.34	0.183	0.012
310	0.84	0.114	0.009
311	1.12	-0.098	0.020
312	0.83	0.032	0.012
313	0.44	0.200	0.038
314	1.46	0.218	0.008
315	1.25	0.021	0.017
316	1.35	-0.103	0.019
317	0.66	0.021	0.023

*standard deviation is as high as 0.62
**standard deviation is as high as 0.36
+standard deviation is as high as 0.004

Chapter 7

Results and Discussion

This chapter deals with the results from the simulations and a comparison with experimental results taken at the University of Saskatchewan. Chapter 7 is broken into two parts: The first part deals with numerical considerations such as discretization scheme, grid refinement studies and the governing hydrodynamic equations. Numerical considerations must be taken into account so that there is confidence in the physical predictions. Part 2 deals with the physical predictions obtained from the simulations. Predicted flow behavior is compared and contrasted against experimental and literature results.

A simulation naming convention using two letters followed by two numbers was followed for book keeping purposes. The first letter refers to the type of simulations used for that particular set of simulations; the second letter refers to the jet velocity and the last two digits refer to individual runs within that test set. For example:

AA01 – refers to:

A – simulation using discretization scheme as the key parameter;

A – jet velocity of 150 m/s;

01 – first run in this set using Hybrid discretizaton.

7.1 Part I: Numerical Considerations

Computational fluid dynamic simulation work requires the use of a computer to solve the governing flow equations for flow geometries of engineering interest. Since computers are limited to fixed finite number systems, errors are introduced due to rounding and truncation. This will introduce numerical errors. As shown in Chapter 3 there are many different ways to approach the volume averaging of the governing flow equations. With so much choice there are certain approaches which may be "better" than others for certain flow modeling scenarios. This first part of the chapter deals with some of the simulations that were carried out to explore the different modeling possibilities available within the CFX 4.2 flow solver. Numerical issues such as residual reduction, computational effort, discretization scheme and grid density are explored. All simulations dealing with numerical considerations are listed in Table 7.1. Each run has its own unique four character identification string.

7.1.1 Three Dimensions and Symmetry

The literature abounds with simulations of fluidized beds in two dimensions; however, preliminary simulations using a two-dimensional bed and a horizontal feed jet were found to produce unrealistic results. Two dimensional simulations with side injection of the gas into the fluidized bed would cause the bed above the jet to lose fluidization and slump. This is not observed in the experimental apparatus because the bed can be thought of as being pseudo-two dimensional. Although the experimental apparatus is very narrow in comparison with its height and width, there still exists a depth

Table 7.1: Numerical Simulations Summary

Axxx series: Discretization Scheme Comparison (section 7.2)

CFD Run	Scheme	U_f	D_o	S	I	D_p	ρ_p	Nozzle CVs
U_{jet}=150 m/s			(m)	(m)	(m)	(μm)	(kg/m³)	(size)
AA01	Hybrid	U_{mf}	0.0099	0.145	0.1175	370	1450	2x2
AA02	Minmod	U_{mf}	0.0099	0.145	0.1175	370	1450	2x2
AA03	SB	U_{mf}	0.0099	0.145	0.1175	370	1450	2x2
U_{jet}=250 m/s								
AB01	Hybrid	U_{mf}	0.0099	0.145	0.1175	370	1450	2x2
AB02	Minmod	U_{mf}	0.0099	0.145	0.1175	370	1450	2x2
AB03	SB	U_{mf}	0.0099	0.145	0.1175	370	1450	2x2
U_{jet}=300 m/s								
AC01	Hybrid	U_{mf}	0.0099	0.145	0.1175	370	1450	2x2
AC02	Minmod	U_{mf}	0.0099	0.145	0.1175	370	1450	2x2
AC03	SB	U_{mf}	0.0099	0.145	0.1175	370	1450	2x2

Dxxx series: Grid Refinement Studies (section 7.3)

CFD Run	Scheme	U_f	D_o	S	I	D_p	ρ_p	Nozzle CVs	Grid	Nodes
U_{jet}=250 m/s			(m)	(m)	(m)	(μm)	(kg/m³)	(size)		
DA01	SB	U_{mf}	0.0099	0.145	0.1175	370	1450	1x1	Coarse	11270
DA02	SB	U_{mf}	0.0099	0.145	0.1175	370	1450	1x1	Normal	30000
DA03	SB	U_{mf}	0.0099	0.145	0.1175	370	1450	1x1	Medium	60480
DA04	SB	U_{mf}	0.0099	0.145	0.1175	370	1450	1x1	Fine	83600
DA05	SB	U_{mf}	0.0099	0.145	0.1175	370	1450	1x1	Fine	83600
U_{jet}=250 m/s										
DB01	SB	U_{mf}	0.0099	0.145	0.1175	370	1450	2x2	Medium	71280
DB02	SB	U_{mf}	0.0099	0.145	0.1175	370	1450	2x2	Fine	98010
U_{jet}=250 m/s										
DC01	SB	U_{mf}	0.0099	0.145	0.1175	370	1450	3x3	Medium	86670
DC02	SB	U_{mf}	0.0099	0.145	0.1175	370	1450	3x3	Fine	116640
DD01	SB	U_{mf}	0.0099	0.145	0.1175	370	1450	3x3	Fine	116640
DD02	SB	U_{mf}	0.0099	0.145	0.1175	370	1450	3x3	Fine	116640

Exxx series: Continuous Phase Pressure Sensitivity Analysis (section 7.4)

CFD Run	Scheme	U_f	D_o	S	I	D_p	ρ_p	Nozzle Nodes	Grid	Nodes
U_{jet}=250 m/s			(m)	(m)	(m)	(μm)	(kg/m³)	(size)		
EA01	SB	U_{mf}	0.0099	0.145	0.1175	370	1450	1x1	Coarse	11270
EA02	SB	U_{mf}	0.0099	0.145	0.1175	370	1450	1x1	Normal	30000
EA03	SB	U_{mf}	0.0099	0.145	0.1175	370	1450	1x1	Fine	83600

Hxxx series: Solids Pressure Sensitivity Analysis

CFD Run	Scheme	U_f	D_o	S	I	D_p	ρ_p	Nozzle Nodes	Restart
U_{jet}=150 m/s			(m)	(m)	(m)	(μm)	(kg/m³)	(size)	
HA01	SB	2.0U_{mf}	0.00292	0.145	0.1175	370	950	2x2	GA01
HA02	SB	3.0U_{mf}	0.00292	0.145	0.1175	370	950	2x2	GA02
U_{jet}=250 m/s									
HB01	SB	2.0U_{mf}	0.00292	0.145	0.1175	370	950	2x2	GB01
HB02	SB	3.0U_{mf}	0.00292	0.145	0.1175	370	950	2x2	GB02
U_{jet}=300 m/s									
HC01	SB	2.0U_{mf}	0.00292	0.145	0.1175	370	950	2x2	GC01
HC02	SB	3.0U_{mf}	0.00292	0.145	0.1175	370	950	2x2	GC02

through which fluidization gas can pass around the sides of the jet. Two-dimensional simulations on a computer completely lack this third dimension, so no fluidization gas can pass around the jet and reach the top of the bed. Further analysis of the flow domain predicted with the simulations have shown that vortex cores around the jet region in vertical YZ planes (the ω_x vorticity) have been observed to shift from side to side (in the Z direction). Without the third dimension in the Z direction this behavior would not have been predicted.

In addition to the three-dimensional requirement the flow domain was allowed to be asymmetric. Symmetry conditions allow the computational effort to be significantly decreased because half or axisymmetric pieces of the flow domain can be studied. However, for these studies it has been found that the zones around the jet in the X direction do not show symmetric behavior on either side of the jet. Plots of the local jet X vorticity in the YZ plane, ω_x, show that the vorticity cores actually shift from side to side with bubble formation at the tip of the jet. Gas void fraction across the depth of the bed (in the Z direction) was also observed to be asymmetric. The flow domain is not symmetric and requires a full three dimensional field description with no symmetry boundary conditions imposed.

7.1.2 Discretization Scheme Comparison

As shown in the discussion on computational techniques, the choice of discretization method has a significant impact on the overall results obtained from a numerical simulation. In light of this fact several simulations were conducted to compare the results obtained from using different discretization schemes. Three different discretization schemes were chosen for comparison: Hybrid, MINMOD TVD and Superbee TVD. A list of the simulation conditions is shown in Table 7.1.

The best way to observe the effect of discretization scheme on the simulation results is to use a qualitative comparison of the jet plume formation within the fluidized bed over several time steps. Figures 7.1-7.3 show a side-by-side comparison of the gas volume fraction iso-surface ($\varepsilon_g=0.8$) at times of 0.25, 0.5, 0.75 and 1.0 seconds of real time for jet velocities of 150, 250 and 300 m/s, respectively. Gas volume fraction iso-surfaces at $\varepsilon_g=0.8$ represent the bubble and jet plume boundaries within the fluidized bed. Although flow velocities are not represented with these figures the overall behavior of the bubbles and jet plumes are well indicated.

With increases in jet velocity from 150 to 300 m/s there is an increase in jet penetration into the fluidized bed. This result is expected due to the increased momentum of the jet. One interesting observation is for Run AA01 (Hybrid) where the jet does not seem to detach from the wall but instead traces up along the wall to form a "finger" of gas out the top surface of the bed.

Characteristic of the first order Hybrid scheme (AA01, AB01, AC01) a large, diffuse mushroom shaped void forms from the tip of the jet and a trailing finger connects the top of the bed to the jet plume. No small bubbles were observed to form when using this type of discretization. The first order nature of the Hybrid scheme has previously been shown in Chapter 3 to be overly diffusive leading to a smearing of waveforms which in turn leads to a smearing of phase boundaries. This probably explains why no bubbles are seen to form when using the Hybrid scheme. Bubble boundaries are smeared leading to large void formation due to the over diffusive nature of the Hybrid discretization scheme.

MINMOD TVD gave results similar to those obtained using the Hybrid scheme especially for jet velocities of 300 m/s, see Figure 7.3. MINMOD is also diffusive and leads to a smearing of phase boundaries. At the higher jet velocities the jet shear with the fluidized bed would be expected to be quite high leading to the entrainment of particles and subsequent formation of bubbles. A trend opposite to this was observed with these preliminary runs (AA02, AB02, AC02); very few bubbles were seen to form with increased jet velocity suggesting that the diffusive nature of the MINMOD scheme does not adequately predict bubble formation.

Superbee TVD results are shown in Figures 7.1-7.3 (runs AC01, AC02, AC03) and a distinct instability is seen forming on the initial jet plume at $t=0.25$s for all inlet jet velocities. This instability leads to the formation of three bubbles off of the initial jet plume and subsequent detachment of the jet plume from the bubbles. The long "finger" and "mushroom" bubble shapes observed with the previous two schemes were not seen with the Superbee scheme. The over compressive nature of Superbee TVD results in a sharpening of the phase boundaries. After discussion with colleagues at the University of Saskatchewan, it was decided that the Superbee TVD scheme gave results which agreed best with experimental observations.

Although it appears that the Superbee discretization scheme is the best choice of the three discretization schemes investigated, there is a tradeoff. Superbee TVD requires more computations per iteration and leads to an increase in overall computation time to produce the same number of outer iterations. To investigate this increased computational demand a work ratio was determined by dividing the amount of real time results by the total computational time to arrive at an expression of work units. Table 7.2 lists the different CPU time demands and related work ratios for the three discretization schemes investigated. The CPU time was taken from the total processing time reported in the OUT file that is automatically generated from a CFX simulation.

Table 7.2:

CPU Demand and Discretization Scheme

Scheme	**CPU Time (s)**	**Real Time (s)**	**Work (Real s / CPU s)$\cdot 10^{-5}$**
Hybrid	708600	3.693	1.92
Hybrid	694200	3.353	2.07
MINMOD	257700	0.922	2.80
Superbee	411300	1.297	3.17
Superbee	423500	1.322	3.20

Based upon these values, the SUPERBEE scheme requires 1.5 times more CPU time than the HYBRID scheme for comparable real time predictions. The MINMOD scheme lies between the work demands of Hybrid and Superbee schemes.

7.1.3 Grid Refinement Studies

Care must be taken in specifying the correct grid size and number of control volumes used to define the nozzle inlet boundary condition. Several runs were conducted to study the effect of mesh density and nozzle boundary condition control volume density. These runs are summarized in Table 7.1. Gas continuity error, or residual, was chosen as the basis for comparison; validation of the different grid densities investigated and continuity

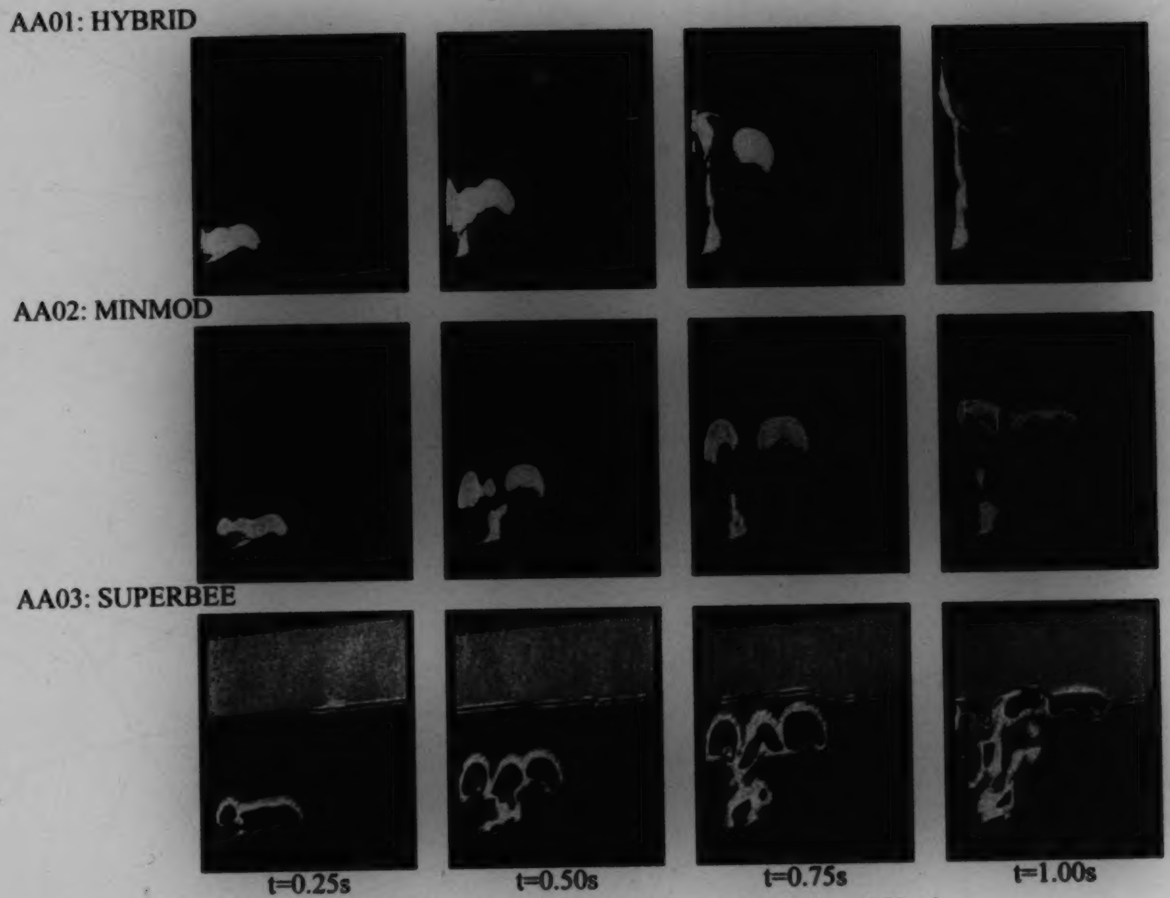
AA01: HYBRID
AA02: MINMOD
AA03: SUPERBEE
t=0.25s
t=0.50s
t=0.75s
t=1.00s

Figure 7.1: Time Series Gas Volume Fraction Isosurface Plots (ε_g=0.8) U_{jet}=150m/s

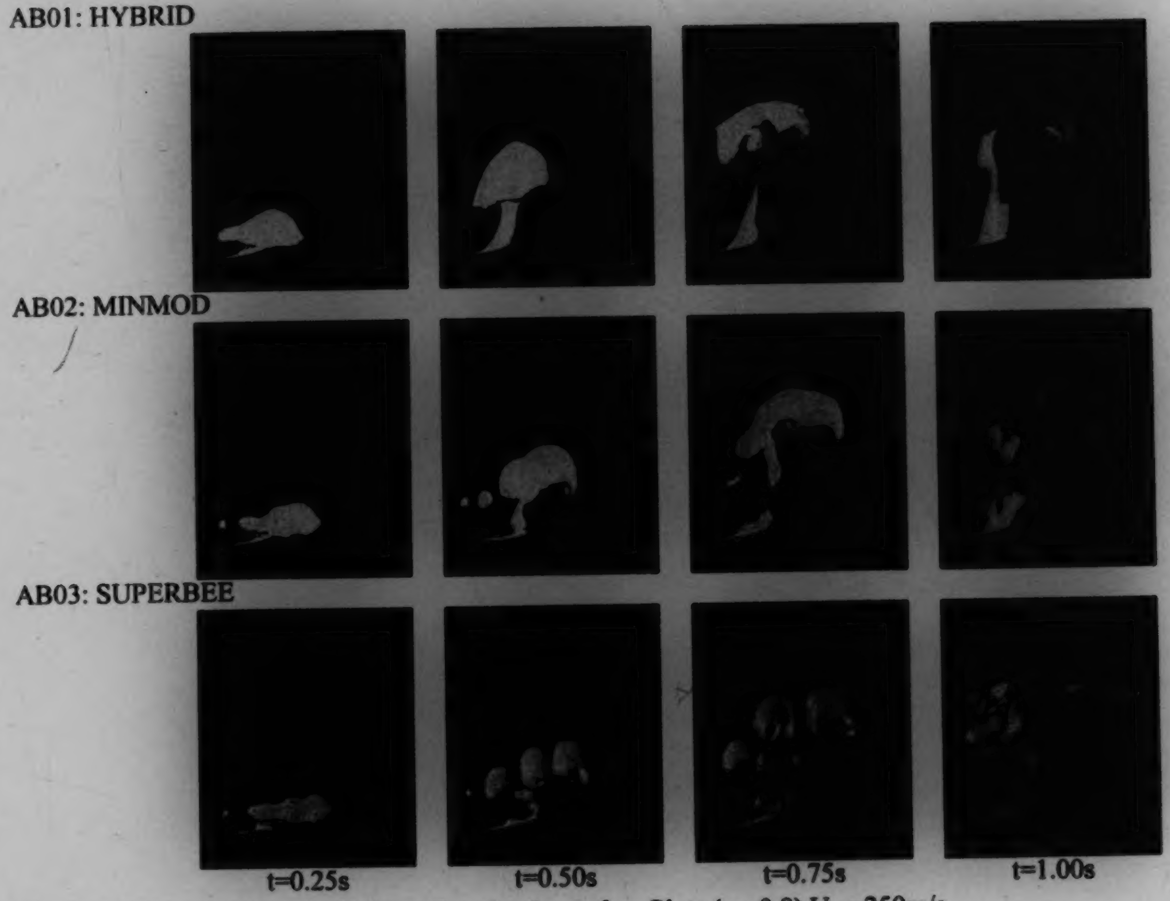

Figure 7.2: Time Series Gas Volume Fraction Isosurface Plots (ε_g=0.8) U_{jet}=250m/s

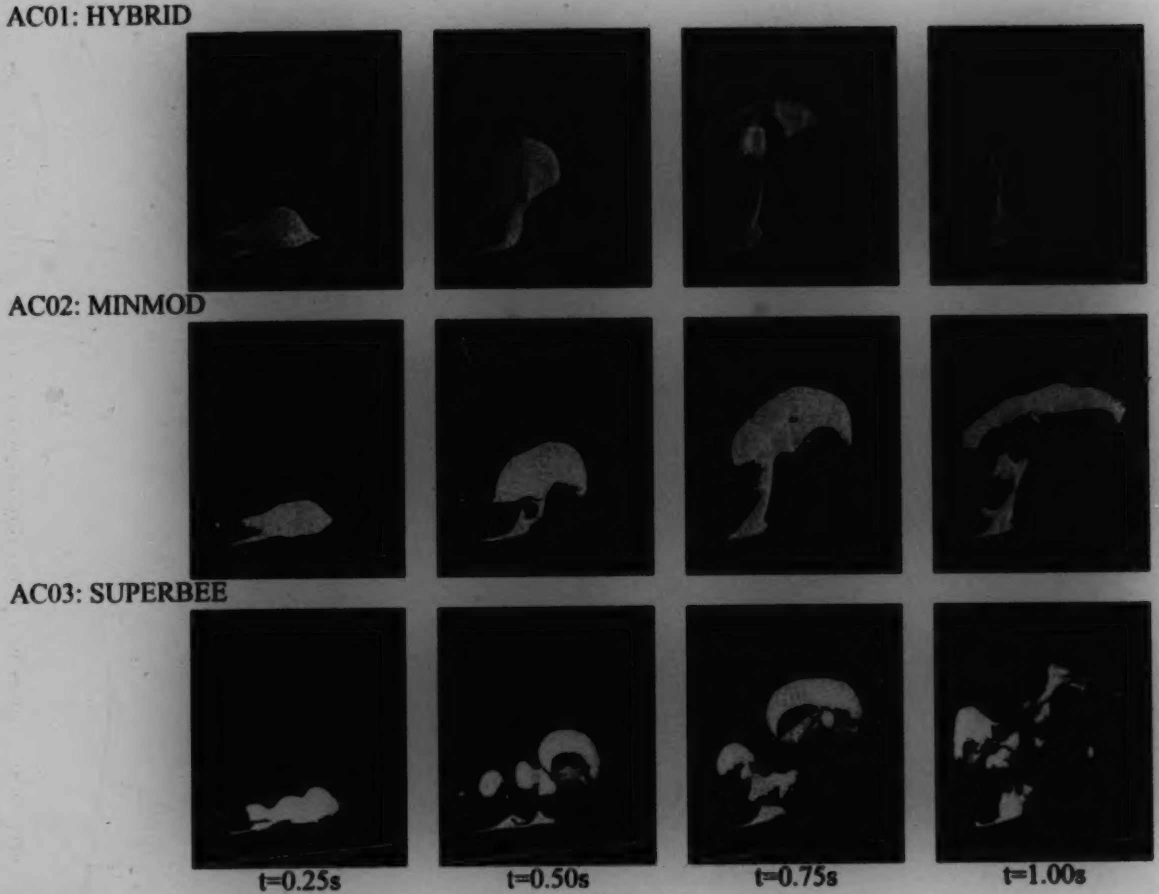

Figure 7.3: Time Series Gas Volume Fraction Isosurface Plots (ε_g=0.8) U_{jet}=300m/s

residuals are presented for runs up to series DC02. Simulations with very fine grids were too costly to generate results for comparison. Simulations for this study were allowed to run for approximately three seconds of real time and comparisons of the residuals were made after the first 1.5 seconds of real time. By comparing results from this time onwards it is expected that any flow instabilities due to initial condition specification have been minimized and the simulations are running in a "steady-state" condition, for further comments about "steady-state" assumption please see section 7.2.5 describing the solids flow patterns with time. The comparison of the gas continuity residuals allows a verification of the model results but does not provide meaningful physical predictions. The aim of this section is to provide a comparative basis on which the grid densities can be contrasted to determine the best and most economical grid density to use for simulations. Comparison of the continuity residuals between different runs should ensure that the numerical schemes are verified between different mesh densities. This analysis assumes that any errors on the coarse grids are decreased by increasing grid density.

Another concern that arose with these simulations is the specification of the nozzle inlet boundary condition. Since the nozzle orifice is small relative to the overall dimensions of the reactor, it is very important to ensure that a smooth grid density variation is realized close to the nozzle orifice. From an economics point of view it is most desirable to have a single control volume for specifying the nozzle inlet boundary condition to minimize the number of control volumes in the entire flow domain resulting in faster production of results. However, a single control volume leads to problems when interpolating and discretizing the derivatives of the transport quantities close to the nozzle orifice, see section 4.2 for a discussion of interpolating convective properties at control volume boundaries. To investigate the influence of control volume number used to specify the nozzle inlet boundary condition three different schemes were set up and solved using identical solver settings. Nozzle inlet boundary conditions were specified using different numbers of control volumes; these three different orifice boundary conditions used 1 x 1, 2 x 2 and 3 x 3 control volumes. Column one in Figure 7.4 shows the three different mesh densities used to specify the nozzle inlet boundary condition; the nozzle orifice is shown by the central gray area. X's on the mesh lines represent the locations of the control volume boundaries at which point the velocity components are interpolated for use in the discretization scheme (see Chapter 4). For the 1 x 1 control volume it can be seen that the interpolated values occur only at four locations; therefore, the interpolated values are based on the central value (directly in the center of the gray square which would represent the desired jet velocity at that point) and from values from outside of the jet boundary condition (i.e. values that don't have anything to do with the desired jet inlet velocity boundary condition). The 2 x 2 control volume specification of the nozzle inlet boundary condition is better because more control volumes are used within the jet inlet boundary condition for the interpolations; the same argument applies for the 3 x 3 specification and even finer grids.

The additional two columns in Figure 7.4 show the horizontal gas phase jet velocity over the width of the bed (in the Z direction) exactly at the nozzle orifice outlet and at a position slightly to the right of the nozzle but at the same elevation as the nozzle. The 1 x 1 nozzle orifice control volume specification is not adequate for specifying the jet inlet velocity and does not even allow the correct velocity to be specified. In this case the maximum interpolated velocity for the 1 x 1 nozzle boundary condition is only about

80 m/s – much smaller than the required boundary condition of 250 m/s. This problem is due to the fact that the jet velocity at that point is based on interpolated values outside of the jet boundary condition. A slight improvement is realized with the 2 x 2 nozzle boundary condition with a velocity spike of 250 m/s located directly at the center of the nozzle boundary condition. A more realistic jet velocity profile is seen with the 3 x 3 nozzle boundary condition. The more control volumes used to specify the nozzle inlet boundary condition will lead to better definition of the initial jetting region into the fluidized bed. It must be remembered, however, that there is a minimum control volume size below which the two fluid continuum model breaks down, see section 3.4.3, Chapter 3. Additionally the increased resolution of the nozzle boundary condition in the Z direction leads to a dramatic increase in the total number of control volumes used in the entire computational domain by adding on another layer of control volumes in the XY plane. Considering the 1 x 1 control volume specification for the nozzle boundary condition it can be concluded that the 1 x 1 control volume for the nozzle inlet boundary condition is not acceptable.

Figures 7.5 to 7.12 are plots of the gas continuity residuals for the simulations on the related meshes with nozzle control volume densities as shown in Table 7.1. These figures show the absolute residual for each of the inner iterations; outer iterations occur when the residuals spike sharply upwards. As expected in Figure 7.5 for run DA01 the residuals show a random pattern in their reduction suggesting that the grid is too coarse to capture the flow phenomena between outer iterations (i.e. between each time step) and as such the data being provided for the next time step is poor. A slight improvement is

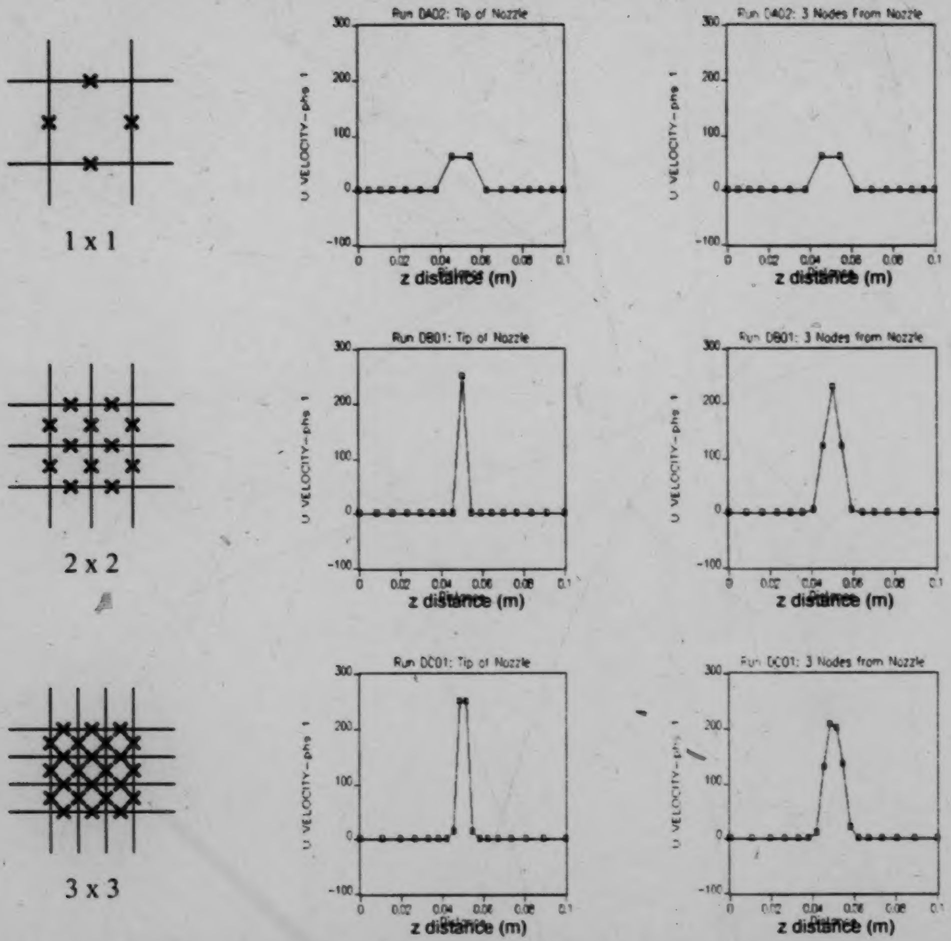

Figure 7.4 – Nozzle inlet boundary control volume specification and jet velocity.

realized with run DA02; however, the residuals still do not show a consistent reduction. These problems might be compounded by the specification of a 1x1 control volume for the nozzle inlet boundary condition. Residual reduction for run DA04 shows the best type of reduction for the first set of simulation results; however, it must be remembered that the nozzle inlet patch is only specified as a 1 x 1 control volume making the use of the mesh in DA04 unacceptable.

Figures 7.9 and 7.10, runs DB01 and DB02 show a marked improvement in residual reduction with iteration; however, contrary to expected CFD experience the increased mesh density of DB02 lead to a flattening out of the residual profile with iteration. These effects are even more pronounced for runs DC01 and DC02 where the tail becomes quite long and residual reduction falls to below one order of magnitude for every 20 iterations performed. The increased resolution of the nozzle inlet boundary condition for these runs at 3 x 3 control volumes might lead to problems when changing from the very fine mesh within the nozzle boundary condition to the coarser mesh used above the nozzle orifice.

Based on these studies it was decided that a nozzle inlet boundary condition of 2 x 2 control volumes is sufficient to properly specify the inlet jet gas velocity. A mesh of approximately 50,000 nodes is sufficient to capture flow detail without being overly computationally expensive and produces control volumes of sizes that are still valid for the two fluid continuum model.

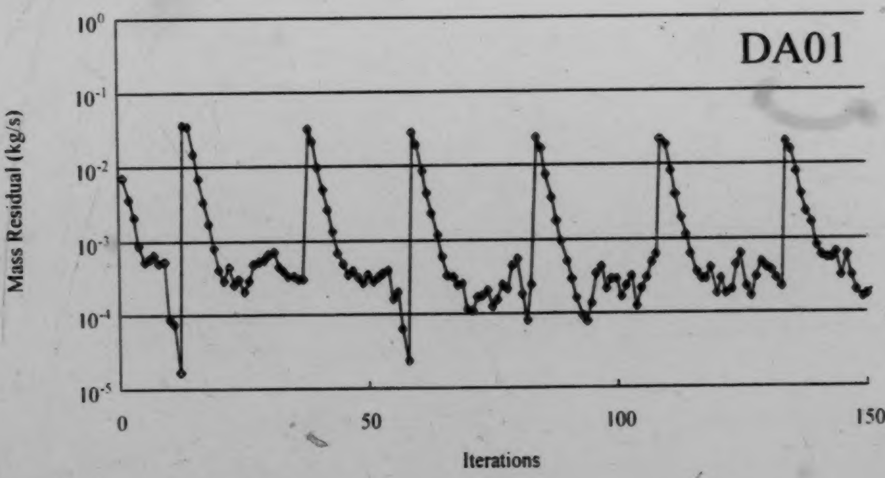

Figure 7.5 - Gas mass residuals versus iteration count for run DA01.

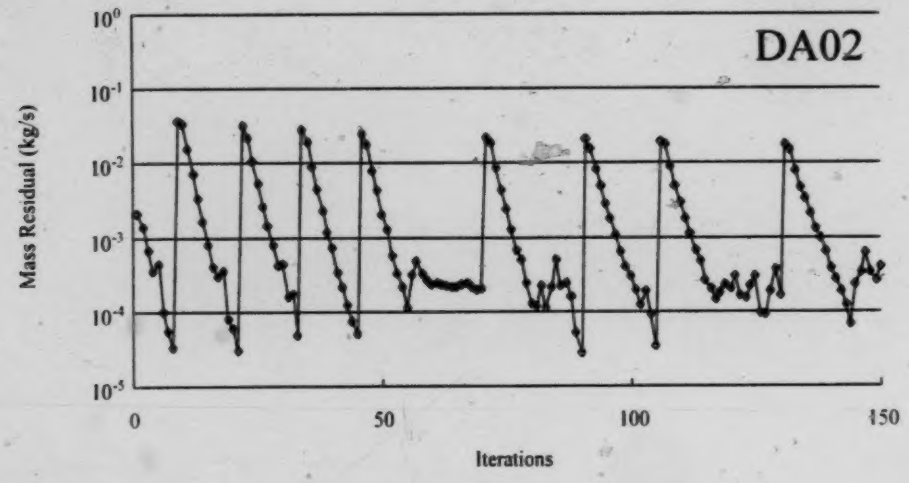

Figure 7.6- Gas mass residuals versus iteration count for run DA02.

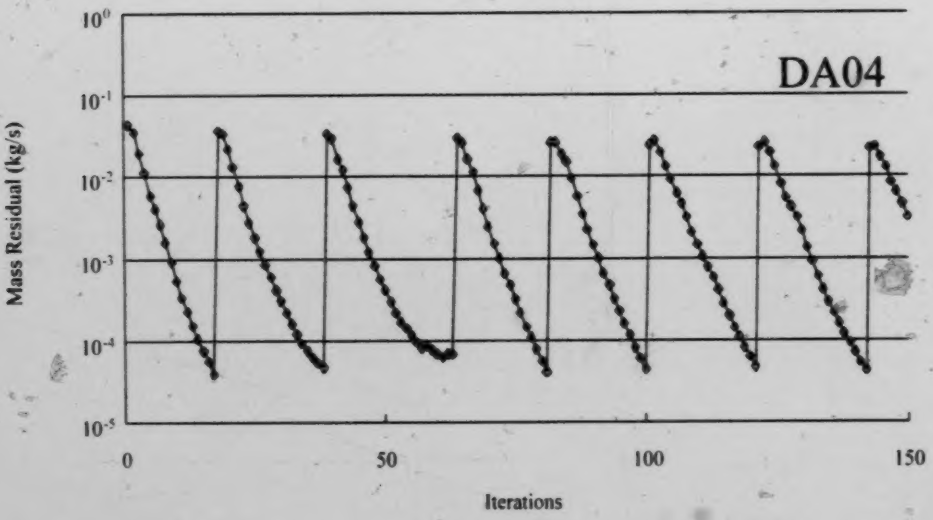

Figure 7.7- Gas mass residuals versus iteration count for run DA04.

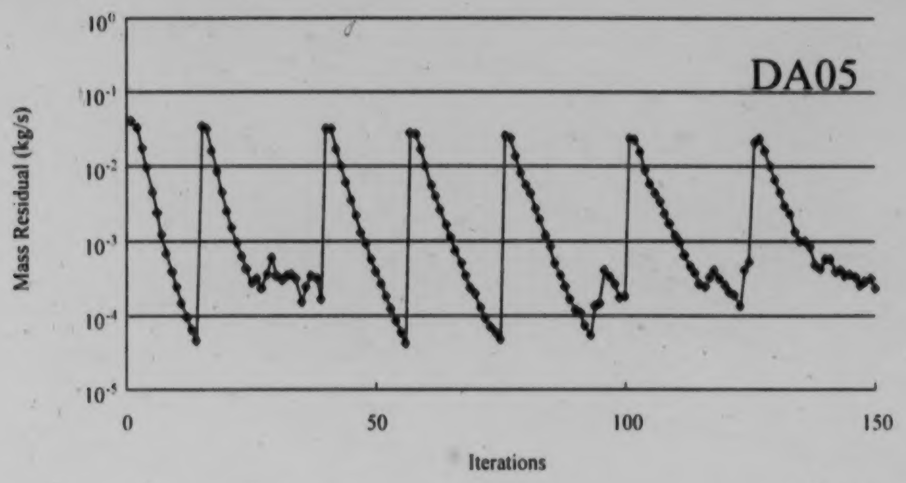

Figure 7.8- Gas mass residuals versus iteration count for run DA05.

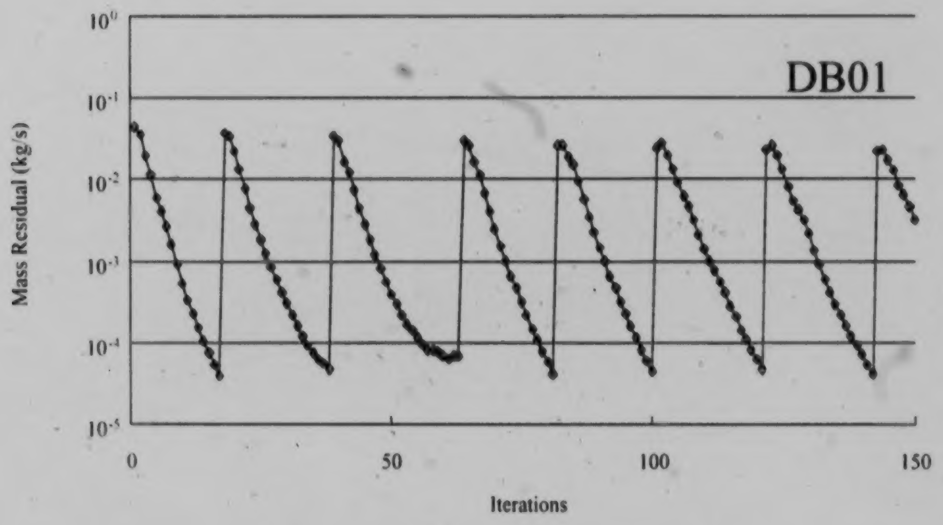

Figure 7.9- Gas mass residuals versus iteration count for run DB01.

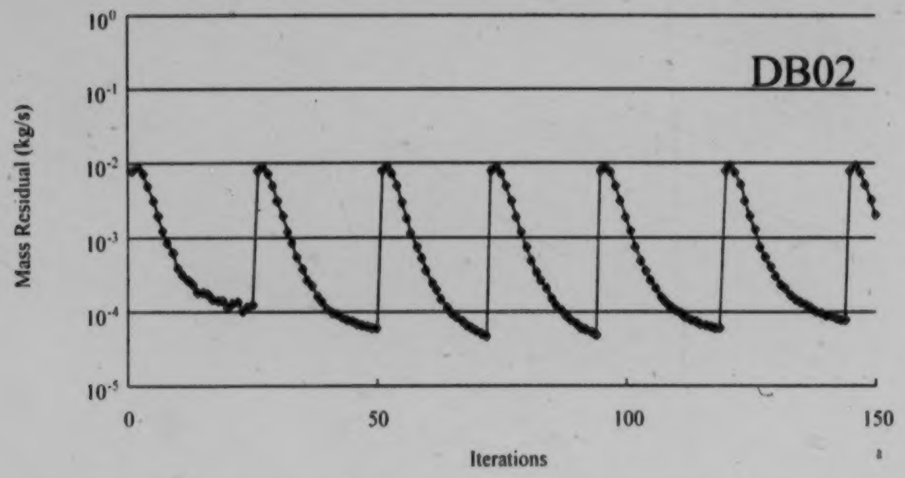

Figure 7.10- Gas mass residuals versus iteration count for run DB02.

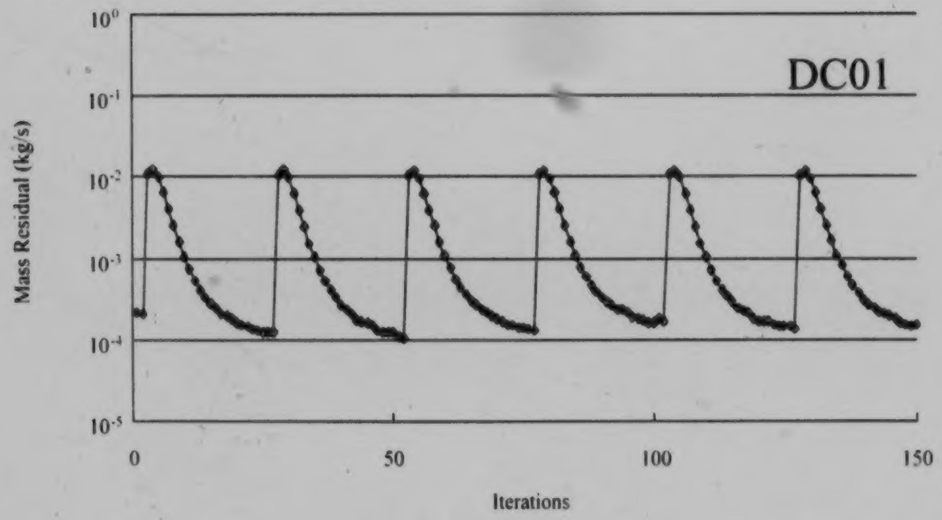

Figure 7.11- Gas mass residuals versus iteration count for run DC01.

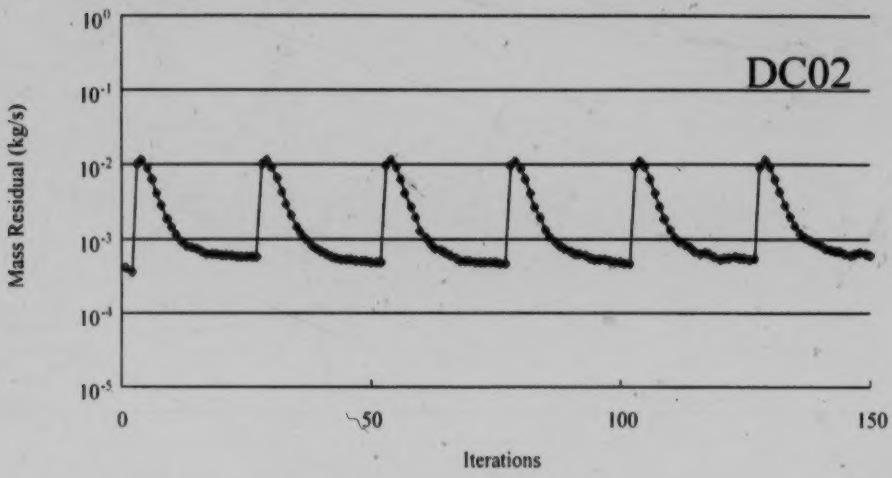

Figure 7.12 - Gas mass residuals versus iteration count for run DC02.

Additional physical arguments can be made as a further comparison of the validity of the grid density used in the simulations. The jet velocity is known and can therefore be interpreted based on the vorticity field that can be calculated from the curl of the velocity field. Figure 7.13 shows the expected vorticity field to be generated around the jet as it issues into the fluidized bed. By relating the strength of the vorticity in each of the coordinate planes and measuring the distance between the vortex cores the Biot-Savart law can be applied to calculate the induced velocity field which should be present centrally between the vortex cores. This comparison offers benefits over the velocity field as a region average of the vorticity can be used to infer the velocity field – only a single value will be used to calculate the jet velocity. The vorticity field thus calculated should be a good representation of the jet velocity condition if the mesh density is sufficient to transport the vorticity information into the surrounding nodes.

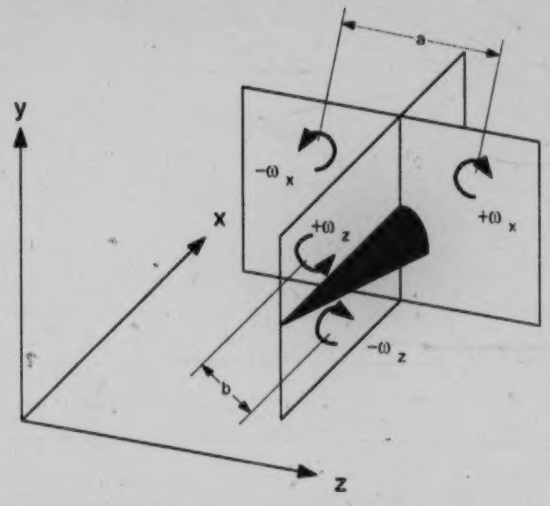

Figure 7.13 – Generalized sense of vorticity in the near jet region.

Table 7.3 summarizes the vorticity contributions calculated for each of the planes shown in Figure 7.13. With much finer grids a secondary vorticity pattern was observed to form near the jet region. In addition to the $\pm\omega_x$ contributions causing the jet to deflect upwards a secondary set of smaller vortices on the top of the jet were observed; these secondary structures are shown in Figure 7.14.

Table 7.3

Vorticity In the Near Jet Region

Run	$+w_x$	$-w_x$	u (m/s)	$+w_y$	$-w_y$	v (m/s)	$+w_z$	$-w_z$	w (m/s)
DA01	-1.16	1.14		-2.40	2.61		-1.16	1.14	
DA02	-1.04	1.10		-4.81	4.82		-1.04	1.10	
DA04	-0.93	0.91		-24.57	24.57		-0.93	0.91	
DA05	-1.14	1.17		-4.44	4.47		-4.83	5.36	
DB01	-0.50	0.44		-28.73	28.70		-15.00	12.42	
DB02	-0.12	0.11		-26.84	26.84		-13.56	11.76	
DC01	-0.09	0.10		-43.08	44.60		-36.27	43.96	
DC02	-0.21	0.21		-40.51	40.51		-33.52	39.48	

The vortex pair atop of the jet induces a net downward velocity while the vortex pair below the jet induces a net upward velocity. Secondary vortices were observed in simulations DA04, DA05 (very slightly for both of the previous runs), DB01, DB02, DC01 and DC02. After looking at these runs at a time of 0.35 seconds and then comparing the results for a much later time in the simulations, it can be assumed that these secondary vortex structures might actually be start up phenomena; however, it is important to note that for very coarse grids these secondary vortex structures were not predicted.

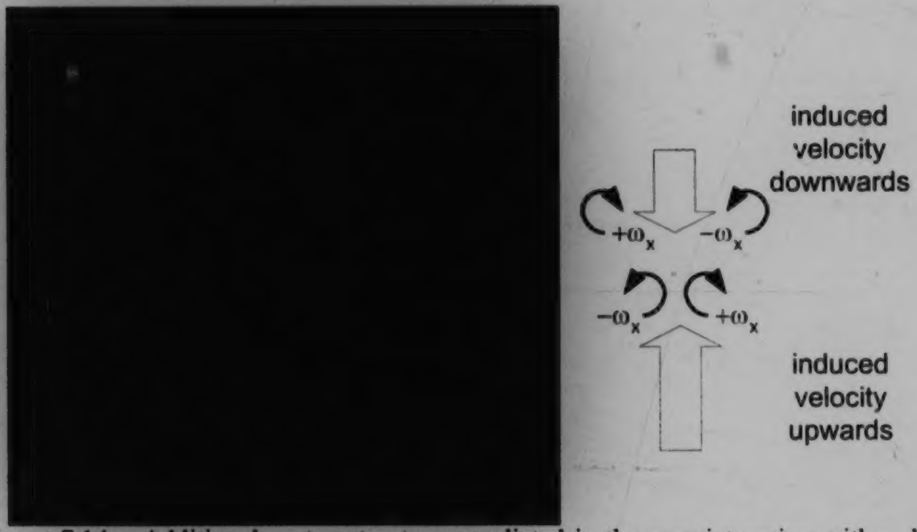

Figure 7.14 – Additional vortex structures predicted in the near jet region with a dense computational mesh.

7.1.4 Sensitivity Analysis: Continuous Phase Pressure Removed from Solids Momentum Equation

Several different formulations for the governing hydrodynamic equations for multiphase flow can be formulated and have been discussed in Chapter 3. Hydrodynamic model A was used for all of the simulations in this study with the exception of those runs in this section which follow the formulation of hydrodynamic model B. Hydrodynamic model A includes the continuous phase pressure (gas phase) in the dispersed phase (solids) momentum equation whereas hydrodynamic model B does not include the continuous phase pressure in the dispersed phase momentum equation. Simulations for this study are listed in Table 7.1. Please note that the nozzle inlet boundary was specified as 1 x 1 to allow for fast solutions. Although this does not provide results of physical significance it does provide a set of data for model verification.

Figure 7.15 shows a series of gas phase volume fraction plots over a series of time steps for simulations EA01 and DA01 (Model B and Model A) in the first and second columns, respectively. These side-by-side pictures allow a qualitative comparison of the predicted jet plume results from the simulations using Model B and Model A. Results for the first 0.50 s of real time (500 outer iterations; Figure 7.15 a-b) appear to give results which are in good qualitative agreement with each other. However, some slight differences are discernible after 0.75 s of real time solution results with discrepancies in the surface of the fluidized bed surface. Although there are slight differences between the simulation results from Model A and Model B they do not appear to be significant for this simulation study. Based on this analysis all of the simulations were continued with the hydrodynamic Model A with the inclusion of the continuous phase pressure in the solids momentum equation.

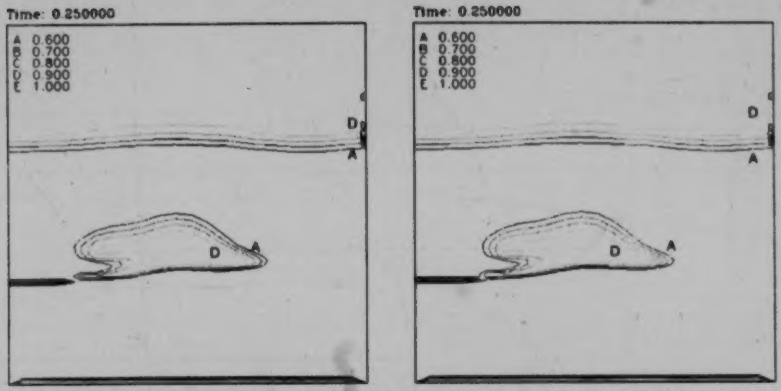

Figure 7.15 a) - Comparison of hydrodynamic model B (left) and model A (right). Plot of gas volume fraction contours, *t*=0.25 s.

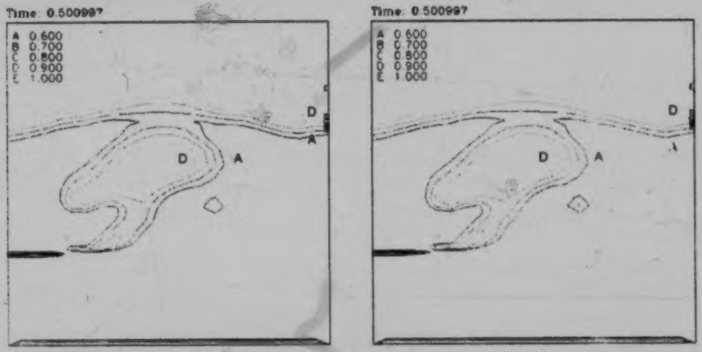

Figure 7.15 b) - Comparison of hydrodynamic model B (left) and model A (right). Plot of gas volume fraction contours, *t*=0.50 s.

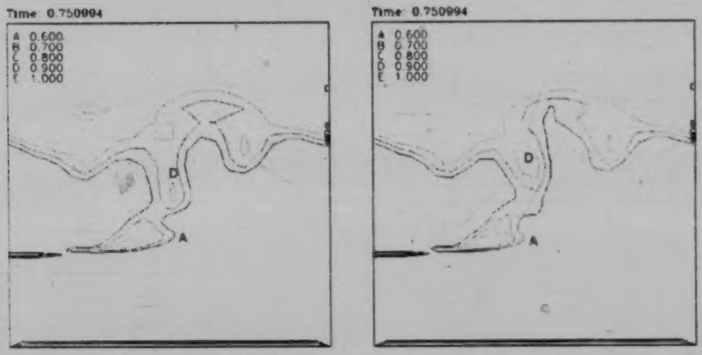

Figure 7.15 c) - Comparison of hydrodynamic model B (left) and model A (right). Plot of gas volume fraction contours, *t*=0.75 s.

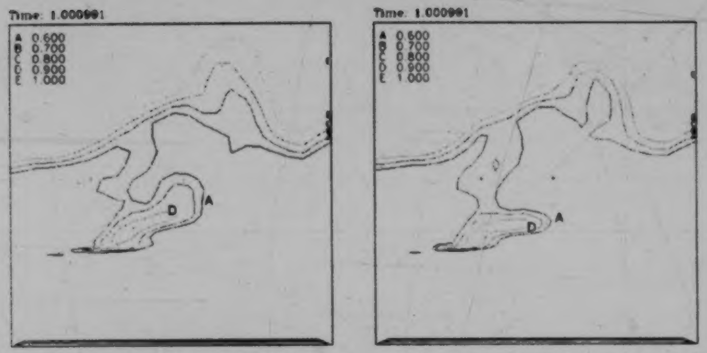

Figure 7.15 d) - Comparison of hydrodynamic model B (left) and model A (right). Plot of gas volume fraction contours, t=1.00 s.

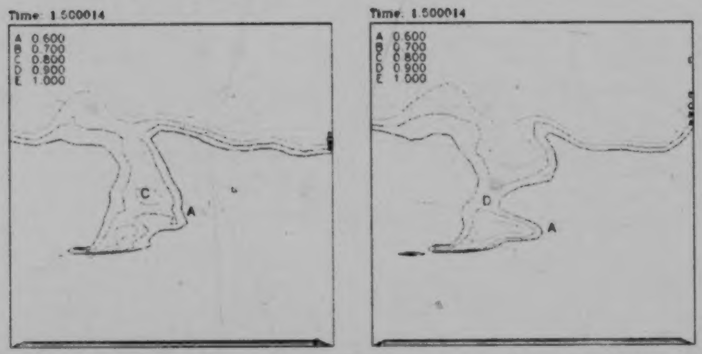

Figure 7.15 e) - Comparison of hydrodynamic model B (left) and model A (right). Plot of gas volume fraction contours, t=1.50 s.

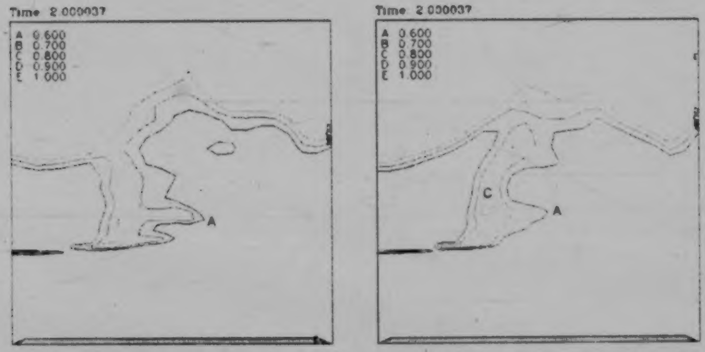

Figure 7.15 f) - Comparison of hydrodynamic model B (left) and model A (right). Plot of gas volume fraction contours, t=2.00 s.

7.1.5 Solids Pressure Sensitivity Analysis

Solids pressure is included in the solids momentum equation as a source to ensure that the solids volume fraction does not reach impossibly high values, see section 3.3.3. Most simulations in this study have used the correlation G_I of Bouillard *et al.* (1989) see Figure 3.3, page 52. The results in this section are for the correlation of Ettehadieh *et al.* (1984) which is very similar to that used by Benyahia *et al.* (1997), relation number 6 Figure 3.3, page 52. Figure 3.3 shows that each of these functions adds a solids repulsion force as the solids volume fraction increases to a maximum packing fraction; however, the expression of Benyahia *et al.* (1997) has a more gradual affect over a wider range of volume fraction. The correlation of Bouillard *et al.* (1989) rapidly increases for solids volume fractions approaching the maximum packing fraction. It is expected that the Benyahia *et al.*(1997) correlation used for the studies in this section will lead to an increase in the number of voids predicted because of the wider range of solids volume fraction that the correlation takes effect. As the solids volume fraction increases the solids pressure or repulsive forces will increase leading to a condition that prefers gas void formation. The simulations in this set of experiments have used a 2 x 2 nozzle inlet boundary condition; however, since the constitutive relationship for the solids pressure has been altered these results must be considered only to be a set of verification test cases.

In order to be able to compare the complex flow phenomena and how the solids pressure function might be affecting the results it is necessary to determine some measurable quantity. For these simulations the flow domain was broken into four regions and the solids circulation was calculated based on each of these regions. The circulation will give some sense of solids residence time in each of the zones. A summation of the magnitude of the particular vorticity contribution was determined for said regions within the flow domain. This pseudo-circulation for the solids can be used as a direct comparison of the solids type residence time within the reactor.

Many of the overall flow patterns were similar for the different solids pressure functions; however, at higher aeration rates there was a definite difference in the formation of bubbles. Jet penetrations did not seem to be affected by the use of the different solids pressure functions.

A series of time animations of the simulations for both Gxxx and Hxxx series were compared side by side to study the effect of the solids pressure function on the production and propagation of bubbles. Iso-surfaces of gas volume fractions 0.8 and 0.7 were plotted on the same animations to study how the voids formed and propagated through the bed.

Comparison of GC01 (Bouillard) with HC01 (Benyahia): Jet plume formation and penetration into the fluidized bed are both predicted equally well with both solids pressure expressions. However, there is a significant difference in the bubble behavior predicted from each of these two different simulations. Bubbles predicted with the GC01 simulation tended to be small and sharp in shape with pointed vertices. Bubbles predicted with simulation HC01 showed coalescing behavior forming larger bubbles above the jet plume boundary. The bubbles predicted with this simulation were round or cap shaped and distributed fairly evenly above the plane of the jet.

Comparison of GB02 and HB02: Both simulations appear to give similar results for jet penetration and plume shape into the fluidized bed. The top surface of the bed also appears to be similar in shape, position and surface disturbances. One of the differences is in the formation and shape of bubbles above the jet zone. For simulation GB02 with the solids pressure expression of Bouillard *et al.* (1989) G_l the bubbles appear to be oblong in shape with major axis parallel to the X axis. The bubbles also have a more jagged or pointed shape at their vertices. Bubbles predicted with the HB02 simulation tend to be rounder, more numerous and more evenly spread above the jet plume within the fluidized bed.

7.1.6 Summary of Numerical Studies

These numerical studies were used to investigate the CFX 4.2 solver options. Based on these results the settings for the physical predictions were determined. A description of the solver settings has already been covered in Chapter 5. In order to maintain reasonable solution accuracy and solution time a discretization mesh of approximately 50,000 nodes is created for the simulations. The nozzle inlet boundary condition is specified using a 2 x 2 control volume. It is felt that this boundary condition is large enough to represent the inlet flow conditions through the nozzle orifice without increasing the grid density and computational expense. The discretization scheme should be the Superbee TVD scheme and implemented on a completely three-dimensional grid with no symmetry assumptions.

For these simulations there was no noticeable qualitative difference between the use of hydrodynamic model A or hydrodynamic model B. However, the use of a different solids pressure function does seem to have an impact on the bubbling behavior especially with aeration rates higher than minimum fluidization. The expression of Bouillard *et al.* (1989) has been observed to produce fewer bubbles than the expression of

Ettehadieh *et al.* (1984) when used with similar geometry, grid spacing and model set up conditions. Further work needs to be done in classifying which relationships to use for specific multiphase simulations.

7.2 Part II: Physical Predictions

Now that studies for the effect of the choice of numerical scheme, hydrodynamic model and mesh refinement have been completed it is possible to continue with analysis of results for predicting real physical behavior. Simulations were carried out to study the effect of nozzle submergence and insertion, the effect of fluidization velocity, and tests under similar experimental operating conditions. All of the simulations used for the physical predictions are listed in Table 7.4. The standard four character simulation identification scheme has been used.

7.2.1 Tests Below U_{mf}

Simulations run at aeration velocities less than U_{mf} were conducted to determine whether the present simulation models could cope with these different operating conditions. Simulations using $0.5U_{mf}$ produced results which agree well with literature predictions of how the jet behavior should change; however, simulations using zero fluidization velocity proved difficult to achieve acceptable converge on the gas continuity residual. This simulation set is listed in Table 7.4 under the Cxxx series.

Description of run CA01: Contour plots of gas volume fraction at $\varepsilon_g=0.8$ provided information about the surface of the bed and bubble formation from the tip of the nozzle. Predominantly the surface of the bed decreased slightly with a decrease in fluidization velocity. Bubbles only present above the jetting region and not in the bulk of the bed – also expected for a lower aeration rate. Bubbles grew in size when rising up through the bed. Less bed material above the bubble leads to a decrease in pressure thereby decreasing the pressure constraining the bubble resulting in an increase in bubble size with distance from the distributor. Bed surface heights above the distributor were measured and plotted against time to observe transient behavior. Unfortunately the formation and explosion of bubbles out of the surface of the bed and into the freeboard area lead to skewed data for the bed surface. While most of the surface of the bed remained at a fixed level, the bubbles over top of the jet tended to increase the overall average bed height. This problem can be averted somewhat by averaging only those values to the right of the bubble zone. Figures 7.16 and 7.17 show bed heights over time as the fluidization gas is halved and then set to zero. Data for the CCxx series of runs was no longer available. Each graph shows that the average bed height decreased for approximately 1.5 seconds as the effects of the reducing the aeration rate to $0.5U_{mf}$ are propagated throughout the bed. On the average the bed surface level is decreasing in height but there are several upsets where the bed level appears to increase. These upsets are caused by the ejection of bubbles out of the top of the bed surface leading to an increase in the bed surface height where the bubble escapes and deforms the bed surface. These upsets are larger for run CB01 relative to run CA01 because the jet velocity in CB01 is 100 m/s faster than that in CA01 leading to an increased gas flux and greater voidage being injected into the fluidized bed. When the fluidization gas was decreased to half minimum fluidization both of the bed surfaces for runs CA01 and CB01 decreased by approximately 6 cm. The bed surface for run CA01 settled to a height of approximately 70 cm while the bed surface for simulation CB01 settled to a height of 73 cm. This difference in bed heights can be explained based on the amount of gas that is

Table 7.4: Physical Predictions Simulation Summary

Bxxx series: Insertion and Submergence Tests

CFD Run	Scheme	U_f	D_o	S	I	D_p	ρ_p	Nozzle CVs
U_{jet}=250 m/s			(m)	(m)	(m)	(μm)	(kg/m³)	(size)
BA01	SB	U_{mf}	0.0099	0.25	0.10	370	1450	2x3
BA02	SB	U_{mf}	0.0099	0.25	0.15	370	1450	2x3
BA03	SB	U_{mf}	0.0099	0.2	0.10	370	1450	2x3
BA04	SB	U_{mf}	0.0099	0.2	0.15	370	1450	2x3

Cxxx series: Tests Below U_{mf}

CFD Run	Scheme	U_f	D_o	S	I	D_p	ρ_p	Nozzle CVs	t_{start}	t_{end}
U_{jet}=150 m/s			(m)	(m)	(m)	(μm)	(kg/m³)	(size)	(s)	(s)
CA01	SB	0.5U_{mf}	0.0099	0.145	0.1175	370	1450	2x2	1.45	4.40
CA02	SB	0.0	0.0099	0.145	0.1175	370	1450	2x2	4.45	5.10
U_{jet}=250 m/s										
CB01	SB	0.5U_{mf}	0.0099	0.145	0.1175	370	1450	2x2	1.35	4.17
CB02	SB	0.0	0.0099	0.145	0.1175	370	1450	2x2	4.2	4.87
U_{jet}=300 m/s										
CC01	SB	0.5U_{mf}	0.0099	0.145	0.1175	370	1450	2x2	1.3	4.1
CC02	SB	0.0	0.0099	0.145	0.1175	370	1450	2x2	4.1	5.0
CC03	SB	0.25U_{mf}	0.0099	0.145	0.1175	370	1450	2x2	4.1	5.0

Fxxx series: Tests Above U_{mf}

CFD Run	Scheme	U_f	D_o	S	I	D_p	ρ_p	Nozzle CVs
U_{jet}=150 m/s			(m)	(m)	(m)	(μm)	(kg/m³)	(size)
FA01	SB	2.0U_{mf}	0.0099	0.145	0.1175	370	1450	2x2
FA02	SB	3.0U_{mf}	0.0099	0.145	0.1175	370	1450	2x2
U_{jet}=250 m/s								
FB01	SB	2.0U_{mf}	0.0099	0.145	0.1175	370	1450	2x2
FB02	SB	3.0U_{mf}	0.0099	0.145	0.1175	370	1450	2x2
U_{jet}=300 m/s								
FC01	SB	2.0U_{mf}	0.0099	0.145	0.1175	370	1450	2x2
FC02	SB	3.0U_{mf}	0.0099	0.145	0.1175	370	1450	2x2

Gxxx series: Runs Conforming to Experimental Operating Conditions

CFD Run	Scheme	U_f	D_o	S	I	D_p	ρ_p	Nozzle CVs
U_{jet}=150 m/s			(m)	(m)	(m)	(μm)	(kg/m³)	(size)
GA01	SB	2.0U_{mf}	0.00292	0.145	0.1175	370	950	2x2
GA02	SB	3.0U_{mf}	0.00292	0.145	0.1175	370	950	2x2
U_{jet}=250 m/s								
GB01	SB	2.0U_{mf}	0.00292	0.145	0.1175	370	950	2x2
GB02	SB	3.0U_{mf}	0.00292	0.145	0.1175	370	950	2x2
GB03	SB	3.0U_{mf}	0.00292	0.145	0.1175	370	950	2x2
U_{jet}=300 m/s								
GC01	SB	2.0U_{mf}	0.00292	0.145	0.1175	370	950	2x2
GC02	SB	3.0U_{mf}	0.00292	0.145	0.1175	370	950	2x2
GC03	SB	3.0U_{mf}	0.00292	0.145	0.1175	370	950	2x2

being injected by the gas feed jet. For run CA01 the jet velocity is 150 m/s while for run CB01 the jet velocity is 250 m/s. The additional gas being injected for CB01 will augment the fluidization gas and cause the surface of the bed to be at a higher level than for run CA01 due to increased bed voidage.

A vertical line was drawn in both figures at the time when the fluidization gas was set to zero; from this point onwards the bed is no longer fluidized and operates as a packed bed. Unfortunately due to the short duration of the runs at zero fluidization the transient effects of turning off the fluidization gas have probably not been transmitted into the bulk of the bed and the simulation results are showing transition behavior. No meaningful observations can be drawn about the steady state behavior of the predicted bed behavior. It is not possible to tell how the bed surface decreases with no aeration. Observations of the predicted flow field just above the jet plume for zero fluidization show that large bubbles are no longer present within the packed bed. A large jet plume region forms from the nozzle orifice and smaller bubbles occasionally break off of the jet plume and propagate up to the surface of the bed. Observations of the experimental apparatus at the UofS under similar operating conditions show that the packed bed condition does not allow the formation of bubbles. Gas from the jet tends to form a void which carves the bulk bed phase and occasionally the bed would collapse in on this void forming a funnel region from the top of the bed to the jet plume.

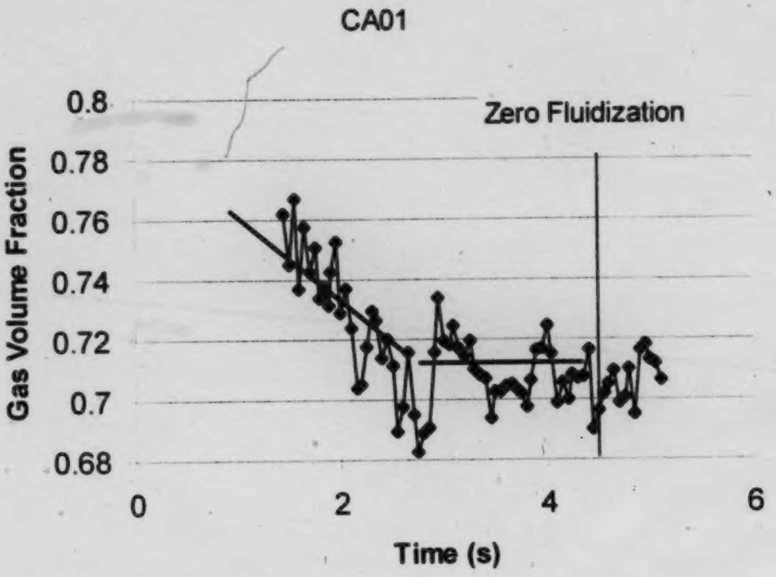

Figure 7.16 – Bed surface height over time for run CA01.

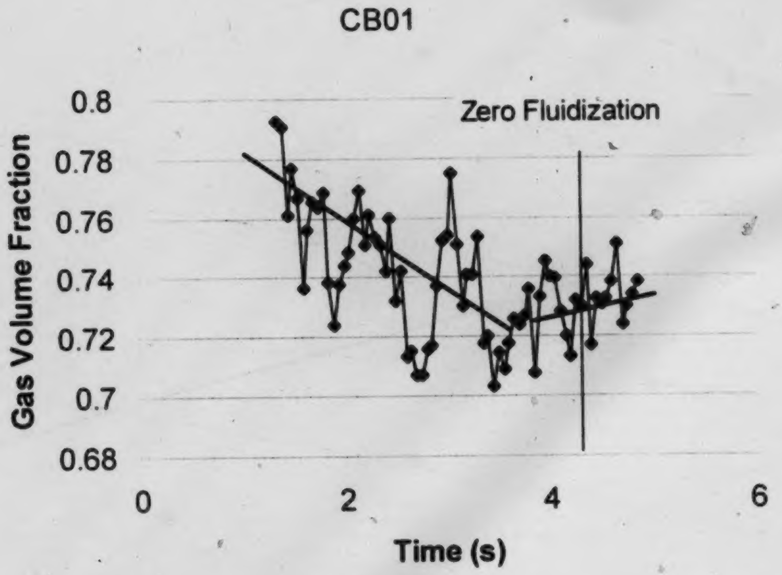

Figure 7.17 – Bed surface height over time for run CB01.

Additional insight into flow development with decreasing fluidization velocity can be found by observing how the jet plume and predicted solids flow patterns change over time. A series of time steps from simulation CA01 was taken at times of 1.45 seconds (just when the aeration rate was decreased to $0.5U_{mf}$), 4.4 seconds (just before the aeration was shut off) and at 5.1 seconds (zero fluidization; packed bed condition). Each of these three figures have solid lines showing predicted instantaneous solids streamlines and shaded iso-surfaces of gas volume fraction of $\varepsilon_g=0.8$. Figure 7.18 shows how the fluidized bed is predicted to behave within an established steady state minimum fluidization flow regime. Two recirculating zones are present; a counter clockwise zone above and to the left of the nozzle and a clockwise zone in bulk of the bed. Bed surface is approximately 76 cm above the distributor. Predicted instantaneous solids streamlines are presented in Figure 7.19 for half minimum fluidization. Two recirculation zones are still present; however, the overall bulk bed circulation is more pronounced and the gas jet has receeded closer to the low X wall. The average bed height has also fallen to approximately 70 cm above the distributor plate. Results for predicted solid flow patterns are shown in Figure 7.20 for a packed bed condition with zero fluidization gas. The large over turning region within the bed has moved closer to the low X wall and the top surface of the bed appears to have sunk near the low X wall. A slight mound has formed on the bed surface due to solid particles being entrained in the jet and carried up to the top surface of the bed where they are deposited; this is the so called "funnel" behavior. This type of behavior was also observed with the experimental apparatus at the UofS under similar operating conditions.

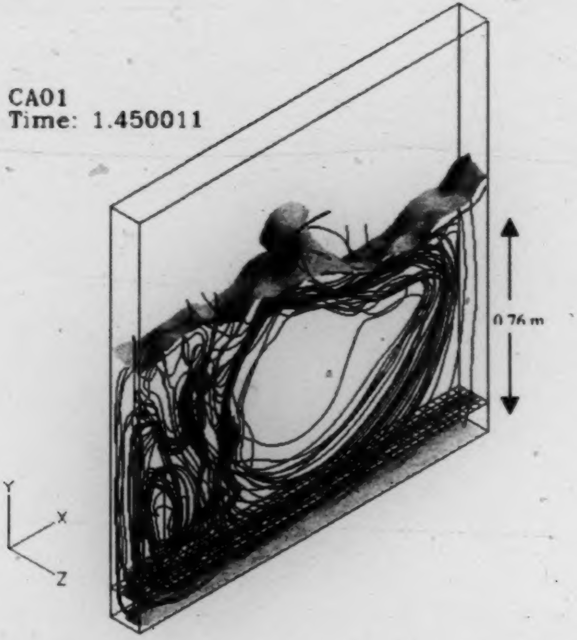
CA01
Time: 1.450011
0.76 m
Y
X
Z

Figure 7.18 – Predicted solids streamlines and bed surface at minimum fluidization.

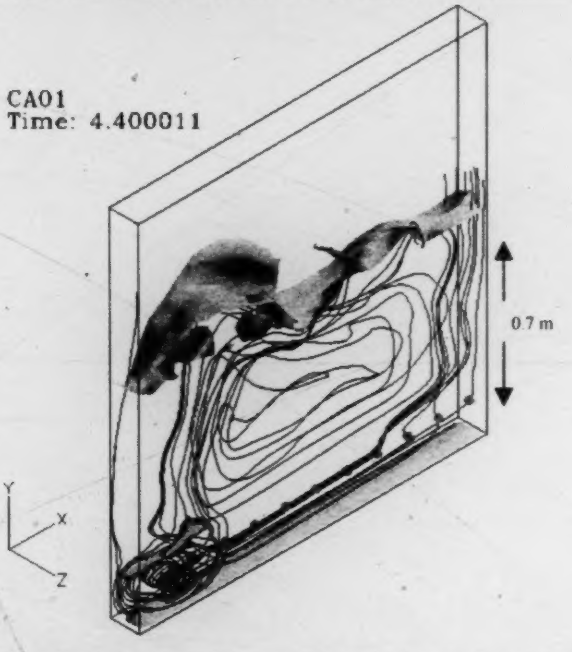
CA01
Time: 4.400011
0.7 m
Y
X
Z

Figure 7.19 – Predicted solids streamlines and bed surface below minimum fluidization.

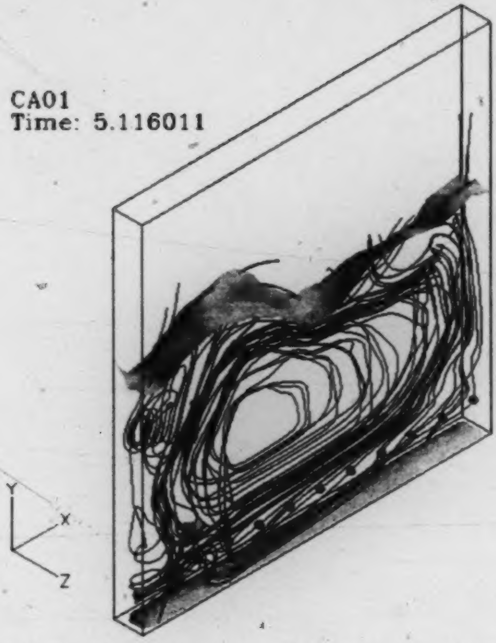

Figure 7.20 – Predicted solids streamlines and bed surface with zero aeration; packed bed condition.

7.2.2 Tests Above U_{mf}

Several simulations were conducted above minimum fluidization to study the effect of increased aeration on the predicted bed behavior. One of the most striking features of these simulations is the transition from minimum fluidization to a higher fluidization velocity over a period of approximately 0.25 seconds. Start up conditions for these simulations above minimum fluidization were provided by restarting previous simulations after 1.2 seconds. Using a set of initial conditions from previous runs allowed the transient start up behavior for the first second to be avoided. Upon initiation of the simulation with the increased fluidization rate a flat gas volume fraction iso-surface of 0.6 was observed to propagate upwards from the distributor plate and into the fluidized bed. Approximately three of these flat surfaces were seen to form and when the top most plane coincided with the Y height of the nozzle orifice all of the following surfaces are seen to form disturbances along their lengths and a series of complete bubbles ensues. Figure 7.21 shows four frames from this behavior for run FB02. Gas volume fraction iso-surfaces of 0.6 are plotted in an isometric view. Simulation results start from minimum fluidization and at time equal to 1.25 seconds the fluidization velocity is increased to three times minimum fluidization; this 1.25 seconds coincides with the first frame of the sequence shown in Figure 7.21 a. Figure 7.21 b shows the three flat volume fraction iso-surfaces forming below the height of the nozzle orifice. These planes move up in the next frame and begin to form waves. Wave amplitude grows in Figure 7.21 c to a point that the successive planes have started to touch; this is the initial formation of bubbles below the jet height. Complete bubbles form in Figure 7.21 d in the lower part of the bed and the simulation has predicted bubbling fluidization behavior. This predicted transitional behavior seems to follow that observed with the experimental apparatus. When the experimental apparatus at the UofS was first fluidized, a plug flow of gas was present which caused the bed surface to rise before homogeneous fluidization was achieved. This plug flow might be the same as that predicted in the simulation. Distinct surfaces on the top and bottom of the plug would rise and then spontaneously break apart into bubbles. This type of behavior was not observed for simulations at or below minimum fluidization. Step changes from minimum fluidization to half minimum fluidization do not show this behavior.

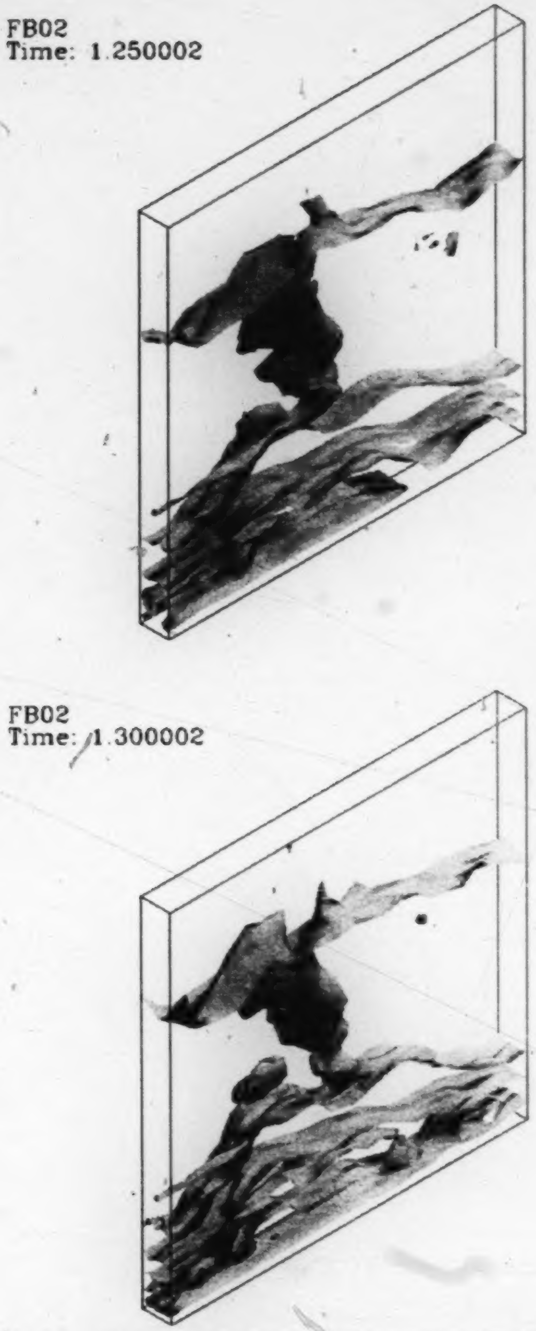
FB02
Time: 1.250002
FB02
Time: 1.300002

Figure 7.21 – Transient bed behavior with a step change in fluidization velocity.

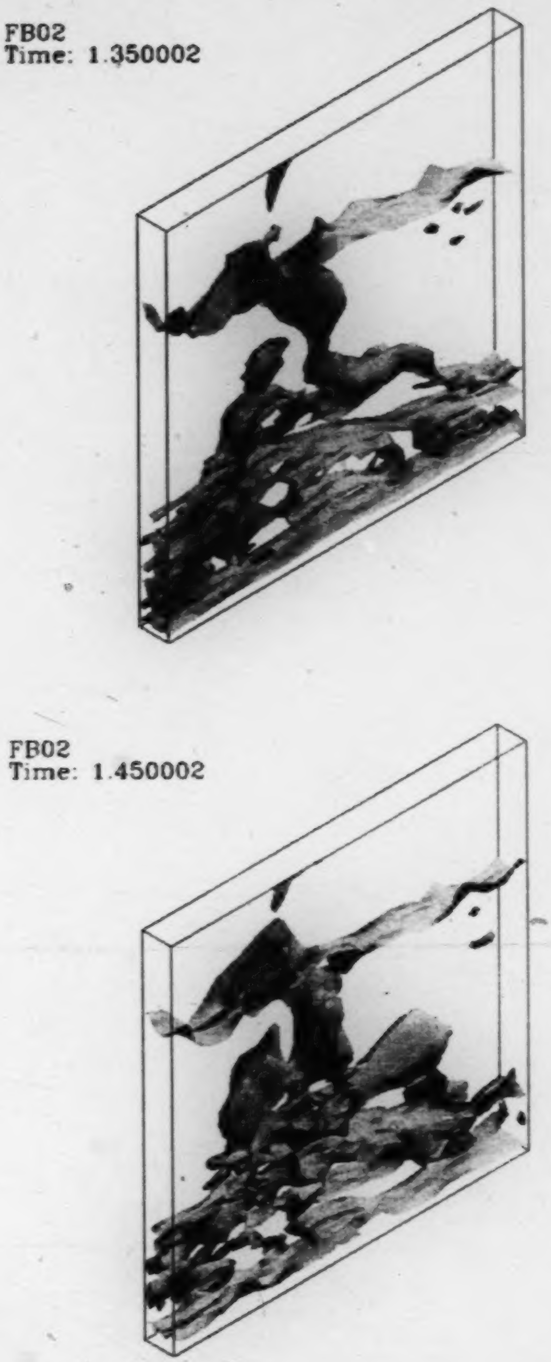
FB02
Time: 1.350002
FB02
Time: 1.450002

Figure 7.21 continued – Transient bed behavior with a step change in fluidization velocity.

7.2.3 Jet Behavior and Penetration Results

One of the most important parameters for design and placement purposes of the horizontal gas feed jet is the penetration to which the gas jet plume reaches into the fluidized bed. To be able to carry out a meaningful evaluation of jet penetration into the fluidized bed it was necessary to determine whether the simulation operating conditions agreed with the jet regime phase diagram of Chyang *et al.* (1997). Figure 7.22 shows in which flow regime each of the simulations documented in this report fall. All simulations with jet velocities greater than 150 m/s fell within the stable jetting region, and should, therefore, provide results which can be analyzed based on jet penetration depths into the fluidized bed.

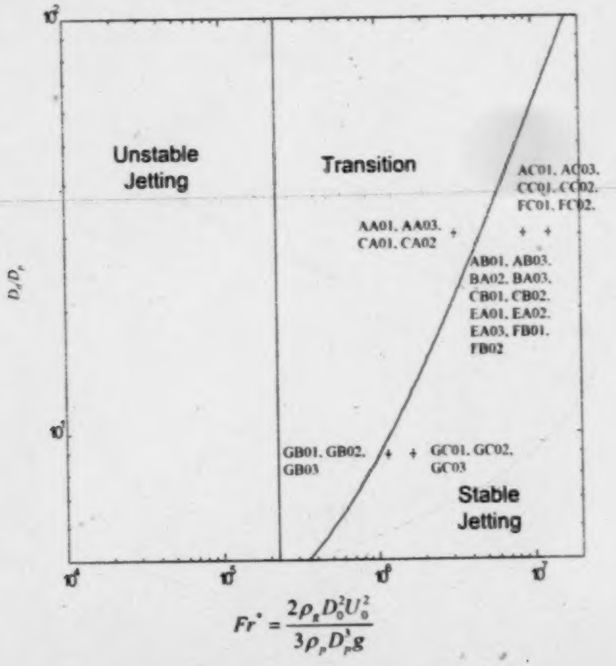

Figure 7.22 – Jet regime phase diagram of Chyang *et al.*(1997) for all simulations.

Penetration results were taken for all simulations by observing the gas volume fraction along the jet axis in the center XY plane. A gas volume fraction of 0.8 was arbitrarily chosen to be the boundary between the fluidized bed and the jet plume. Jet penetration was defined as the distance from the tip of the nozzle (i.e. the location of the nozzle inlet boundary condition) to the furthest gas volume fraction contour of 0.8. In cases where the gas jet curved upwards or began to pinch off to form a bubble the maximum penetration was defined to occur at the end of curvature or the pinch point itself as shown in Figure 7.23. Based on this penetration criteria results were obtained for the jet penetration every 0.05 seconds and then averaged to determine a representative penetration depth for that simulation. The first second of data was ignored to avoid transient start up phenomena. In many cases determining the actual jet penetration was very difficult due to jet curvature, bubble formation and gas volume fractions that changed along the length of the jet. This problem was compounded by the fact that simulation results were only saved every 0.05 seconds and the average behavior between these times is lost whereas with experimental results a continuous measurement can be taken very quickly using a ruler. Defining the penetration depth has been a problem for many researchers and can account for the different results obtained from different studies at similar operating conditions. Penetration results were compared with the correlation of Merry (1971) and nondimensionalized with nozzle diameter; results from this analysis are shown in Figure 7.24. Maximum and minimum penetration depths are also plotted on this figure with abscissa error markers off of each data point. Data markers have been grouped into gross groups representing simulations at minimum fluidization (series

Axxx, Bxxx and Exxx), those results from below minimum fluidization (series Cxxx) and those runs above minimum fluidization (series Fxxx and Gxxx).

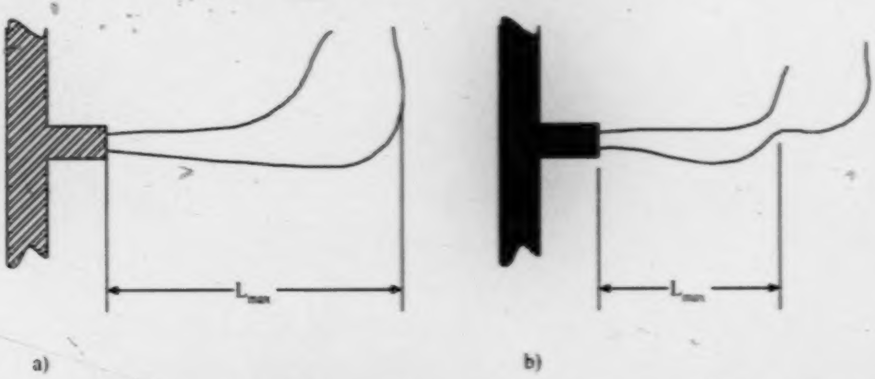

a) b)

Figure 7.23 - Maximum jet penetration defined on a gas iso-contour of 0.8 from tip of nozzle to a) jet curve and b) jet pinch point.

Predicted penetrations from the Axxx series of simulations show the merits of using the Superbee TVD (open triangles △) discretization scheme over the Hybrid scheme (closed triangles ▲). All of the Superbee predicted penetration depths lie on top of Merry's correlation. Maximum and minimum error bounds on each of these data markers are also very narrow when compared with those for the Hybrid scheme. Predicted penetration depths for the case of zero fluidization, series Cxxx, ◇ show that the penetration depth remains relatively small for lower jet velocities of 150 and 250 m/s. At 300 m/s the penetration increases but is still over predicted when compared to Merry's correlation. Similar results are found for the series Cxxx ◆ at half minimum fluidization. Jet penetration increases dramatically for the 300 m/s inlet jet velocity but all of the predicted penetration results are greater than that predicted from the correlation.

Interesting results are obtained for the test of Hydrodynamic model B with the Exxx series of simulations symbol +. All of the predicted penetration depths are identical for different jet velocities as shown by the constant *L/d_0* value for all three Exxx simulations. This result seems contrary to physical expectation since an increase in inlet jet velocity should lead to an increase in jet penetration into the fluidized bed. Although qualitative results comparing Hydrodynamic model A (series Dxxx) and Hydrodynamic model B (series Exxx) in section 7.1.4 showed very little variation in the predicted gas volume fraction contours within the fluidized bed it appears that the physical predictions with Model B do not give results that are in accordance with expected physical behavior.

Results from the Gxxx series, those with a much smaller nozzle orifice size and solids properties agreeing with the experimental fluidized bed, under predicted the gas jet penetration into the fluidized bed when compared with Merry's expression. Additionally the error bounds representing maximum and minimum penetration depths showed a greater range than most other simulations. Only the GC03 and GB03 simulations predicted penetration depths within expected error ranges. Both of these simulations used a jet velocity of 300 m/s which might explain why the penetration was greater and hence closer to that predicted with the Merry's expression. The much smaller nozzle orifice size might contribute to problems associated with simulations for the Gxxx series. This small inlet boundary condition decreased the gas flux across the orifice area subsequently leading to a decrease in jet momentum. Decreased jet momentum will lead to a decrease in jet penetration into the fluidized bed.

By creating animated movies of the gas volume fraction iso-surface of 0.8 it was possible to observe how the jet plume and penetration progressed with time. In general the jet would penetrate into the bed at start up forming large bubbles which would progress upwards and out of the bed surface. After this initial start up regime, the jet would settle down into a characteristic fluctuating behavior. First the jet would penetrate into the bed and then a bubble would form at the tip from a "pinch point". The jet would then recede slightly (the penetration would decrease somewhat) and this cycle would be repeated. This periodic increase and then decrease in jet penetration was also observed in the experimental tests at the University of Saskatchewan.

7.2.4 Overall Flow Patterns

Simulation results tended to over predict recirculatory flow patterns within the fluidized bed both above and to the right of the jet within the flow domain when compared with the observations taken at the UofS. These large recirculating cells were not observed in the experimental apparatus under any operating conditions. A representative solids velocity field is shown in Figure 7.25. A counter clockwise (CCW) rotating area is seen to form above the jet with solids moving down along the wall and becoming entrained in the jet. A large clockwise (CW) recirculation flow pattern is present to the right of the jet and the fluidized bed is seen to slowly turn over with solids recirculating into the bottom of the jet after being carried along to the left just above the distributor plate. Solids entrained in the central part of the jet were carried upwards and deposited on the top of the bed surface.

Similar recirculating zones were found in Figure 7.26 for the BA03 simulations although the counter clockwise recirculation zone above the jet appears to be more elongated in the Y direction. As shown in Table 7.4, the insertion for BA03 is 0.05 m less than for run BA02. This decrease in fluidized bed above the jet inlet might cause the dragging zone above the jet to be shortened thereby forming a shorter recirculation zone.

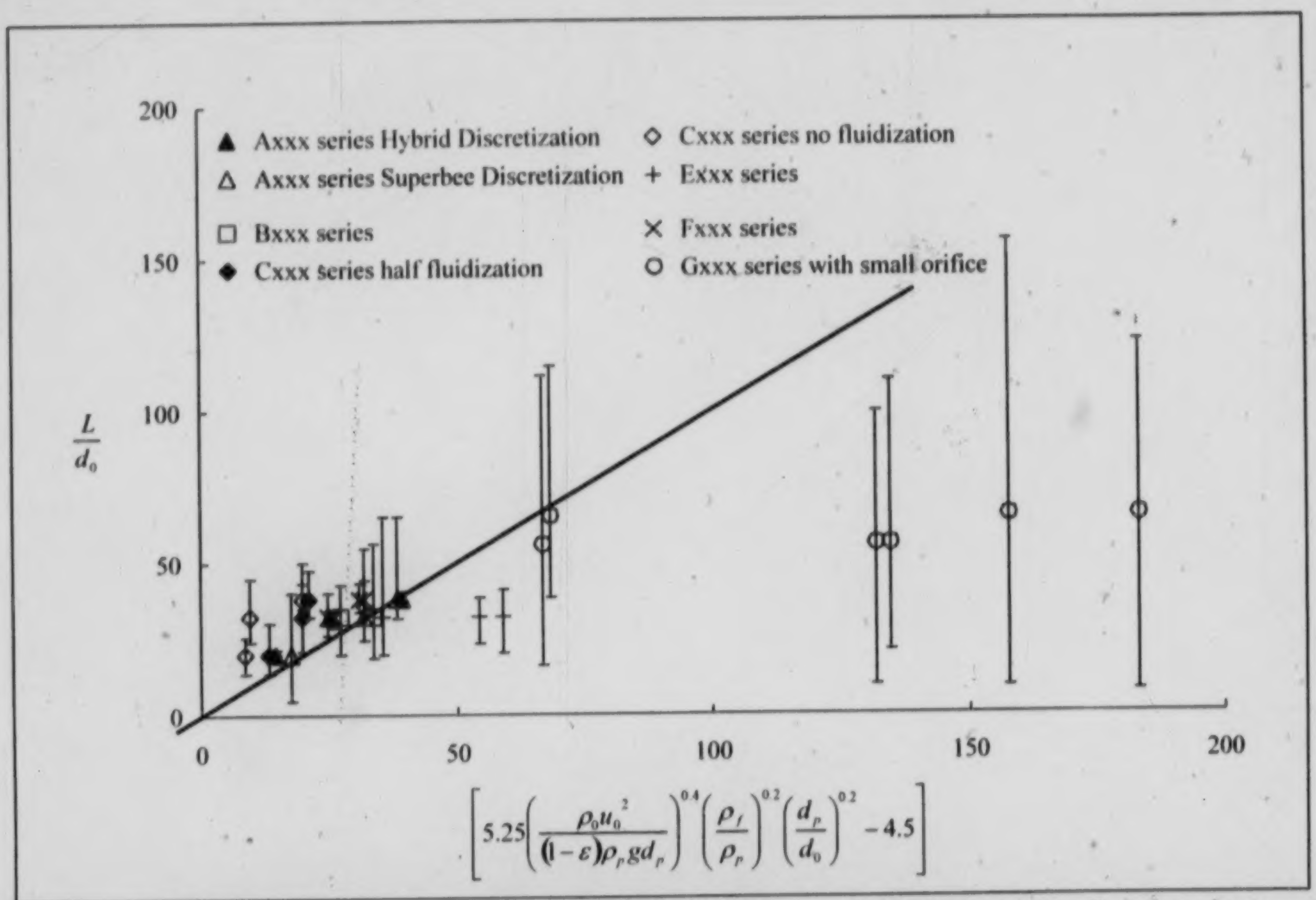

Figure 7.24 - Penetration results from simulations compared with the expression of Merry (1971). Error bars denote maximum and minimum penetrations based on a solids volume fraction iso-surface plot of 0.8.

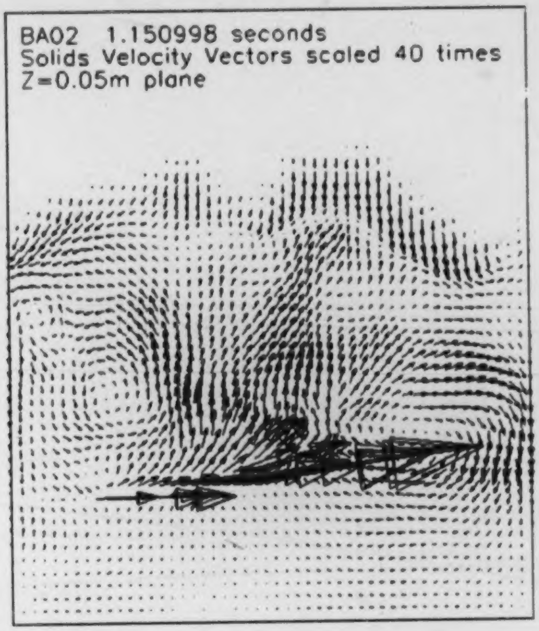

Figure 7.25 - BA02 solids flow pattern vectors in the fluidized bed.

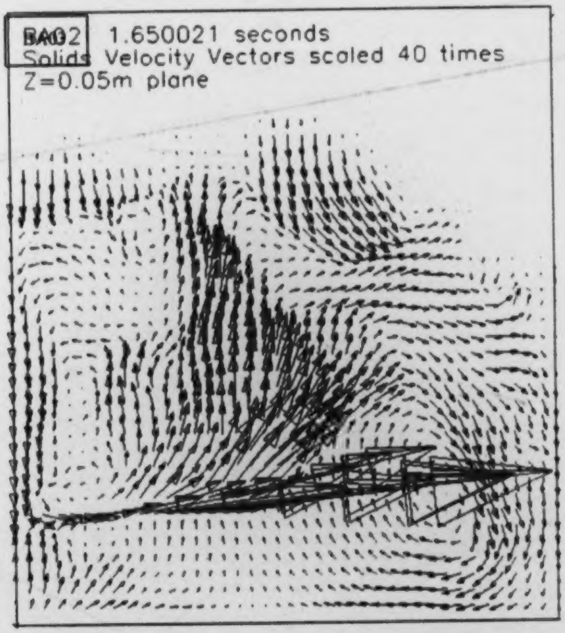

Figure 7.26 - BA03 solids flow pattern vectors in the fluidized bed.

A pair of counter rotating vortices were also predicted to form below the nozzle inlet pipe and close to the low X wall, see Figure 7.27. Solids down flow along the wall impacts on the nozzle inlet pipe and is forced to either side of the pipe leading to a wake region just behind (or below) the nozzle pipe. This behavior was predicted for all simulations and is in agreement with the experimental observations of how the solids behaved close to the nozzle pipe. Solids appeared to be entrained into the gas jet through a line sink shown schematically in Figure 7.28. The entrainment from below the nozzle pipe might be due to this wake region that was predicted in the simulations. Solids are carried down and then back up directly below the pipe being entrained into the gas jet and forming the solids sink.

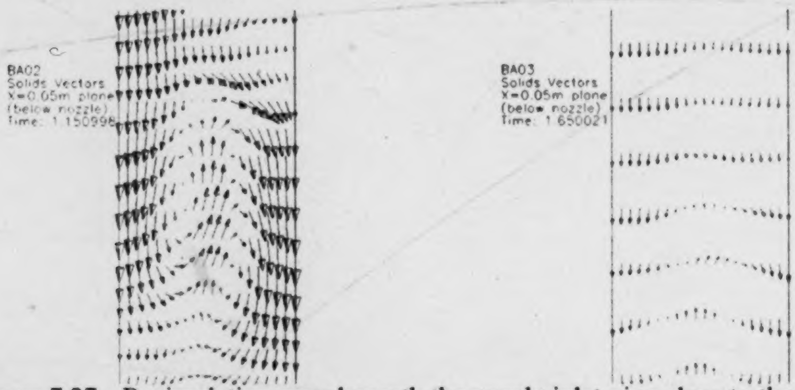

Figure 7.27 - Recirculation zone beneath the nozzle inlet pipe close to the low X wall of the simulation.

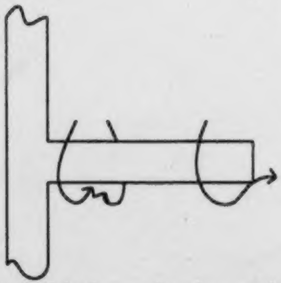

Figure 7.28 – Solids wake region behind nozzle pipe and entrainment into jet.

7.2.5 Particle Tracking

Using FIELDView (FIELDView User Manual, 1999) from Intelligent Light software it is possible to seed a simulated flow field with virtual particles to track how they would move within that given flow field. It has to be emphasized that these particle tracks are not Lagrangian but merely show how particles would move within that flow field at that given instant in time and represent instantaneous streamlines. Ten virtual seed particles were randomly scattered on a gas iso-surface of 0.8 in the region where the jet plume issues into the fluidized bed. Two streamline patterns were seeded with one set of ten particles on the top surface of the gas jet and another set of ten particles being seeded on the lower surface of the jet. After randomly seeding the top and bottom parts of the jet plume, an integration of the velocity field was carried out to predict where these virtual massless particles move.

Figures 7.29-30 are isometric views showing how virtual particles would move if they were to follow the predicted *solids* velocity field. The seed particles above the jet, shown in Figure 7.29, are seen to be carried predominantly up and to the left of the jet into a counter clockwise recirculation zone. Seed particles on the lower surface of the jet plume, shown in Figure 7.30, are also entrained into the jet and carried into a larger clockwise circulating zone which represents a gradual turn over of the fluidized bed material. It appears from these analyses that solids particles within this fluidized bed will be segregated into two zones: a CCW recirculation zone to the left and above the jet and a larger CW zone to the right of the jet representing a gradual turn over of the bed material. It is possible that solids particles along the wall of the reactor are becoming trapped in a recirculatory pattern. This increased residence time could lead to catalyst degradation in the commercial unit which in turn could further lead to reactor fouling by the action of coke build-up above the nozzle pipe.

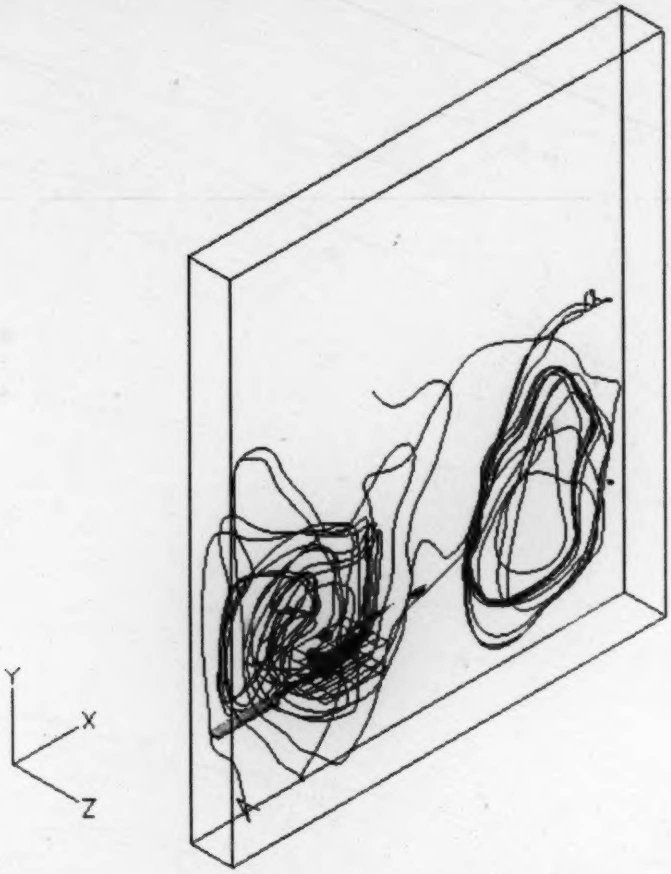

Figure 7.29 – Instantaneous solids flow patterns for seeding above the jet plume. Run BA02, t=2.0 s.

A set of predicted flow patterns was created over a time period to provide visualization of the transient predicted flow patterns within the fluidized bed. Figure 7.31 shows the predicted gas and solids particle tracking in the left and right columns respectively at time increments of 0.25 seconds. All of the seed particles were placed in a straight line at Z=0.05 m along the lower section of the fluidized bed. The gas particles were seeded on the distributor plate while the solids particles were placed slightly higher.

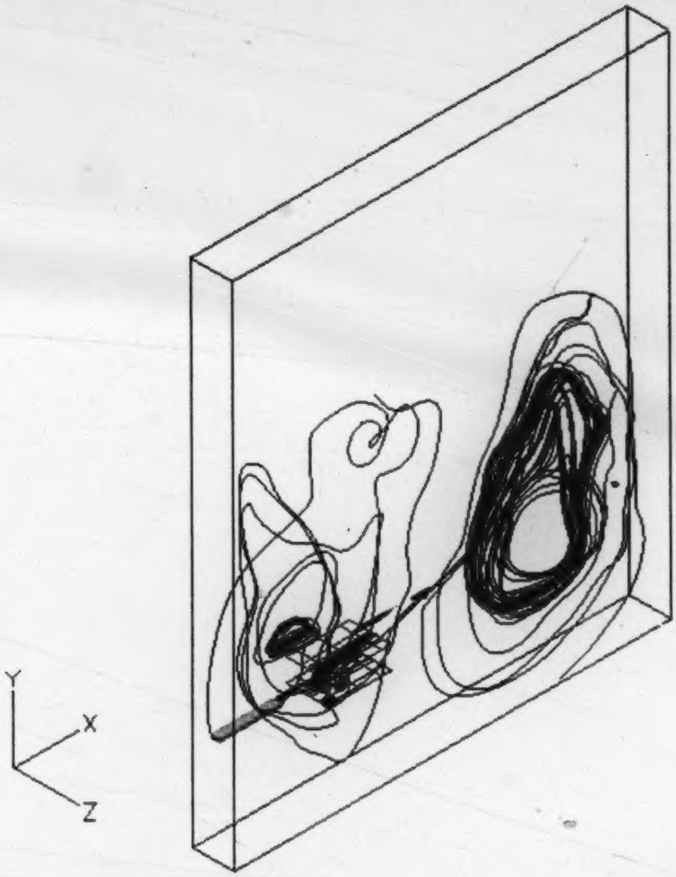

Figure 7.30 – Instantaneous solids flow patterns for seeding below the jet plume. Run BA02, t=2.0 s.

Each row of visualizations is for the same real time step. Start up conditions are evident for Figure 7.31 a at a time of 0.05 seconds. Most of the gas channels directly out of the fluidized bed and the solids move towards the jet plume region. After 0.5 seconds (Figure 7.31 c) two solids recirculation zones have formed and the gas flow behavior has become more chaotic. Fluidization gas appears to bypass the region above the jet plume and become caught in the recirculation zone in the bulk of the bed. Problems with loss of fluidization above the gas jet in two-dimensional simulations were discussed previously in section 7.1.1. Depth in the three dimensional simulation allows the fluidization gas to pass around the jet fluidizing the top section and can be observed for the gas flow for all predicted gas streamlines at times greater than 0.75 seconds. The prediction that the fluidization gas flow above the jet is affected in three dimensions suggests that there might be a slight loss of fluidization due to the presence of the jet in the bed. All simulation results for times greater than 0.5 seconds show that the two solids recirculation zones persist and become even more pronounced, see Figure 7.31e 1.0 seconds. Gas channeling up through the center of the bed is evident in Figure 7.31 g. Channeling will lead to poor gas-solid contacting and decrease the residence time of the gas phase resulting in decreased reactor performance and yield.

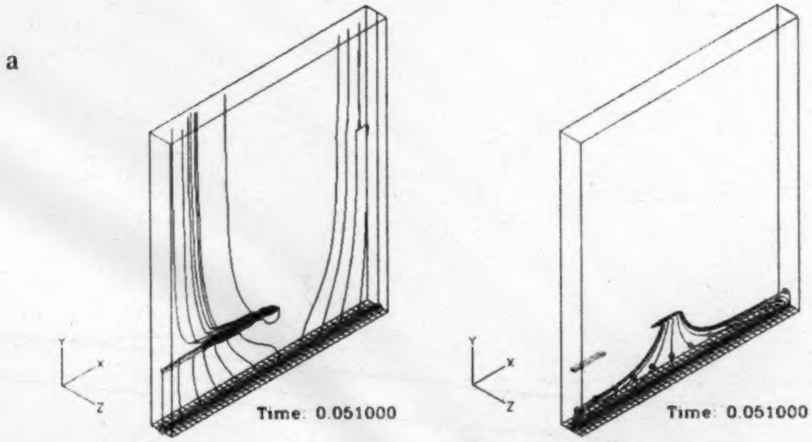

Figure 7.31– Predicted gas (left) and solids (right) instantaneous streamlines.

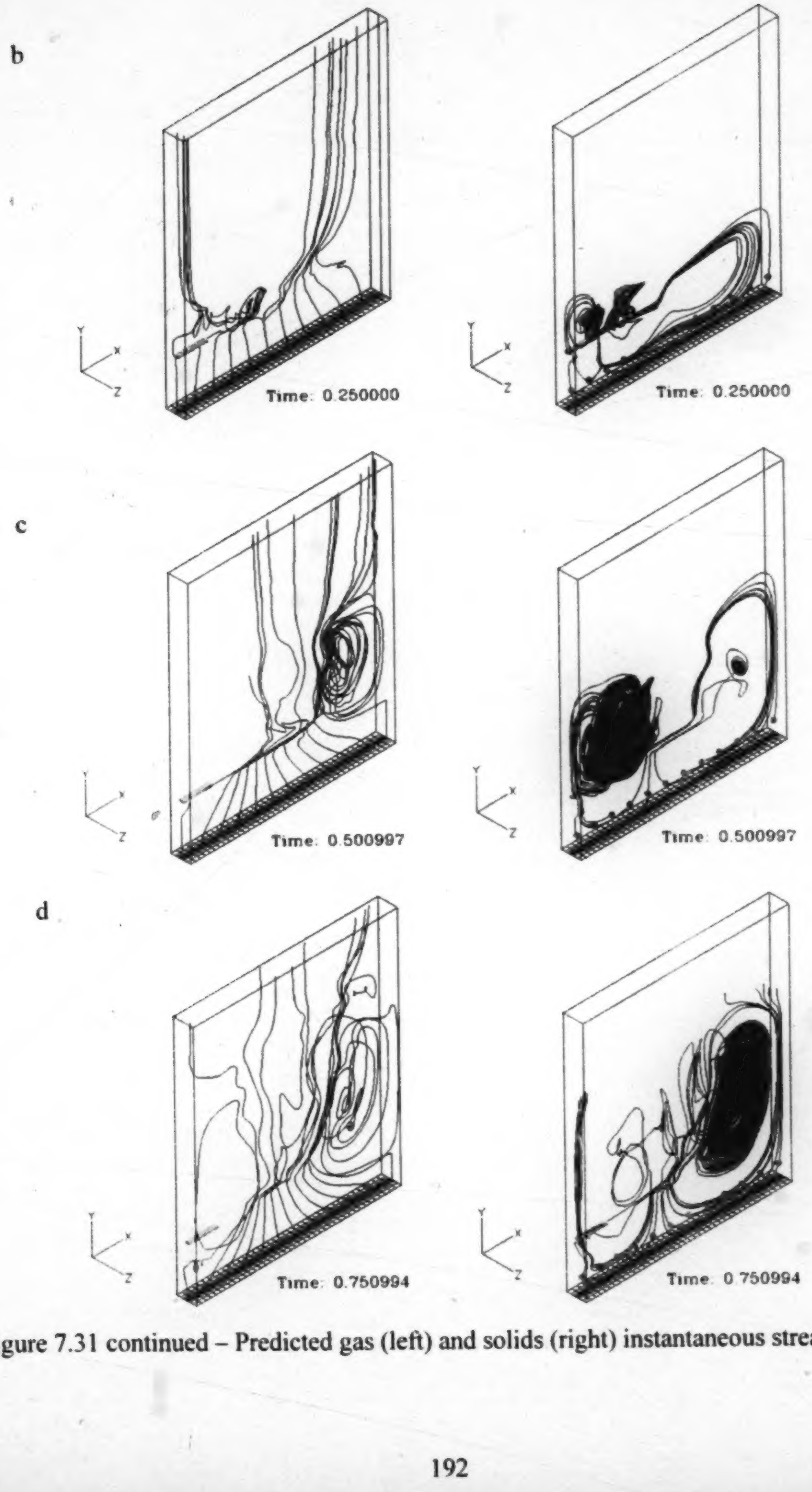
b
Y
X
Z
Time: 0.250000
Y
X
Z
Time: 0.250000
c
Y
X
Z
Time: 0.500997
Y
X
Z
Time: 0.500997
d
Y
X
Z
Time: 0.750994
Y
X
Z
Time: 0.750994

Figure 7.31 continued – Predicted gas (left) and solids (right) instantaneous streamlines.

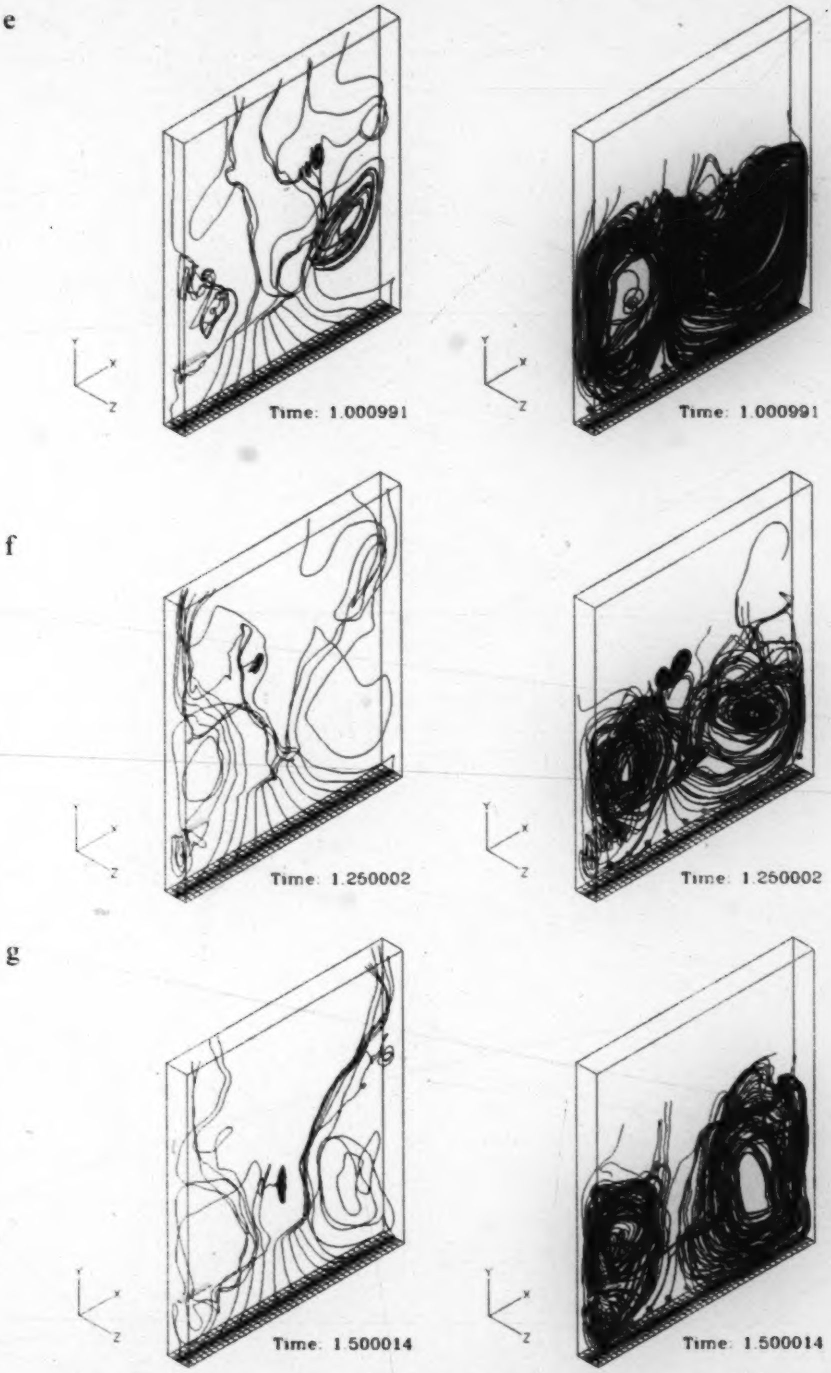

Figure 7.31 continued – Predicted gas (left) and solids (right) instantaneous streamlines.

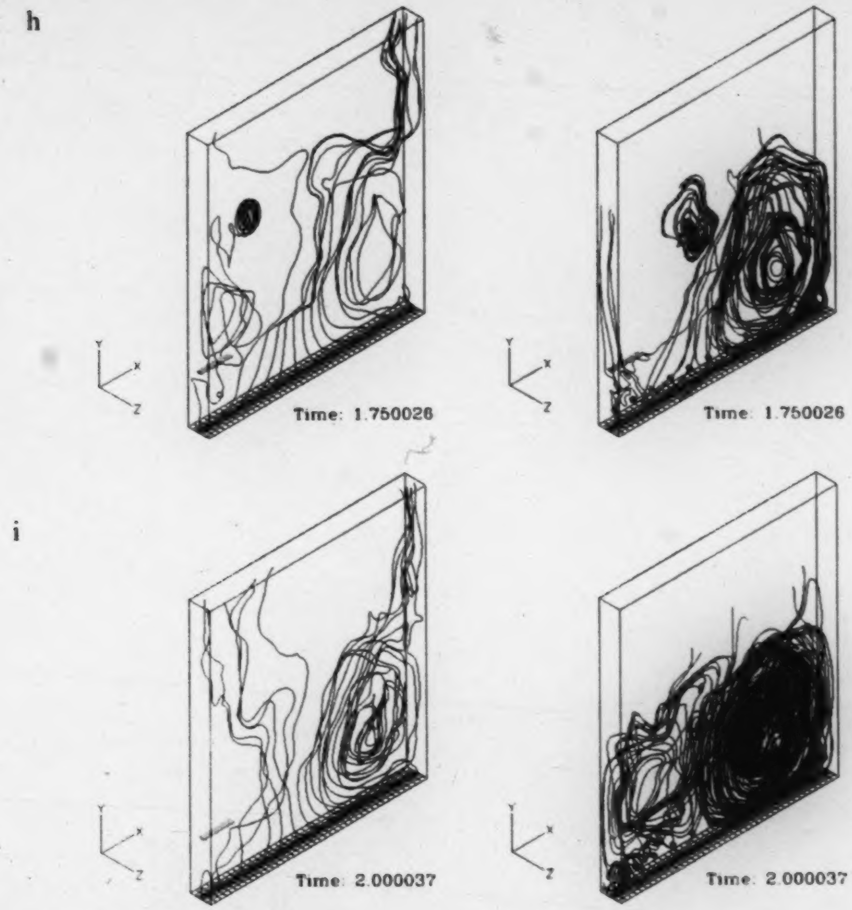

Figure 7.31 continued – Predicted gas (left) and solids (right) instantaneous streamlines.

7.2.6 Bubble Shapes

Bubbles were isolated based on a gas volume fraction contour of 0.8 and the solids velocity vector field was plotted through the central plane of the bubble. Four different flow scenarios were chosen to study bubble shapes:

i) startup conditions at minimum fluidization (the unsteady behavior) - simulation AB03;

ii) $<U_{mf}$ conditions where bubbles were formed below minimum fluidization after allowing enough time for a steady state flow field to be set up (approximately 1.5 seconds) - simulation CB01;

iii) $>U_{mf}$ conditions where bubbles were formed above minimum fluidization after allowing enough time for a steady state flow field to be set up - simulation FB02;

iv) $0U_{mf}$ jet discharge into the fluidized bed with no aeration assuming that the flow field had attained a steady state – simulation CB02.

Bubbles were selected above the jet plume region in the upper section of the bed almost directly above where the jet plume discharges.

Case i) *Bubbles at Start Up*: Run AB03 was chosen to study the bubble shape and solids velocity vector field around the bubble. Figure 7.32 shows gas volume fraction contours and an overlay of the solids vector field for a bubble present at simulation start up. Bubbles at start up were typically observed to be spherical cap shape with strong solids recirculation up through the bubble, sweeping down from the top and sides. This behavior is similar to that of fast bubbles where bubble rise velocity is greater than the fluidization velocity.

Case ii) *Bubbles in a bed with* $<U_{mf}$. Run CB01 was chosen to study bubble shape below minimum fluidization; results from this analysis are shown in Figure 7.33. In this case the bubbles were round in shape and solids were observed to flow through the bubbles with no recirculation back around to the base of the bubble. This behavior is

characteristic of slow bubbles in fluidized beds where the bubbles rise more slowly than the fluidization gas.

Case iii) *Bubbles in a bubbling fluidized bed.* Simulation FB02 was chosen to study bubbles at greater than minimum fluidization; results are shown in Figure 7.34. Above minimum fluidization most of the bubbles assumed an oblong shape. Solids flowed up and through the bubbles with some slight down flow around the edges of the bubbles. At these higher fluidization velocities more bubbles were observed to form than for minimum and lower than minimum fluidization. Many of the bubbles present in the lower part of the bed below the nozzle orifice height tended to coalesce in the upper part of the bed. This behavior seems to have been induced by the presence of the jet void. Similar behavior was observed with the experimental apparatus at the UofS. Bubbles formed below the jet tended to move towards the jet and amalgamate with the voids formed from the jet plume.

Case iv) *Bubbles in a packed bed* $0U_{mf}$. Simulation CB02 was chosen to study bubbles in the packed bed. With zero aeration very few bubbles were formed within the fluidized bed. The jet plume was still present and formed a large void into the bed but bubbles were not observed to pinch off regularly from the tip of the jet. Figure 7.35 shows a small void variation within the fluidized bed. The solids particles have a very strong horizontal velocity and are being swept to the right of the bed by the action of the gas jet. Bubble motion within the packed bed has little effect on the overall solids motion.

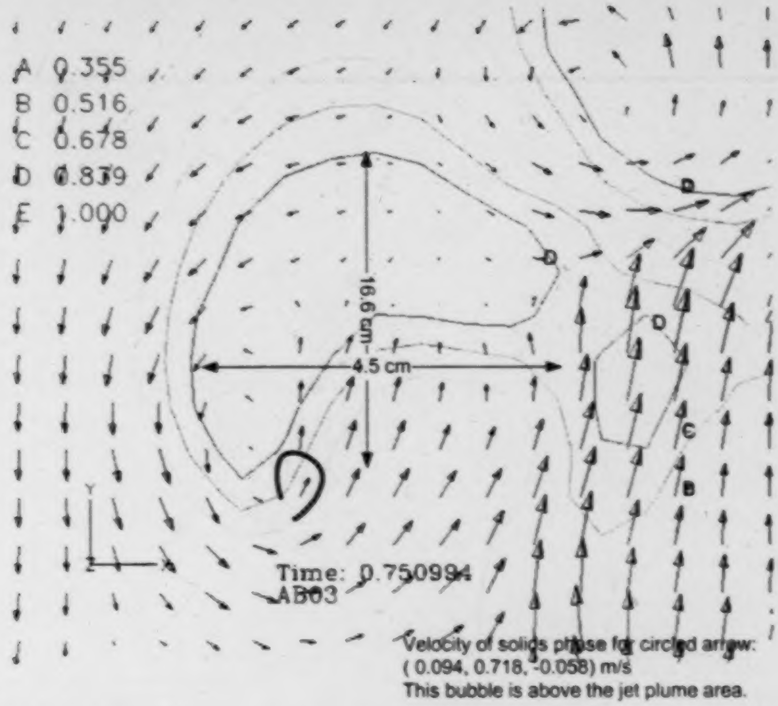

Velocity of solids phase for circled arrow:
(0.094, 0.718, -0.058) m/s
This bubble is above the jet plume area.

Figure 7.32 – Predicted bubble in a fluidized bed at start up.

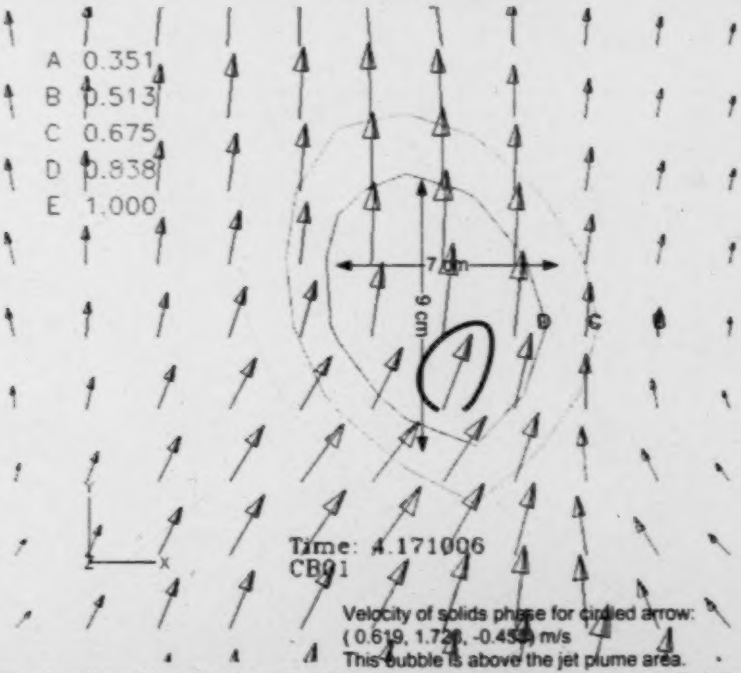

Velocity of solids phase for circled arrow:
(0.619, 1.72[illegible], -0.45[illegible]) m/s
This bubble is above the jet plume area.

Figure 7.33 – Predicted bubble in a fluidized bed at less than minimum fluidization.

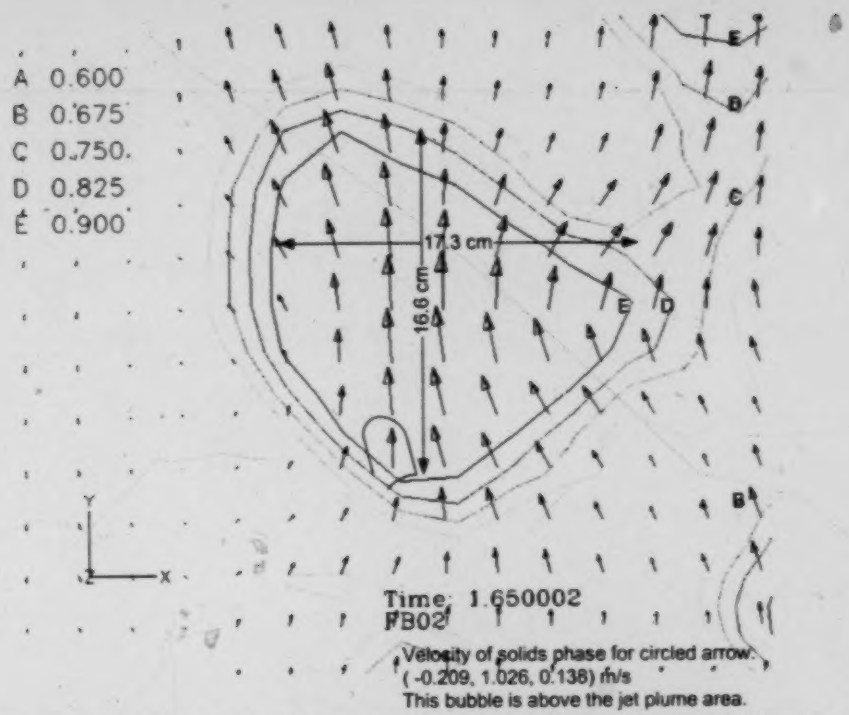

Velocity of solids phase for circled arrow:
(-0.209, 1.026, 0.138) m/s
This bubble is above the jet plume area.

Figure 7.34 – Predicted bubble in a fluidized bed at greater than minimum fluidization.

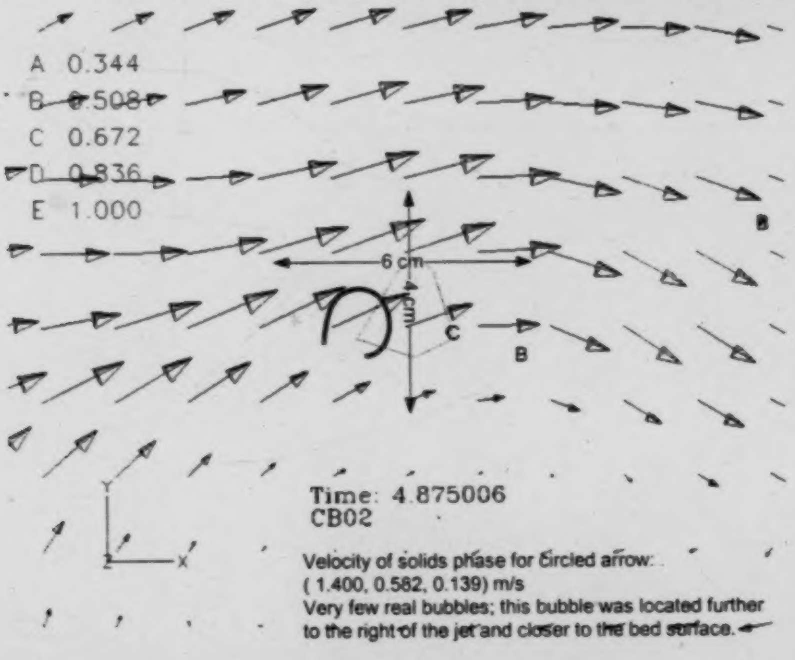

Velocity of solids phase for circled arrow:
(1.400, 0.582, 0.139) m/s
Very few real bubbles; this bubble was located further to the right of the jet and closer to the bed surface.

Figure 7.35 – Predicted bubble in a packed bed or zero fluidization.

7.2.7 Bubble Velocities

Quantitative comparison between different simulations based on the size and velocity of bubbles was conducted to determine any trends. Bubble dimensions were determined using the same technique outlined in the Chapter 6 on experimental data whereby the horizontal and vertical boundaries of the bubbles were recorded and a centroid calculated.

Bubble horizontal and vertical velocities in the Z=0.05 m XY plane were calculated based on the difference in bubble centroid between time steps. For these analyses the data was analyzed every 0.05 seconds and average bubble velocities were determined for each run listed in Table 7.5. Most of the data from this analysis suggests that the bubble rise velocities were of the order of 0.1 m/s with some data showing a negative upward velocity. This negative velocity was not observed in the experimental apparatus because all of the bubbles exit through the top of the bed and should have a net positive average vertical velocity. One possible explanation for this is that the use of data spaced every 0.05 seconds could lead to some bias with the results.

Horizontal velocities show more variation than the vertical velocity results and can be attributed to the deformation of bubbles as they progress up the bed. This deformation created difficulties when trying to determine the correct edge of the bubble in the simulation results and lead to errors in horizontal bubble velocities.

7.2.8 Time Averaged Data

Many researchers have presented time averaged data to ascertain the flow characteristics within fluidized beds. This approach might shed some light on certain regions where large scale flow patterns dominate. A set of comparison graphs are

Table 7.5

Average Bubble Rise Velocities from Simulations

Run	V velocity (m/s)	U Velocity (m/s)
FB01	0.300	0.030
FB02	0.039	0.045
FC01	0.026	0.258
FC02	-0.094	-0.136
GB01	0.471	-0.016
GB02	1.459	2.100
GB03	0.673	0.426
GC01	-0.291	-0.020
GC03	0.084	-0.015

included to compare the different time averaged volume fraction profiles for several different simulations. Figures 7.36 to 7.38 show time averaged results for runs below minimum fluidization. At conditions lower than minimum fluidization the bed acted like a packed medium and few bubbles were formed. In these cases the only region within the bed to be affected by the jet is that directly above the jet plume shown by the distinct maximum located between approximately X=0.2 to 0.3 m increasing with increased jet velocity. Beyond this region the bed tended to remain at a constant voidage of approximately ε_g=0.36. Bed surface tilt is present for all of the simulations under taken below minimum fluidization. It appears that the bed surface forms a mound to the right of where the jet plume exits out of the top surface. This is the so called "funnel behavior that was described in section 7.2.2.

With an increase in aeration to twice minimum fluidization the bulk bed voidage increased to approximately ε_g=0.45, see Figures 7.39 to 7.40. The void fractions around the jet are seen to increase in size and shift slightly right to between X=0.2 and 0.8 showing that the gas jet is penetrating more easily into the fluidized bed. Increased aeration resulted in increased bed voidage and a subsequent decrease in bulk bed density. A decrease in bed density reduces the local grid Reynolds number decreasing the local drag forces exerted on the gas phase thereby decreasing the momentum transfer from the jet to the fluidized bed resulting in an increase in jet penetration for similar jet momentum fluxes through the nozzle orifice. Further increase in aeration velocity to three times minimum fluidization, Figures 7.41 to 7.42 resulted in erratic voidage levels across the width of the bed. At this high aeration velocity the fluidized bed is operating in the bubbling regime bed and the formation of voids or bubbles from the distributor plate propagate up through the bed making the average gas volume fractions erratic. A time averaged analysis of volume fraction data across the bed is not entirely applicable to a bubbling bed regime. Instead point averages within the bed with respect to time should be used to give an indication of bubble frequency. From these data it is unclear whether the jet penetration decreases with increasing fluidization as reported by Chyang *et al.*(1997), see Figure 2.4.

Time averaged data for the Gxxx series of runs show unexpected behavior with increased jet velocity. Comparing Figures 7.43 and 7.44 suggests that the influence of the jet on the fluidized bed is more pronounced for the lower jet velocity of 150 m/s than for the simulations using a jet velocity of 300 m/s; the same trend is seen for three times minimum fluidization in Figures 7.45 to 7.46. This behavior is contrary to that observed from the previous comparison of time averaged data. Two possible factors may be contributing to these results. First the density and size of the solids particles used in these simulations is lower than that for the previous set of simulations. There is a possibility that the smaller particle size and density influences the flow behavior within the fluidized bed and/or affects the jet behavior. Referring to the jet phase diagram Figure 7.22 shows that simulations GB01, GB02 and GB03 lie very close to the border between transition and stable jetting. It is possible that the small nozzle orifice size with the possible overlap of flow regimes produced with this set of operating conditions is not properly resolved with the numerical simulations. Further investigation of these problems are required to draw significant conclusions.

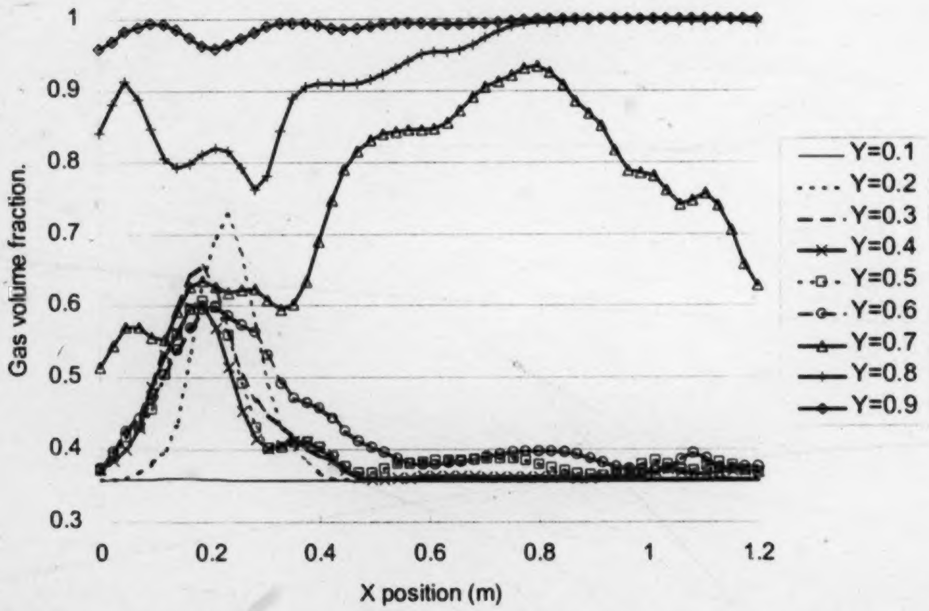

Figure 7.36 – Predicted time averaged gas volume fraction data for run CA01 across the width of the bed. *0.5*U_{mf} U_{jet}*=150m/s*.

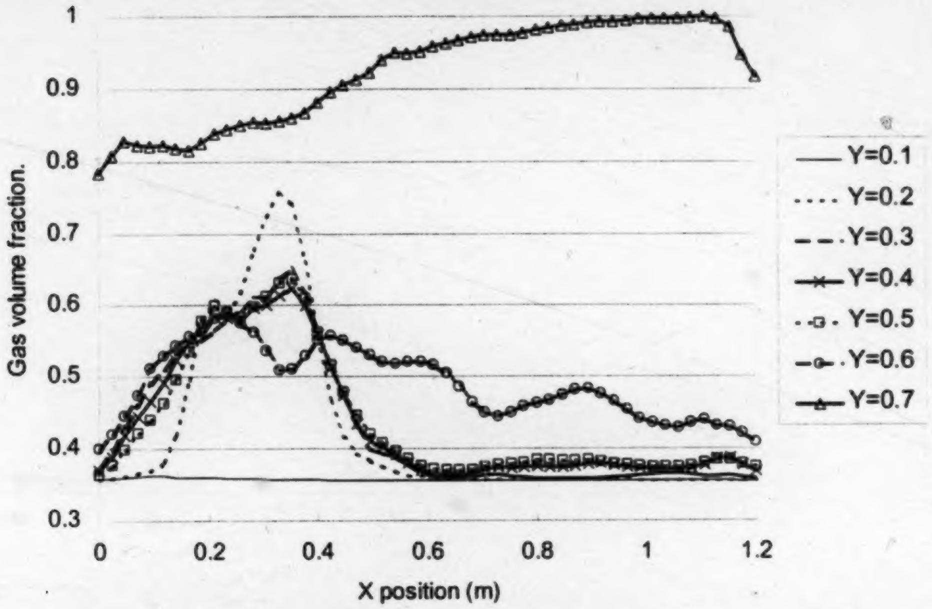

Figure 7.37 - Predicted time averaged gas volume fraction data for run CB01 across the width of the bed. *0.5*U_{mf} U_{jet}*=250m/s.*

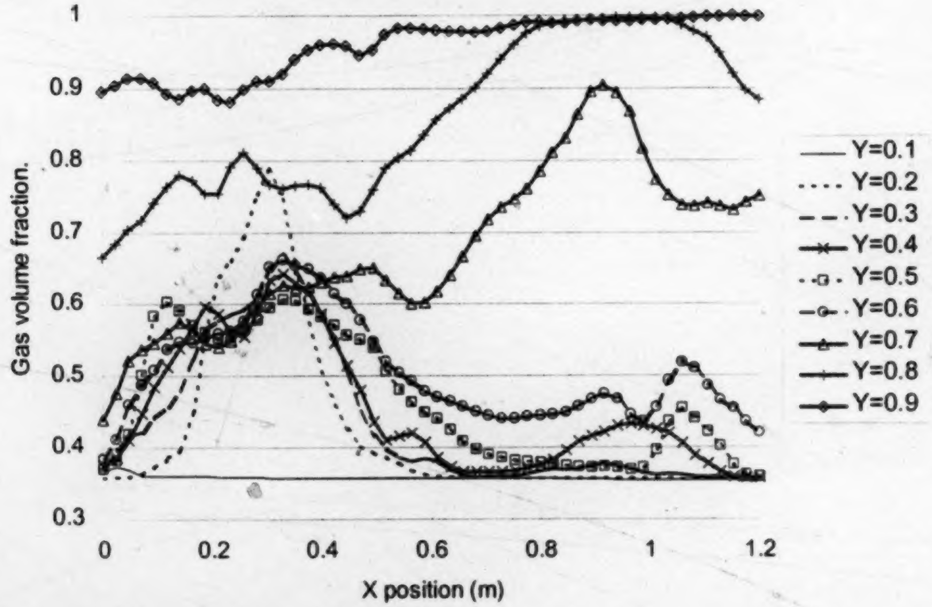

Figure 7.38 - Predicted time averaged gas volume fraction data for run CC01 across the width of the bed. U_{mf}*=0.5*U_{mf} U_{jet}*=300m/s.*

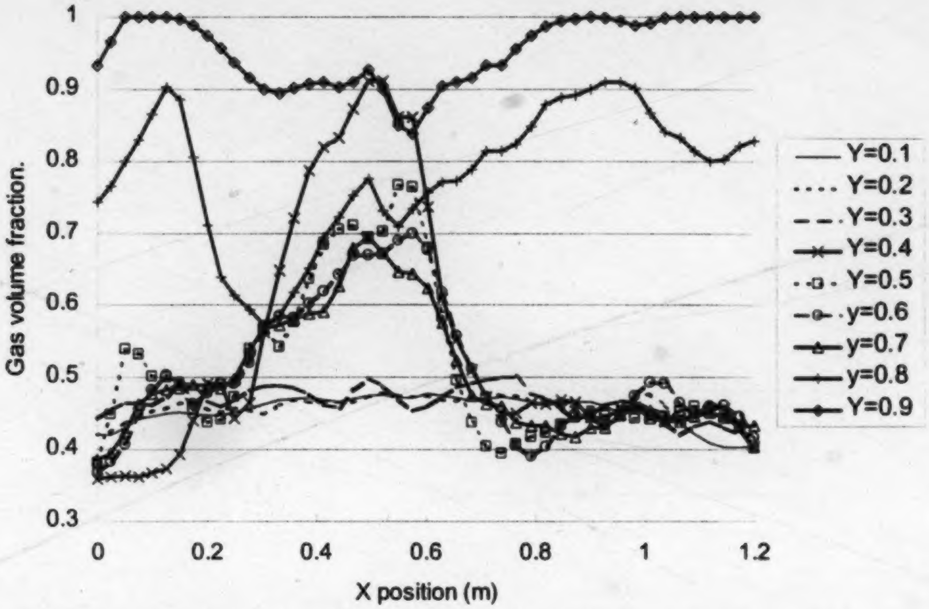

Figure 7.39 – Predicted time averaged gas volume fraction data for run FB01 across the width of the bed. $2U_{mf}$ $U_{jet}=250m/s$.

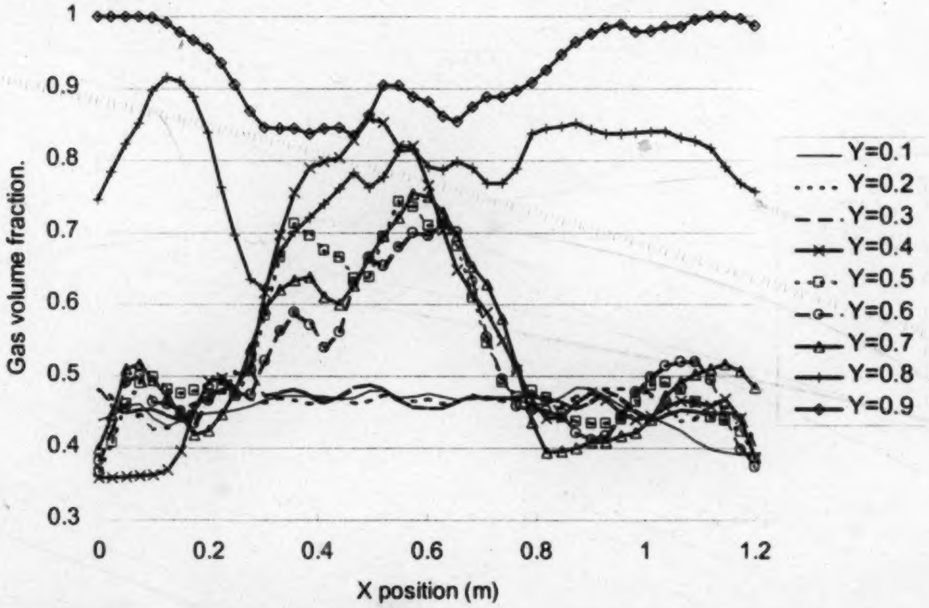

Figure 7.40 – Predicted time averaged gas volume fraction data for run FC01 across the width of the bed. $2U_{mf}$ $U_{jet}=300m/s$.

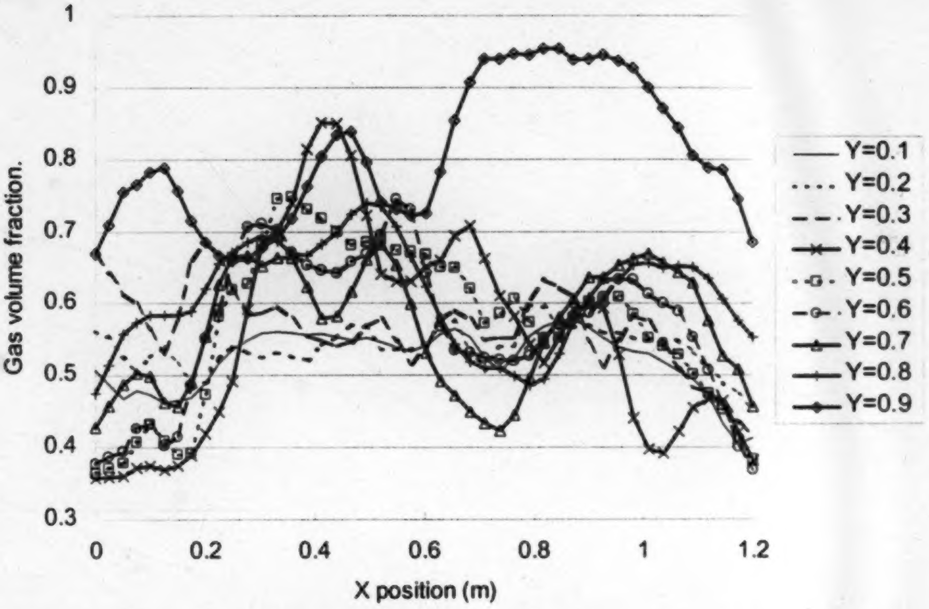

Figure 7.41 – Predicted time averaged gas volume fraction data for run FB02 across the width of the bed. *$3U_{mf}$ U_{jet}=250m/s.*

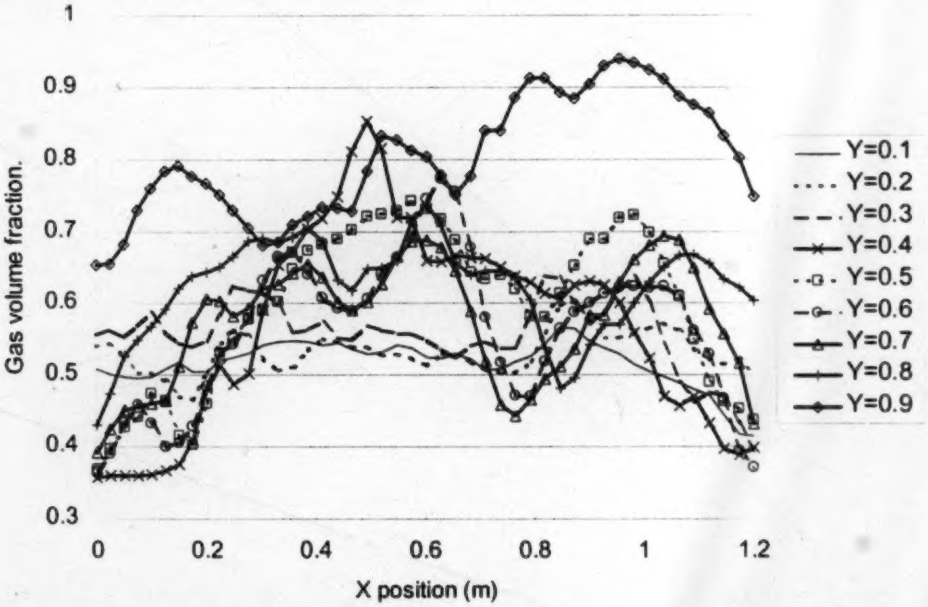

Figure 7.42 – Predicted time averaged gas volume fraction data for run FC02 across the width of the bed. *$3U_{mf}$ U_{jet}=300m/s.*

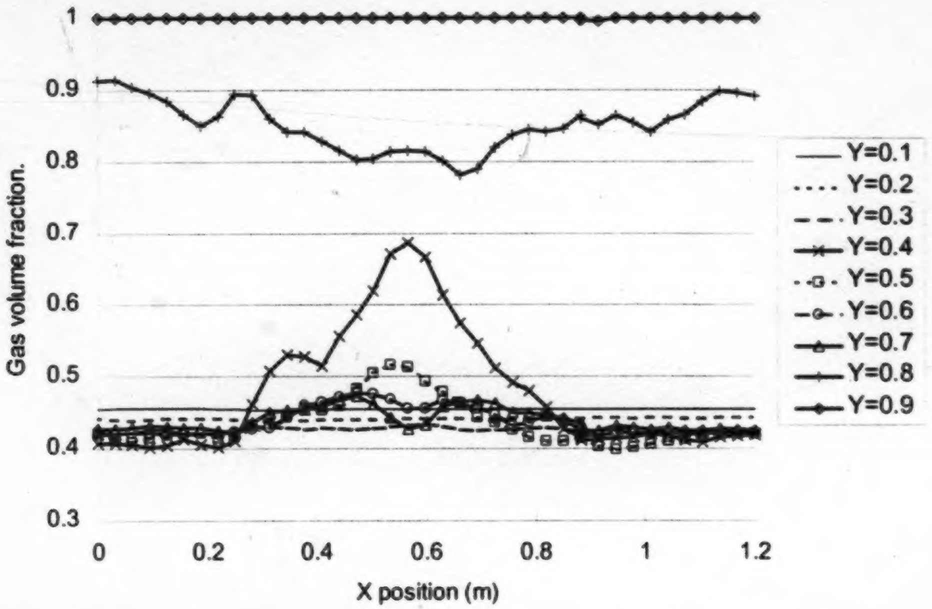

Figure 7.43 – Predicted time averaged gas volume fraction data for run GB01 across the width of the bed. $2U_{mf}$ $U_{jet}=150m/s$.

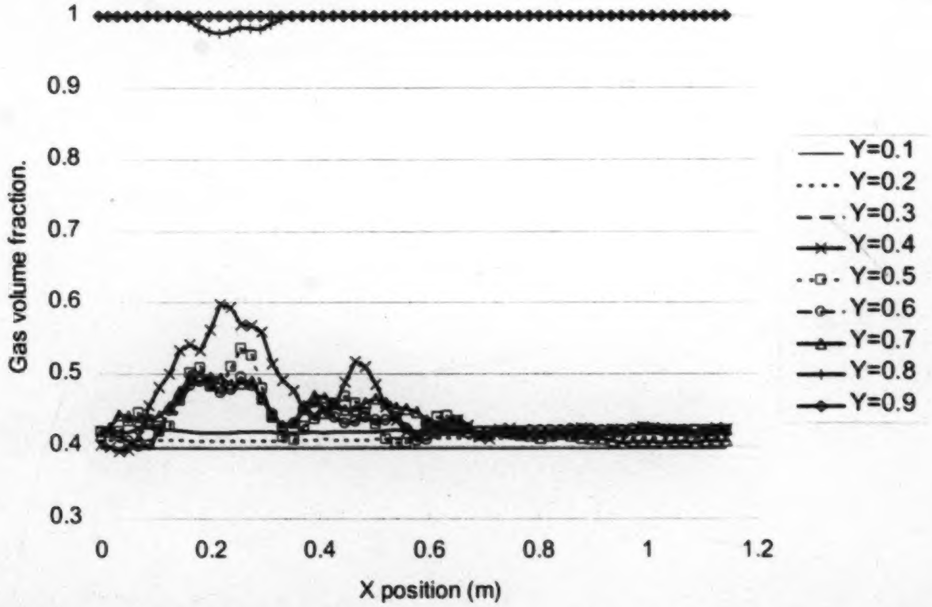

Figure 7.44 – Predicted time averaged gas volume fraction data for run GB03 across the width of the bed. $2U_{mf}$ $U_{jet}=300m/s$.

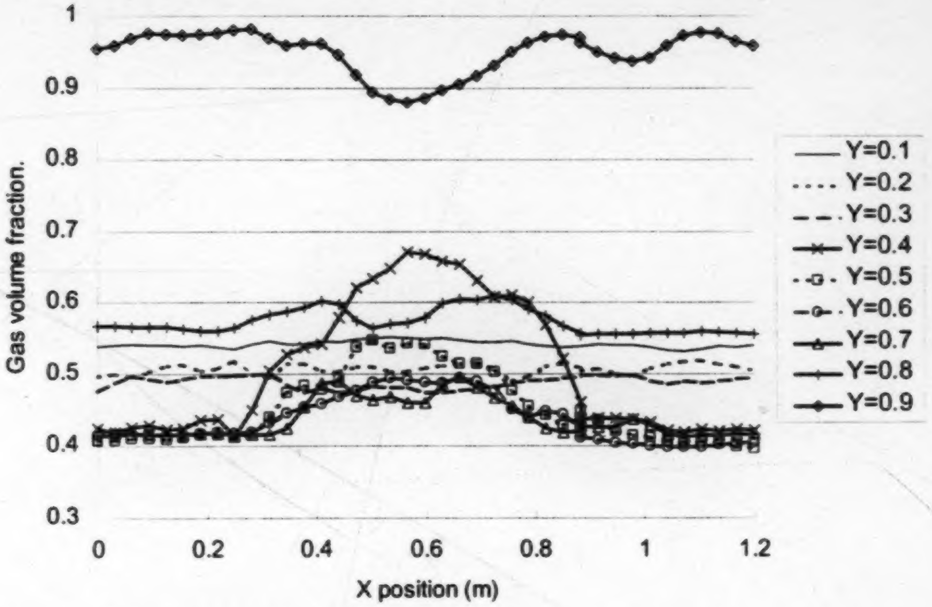

Figure 7.45 – Predicted time averaged gas volume fraction data for run GC01 across the width of the bed. *3U_{mf} U_{jet}=150m/s.*

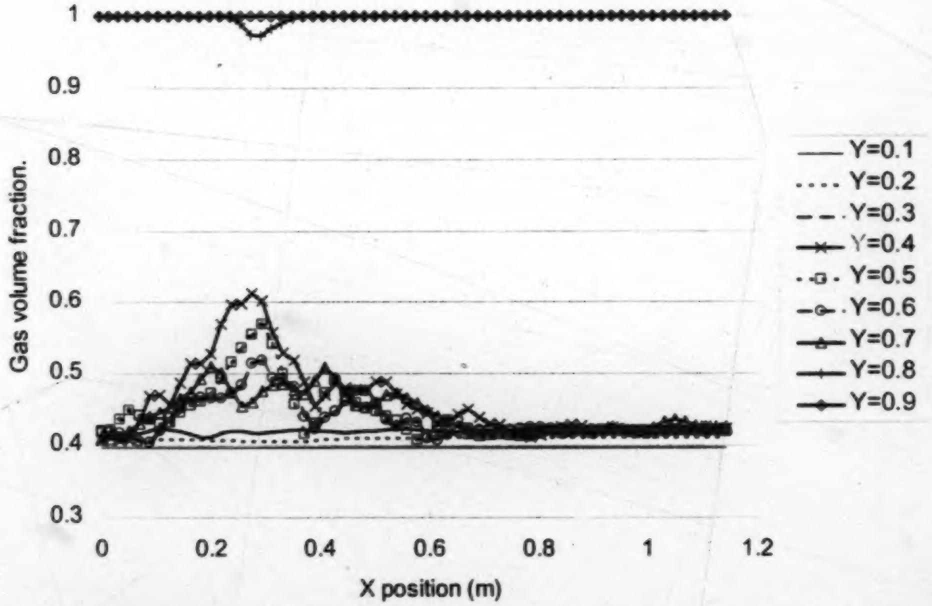

Figure 7.46 – Predicted time averaged gas volume fraction data for run GC03 across the width of the bed. *3U_{mf} U_{jet}=300m/s.*

7.2.9 Summary of Physical Predictions

Results from the physical predictions have shown that the flow within the fluidized bed is extremely complicated and poses certain difficulties with modeling and interpretation of results. Overall flow patterns within the fluidized bed are characterized by two recirculating zones either side of the region through which the jet plume escapes upwards out of the surface of the fluidized bed. A smaller, elongated counter clockwise rotating recirculation zone is present above and to the left of the nozzle pipe. This recirculation zone has been shown to entrain solids from the top surface of the jet with the possibility of a dead zone within which entrained solids particles are constantly recirculated. This dead zone could lead to the formation of buildup on top surface of the nozzle pipe resulting in coking problems within the commercial reactor unit. A large clockwise solids recirculation zone was predicted in the bulk of the bed to the right of the nozzle. Solids in this zone have been predicted to be entrained from the lower surface of the gas jet. When operating in the bubbling fluidized bed regime the gas to solids contacting should be fairly good within the bulk of the bed due to the slow bed turnover and formation of bubbles within the bulk of the bed.

Fluidized bed behavior has been well predicted for different fluidization velocities with the CFX 4.2 solver. Aeration rates below minimum fluidization resulted in the formation of slow bubbles showing solids carrying through the bubble. Aeration rates at zero fluidization, or in the packed bed regime, proved difficult to achieve good numerical convergence. However, void fractions for this operating condition collapsed to the solids packing fraction and very few bubbles were predicted to form within the bulk of the bed. This behavior appears to agree with expected physical behavior in this flow regime.

Simulations above minimum fluidization resulted in the bed operating as a bubbling bed and predicted the formation of bubbles off of the distributor plate. This behavior is in agreement with experimental observations. The transition from minimum fluidization to higher fluidization rates showed interesting plug flow like behavior and the formation of bubbles from flat gas volume fraction iso-surfaces. Bubbles within this flow regime exhibited slow bubble behavior. Bed surface heights behaved in accordance with expected experimental observations when the fluidization velocity was decreased. Decreased fluidization velocity caused a decrease in bed height; however, the ejection of bubbles out of the surface of the bed caused problems when trying to evaluate an average bed height.

Jet penetration depths agreed well with the literature correlation of Merry (1971); however, the simulations in the Gxxx series consistently underpredicted penetrations. Further problems occurred when trying to relate time averaged data for the Gxxx series to previous runs with larger orifice sizes. Continued efforts need to be expended to properly classify the flow regime within the Gxxx series of runs to get properly converged and reliable data.

Chapter 8

Conclusions and Recommendations

This chapter summarizes the findings from the simulation studies that were conducted using CFX 4.2 from AEA Technologies. The two fluid models available in CFX 4.2 appear to produce predictions which are in good qualitative agreement with gross bed properties such as jet penetration and bubble formation. More work is required to build confidence in the predictive capabilities of the much smaller scales within the fluidized beds.

8.1 Numerical Considerations

The two fluid model used in CFX 4.2 to predict the behavior of a multiphase gas/solids flow within a fluidized bed produced bubble and jet behavior qualitatively similar to that observed in the companion two dimensional fluidized bed at the University of Saskatchewan. Through extensive validation tests the following conclusions and recommendations are made in regard to using CFX 4.2 to model multiphase flows:

- Superbee discretization should be used with the solver so that bubble boundaries become distinct;
- A grid size of at least 30,000 control volumes should be used for the 1.2 x 1.2 x 0.1 m rectangular reactor geometry;
- Under relaxation parameters should be set to 0.6 for all momentum equations;
- The nozzle inlet boundary condition must be specified to be at least 2 x 2 control volumes in size to avoid interpolation problems associated with the velocity fields;
- Control volume sizes must be chosen so that the continuum modeling assumption is still statistically valid;
- Little difference in produced results was observed for Hydrodynamic model A or B. Use of either of these model for these simulations is acceptable;
- Further work needs to be done to investigate the effect of the solids pressure functions. Results for two different functions resulted in significant differences in bubble shape and formation within the fluidized bed. It is felt that the solids pressure function given by Benyahia *et al.* (1997) produces bubbles which are more realistic than those predicted with the function of Bouillard *et al.* (1989).

8.2 Physical Predictions

Qualitatively the predicted results agreed quite well with literature and experimental observations. Jet penetration depths agreed well with the correlation of Merry (1971); however, for much smaller nozzle diameters these predictions were poor. Continued work needs to address the effect of very small nozzle inlet diameters on the predicted penetration depth of the jet.

Two recirculation zones were predicted to form within the fluidized bed for all jet velocities at fluidization velocities greater than zero. A large clockwise rotating circulation zone was present in the bulk of the bed and a smaller counter clockwise recirculation zone was present above and to the left of the nozzle inlet pipe. Virtual seed particles have shown that solids above the jet plume within the fluidized bed were predicted to become "entrapped" in the counter clockwise recirculation zone above and to the left of the nozzle pipe. Those particles entrained into the jet from below tended to be swept into the larger clockwise recirculation zone in the bulk of the bed. The simulations tended to over predict this recirculatory behavior in comparison with observations from the experimental apparatus.

8.3 Recommendations

Computational fluid dynamic simulations of a two phase gas/solid fluidized bed are possible with the two fluid models available in CFX 4.2. The following are recommendations and future directions that should be pursued when implementing these models:

- First order discretization schemes must not be used for predictions. Higher order bounded schemes should be implemented. For these studies the Superbee TVD scheme was found to be most applicable. It is recommended that studies using the UNO and SONIC schemes be carried out to investigate the use of a completely second order discretization scheme;
- For larger simulations involving several feed nozzles in a more complicated geometry it is recommended that a nonstructured mesh be used. This facility is not currently available in CFX 4.2; however, AEA technology should be implementing this within the next year. Nonstructured meshing will allow greater flexibility for grid refinement close to the nozzle inlet boundary;
- Multiphase simulations produce vast quantities of data that must be interpreted. Visualization of this data is a problem and can be misleading. It is recommended that complete flow field data be saved every 0.05 seconds for analysis and rendering as animated movies. These movies provide a qualitative means by which the quality and realism of the simulations can be judged in addition to the question of numerical convergence. Saving point data from simulations can be very valuable to study time transients; however, if the simulation is predicting flow fields which look unreasonable, then there might be little value in these point measurements. Experimentalists are fortunate in that mere visual observation of an apparatus can be enough to determine whether it is functioning reasonably. This same approach should be applied to the computational results;
- There is a need for more thorough observations from experimental studies. Simulation results are only as good as the physical models, boundary and initial

conditions provided to the solver. It is recommended that all numerical simulations be validated against some experimental data.

REFERENCES

Abramovich, G.N. (1963) The Theory of Turbulent Jets. *MIT Press*, Massachusetts Institute of Technology. Cambridge, Massachusetts.

Alder, B.J., and Wainright, T.E. (1960) *J. Chem. Phys.*, **33**, 1439-1451.

Anderson, T.B., and Jackson, R. (1967) A Fluid Mechanical Description of Fluidized Beds. *I&EC Fund.*, **6**, 4, 527-539.

Andrews, M.J., and O'Rourke, P.J. (1996) The Multiphase Particle-In-Cell (MP-PIC) Method for Dense Particulate Flows. *Int. J. Multiphase Flow*, **22**, 2, 379-402.

Arastoopour, H., Lin, S.-C., and Weil, S.A. (1982) Analysis of Vertical Pneumatic Conveying of Solids Using Multiphase Flow Models. *AIChE J.*, **28**, 3, 467-473.

Arastoopour, H., and Gidaspow, D. (1979) Analysis of IGT Pneumatic Conveying Data and Fast Fluidization Using a Thermodynamic Model. *Powder Technology*, **22**, 77-87.

Aris, R. (1962) Vectors, Tensors and the Basic Equations of Fluid Mechanics. Dover Publications Inc., New York.

Bader, R., Findlay, J., and Knowlton, T.M. (1988) Gas/Solid Flow Patterns in a 30.5cm Diameter Circulating Fluidized Bed. *2nd Int. Circulating Fluidized Bed Conf.*, March 14-18, Compeigne, France.

Basov, V.A., Markhevka, V.I., Melik-Akhnazarov, T.Kh., and Orochko, D.I. (1969). Investigation of the Structure of a Non-uniform Fluidized Bed. *Int. Chem. Eng.*, **9**, 263.

Basset, A.B. (1888). *A Treatise on Hydrodynamics*, **2**. Cambridge: Deighton, Bell; (1961) New York: Dover.

Behie, L.A., Bergougnou, M.A., and Baker, C.G.J. (1975), Heat Transfer From a Grid Jet in a Large Fluidized Bed. *The Can. J. of Chem. Engr.*, **53**, 25-30.

Behie, L.A., and Kehoe, P. (1973). Grid Region in a Fluidized Bed Reactor. *AIChE J.*, **19**, 5, 1070-1072.

Behie, L.A., Bergougnou, M.A., Baker, C.G.J., and Bulani, W. (1970) Jet Momentum Dissipation at a Grid of a Large Gas Fluidized Bed. *The Can. J. of Chem. Eng.*, **48**, 158-161.

Benyahia, S., Arastoopour, H., and Knowlton, T. (1997) Numerical Analysis of Two-Dimensional Transient Gas-Solid Flow in a Pneumatic Conveying Line and in a Fluidized Bed with a Central Jet. *1997 ASME Fluids Engineering Division Summer Meeting FEDSM'97* June 22-26, 1997.

Berruti, F., Chaouki, J., Godfroy, L., Pugsley, T.S., and Patience, G.S. (1995) Hydrodynamics of Circulating Fluidized Bed Risers: A Review. *The Can. J. of Chem. Engr.*, **73**, 579-602.

Bird, R.B., Stewart, W.E., and Lightfoot, E.N. (1960) Transport Phenomena. John Wiley and Sons Inc.

Bouillard, J.X., Gidaspow, D., and Lyczkowski, R.W. (1991) Hydrodynamics of Fluidization: Fast-Bubble Simulation in a Two-Dimensional Fluidized Bed. *Powder Technology*, **66**, 107-118.

Bouillard, J.X., Lyczkowski, R.W., and Gidaspow, D. (1989) Porosity Distributions in a Fluidized Bed with an Obstacle. *AIChE J.*, **35**, 6, 908-922.

Capes, C., and Nakamura, K. (1988) Vertical Pneumatic Conveying: An Experimental Study with Particles in the Intermediate and Turbulent Flow Regimes. *The Can. J. of Chem. Engr.*, **51**, 31.

Carnahan, N.F., and Starling, K.E.(1969). *J. Chem. Phys.*, **51**. 635-636.

CFX 4.2 Solver Manual. AEA Technology, UK.

Chen, L., and Weinstein, H. (1997) Temperature Distribution Around Heated Horizontal Jet in Fluidized Bed. *AIChE J.*, **43**, 2373-2375.

Chen, L., and Weinstein, H. (1993) Shape and Extent of the Void Formed by a Horizontal Jet in a Fluidized Bed. *AIChE J.*, **39**, 12, 1901-1909.

Chyang, C.S., Chang, C.H., and Chang, J.H. (1997). Gas Discharge Modes at a Single Horizontal Nozzle in a Two Dimensional Fluidized Bed. *Powder Technology*. **90**, 71-77.

Clift, R. (1986). Hydrodynamics of Bubbling Fluidized Beds. In *Gas Fluidization Technology*. Ed. D. Geldart. New York: John Wiley & Sons.

Clift, R., and Grace, J.R. (1985). Continuous Bubbling an Slugging. In *Fluidization*, 2nd ed. Ed. Davidson, Clift and Harrison. London: Academic Press.

Crowe, C., Sommerfield, M., and Tsuji, Y. (1998) Multiphase Flows with Droplets and Particles. CRC Press LLC, 2000 Corporate Blvd., N.W., Boca Raton, Florida.

Davidson, J.F., and Harrison, D. (1963) Fluidized Particles. Cambridge, UK: Cambridge University Press.

Davidson, J.F. (1961a) Symposium on Fluidization - Discussion. *Trans. Inst. Chem. Eng.*, **39**, 230-232.

Davidson, J.F. (1961b) *Trans. Inst. Chem. Eng.*, **39**, 230.

Ding, J., and Gidaspow, D. (1990) A Bubbling Fluidization Model Using Kinetic Theory of Granular Flow. *AIChE J.*, **36**, 4, 523-538.

Eames, I., and Duursma, G. (1997) Displacement of Horizontal Layers by Bubbles Injected into Fluidized Beds. *Chem. Eng. Sci.*, **56**, 16, 2697-2705.

El-Kaissy, M.M. and Homsy, G.M. (1976). Instability Waves and the Origin of Bubbles in Fluidized Beds. *Int. J. Multiphase Flow.* **2**, 379-395.

Ettehadieh, B., Gidaspow, D. and Lyczkoski, R.W. (1984) Hydrodynamics of Fluidization in a Semicircular Bed with a Jet. *AIChE J.*, **30**, 4, 529-536.

Fan, L.-S., and Zhu, C. (1998) Principles of Gas-Solid Flows. *Cambridge University Press*. Cambridge, UK.

Fan, L.-S., and Tsuchiya, K. (1990). Bubble Wake Dynamics in Liquids and Liquid-Solid Suspensions. Boston: Butterworths.

Fanucci, J.B., Ness, N., and Yen, R.-H. (1979) On the Formation of Bubbles in Gas-Particulate Fluidized Beds. *J. Fluid Mech.*, **94**, part 2, 353-367.

FIELDView Manual (1999), Intelligent Light Visualization Solutions, 1290 Wall Street West, Third Floor, Lyndhurst, NJ 07071.

Filla, M., Massimilla, L., and Vaccaro, S. (1983) Gas Jets in Fluidized Beds and Spouts: A Comparison of Experimental Behavior and Models. *The Can. J. of Chem. Engr.* **61**, 370-376.

Foscolo, P.U., and Gibilaro, L.G. (1984). A Fully Predictive Criterion for the Transition between Particulate and Aggregate Fluidization. *Chem. Eng. Sci.* **39**, 1667-1675.

Gabor, J.D. (1972) On the Mechanics of Fluidized Particle Movement. *Chem. Eng. J.*, **4**, 118-126.

Gajdos, L., and Bierl, T. (1978) Studies in Support of Recirculating Bed Reactors for the Processing of Coal. Topical rept. for U.S. Dept. of Energy, Carnegie-Mellon Univ., Contract No. EX-76-c-01-2449.

Garg, S.K., and Pritchett, J.W. (1975). Dynamics of Gas-Fluidized Beds. *J. Appl. Phys.* **46**, 4493-4500.

Geldart, D. (1973) Types of Gas Fluidization. *Powder Technology*, **7**, 285-292.

Gidaspow, D. (1994). Multiphase Flow and Fluidization. San Diego, California. Academic Press.

Gidaspow, D., Tsuo, Y.P., and Luo, K.M. (1989) Computed and Experimental Cluster Formation and Velocity Profiles in Circulating Fluidized Beds. *Fluidization IV*, Int. Fluidization Conf., Banff, Alberta, Canada, May.

Gidaspow, D. (1986) Hydrodynamics of Fluidization and Heat Transfer: Supercomputer Modeling. *Appl. Mech. Rev.*, **39**, 1, 1-23.

Gidaspow, D., Lin, C., and Seo, Y.C. (1983a). Fluidization in Two-Dimensional Beds with a Jet. 1. Experimental Porosity Distributions. *Ind. Eng. Chem. Fundam.*, **22**, 187-193.

Gidaspow, D., and Ettehadieh, B. (1983b) Fluidization in Two-Dimensional Beds with a Jet. 2. Hydrodynamic Modeling. *Ind. Eng. Chem. Fundam.*, **22**, 193-201.

Gidaspow, D., and Solbrig, C.W. (1976) Transient Two Phase Flow Models in Energy Production. State of the Art Paper presented at the AIChE 81st National Meeting, 11-14 April 1976.

Grace, J.R., Avidan, A.A., and Knowlton, T.M. (1997). Circulating Fluidized Beds. London, UK: Blackie Academic and Professional.

Guedon, M.O., Baron, M.O.G., Briens, C.L., and Knowlton, T.M. (1994). Intermittent Injection of Prepolymer in a Pressurized Fluidized Bed. *Powder Technology*, **78**, 25-32.

Harris, S.E., and Crighton, D.G. (1994) Solitons, Solitary Waves and Voidage Disturbances in Gas-Fluidized Beds. *J. Fluid Mech.*, **266**, 243-276.

Hartge, E., Li, Y., and Werther, J. (1986) Analysis of the Local Structure of the Two-Phase Flow in a Fast Fluidized Bed. *Circulating Fluidized Bed Technology*, ed. P. Basu, Pergamon, Oxford.

Hong, R., Li, H., Li, H,. and Wang, Y. (1997) Studies on the Inclined Jet Penetration Length in a Gas-Solid Fluidized Bed. *Powder Technology*. **92**, 202-212.

Hoomans, B.P.B., Kuipers, J.A.M., Briels., W.J., and Van Swaaij, W.P.M. (1996) Discrete Particle Simulation of Bubble and Slug Formation in a Two-Dimensional Gas-Fluidized Bed: A Hard Sphere Approach. *Chem. Eng. Sci.*, **51**, 99-118.

Hrenya, C.M. and Sinclair, J.L. (1997) *AIChE J.*, **43**, 853-869.

Jackson, R. (1963). The Mechanics of Fluidized Beds. *Trans. Inst. Chem. Eng.* **41**, 13-38.

Kozanoglu, B., and Levy, E.K. (1991). Transient Mixing of Homogeneous Solids in a

Bubbling Fluidized Bed. *AIChE Symp. Ser.*, **87** (281), 58.

Krishna, R. (1993). Analogies in Multiphase Reactor Hydrodynamics. In *Encyclopedia of Fluid Mechanics*. Supplement 2. *Advances in Multiphase Flow*. Ed. N.P. Chereminisoff. Houston: Gulf Publishing.

Kuipers, J.A.M., Van Duin, K.J., Van Beckum, F.P.H. and Van Swaaij, W.P.M. (1992) A Numerical Model of Gas-Fluidized Beds. *Chem. Eng. Sci.*, **47**, 8, 1913-1924.

Kunii, D., and Levenspiel, O. (1991). Fluidization Engineering, 2nd ed., Butterworth-Heinemann, Boston.

Littman, H., and Homolka, G.A.J. (1973) The Pressure Field Around a Two-Dimensional Gas Bubble in a Fluidized Bed. *Chem. Eng. Sci.*, **28**, 2231-2243.

Lo, S.M. (1989) *Mathematical Basis of a Multi-Phase Flow Model*. United Kingdom Atomic Energy Authority. Report #AERE-R13432.

Lummi, A.P., and Baskakov, A.P. (1967) *Khim. Prom.*, **43**, 7, 522.

Lun, C.K.K, and Savage, S.B. (1986). *Acta Mechanica*, **63**, 15-44.

Lun, C.K.K., Savage, S.B., Jeffrey, D.J., and Chepurniy, D. (1984) Kinetic Theories for Granular Flow: Inelastic Particles in Couette Flow and Slightly Inelastic Particles. *J. Fluid Mech.*, **140**, 223-256.

Lyczkowski, R.W., Gamwo, I.K., Dobran, F., Ai, Y.H., Chao, B.T., Chen, M.M., and Gidaspow, D. (1993) Validation of Computed Solids Hydrodynamics and Pressure Oscillations in a Bubbling Atmospheric Fluidized Bed. *Powder Technology*, **76**, 65-77.

Lyczkowski, R.W., Gidaspow, D., and Solbrig, C.W. (1982) Multiphase Flow-Models for Nuclear, Fossil and Biomass Energy Production. Chapter in *Advances in Transport Processes*, ed. Mujumdar and Mashelkar, Wiley-Eastern, New York, 198-351.

Lyczkowski, R.W., Gidaspow, D., Solbrig, C.W., and Hughes, E.D. (1978) Characteristics and Stability Analyses of Transient One-Dimensional Two-Phase Flow Equations and Their Finite Difference Approximations. *Nucl. Sci. and Eng.*, **66**, 378-396.

Magnus, G. (1852). *Uber die Abweichung der geschosse, nebst einem Anhange: Uber eine auffallende Erscheinung bei rotirenden Korpern*. Berlin: F. Dummler.

Markhevka, V.I., Basov, V.A., Melik-Akhnazarov, T.Kh., and Orochko, D.I. (1971). The Flow of a Gas Jet into a Fluidized Bed. *Theor. Found. Chem. Eng.* **5**, 80.

Merry, J.M.D. (1975). Penetration of Vertical Jets into Fluidized Beds. *AIChE J.*, **21**, 3, 507-510.

Merry, J.M.D. (1971) Penetration of a Horizontal Gas Jet Into a Fluidised Bed. *Trans. Instn. Chem. Engrs.* **49**, 189-195.

Miller, A., and Gidaspow, D. (1992) Dense, Vertical Gas-Solid Flow in a Pipe. *AIChE J.*, November, **38**, 11, 1801-1815.

Mutsers, S.M.P, and Rietema, K. (1977). The Effect of Interparticle Forces on the Expansion of a Homogeneous Gas Fluidized Bed. *Powder Technology*. **18**, 239-248.

Nakamura, K., and Capes, C.E. (1973) Vertical Pneumatic Conveying: A Theoretical Study of Uniform and Annular Particle Flow Models. *The Can. J. of Chem. Engr.*, **51**, 39-46.

Patankar, S.V. (1980) Numerical Heat Transfer and Fluid Flow. Taylor and Francis.

Patankar, S.V., and Spalding. (1972) *Int. J. Heat and Mass Transfer*, **15**, 1787-1806.

Piepers, H.W., Cottar, E.J.E., Verkooijen, A.H.M., and Rietema, K. (1984). Effects of Pressure and Type of Gas on Particle-Particle Interaction and the Consequences for Gas-Solid Fluidization Behavior. *Powder Technology*, **37**, 55-70.

Pigford, R.L., and Baron, T. (1965) Hydrodynamic Stability of a Fluidized Bed. *Ind. Eng. Chem. Fundamentals*, **4**, 81-87.

Rasouli, R. (1981). One Dimensional Transient Unequal Velocity Two-Phase Flow by the Method of Characteristics. Ph.D. Thesis. Chicago, Illinois: Illinois Institute of Technology.

Rhie, C.M., and Chow, W.L. (1983) Numerical Study of the Turbulent Flow Past an Airfoil with Trailing Edge Separation. *AIAA Journal*, **21**, 11, 1525-1532.

Richardson, J.F., and Zaki, W.N. (1954) *Trans. Inst. Chem. Eng.*, **32**, 35-53.

Rietema, K. (1984). Powders: What are They? *Powder Technology*. **37**, 5-23.

Rietema, K. and Mutsers, S.M.P (1973). The Effect of Interparticle Forces on Expansion of a Homogeneous Gas-Fluidized Bed. pp. 32-33 in *Proceedings of International Symposium on Fluidization*. Toulouse, France.

Rots, P.E.A., Mudde, R.F., Van Den Akker, H.E.A., Van Der Hagen, T.H.J.J., and Van Dam, H. (1996) Fluidized Bed Nuclear Fission Reactor. *Chem. Eng. Sci.*, **51**, 11, 2763-2768.

Rowe, P.N., and Partridge, B.A. (1965). An X-Ray Study of Bubble in Fluidized Beds. *Trans. Instn. Chem. Engrs.*, **43**, 157.

Saffman, P.G. (1965) The Lift on a Small Sphere in a Slow Shear Flow. *J. Fluid Mech.*, **22**, 385.

Schiller and Nauman (1933) *Verein Deutscher Ingenieure*, **77**, 318.

Shakhova, N.A. (1972). Aerodynamics of Jets Discharged into Fluidized Beds. *Heat Transfer – Soviet Research*, **4**, 1, 133-142.

Shakhova, N.A. (1968) Discharge of Turbulent Jets into a Fluidized Bed. *J. Eng. Phys.*, **14**, 61-69.

Sinclair, J.L. (1997) *Hydrodynamic Modeling* in Circulating Fluidized Beds. Ed. Grace, J.R., Avidan, A.A., and Knowlton, T.M. Blackie Academic and Professional. London, England.

Sinclair, J.L., and Jackson, R. (1989) Gas-Particle Flow in a Vertical Pipe with Particle-Particle Interactions. *AIChE J.*, September, **35**, 9, 1473-1486.

Smith, J.M., Van Ness, H.C. and Abbott, M.M. (1949) Introduction to Chemical Engineering Thermodynamics. The McGraw-Hill Companies, Inc. 501-525.

Soo, S.L. (1989) *Particulates and Continuum: Multiphase Fluid Dynamics*. New York: Hemisphere.

Syamal, M., Rogers, W., and O'Brien, T.J. (1993) MFIX Documentation Theory Guide, U.S. Dept. of Energy, Office of Fossil Energy, DOE/METC-94/1004 DE94000087, Technical Note.

Tchen, C.M. (1947). *Mean Value and Correlation Problems Connected with the Motion of Small Particles in a Turbulent Field*. Ph.D. dissertation. Delft University, Netherlands.

Tsuo, Y.P,. and Gidaspow, D. (1990) Computation of Flow Patterns in Circulating Fluidized Beds. *AIChE J.*, **36**, 6, 885-896.

Tyler, J., and Mees, P.A.J. (1999) Computer Modeling of the Effect of a Horizontal Feed Jet on the Hydrodynamics of a Two-Dimensional Fluidized Bed. *Proceedings of the 3rd ASME/JSME Joint Fluids Engineering Conference*, July 18-23, San Francisco, California. Paper #FEDSM99-7905

Valenzuela, J.A., and Glicksman, L.R. (1984) An Experimental Study of Solid Mixing in a Freely Bubbling Two-Dimensional Fluidized Bed. *Powder Technology*. **38**, 63-72.

Van Den Akker, H.E.A. (1998) Coherent Structures in Multiphase Flows. *Powder Technology*., **100**, 123-136.

Van Wachem, B.G.M., Schouten, J.C., Krishna, R., van den Bleek, C.M., and Sinclair, J.L. (1999). CFD Modeling for Gas-Solid Flows: Qualitative and Quantitative Analysis of the Various Treatments. Proceedings of the 3rd ASME/JSME Joint Fluids Engineering Conference, July 18-23, San Francisco, California. Paper #FEDSM99-7899

Verloop, J., and Heertjes, P.M. (1970). Shock Waves as a Criterion for the Transition from Homogeneous to Heterogeneous Fluidization. *Chem. Eng. Sci.***25**, 828-832.

Weinstein, H., Shao, M., Schnitzlein, and Graff, R.A. (1986) Radial Variation in Void Fraction in a Fast Fluidized Bed. *Fluidization V, Proc. 5th Eng. Found. Conf. Fluidization, Elsinore, Denmark,* K. Ostergaard, A. Sorensen, eds., 329.

Wen, C.Y., Deole, N.R., and Chen, L.H. (1981) A Study of Jets in a Three-Dimensional Gas Fluidized Bed. 175-184.

Werther, J. and Xi, W. (1993) Jet Attrition of Catalyst Particles in Gas Fluidized Beds. *Powder Technology,* **76**, 39-46.

Witt, P.J., and Perry, J.H. (1995a) A Study in Multiphase Modeling of Fluidized Beds. *Proceedings of Computational Techniques and Applications: CTAC95.* July 3-5, 1995.

Witt, P.J., and Perry, J.H. (1995b) Prediction of the Hydrodynamic Behavior and Outlet Gas Composition of a Fluidized Bed Coal Gasifier. *Proceedings of Australian Symposium on Combustion including 4th Australian Flame Days*, Adelaide, November 9-10, 1995.

Witt, P.J., Perry, J.H., and Schwarz, M.P. (1998) A Numerical Model for Predicting Bubble Formation in a 3D Fluidized Bed. *Appl. Math.. Mod.*, **22**, 1071-1080.

Xuereb, C., Laguérie, and Baron, T. (1991) Etude du comportement de jets continus horizontaux ou inclines introduits dans un lit fluidisé par un gaz I: Morphologie des jets. *Powder Technology*, **67**, 43-56.

Yang, W.C., and Keairns, D.L. (1970). Recirculating Fluidized Bed Reactor Data Utilizing a Two-Dimensional Cold Model. *IAChE Symp. Ser. No. 141*, **70**, 27.

Yerushlmi, J., Turner, D.H., and Squires, A.M. (1976) The Fast Fluidized Bed. *Ind. Eng. Chem Process Des. Dev.*, **15**, 1, 47.

Zenz, F.A. (1968a). Bubble Formation and Grid Design. In *J.M.* Ed. Pirie, *Fluidization*, 136, Inst. Chem. Eng., London.

Zenz, F.A., (1968b) *Inst. Chem. Eng. Symp.* ser. 30, p 136.

APPENDIX A: Mathematical Proofs

A.1: Total Derivative of the Jacobian

As shown previously in Chapter 3 concerning the general conservation equation the transformation from a coordinate system to another results in the Jacobian matrix to account for volume changes. In this new coordinate system the volume of integration does not vary with time and as such the total derivative can be brought inside of the integral.

$$\frac{d}{dt}\bar{\bar{J}} = \frac{d}{dt}\left(\frac{\partial \bar{x}}{\partial \bar{\xi}}\right) = \frac{\partial}{\partial \bar{\xi}}\frac{d\bar{x}}{dt} = \frac{\partial \bar{v}}{\partial \bar{\xi}} \tag{A1.1}$$

Since $\bar{\xi}$ is constant with respect to time, the order of integration can be interchanged. The velocity vector $\bar{v}$ is considered to only be a function of the position vector $\bar{x}$ and the above expression can be expanded to:

$$\frac{\partial \bar{v}}{\partial \bar{\xi}} = \frac{\partial \bar{v}}{\partial x_1}\frac{\partial x_1}{\partial \bar{\xi}} + \frac{\partial \bar{v}}{\partial x_2}\frac{\partial x_2}{\partial \bar{\xi}} + \frac{\partial \bar{v}}{\partial x_3}\frac{\partial x_3}{\partial \bar{\xi}} \tag{A1.2}$$

Recall from the definition of a determinant of an *n x n* matrix:

$$\det \bar{\bar{A}} = \left|\bar{\bar{A}}\right| = \sum \pm a_{1i} a_{2j} \ldots a_{np} \tag{A1.3}$$

Where summation is over all permutations of *i,j,…,p* of *1,2,…,n* and the sign agrees with the parity of the permutation (i.e. negative for out of order permutation and positive for ordered permutations). The determinant of a *3 x 3* matrix would then have the following value:

$$\left|\overline{\overline{A}}_{3,3}\right| = a_{11}a_{22}a_{33} + a_{12}a_{23}a_{31} + a_{13}a_{21}a_{32} - a_{12}a_{21}a_{33} - a_{11}a_{23}a_{32} - a_{13}a_{22}a_{31} \quad \text{(A1.4)}$$

If the elements of the matrix are functions of some variable, in this case functions of t, differentiation of the matrix determinant will have to be expanded with respect to each variable using the chain rule resulting in a summation of determinants. The derivative of $\left|\overline{\overline{A}}\right|$ with respect to $\overline{x}$ is the sum of the n determinants obtained by replacing one row (or column) by the derivatives of its elements.

Continuing with the discussion of the full derivative of the Jacobian matrix and expressing it in terms of cofactors, A_{ij}:

$$\begin{aligned}\frac{d\overline{\overline{J}}}{dt} = \frac{d}{dt}\left(\frac{\partial x_1}{\partial \xi_1}\right)A_{11} + \frac{d}{dt}\left(\frac{\partial x_1}{\partial \xi_2}\right)A_{12} + \frac{d}{dt}\left(\frac{\partial x_1}{\partial \xi_3}\right)A_{13} + \\ \frac{d}{dt}\left(\frac{\partial x_2}{\partial \xi_1}\right)A_{21} + \frac{d}{dt}\left(\frac{\partial x_2}{\partial \xi_2}\right)A_{22} + \frac{d}{dt}\left(\frac{\partial x_2}{\partial \xi_3}\right)A_{23} + \\ \frac{d}{dt}\left(\frac{\partial x_3}{\partial \xi_1}\right)A_{31} + \frac{d}{dt}\left(\frac{\partial x_3}{\partial \xi_2}\right)A_{32} + \frac{d}{dt}\left(\frac{\partial x_3}{\partial \xi_3}\right)A_{33} \quad \text{(A1.5)}\end{aligned}$$

This expression is most easily represented using tensor notation as follows:

$$\frac{d\overline{\overline{J}}}{dt} = \frac{d}{dt}\left(\frac{\partial x_i}{\partial \xi_\alpha}\right)A_{\alpha i} \quad \text{(A1.6)}$$

Interchanging the order of differentiation and using the cofactor property of determinants:

$$\frac{d}{dt}\left(\frac{\partial x_i}{\partial \xi_\alpha}\right)A_{\alpha i} = \frac{\partial}{\partial \xi_\alpha}\left(\frac{dx_i}{dt}\right)A_{\alpha i} = \frac{\partial v_i}{\partial \xi_\alpha}A_{\alpha i} \quad \text{(A1.7)}$$

$$= \frac{\partial v_i}{\partial x_j}\frac{\partial x_j}{\partial \xi_\alpha}A_{\alpha i} = \frac{\partial v_i}{\partial x_j}\delta_{ij}\overline{\overline{J}} \quad \text{(A1.8)}$$

$$= \frac{\partial v_i}{\partial x_i} \overline{\overline{J}} = \overline{\overline{J}} \left(\nabla \cdot \bar{v} \right) \qquad \text{(A1.9)}$$

The material or total derivative of the Jacobian is:

$$\frac{d\overline{\overline{J}}}{dt} = \overline{\overline{J}} \left(\nabla \cdot \bar{v} \right) \qquad \text{(A1.10)}$$

A.2: Gauss' or the Divergence Theorem

Let A be a closed surface bounding a volume v. A positive outward normal is defined on the surface A as $\hat{n}$ and define a vector function $\overline{F}$ to be continuous in this volume. The divergence theorem states:

$$\iiint_v \nabla \cdot \overline{F} dv = \iint_A \hat{n} \cdot \overline{F} dA \qquad \text{(A2.1)}$$

Proof:

If we write $\overline{F}$ and $\hat{n}$ in components,

$\overline{F} = F_1 \hat{i} + F_1 \hat{j} + F_3 \hat{k}$ and $\hat{n} = \cos \alpha \hat{i} + \cos \beta \hat{j} + \cos \gamma \hat{k}$ where α, β and γ are the angles between $\hat{n}$ and the unit axes, then the formula takes the form:

$$\iiint_v \left(\frac{\partial F_1}{\partial x} + \frac{\partial F_2}{\partial y} + \frac{\partial F_3}{\partial z} \right) dxdydz = \iint_A \left(F_1 \cos \alpha \hat{i} + F_2 \cos \beta \hat{j} + F_3 \cos \gamma \hat{k} \right) dA \qquad \text{(A2.2)}$$

The above expression must be true if each of the vector components can be shown to be equivalent. That is:

$$\iiint_v \frac{\partial F_1}{\partial x}\, dxdydz = \iint_A F_1 \cos\alpha dA \tag{A2.3}$$

The proof is for a special region v that is bounded by a piecewise smooth orientable surface A and has the property that any straight line parallel to any one of the coordinate axes and intersecting v has at most one segment (or a single point) in common with v. This implies that v can be represented in the form

$$f_1(x,y) \le z \le f_2(x,y) \tag{A2.4}$$

where (x,y) varies in the orthogonal projection S of v in the xy-plane; see Figure A2.1.

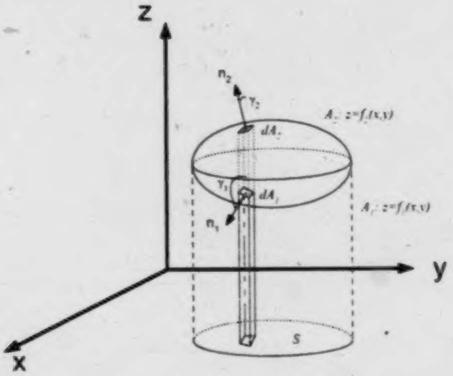

Figure A2.1 – Orientable surface showing projected area on plane axes.

The integration over z can be replaced using functional integrations as the limits

$$\iiint_v \frac{\partial F_1}{\partial x}\, dxdydz = \iint_A \left[\int_{z=f_1(x,y)}^{z=f_2(x,y)} \frac{\partial F_1}{\partial x}\, dz \right] dydx \tag{A2.5}$$

$$= \iint_S F_1(x,y,z)\Big|_{z=f_1}^{f_2} dydx = \iint_S \left[F_1(x,y,f_2) - F_1(x,y,f_1)\right] dydx \tag{A2.6}$$

For the upper bounding surface A_2, $dydx=\cos\gamma_2 dA_2=\hat{k}\cdot\hat{n}_2 dA_2$ since the normal forms an acute angle γ_2 with the Cartesian basis vector $\hat{k}$. The same arguments can be applied to the lower bounding surface A_1 but since the normal forms an obtuse angle with the Cartesian basis vector $\hat{k}$ the sign of the cosine function is negative:

$$dydx=-\cos\gamma_1 dA_1=-\hat{k}\cdot\hat{n}_1 dA_1 \tag{A2.7}$$

Making these substitutions into the previous expression gives:

$$\begin{aligned} &= \iint_S \left[F_1(x,y,f_2)-F_1(x,y,f_1)\right]dydx = \iint_{A_2} F_1\hat{k}\cdot\hat{n}_2 dA_2 - \iint_{A_1} -F_1\hat{k}\cdot\hat{n}_1 dA_1 \\ &= \iint_A F_1\hat{k}\cdot\hat{n}dA \end{aligned} \tag{A2.8}$$

It has been shown that

$$\iiint_v \frac{\partial F_1}{\partial x}dv = \iint_A F_1\hat{k}\cdot\hat{n}\alpha dA \tag{A2.9}$$

for a single component. By projecting the surface onto the other axes, it can be shown to be true for the other components.

A.3: Number Density

The number density, *n*, is a statistical measure of the number of particles within a specific volume. As this volume increases an asymptotic number density is reached. Figure A3.1 defines the three different volumes (in this case shown as shaded areas) that are required to define the averages.

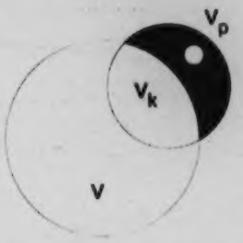

Figure A3.1 – Definition of local and intrinsic volume fractions.

$$n = \frac{\#\, particles}{unit\_volume} \tag{A3.1}$$

$$n = \frac{volume\_of\_one\_particle}{\left(volume\_of\_particles/total\_volume\right)} = v_p \frac{v}{v_k} \tag{A3.2}$$

$$\begin{aligned} &= \frac{4}{3}\pi r^3 \frac{1}{\varepsilon_p} \\ &= \frac{\pi}{6}\frac{D_p^3}{\varepsilon_p} \end{aligned} \tag{A3.3}$$

The number density has units of number of particles per unit volume.

APPENDIX B: Computer Codes

B.1: Minimum Control Volume MATLAB .M File

This MATLAB .M file will create the minimum control volume radius, R_{min}, based on a convergence tolerance bound of $\delta=1\%$ over a particle diameter range $50\mu m \le D_p \le 950\mu m$ and particle volume fraction of $0.01 \le \varepsilon_p \le 0.95$. A three dimensional surface plot is created; axes are not automatically labeled.

```
%[Z]=minimum_radius(delta,Dp,Alpha)
% Z  is a Dp x Alpha Matrix of the minimum CV radius
% delta is the required accuracy
% Dp is a vector of particle diameters in µm
% Alpha is the range of particle volume fractions

function [Z]=minimum_radius(delta,Dp,Alpha)

delta=0.01;
Dp=50:25:975;
Alpha=0.01:0.05:0.9;

for ni=1:size(Dp,2)
   for nj=1:size(Alpha,2)
      Z(ni,nj)=Dp(ni)*(Alpha(nj)^(-1/3)/sqrt(delta*2))*(1-
Alpha(nj));
   end
end

Z=Z/10^3;
%convert Z to units of mm from µm

surf(Alpha,Dp,Z)
view([10,-10,10])
colormap(white)
```

B.2: C Computer Code for Comparison of Different Discretization Schemes

The following computer code was used to discretize the one dimensional convection equation (Equation XXX in Chapter 3). Comments within the code should be sufficient to explain the purpose of each routine and the construction of the various discretization schemes.

```
//MECE 639: Assignment 4
//
// Jonathan Tyler
// November 19, 1998
//
// Revision:  003
// 11/06/98    Rewrote numerical routines to be float and
//             not double
//             Changed double 2D U array to a 1D array
//             calculate_TV routine corrected to use fabs
//             function, not abs
// 11/08/98   Rewrote file routine to write columnar data
//             as opposed to row data
//             Set up a new C++ project to work on the TVD
//             method.  All routines are the same as those
//             used for the flux limiter equations.
// 11/10/98    Rewrote all numerical schemes to share the
//             general flux limited equations.  TVD methods
//             now included in computation.
// 11/19/98    Nonoscillatory higher order upwind schemes
//             implemented on the old TVD code from
//             assignment 3
//             New routines added: MINMOD, MEDIAN3,
//             MEDIAN5, SIGN


#include <stdio.h>
#include <math.h>
#include <string.h>
#include <conio.h>
#include <stdlib.h>

//Define Subroutines
void set_initial_conditions(float *);
void display(float *);
void flux_limiter(int,float *,float *,float);
void calculate_TV(float *,float *,int);
```

```
FILE *create_output_file(int method,float Courant,int
frequency);
void write_data(FILE *,float *,float *,int,int);
void display2 (float *,float *);

//Routines added 11/19/98
float median5(float, float, float, float, float);
float median3(float, float, float);
float sign(float);
float minmod(float, float);


void main (void)
{

//Define variables

     int n;                     //number of time steps
     int frequency;             //every frequency iterations,
                                //write data
     int window=100;            //width of the window for
                                //writing
     FILE *fp;                  //output file pointer

     float *U1,*U2,*TV;
     U1=new float[900];         //Solution array1
     U2=new float[900];         //Solution array2
     TV=new float[3000];        //Total Variation array

     float Courant;             //Courant number
     int i,j,k,r,method=5;      //Generic counters and method
                                //select

/*   METHOD = 1 ==>  FIRST ORDER UPWIND
     METHOD = 2 ==>  LAX WENDROFF
     METHOD = 3 ==>  WARMING BEAN
     METHOD = 4 ==>  MINMOD TVD
     METHOD = 5 ==>  MUSCL TVD
     METHOD = 6 ==>  SUPERBEE TVD
     METHOD = 7 ==>  JONATHAN TVD*/

     char temp[19],key;

     do{
     printf("\n\nEnter method number (1-8)\n");
     printf("\t1.\tFIRST ORDER UPWIND\n");
     printf("\t2.\tLAX WENDROFF\n");
     printf("\t3.\tWARMING-BEAM\n");
     printf("\t4.\tMINMOD TVD\n");
     printf("\t5.\tMUSCL TVD\n");
     printf("\t6.\tSUPERBEE TVD\n");
     printf("\t7.\tJonathan TVD\n");
     printf("\t8.\tNonoscillatory MINMOD\n");
     printf("\t9.\tNonoscillatory SUPERBEE\n");
     printf("\t10.\tUNO2\n");
     printf("\t11.\tSONIC\n");

     scanf("%i",&method);

     printf("\nEnter the Courant number: ");
     scanf("%f",&Courant);

     n=int(600.0/Courant);

printf("\nMaximum number of time iterations is calculated
to be %i",n);

     printf("\nOutput data every ???? iterations: ");
     scanf("%i",&frequency);

     printf("\nContinue? (y/n)");
     } while((key=getch())!='y');



     fp=create_output_file(method,Courant,frequency);

     set_initial_conditions(U1);
     set_initial_conditions(U2);

     for(i=1;i<=3000;i++) TV[i]=0.0;     //Zero the TV
                                         //variable

//write file header data
          switch(method)
          {
          case 1:
               strcpy(temp,"FIRST ORDER UPWIND");
               break;
          case 2:
               strcpy(temp,"LAX WENDROFF      ");
               break;
          case 3:
               strcpy(temp,"WARMING-BEAM      ");
               break;
          case 4:
               strcpy(temp,"MINMOD TVD        ");
               break;
          case 5:
               strcpy(temp,"MUSCL TVD         ");
               break;
          case 6:
               strcpy(temp,"SUPERBEE TVD      ");
               break;
          case 7:
               strcpy(temp,"JONATHAN TVD      ");
               break;
          case 8:
               strcpy(temp,"NOI MINMOD        ");
               break;
          case 9:
               strcpy(temp,"NOI SUPERBEE      ");
               break;
          case 10:
               strcpy(temp,"UNO2              ");
               break;
          case 11:
               strcpy(temp,"SONIC             ");
               break;
          case 12:
               strcpy(temp,"Jon's power scheme");
               break;
          }
          fprintf(fp,"CFD method: %s\n",temp);
          fprintf(fp,"Courant=%f\n",Courant);
          fprintf(fp,"Output every %f
iterations\n",frequency);



     for(i=1;i<=n;i++)          //Time iteration n steps
     {


          for(k=2;k<=800;k++)
               TV[i]=TV[i]+fabs(U1[k]-U1[k-1]);
          flux_limiter(method,U1,U2,Courant);

          for (j=1;j<=900;j++)     //Exchange old with new
               U1[j]=U2[j];

     if(fmod(i,frequency)==0||i==1)
          write_data(fp,U1,TV,i,window);

     }
     fprintf(fp,"\nCourant=%f",Courant);

     for(i=1;i<=n;i++)
          fprintf(fp,"\nTV[%i]=\t%f",i,TV[i]/TV[1]);


     delete U1;          //clean up memory allocations
     delete U2;
     delete TV;

     fclose(fp);
}



     /*******************************************
     **           SUBROUTINES                  **
     *******************************************/

void set_initial_conditions(float *U)
{
//This subroutine sets the initial parabola, spike and
//top hat wave form on the one dimensional mesh.
     int i;
     float dx=1.0;
     float x=0.0;

     for (i=1;i<=900;i++)U[i]=0.0;
//Zero all values on the mesh

     for (i=20;i<=40;i++)
//Create the parabola
     {
          x=float(i)*dx;
          U[i]=sqrt(1.0 - pow(x-30.0*dx,2.0) /
(pow(10.0*dx,2.0)) );
     }
     for (i=60;i<=70;i++)
//Create the spike
     {
          x=float(i)*dx;
          U[i]=(x-60.0*dx)/(10.0*dx);
     }

     for (i=70;i<=80;i++)
     {
          x=float(i)*dx;
          U[i]=1.0-(x-70.0*dx)/(10.0*dx);
     }

     for (i=100;i<=120;i++)
//Create the top hat (square or shock wave)
     {
          U[i]=1.0;
     }
}

void display (float *U)
{
     int i,j;

     for (j=0;j<=20;j++)
     {
          for (i=1;i<20;i++)
          {
               printf("\nU[%i,1]=%f",j*20+i,U[j*20+i]);
          }
          getchar();
     }
}


void flux_limiter(int method,float *U1,float *U2,float
Courant)
{
     float
r1,r2,phi1,phi2,temp1,temp2,eps,hold,hold1,hold2;
     float UC,Uup,Uup2,U_plus_half,U_minus_half;
     float Uc_minus_half,Uc_plus_half,Uc_minus_3half,

     Uup_plus_half,Uup_minus_half,Uup2_plus_half,Uup2_minus
_half,
        modify1,modify2,modify;

    int i;                  //generic counter to run
                            //through grid
    modify=0.25;
    eps=1.0e-12;

    for(i=5;i<=899;i++)
    {

    switch (method)
    {
    case 1:
        //FIRST ORDER UPWINDING
        phi1=0.0;
        phi2=0.0;
        break;

    case 2:
        //LAX-WENDROFF UPWINDING
        phi1=1.0;
        phi2=1.0;
        break;

    case 3:
        //WARMING-BEAM 2ND ORDER UPWIND
        temp2=0.5*Courant*(1-Courant)*(U1[i]-2.0*U1[i-
1]+U1[i-2]);
        phi2=1.0;
        phi1=0.0;
        break;

        //TVD METHODS BELOW
    case 4:
        //MIN-MOD TVD
        r1=(U1[i-1]-U1[i-2])/(U1[i]-U1[i-1]+eps);
        r2=(U1[i]-U1[i-1])/(U1[i+1]-U1[i]+eps);

        hold=min(float(1.0),r1);
        phi1=max(float(0.0),hold);

        hold=min(float(1.0),r2);
        phi2=max(float(0.0),hold);
        break;

    case 5:
        //MUSCL TVD
```

```
     r1=(U1[i-1]-U1[i-2])/(U1[i]-U1[i-1]+eps);
     r2=(U1[i]-U1[i-1])/(U1[i+1]-U1[i]+eps);

     phi1=(fabs(r1)+r1)/(1.0+fabs(r1));
     phi2=(fabs(r2)+r2)/(1.0+fabs(r2));
     break;

case 6:
     //SUPERBEE TVD
     r1=(U1[i-1]-U1[i-2])/(U1[i]-U1[i-1]+eps);
     r2=(U1[i]-U1[i-1])/(U1[i+1]-U1[i]+eps);

     hold=min(float(2.0*r1),float(1.0));
     hold1=min(r1,float(2.0));
     hold2=max(hold,hold1);
     phi1=max(float(0.0),hold2);

     hold=min(float(2.0*r2),float(1.0));
     hold1=min(r2,float(2.0));
     hold2=max(hold,hold1);
     phi2=max(float(0.0),hold2);
     break;

case 7:
     //JONATHAN TVD
     r1=(U1[i-1]-U1[i-2])/(U1[i]-U1[i-1]+eps);
     r2=(U1[i]-U1[i-1])/(U1[i+1]-U1[i]+eps);

     hold=min(float(1.7*r1),float(1.0));
     hold1=min(r1,float(1.5));
     hold2=max(hold,hold1);
     phi1=max(float(0.0),hold2);

     hold=min(float(1.7*r2),float(1.0));
     hold1=min(r2,float(1.5));
     hold2=max(hold,hold1);
     phi2=max(float(0.0),hold2);
     break;


//Nonoscillatory schemes below
case 8:
//Nonoscillatory MINMOD

Uc_plus_half=0.5*(U1[i]+U1[i+1]);
Uc_minus_half=0.5*(U1[i-1]+U1[i]);
```

```
     Uc_minus_3half=0.5*(U1[i-2]+U1[i-1]);

     Uup_plus_half=U1[i]+(U1[i]-Uc_minus_half);
     Uup_minus_half=U1[i-1]+(U1[i-1]-Uc_minus_3half);

     Uup2_plus_half=U1[i]+(U1[i]-U1[i-1]);
     Uup2_minus_half=U1[i-1]+(U1[i-1]-U1[i-2]);

     U_plus_half=median3(U1[i],Uc_plus_half,Uup_plus_half);
     U_minus_half=median3(U1[i-
1],Uc_minus_half,Uup_minus_half);
     break;

     case 9:
     //Nonoscillatory SUPERBEE
     Uc_plus_half=0.5*(U1[i]+U1[i+1]);
     Uc_minus_half=0.5*(U1[i-1]+U1[i]);
     Uc_minus_3half=0.5*(U1[i-2]+U1[i-1]);

     Uup_plus_half=U1[i]+(U1[i]-Uc_minus_half);
     Uup_minus_half=U1[i-1]+(U1[i-1]-Uc_minus_3half);

     Uup2_plus_half=U1[i]+(U1[i]-U1[i-1]);
     Uup2_minus_half=U1[i-1]+(U1[i-1]-U1[i-2]);

     U_plus_half=median5(U1[i],Uc_plus_half,Uup_plus_half,U
1[i+1],Uup2_plus_half);
     U_minus_half=median5(U1[i-
1],Uc_minus_half,Uup_minus_half,U1[i],Uup2_minus_half);
     break;



     case 10:
     //UNO2

     //Calculate LW parabolic interpolation of central
difference
     temp1=U1[i+1]-2.0*U1[i]+U1[i-1];             //Di
     temp2=U1[i+2]-2.0*U1[i+1]+U1[i];             //Di+1

     Uc_plus_half=0.5*(U1[i]+U1[i+1])-
0.25*minmod(temp1,temp2);

     temp1=U1[i]-2.0*U1[i-1]+U1[i-2];             //Di-1
     temp2=U1[i+1]-2.0*U1[i]+U1[i-1];             //Di
     Uc_minus_half=0.5*(U1[i-1]+U1[i])-
0.25*minmod(temp1,temp2);

     temp2=U1[i-1]-2.0*U1[i-2]+U1[i-3];              //Di-2
     temp1=U1[i]-2.0*U1[i-1]+U1[i-2];                //Di-1

     Uc_minus_3half=0.5*(U1[i-2]+U1[i-1])-
0.25*minmod(temp1,temp2);

     //Calculate first order upwinding based on parabolic
     //interpolation
     Uup_plus_half=U1[i]+(U1[i]-Uc_minus_half);
     Uup_minus_half=U1[i-1]+(U1[i-1]-Uc_minus_3half);

     //Calculate second order upwinding
     Uup2_plus_half=U1[i]+(U1[i]-U1[i-1]);
     Uup2_minus_half=U1[i-1]+(U1[i-1]-U1[i-2]);

     U_plus_half=median3(U1[i],Uc_plus_half,Uup_plus_half);
     U_minus_half=median3(U1[i-
1],Uc_minus_half,Uup_minus_half);


     break;

     case 11:
//SONIC
//Calculate LW parabolic interpolation of central
// difference
     temp1=U1[i+1]-2.0*U1[i]+U1[i-1];              //Di
     temp2=U1[i+2]-2.0*U1[i+1]+U1[i];              //Di+1

     Uc_plus_half=0.5*(U1[i]+U1[i+1])-
0.25*minmod(temp1,temp2);

     temp1=U1[i]-2.0*U1[i-1]+U1[i-2];                //Di-1
     temp2=U1[i+1]-2.0*U1[i]+U1[i-1];                //Di

     Uc_minus_half=0.5*(U1[i-1]+U1[i])-
0.25*minmod(temp1,temp2);

     temp2=U1[i-1]-2.0*U1[i-2]+U1[i-3];              //Di-2
     temp1=U1[i]-2.0*U1[i-1]+U1[i-2];                //Di-1

     Uc_minus_3half=0.5*(U1[i-2]+U1[i-1])-
0.25*minmod(temp1,temp2);
```

```
     //Calculate first order upwinding based on parabolic
     //interpolation
     Uup_plus_half=U1[i]+(U1[i]-Uc_minus_half);
     Uup_minus_half=U1[i-1]+(U1[i-1]-Uc_minus_3half);


     //Calculate second order upwinding
     Uup2_plus_half=U1[i]+(U1[i]-U1[i-1]);
     Uup2_minus_half=U1[i-1]+(U1[i-1]-U1[i-2]);

     U_plus_half=median5(Uc_plus_half,Uup_plus_half,U1[i],U
1[i+1],Uup2_plus_half);

     U_minus_half=median5(Uc_minus_half,Uup_minus_half,U1[i
-1],U1[i],Uup2_minus_half);

     break;


     case 12:
     //jon's scheme

     if(fabs(U1[i+1]-U1[i]) > fabs(U1[i-1]-U1[i]))
          modify=0.40;
     if(fabs(U1[i+1]-U1[i]) < fabs(U1[i-1]-U1[i]))
          modify=0.1;

//Calculate LW parabolic interpolation of central
//difference
     temp1=U1[i+1]-2.0*U1[i]+U1[i-1];                //Di
     temp2=U1[i+2]-2.0*U1[i+1]+U1[i];                //Di+1


     Uc_plus_half=0.5*(U1[i]+U1[i+1])-
modify*minmod(temp1,temp2);

     temp1=U1[i]-2.0*U1[i-1]+U1[i-2];                //Di-1
     temp2=U1[i+1]-2.0*U1[i]+U1[i-1];                //Di

     Uc_minus_half=0.5*(U1[i-1]+U1[i])-
modify*minmod(temp1,temp2);

     temp2=U1[i-1]-2.0*U1[i-2]+U1[i-3];              //Di-2
     temp1=U1[i]-2.0*U1[i-1]+U1[i-2];                //Di-1
     Uc_minus_3half=0.5*(U1[i-2]+U1[i-1])-
modify*minmod(temp1,temp2);

     //Calculate first order upwinding based on parabolic
     //interpolation
     Uup_plus_half=U1[i]+(U1[i]-Uc_minus_half);
     Uup_minus_half=U1[i-1]+(U1[i-1]-Uc_minus_3half);



     //Calculate second order upwinding
     Uup2_plus_half=U1[i]+(U1[i]-U1[i-1]);
     Uup2_minus_half=U1[i-1]+(U1[i-1]-U1[i-2]);

     U_plus_half=median5(Uc_plus_half,Uup_plus_half,U1[i],U
1[i+1],Uup2_plus_half);

     U_minus_half=median5(Uc_minus_half,Uup_minus_half,U1[i
-1],U1[i],Uup2_minus_half);

     break;
     }

          if(method<9)
          {
          temp1=U1[i]-Courant*(U1[i]-U1[i-1]);
//first half of flux equation
          temp2=0.5*Courant*(1-Courant)*(U1[i+1]-
2.0*U1[i]+U1[i-1]);
//second half of flux equation

          U2[i]=temp1-0.5*Courant*(1-
Courant)*(phi2*(U1[i+1]-U1[i])-
                         phi1*(U1[i]-U1[i-1]));
          //put the flux limited equation together
          }

          else
          {
          U2[i]=U1[i]-Courant* (U_plus_half - U_minus_half)
+ pow(Courant,2.0) *(U_plus_half-U1[i] - U_minus_half+U1[i-
1]);
          //working equation for the nonoscillatory schemes
          }

          U2[1]=0.0;
          U2[900]=0.0;
          //reset boundary conditions

     }

}

void calculate_TV(float *U1,float *TV,int step)
{
     int i;
     TV[step]=0.0;
     for (i=2;i<=900;i++)
          TV[step]=TV[step]+fabs(U1[i]-U1[i-1]);

}



FILE *create_output_file(int method,float Courant,int
frequency)
{
     FILE *fp;
     char filename[40];            //File name and path
     char temp[19];                     //Just a string


     printf("\nPlease enter filename and dos path:\n");
     scanf("%s",&filename);


     if ((fp = fopen(filename, "w"))
           == NULL)
     {
          fprintf(stderr, "Cannot open input file.\n");
     }



          if (fp!=NULL)
     {
          printf("\nFile opened, writing header");


     }
     return fp;
}
```

```
void write_data(FILE *fp,float *U1,float *TV,int i,int
window)
{
     int j;

     fprintf(fp,"\n\nITERATION IS %i and window
%f",i,window);

     for (j=1;j<=900;j++)
     {
          fprintf(fp,"%i\t%f\n",j,U1[j]);
     }
}


void display2 (float *U1,float *U2)
{
     int i,j;

     for (j=0;j<=20;j++)
     {
          for (i=0;i<20;i++)
          {

     printf("\nU1[%i]=%f\tU2[%i]=%f",j*20+i,U1[j*20+i],j*20
+i,U2[j*20+i]);
          }
          getchar();
     }
}

float sign(float value)
{
/* Sign function returns the sign of the argument passed to
it*/
/* -1 is for a negative argument
      1 is for a positivie argument*/

     if (value<0.0) return -1.0;
          return 1.0;
}


float minmod(float A, float B)
{
/*MINMOD function which is defined as:
      SIGN(A)*MAX(0,SIGN(AB)MIN(|A|,|B|) */
     return
(sign(A)*max(0.0,sign(A*B)*min(fabs(A),fabs(B))));
}

float median3(float A, float B, float C)
{
     return(A+minmod(B-A,C-A));
}

float median5(float A, float B, float C, float D, float E)
{
//Returns the median value from a list of five numbers
     float X1, X2,temp1,temp2;
     X1=median3(A,B,C);
     temp1=max(A,B);
     temp2=max(C,D);
     X2=A+B+C+D-max(temp1,temp2);
     temp1=min(A,B);
     temp2=min(C,D);
     X2=X2-min(temp1,temp2)-X1;
     return (median3(X1,X2,E));
}
```

Appendix C: CFX 4.2 Command and Fortran Files

These two files are a representative sample of the command and FORTRAN files used to set up the computational fluid dynamics simulation. Comments in the code will provide information about modifications for future tests.

*C.2: CFX 4.2 Command File *.fc*

More information about the structure of the CFX command file can be found in the CFX Solver Manual.

```
/* CFX 4.2 Command File for Fluidized Bed Simulations*/

/* September 22, 1999*/
/* Jonathan Tyler*/
/* Dept of Chemical and Materials Engineering*/
/* University of Alberta*/
/* Edmonton, Alberta, Canada*/

/* Two phase fluidized bed simulation with side injection*/
/* horizontal gas feed jet.  Part of Jonathan Tyler's*/
/* Masters thesis work.*/


/* JUNE 17, 1999*/
/* GRID REFINEMENT TESTS: PARTICLE DENSITY SET TO*/
/* 1450KG/M^3*/


/* JUNE 11, 1999*/
/* 3X3 NOZZLE, PARTICLE DENSITY CHANGED TO 930KG/M^3*/
/* NOZZLE DIAMETER NOW SET AT 2.9245E-3M TO MORE */
/* ACCURATELY REPRESENT DR. BERUTTI'S NOZZLE*/

/* MAY 18, 1999 */
/* CONTINUATION RUNS OF PREVIOUS SIMULATIONS FROM CDROM 2*/
/* THIS RUN CONTINUES FROM CD2/SUPERBEE/V_AT_300/M05.DMP */
/* FLUIDIZATION GAS REDUCED TO 50% OF MINIMUM*/
/* FLUIDIZATION*/
/* AMG AND UNDERRELAXATION FACTORS SET*/
/* MAX ITERATIONS REDUCED TO 30*/

/* RUN TO SIMULATE DR BERRUTI'S SIMULATIONS */
/* FEB 16, 1999 */


/* RUN TO SIMULATE DR BERRUTI'S SIMULATIONS */
/* FEB 16, 1999 */


/*  Physical Properties  */
#CALC
DP=3.7E-4;
RHOP=950;
VISCP=1.0E-12;
EMIN=0.49;

EPTCEL=0.0001;
G=-600;
CMPVF=0.376;

RHOG=1.2;
VISCG=1.8e-5;

GASVL=RHOG*(RHOP-RHOG)*9.81*DP*DP*0.091/(150*VISCG);
GASVEL=2.0*GASVL/RHOG;
#ENDCALC


/*  INLET BOUNDARY CONDITIONS  */
#CALC
VELNOZ=300.0;
#ENDCALC

/*  PROGRAM CONTROL  */
#CALC
MASSTOL=5.0E-6;
MAXITER=30;
MINITER=1;
#ENDCALC

>>CFX4
  >>SET LIMITS
    LARGE
    TOTAL REAL WORK SPACE 30000000
    TOTAL INTEGER WORK SPACE 30000000
    END
  >>OPTIONS
    THREE DIMENSIONS
    NUMBER OF PHASES     2
    TRANSIENT FLOW
    BUOYANT FLOW
    END
  >>USER FORTRAN
    USRINT
    USRGRD
    USRTPL
    END
>>MODEL TOPOLOGY
>>MODEL DATA
  >>DIFFERENCING SCHEME
    ALL EQUATIONS 'SUPERBEE'
    VOLUME FRACTION 'SUPERBEE'
    PRESSURE 'CENTRAL'
    END
  >>TITLE
    PROBLEM TITLE 'RUN GC02'
    END
  >>WALL TREATMENTS
    SLIP
    END
  >>RHIE CHOW SWITCH
    STANDARD
    END
  >>PHYSICAL PROPERTIES
    >>BUOYANCY PARAMETERS
      GRAVITY VECTOR 0.0 -9.81 0.0
      BUOYANCY REFERENCE DENSITY 1.2
      END
    >>FLUID PARAMETERS
      PHASE NAME 'PHASE1'
      VISCOSITY #VISCG
      DENSITY #RHOG
      END
    >>FLUID PARAMETERS
      PHASE NAME 'PHASE2'
      VISCOSITY #VISCP
      DENSITY  #RHOP
      END
    >>TRANSIENT PARAMETERS
      >>FIXED TIME STEPPING
        TIME STEPS 2000 * 0.001
     END
    >>MULTIPHASE PARAMETERS
      >>INTER PHASE TRANSFER MODELS
        >>MOMENTUM
          >>PARTICLE DRAG MODEL
```

```
         FLOW REGIME 'AUTOMATIC'
         VISCOUS REGIME CORRELATION 'SCHILLER-NAUMANN'
         NEWTON COEFFICIENT 0.44
            DENSE PARTICLE EFFECTS 'GIDASPOW'
            END
      >>PHASE DESCRIPTION
     PHASE NAME 'PHASE1'
        GAS
     CONTINUOUS
     END
      >>PHASE DESCRIPTION
     PHASE NAME 'PHASE2'
     SOLID
     DISPERSE
     MEAN DIAMETER #DP
     SOLID PRESSURE
     SOLID COMPACTION MODULUS #G
     COMPACTION VOLUME FRACTION #CMPVF
     MODIFY EMPTY CELL VELOCITY #EPTCEL
     END
>>SOLVER DATA
  >>UNDER RELAXATION FACTORS
    U VELOCITY 0.6
    V VELOCITY 0.6
    W VELOCITY 0.6
    END
  >>ALGEBRAIC MULTIGRID PARAMETERS
    CONNECTIVITY TOLERANCE 1.0E-14
    SINGULARITY TOLERANCE 1.0E-3
    WORK SPACE FACTOR 2.0
    JACOBI SMOOTHER
    END
  >>PRESSURE CORRECTION
    PISO
    NUMBER OF PISO CORRECTION STEPS 2
    END
  >>EQUATION SOLVERS
    ALL PHASES
    U VELOCITY 'AMG'
    V VELOCITY 'AMG'
    W VELOCITY 'AMG'
    PRESSURE 'ICCG'
    VOLUME FRACTION 'AMG'
    END
  >>PROGRAM CONTROL
    MINIMUM NUMBER OF ITERATIONS   #MINITER
    MAXIMUM NUMBER OF ITERATIONS   #MAXITER
    PRESSURE REFERENCE POINT BLOCK 'BLOCK-1'
    PRESSURE REFERENCE POINT 10 10 3
    OUTPUT MONITOR POINT 15 20 4
    MASS SOURCE TOLERANCE #MASSTOL
    END
>>CREATE GRID
>>MODEL BOUNDARY CONDITIONS
  >>PRESSURE BOUNDARIES
    PATCH NAME 'OUTLET'
    PHASE NAME 'PHASE1'
    VOLUME FRACTION 1.0
    PRESSURE 0.0
    END
  >>PRESSURE BOUNDARIES
    PATCH NAME 'OUTLET'
    PHASE NAME 'PHASE2'
    VOLUME FRACTION 0.0
    PRESSURE 0.0
    END
  >>INLET BOUNDARIES
    PATCH NAME 'DISTRIBUTOR'
    PHASE NAME 'PHASE1'
    VOLUME FRACTION 1.0
    V VELOCITY #GASVEL
    U VELOCITY 0.0
    W VELOCITY 0.0
    END
  >>INLET BOUNDARIES
    PATCH NAME 'DISTRIBUTOR'
    PHASE NAME 'PHASE2'
    VOLUME FRACTION 0.0
    U VELOCITY 0.0
    V VELOCITY 0.0
    W VELOCITY 0.0
    END
  >>INLET BOUNDARIES
    PATCH NAME 'NOZZLE'
    PHASE NAME 'PHASE1'
    VOLUME FRACTION 1.0
    U VELOCITY #VELNOZ
    V VELOCITY 0.0
    W VELOCITY 0.0
    END
  >>INLET BOUNDARIES
    PATCH NAME 'NOZZLE'
    PHASE NAME 'PHASE2'
    VOLUME FRACTION 0.0
    U VELOCITY 0.0
    V VELOCITY 0.0
    W VELOCITY 0.0
    END
>>OUTPUT OPTIONS
  >>FRONTEND PRINTING
    NO TOPOLOGY STRUCTURE
    END
  >>LINE GRAPH DATA
    XYZ  0.30 0.37 0.05
    EACH TIME STEP
    FILE NAME 'PLOT_1'
    PHASE NAME 'PHASE1'
    U VELOCITY
    VOLUME FRACTION
    END
  >>LINE GRAPH DATA
    XYZ  0.35 0.37 0.05
    EACH TIME STEP
    FILE NAME 'PLOT_2'
    PHASE NAME 'PHASE1'
    U VELOCITY
    VOLUME FRACTION
    END
  >>LINE GRAPH DATA
    XYZ  0.40 0.37 0.05
    EACH TIME STEP
    FILE NAME 'PLOT_3'
    PHASE NAME 'PHASE1'
    U VELOCITY
    VOLUME FRACTION
    END
  >>LINE GRAPH DATA
    XYZ  0.45 0.37 0.05
    EACH TIME STEP
    FILE NAME 'PLOT_4'
    PHASE NAME 'PHASE1'
    U VELOCITY
    VOLUME FRACTION
    END
  >>LINE GRAPH DATA
    XYZ  0.60 0.37 0.05
    EACH TIME STEP
    FILE NAME 'PLOT_5'
    PHASE NAME 'PHASE1'
    U VELOCITY
    VOLUME FRACTION
    END
  >>LINE GRAPH DATA
    XYZ  0.35 0.70 0.05
    EACH TIME STEP
    FILE NAME 'PLOT_6'
    PHASE NAME 'PHASE1'
    U VELOCITY
    VOLUME FRACTION
    END
  >>PRINT OPTIONS
    >>WHAT
      NO VARIABLES
      NO WALL PRINTING
      NO GEOMETRIC INFORMATION
      END
  >>DUMP FILE OPTIONS
    ALL VARIABLES
    TIME INTERVAL 0.05
    END
>>STOP
```

C.2: CFX 4.2 Fortran File

This is the accompanying fortran file that must be used in conjunction with the CFX 4.2 command file to set up the fluidized bed simulations used for this work. Values used in this fortran file are typical and can be changed to specify new geometry and flow conditions. Please note that some incorrect formatting may have resulted form importing this source code into the word processor.

```
C Fortran File for CFX 4.2 Fluidized Bed Simulations
C Jonathan Tyler
C September 22, 1999
C Dept of Chemical and Materials Engineering
C University of Alberta
C Edmonton, Alberta, Canada
C
C This fortran file creates the discretization mesh,
C maps related patches for nozzle inlets, pipes, etc…
C and sets the initial conditions for the CFX 4.2
C multiphase flow solver.  It is included as part
C of Jonathan Tyler's Masters thesis.
C
C JUNE 28, 1999
C RUNS FOR GB01,GB02,GC01,GC02
```

```
C MODIFIED JUNE 16, 1999
C MODIFICATION C - FIXED X GRIDDING

C MODIFIED JUNE 16, 1999
C MODIFICATION A:
C NOW THE Z GRIDDING IS MATCH TO THE DZ VALUE CALCULATED
C USING THE NOZDEN VARIABLE.  THIS SHOULD BETTER MATCH THE
C SIZE IN THE Z DIRECTION.
C
C MODIFICATION B:
C Y GRIDDING SECTION CORRECTED SO THAT THE GEOMETRIC
PROGRESSION
C IS BASED ON THE SMALLEST MESH DIVISION WITHIN THE NOZZLE
C INLET PATCH.

C MODIFIED JUNE 11, 1999
C NOZZLE CV DENSITY CAN NOW BE SPECIFIED USING THE
C NOZDEN VARIABLE IN THE /UCBLOK/ COMMON AREA
C THIS WILL CONTROL HOW MANY CVS ARE USED IN THE
C NOZZLE INLET PATCH BC.


C MODIFIED JUNE 10, 1999
C THE ERROR WITH PLACEMENT OF THE NOZZLE INLET AND THE
C PIPE HAVE BEEN CORRECTED.  THE LOWER LEFT CORNER OF CVS
C ARE USED TO LOCATE THE POSITION OF THE BOUNDARIES.

C MODIFIED MARCH 11, 1999
C MODIFIED MARCH 26, 1999
C *************** DATA BLOCKS ************************
      BLOCK DATA BDATA

      COMMON /UCBLOK/ YNOZUP,YWIDTH,FINES,BDHGHT,NTOP,
     +         BDWDTH,BDDPTH,
     +         ZWIDTH,NUMZ,
     +          FACTOR,DIAM,
     +          RNSERT,WALL,
     +          NOZDEN

C SET THE FOLLOWING VARIABLES TO DEFINE GEOMETRY:

C YNOZUP   -  DISTANCE FROM DISTRIBUTOR TO BOTTOM OF NOZZLE
C YWIDTH   -  Y DIMENSION OF THE RECTANGULAR NOZZLE
C FINES    -  SHOULD BE SET EQUAL TO YNOZUP
C BDHGHT   -  TOTAL HEIGHT OF THE REACTOR
C NTOP     -  NUMBER OF GRID SPACES IN LINEAR FREEBOARD
```

```
C BDWDTH    -  X DIMENSION OF THE REACTOR
C BDDPTH    -  Z DIMENSION OF THE REACTOR
C ZWIDTH    -  Z DIMENSION OF THE RECTANGULAR NOZZLE
C NUMZ      -  ODD NUMBER OF CONTROL VOLUMES IN K DIRECTION
C FACTOR    -  DESIRED HEIGHT OF BED INITIALLY FILLED WITH
SOLIDS
C DIAM      -  PARTICLE DIAMETER
C RNSERT    -  NOZZLE INSERTION FROM WALL
C WALL      -  NOZZLE PIPE WALL THICKNESS
C NOZDEN    -  GRID DENSITY AT NOZZLE
C              1  USE A SINGLE CV
C              2  USE A 3 X 3 CV
C              3  USE A 4 X 4 CV

      DATA YNOZUP,YWIDTH,FINES,BDHGHT,NTOP,
     +          BDWDTH,BDDPTH,
     +          ZWIDTH,NUMZ,
     +           FACTOR,DIAM,
     +           RNSERT,WALL,
     +           NOZDEN
     +          /0.35 ,  0.00292 , 0.35, 1.2 ,18,
     +           1.2 , 0.1 ,
     +           0.00292 , 15 ,
     +            0.71,3.7e-4,
     +            0.25,0.002,
     +            1/

         COMMON /UCGRID/ XGRID(200),YGRID(200),ZGRID(200),
     +          NI,NJ,NK,NNOZUP,NNOZDP


      END
C *****************************************************


       SUBROUTINE
USRINT(U,V,W,P,VFRAC,DEN,VIS,TE,ED,RS,T,H,RF,SCAL
     +                    ,CONV,XC,YC,ZC,XP,YP,ZP
     +
,VOL,AREA,VPOR,ARPOR,WFACT,DISWAL,IPT
     +
,IBLK,IPVERT,IPNODN,IPFACN,IPNODF,IPNODB,IPFACB
     +                    ,WORK,IWORK,CWORK)
C
```

```
C*********************************************************
************
C    FORTRAN ROUTINES MODIFIED BY TAKING OUT THE USRBCS
ROUTINE ON JULY 27/98
      LOGICAL LDEN,LVIS,LTURB,LTEMP,LBUOY,LSCAL,LCOMP
     +       ,LRECT,LCYN,LAXIS,LPOROS,LTRANS
      LOGICAL LRDISK,LWDISK
C
      CHARACTER*(*) CWORK
C
C++++++++++++++++ USER AREA 1
+++++++++++++++++++++++++++++++++++++++++
C---- AREA FOR USERS EXPLICITLY DECLARED VARIABLES
C
C++++++++++++++++ END OF USER AREA 1
++++++++++++++++++++++++++++++++++
C
      COMMON
     + /ALL/    NBLOCK,NCELL,NBDRY,NNODE,NFACE,NVERT,NDIM
     + /ALLWRK/ NRWS,NIWS,NCWS,IWRFRE,IWIFRE,IWCFRE
     + /ADDIMS/ NPHASE,NSCAL,NVAR,NPROP
     +
,NDVAR,NDPROP,NDXNN,NDGEOM,NDCOEF,NILIST,NRLIST,NTOPOL
     + /CHKUSR/ IVERS,IUCALL,IUSED
     + /DEVICE/ NREAD,NWRITE,NRDISK,NWDISK
     + /IDUM/   ILEN,JLEN
     + /IOLOGC/ LRDISK,LWDISK
     + /LOGIC/  LDEN,LVIS,LTURB,LTEMP,LBUOY,LSCAL,LCOMP
     +         ,LRECT,LCYN,LAXIS,LPOROS,LTRANS
     + /MLTGRD/ MLEVEL,NLEVEL,ILEVEL
     + /SGLDBL/ IFLGPR,ICHKPR
     + /TRANSI/ NSTEP,KSTEP,MF,INCORE
     + /TRANSR/ TIME,DT,DTINVF,TPARM
C
C++++++++++++++++ USER AREA 2
+++++++++++++++++++++++++++++++++++++++++
C---- AREA FOR USERS TO DECLARE THEIR OWN COMMON BLOCKS
C     THESE SHOULD START WITH THE CHARACTERS 'UC' TO ENSURE
C     NO CONFLICT WITH NON-USER COMMON BLOCKS
C
      COMMON /UCBLOK/ YNOZUP, YWIDTH, FINES, BDHGHT, NTOP,
     +         BDWDTH, BDDPTH,
     +         ZWIDTH, NUMZ,
     +          FACTOR,DIAM,
     +          RNSERT,WALL,
     +          NOZDEN
```

```
      COMMON /UCGRID/ XGRID(200),YGRID(200),ZGRID(200),
     +         NI,NJ,NK,NNOZUP,NNOZDP


C++++++++++++++++ END OF USER AREA 2
++++++++++++++++++++++++++++++++++
C
      DIMENSION
     + U(NNODE,NPHASE),V(NNODE,NPHASE),W(NNODE,NPHASE)
     +,P(NNODE,NPHASE),VFRAC(NNODE,NPHASE)
     +,TE(NNODE,NPHASE),ED(NNODE,NPHASE),RS(NNODE,NPHASE,6)
     +,T(NNODE,NPHASE),H(NNODE,NPHASE),RF(NNODE,NPHASE,4)
     +,SCAL(NNODE,NPHASE,NSCAL)

+,DEN(NNODE,NPHASE),VIS(NNODE,NPHASE),CONV(NFACE,NPHASE)
      DIMENSION
     +
XC(NVERT),YC(NVERT),ZC(NVERT),XP(NNODE),YP(NNODE),ZP(NNODE)
     +,VOL(NCELL),AREA(NFACE,3),VPOR(NCELL),ARPOR(NFACE,3)
     +,WFACT(NFACE),DISWAL(NCELL)
      DIMENSION
     + IPT(*),IBLK(5,NBLOCK)

+,IPVERT(NCELL,8),IPNODN(NCELL,6),IPFACN(NCELL,6),IPNODF(NF
ACE,4)
     +,IPNODB(NBDRY,4),IPFACB(NBDRY)
      DIMENSION
     + IWORK(NIWS),WORK(NRWS),CWORK(NCWS)
C
C+++++++++++++++ USER AREA 3
+++++++++++++++++++++++++++++++++++++++++
C---- AREA FOR USERS TO DIMENSION THEIR ARRAYS
C
C---- AREA FOR USERS TO DEFINE DATA STATEMENTS
C
C++++++++++++++++ END OF USER AREA 3
+++++++++++++++++++++++++++++++++++
C
C---- STATEMENT FUNCTION FOR ADDRESSING
      IP(I,J,K)=IPT((K-1)*ILEN*JLEN+(J-1)*ILEN+I)
C
C----VERSION NUMBER OF USER ROUTINE AND PRECISION FLAG
C
      IVERS=3
      ICHKPR = 1
C
```

```
C++++++++++++++++ USER AREA 4
+++++++++++++++++++++++++++++++++++++++++
C---- TO USE THIS USER ROUTINE FIRST SET IUSED=1
C
       IUSED=1
C
C++++++++++++++++ END OF USER AREA 4
++++++++++++++++++++++++++++++++++
C
       IF (IUSED.EQ.0) RETURN
C
C---- FRONTEND CHECKING OF USER ROUTINE
      IF (IUCALL.EQ.0) RETURN
C
C++++++++++++++++ USER AREA 5
+++++++++++++++++++++++++++++++++++++++++
C
C---- AREA FOR INITIALISING VARIABLES
U,V,W,P,VFRAC,TE,ED,RS,T,SCAL
C     ONLY.
C
C PHASE 1 = CONTINUOUS PHASE - GAS
C PHASE 2 = DISPERSED PHASE  - SOLID
      IC=1
      ID=2
C FLAG IS USED TO FIND THE DESIRED BED HEIGHT
      FLAG=.TRUE.
C
C  GET SOLID AND GAS PHASE DENSITY SET IN COMMAND FILE
C
       CALL GETADD('USRINT','RPHYS ','DENSIT',ILEVEL,JDENS)
       DENSOL=WORK(JDENS-1+ID)
       DENGAS=WORK(JDENS-1+IC)
C
C  GET GAS VISCOSITY SET IN COMMAND FILE
C
       UGAS=1.8E-5
C
C  GET PARTICLE DIAMETER SET IN COMMAND FILE
C
c      CALL GETADD('USRINT','RPHYS ','D     ',ILEVEL,JDIA)
C

C  SET INITIAL BED GAS VELOCITY TO MINIMUM FLUIDISATION
VELOCITY
        VELP1=(DENSOL-
DENGAS)*9.81*DIAM**2.0*0.091/(150.0*UGAS)
```

```
C  SET INITIAL BED GAS VOLUME FRACTION
      VFINIT=0.42
      VELP2=0.001
C
      EMPTY=1.0E-10
      FULL=1.0-EMPTY
C
C
C ONLY SET INITIAL CONDITIONS IF NOT DOING A RESTART
      IF(.NOT.LRDISK) THEN
C
C ----  GET OUTLET PATCH - PRESSURE BOUNDARY
C
        CALL
IPREC('OUTLET','PATCH','CENTRES',IPT,ILEN,JLEN,
     +           KLEN,CWORK,IWORK)
C ----  FIND THE OUTLET PRESSURE
        INODE=IP(1,1,1)
        POUT=P(INODE,IC)
C
C ----  GET CELL VERTICES TO CALCULATE BED HEIGHT
C
        CALL IPREC('BLOCK-
1','BLOCK','VERTICES',IPT,ILEN,JLEN,
     +           KLEN,CWORK,IWORK)
C ----  FIND POINTERS TO TOP & BOTTOM OF BED

C NEW PART FEB 10, 1999
C BASED ON FACTOR VALUE SCAN FROM TOP OF YGRID TO FIND GRID
CELL VALUE
C THAT IS CLOSEST TO THE DESIRED INITIAL BED HEIGHT.  ONCE
THIS IS
C FOUND, TAKE THE K VALUE TO FEED INTO THE SOLIDS FILLING
ROUTINE
        FLAG=.TRUE.
        DO 90 J=JLEN,1,-1
           IF( (FACTOR .GT. YGRID(J)) .AND. (FLAG .EQ.
.TRUE.) ) THEN
               KHOLD=J+1
               FLAG=.FALSE.
           END IF
90      CONTINUE

        IVBOT=IP(1,1,1)
        IVTOP=IP(1,KHOLD,1)

C ----  TOTAL BED HEIGHT
        TOTHIG=YC(IVTOP)-YC(IVBOT)
C
C ====  START SETTING VARIABLES
=========================================
C
C ----  GET CELL NODES
C
        CALL IPREC('BLOCK-
1','BLOCK','CENTRES',IPT,ILEN,JLEN
     +             ,KLEN,CWORK,IWORK)

C ----  FIRST SET ALL CELLS ASSUMING NO SOLIDS
C
        DO 103 K=1,KLEN
          DO 102 J=1,JLEN
            DO 101 I=1,ILEN
              INODE=IP(I,J,K)
C
              VFRAC(INODE,IC)=FULL
              VFRAC(INODE,ID)=EMPTY
C ----  AIR VELOCITY SET TO MIN. FLUIDIZATION VEL.
              V(INODE,IC)=VELP1
              V(INODE,ID)=VELP2
C ----  SET PRESSURES TO OUTLET PRESSURE
              P(INODE,IC)=POUT
              P(INODE,ID)=POUT
 101        CONTINUE
 102      CONTINUE
 103    CONTINUE
C
C ----  SET INITAL CONDITIONS IN LOWER SECTION OF BED
C
        PCONST=DENSOL*(1-VFINIT)*9.81
C
        DO 203 K=1,KLEN
          DO 202 J=1,KHOLD
            DO 201 I=1,ILEN
              INODE=IP(I,J,K)
C
              VFRAC(INODE,IC)=VFINIT
              VFRAC(INODE,ID)=1.0-VFRAC(INODE,IC)
C ----   SET VELOCITIES
C              V(INODE,IC)= V(INODE,IC) / VFRAC(INODE,IC)
              V(INODE,IC)=0.33
              V(INODE,ID)=VELP2
C ----   SET PRESSURE - ASSUMING CONSTANT DENSITY & VF IN
BED
              P(INODE,IC)=PCONST*(YC(IVTOP)-YP(INODE))+POUT
              P(INODE,ID)=P(INODE,IC)
 201        CONTINUE
 202      CONTINUE
 203    CONTINUE
C
C ----  END OF INITIAL CONDITION SETUP
C
      ENDIF
C
C++++++++++++++++ END OF USER AREA 5
+++++++++++++++++++++++++++++++++
C
      RETURN
      END


      SUBROUTINE
USRGRD(U,V,W,P,VFRAC,DEN,VIS,TE,ED,RS,T,H,RF,SCAL,
     +                  XP,YP,ZP,VOL,AREA,VPOR,ARPOR,WFACT,
     +                  XCOLD,YCOLD,ZCOLD,XC,YC,ZC,IPT,
     +
IBLK,IPVERT,IPNODN,IPFACN,IPNODF,IPNODB,IPFACB,
     +                  WORK,IWORK,CWORK)
C
C**********************************************************
************
C
C   USER SUBROUTINE TO ALLOW USERS TO GENERATE A GRID FOR
CFX-4
C
C   >>> IMPORTANT
<<<
C   >>>
<<<
C   >>> USERS MAY ONLY ADD OR ALTER PARTS OF THE SUBROUTINE
WITHIN  <<<
C   >>> THE DESIGNATED USER AREAS
<<<
C
C**********************************************************
************
C
```

```
C   THIS SUBROUTINE IS CALLED BY THE FOLLOWING SUBROUTINES
C      CREATE  CUSR
C
C***********************************************************
************
C   CREATED
C      27/04/90  ADB
C   MODIFIED
C      05/08/91  IRH  NEW STRUCTURE
C      09/09/91  IRH  CORRECT EXAMPLE
C      01/10/91  DSC  REDUCE COMMENT LINE GOING OVER 72
COLUMNS.
C      29/11/91  PHA  UPDATE CALLED BY COMMENT, ADD RF
ARGUMENT,
C                     CHANGE LAST DIMENSION OF RS TO 6 AND
IVERS TO 2
C      03/06/92  PHA  ADD PRECISION FLAG AND CHANGE IVERS
TO 3
C      03/07/92  DSC  CORRECT COMMON MLTGRD.
C      23/11/93  CSH  EXPLICITLY DIMENSION IPVERT ETC.
C      03/02/94  PHA  CHANGE FLOW3D TO CFDS-FLOW3D
C      03/03/94  FHW  CORRECTION OF SPELLING MISTAKE
C      22/08/94  NSW  MOVE 'IF(IUSED.EQ.0) RETURN' OUT OF
USER AREA
C      19/12/94  NSW  CHANGE FOR CFX-F3D
C      02/07/97  NSW  UPDATE FOR CFX-4
C
C***********************************************************
************
C
C   SUBROUTINE ARGUMENTS
C
C     U       - U COMPONENT OF VELOCITY
C     V       - V COMPONENT OF VELOCITY
C     W       - W COMPONENT OF VELOCITY
C     P       - PRESSURE
C     VFRAC   - VOLUME FRACTION
C     DEN     - DENSITY OF FLUID
C     VIS     - VISCOSITY OF FLUID
C     TE      - TURBULENT KINETIC ENERGY
C     ED      - EPSILON
C     RS      - REYNOLD STRESSES
C     T       - TEMPERATURE
C     H       - ENTHALPY
C     RF      - REYNOLD FLUXES
C     SCAL    - SCALARS (THE FIRST 'NCONC' OF THESE ARE MASS
FRACTIONS)
```

```
C     XP     - X COORDINATES OF CELL CENTRES
C     YP     - Y COORDINATES OF CELL CENTRES
C     ZP     - Z COORDINATES OF CELL CENTRES
C     VOL    - VOLUME OF CELLS
C     AREA   - AREA OF CELLS
C     VPOR   - POROUS VOLUME
C     ARPOR  - POROUS AREA
C     WFACT  - WEIGHT FACTORS
C   * XC     - X COORDINATES OF CELL VERTICES
C   * YC     - Y COORDINATES OF CELL VERTICES
C   * ZC     - Z COORDINATES OF CELL VERTICES
C     XCOLD  - X COORDINATES OF CELL VERTICES AT START OF
TIME STEP
C     YCOLD  - Y COORDINATES OF CELL VERTICES AT START OF
TIME STEP
C     ZCOLD  - Z COORDINATES OF CELL VERTICES AT START OF
TIME STEP
C
C     IPT    - 1D POINTER ARRAY
C     IBLK   - BLOCK SIZE INFORMATION
C     IPVERT - POINTER FROM CELL CENTERS TO 8 NEIGHBOURING
VERTICES
C     IPNODN - POINTER FROM CELL CENTERS TO 6 NEIGHBOURING
CELLS
C     IPFACN - POINTER FROM CELL CENTERS TO 6 NEIGHBOURING
FACES
C     IPNODF - POINTER FROM CELL FACES TO 2 NEIGHBOURING
CELL CENTERS
C     IPNODB - POINTER FROM BOUNDARY CENTERS TO CELL
CENTERS
C     IPFACB - POINTER FROM BOUNDARY CENTERS TO BOUNDARY
FACESS
C
C     WORK   - REAL WORKSPACE ARRAY
C     IWORK  - INTEGER WORKSPACE ARRAY
C     CWORK  - CHARACTER WORKSPACE ARRAY
C
C   SUBROUTINE ARGUMENTS PRECEDED WITH A '*' ARE ARGUMENTS
THAT MUST
C   BE SET  BY THE USER IN THIS ROUTINE.
C
C   NOTE THAT OTHER DATA MAY BE OBTAINED FROM CFX-4 USING
THE
C   ROUTINE GETADD, FOR FURTHER DETAILS SEE THE VERSION 4
C   USER MANUAL.
C
```

```
C************************************************************
************
C
      LOGICAL LDEN,LVIS,LTURB,LTEMP,LBUOY,LSCAL,LCOMP
     +       ,LRECT,LCYN,LAXIS,LPOROS,LTRANS
C
      CHARACTER*(*) CWORK
C
C+++++++++++++++++ USER AREA 1
++++++++++++++++++++++++++++++++++++++++
C---- AREA FOR USERS EXPLICITLY DECLARED VARIABLES
C
     LOGICAL SHOW
c    SHOW=.FALSE.
C
C+++++++++++++++++ END OF USER AREA 1
+++++++++++++++++++++++++++++++++
C
      COMMON
     + /ALL/    NBLOCK,NCELL,NBDRY,NNODE,NFACE,NVERT,NDIM
     + /ALLWRK/ NRWS,NIWS,NCWS,IWRFRE,IWIFRE,IWCFRE
     + /ADDIMS/ NPHASE,NSCAL,NVAR,NPROP
     +
,NDVAR,NDPROP,NDXNN,NDGEOM,NDCOEF,NILIST,NRLIST,NTOPOL
     + /CHKUSR/ IVERS,IUCALL,IUSED
     + /CONC/   NCONC
     + /DEVICE/ NREAD,NWRITE,NRDISK,NWDISK
     + /IDUM/   ILEN,JLEN
     + /LOGIC/  LDEN,LVIS,LTURB,LTEMP,LBUOY,LSCAL,LCOMP
     +         ,LRECT,LCYN,LAXIS,LPOROS,LTRANS
     + /MLTGRD/ MLEVEL,NLEVEL,ILEVEL
     + /SGLDBL/ IFLGPR,ICHKPR
     + /SPARM/
SMALL,SORMAX,NITER,INDPRI,MAXIT,NODREF,NODMON
     + /TIMUSR/ DTUSR
     + /TRANSI/ NSTEP,KSTEP,MF,INCORE
     + /TRANSR/ TIME,DT,DTINVF,TPARM
C
C+++++++++++++++++ USER AREA 2
++++++++++++++++++++++++++++++++++++++++
C---- AREA FOR USERS TO DECLARE THEIR OWN COMMON BLOCKS
C     THESE SHOULD START WITH THE CHARACTERS 'UC' TO ENSURE
C     NO CONFLICT WITH NON-USER COMMON BLOCKS
C *************** START OF MAIN ********************

          COMMON /UCBLOK/ YNOZUP, YWIDTH, FINES, BDHGHT,
NTOP,
     +         BDWDTH, BDDPTH,
     +         ZWIDTH, NUMZ,
     +          FACTOR,DIAM,
     +          RNSERT,WALL,
     +          NOZDEN

          COMMON /UCGRID/ XGRID(200),YGRID(200),ZGRID(200),
     +          NI,NJ,NK,NNOZUP,NNOZDP


C++++++++++++++++ END OF USER AREA 2
+++++++++++++++++++++++++++++++++
C
      DIMENSION
     +
U(NNODE,NPHASE),V(NNODE,NPHASE),W(NNODE,NPHASE),P(NNODE,NPH
ASE)

+,VFRAC(NNODE,NPHASE),DEN(NNODE,NPHASE),VIS(NNODE,NPHASE)
     +,TE(NNODE,NPHASE),ED(NNODE,NPHASE),RS(NNODE,NPHASE,6)
     +,T(NNODE,NPHASE),H(NNODE,NPHASE),RF(NNODE,NPHASE,4)
     +,SCAL(NNODE,NPHASE,NSCAL)
      DIMENSION
     +
XP(NNODE),YP(NNODE),ZP(NNODE),XC(NVERT),YC(NVERT),ZC(NVERT)
     +,XCOLD(NVERT),YCOLD(NVERT),ZCOLD(NVERT)
     +,VOL(NCELL),AREA(NFACE,3),VPOR(NCELL),ARPOR(NFACE,3)
     +,WFACT(NFACE)
     +,IPT(*),IBLK(5,NBLOCK)

+,IPVERT(NCELL,8),IPNODN(NCELL,6),IPFACN(NCELL,6),IPNODF(NF
ACE,4)
     +,IPNODB(NBDRY,4),IPFACB(NBDRY)
     +,IWORK(*),WORK(*),CWORK(*)
C
C++++++++++++++++ USER AREA 3
++++++++++++++++++++++++++++++++++++++++
C---- AREA FOR USERS TO DIMENSION THEIR ARRAYS
C
C---- AREA FOR USERS TO DEFINE DATA STATEMENTS
C
C++++++++++++++++ END OF USER AREA 3
+++++++++++++++++++++++++++++++++
C
C---- STATEMENT FUNCTION FOR ADDRESSING
      IP(I,J,K)=IPT((K-1)*ILEN*JLEN+(J-1)*ILEN+I)
C
```

```
C---- VERSION NUMBER OF USER ROUTINE AND PRECISION FLAG
C
      IVERS=3
      ICHKPR = 1
C
C++++++++++++++++ USER AREA 4
+++++++++++++++++++++++++++++++++++++++
C---- TO USE THIS USER ROUTINE FIRST SET IUSED=1
C
       IUSED=1
       SHOW=.FALSE.

C
C++++++++++++++++ END OF USER AREA 4
++++++++++++++++++++++++++++++++
C
       IF (IUSED.EQ.0) RETURN
C
C---- FRONTEND CHECKING OF USER ROUTINE
       IF (IUCALL.EQ.0) RETURN
C
C++++++++++++++++ USER AREA 5
+++++++++++++++++++++++++++++++++++++++
C
       CALL IPREC('BLOCK-
1','BLOCK','VERTICES',IPT,ILEN,JLEN,
     +            KLEN,CWORK,IWORK)


C-- LOOP OVER BLOCK
      DO 100 K=1,KLEN
        DO 120 J=1,JLEN
          DO 130 I=1,ILEN
C-- USE STATEMENT FUNCTION IP TO GET ADDRESSES
            IVERT = IP(I,J,K)
C-- DEFINE LOCATION OF GRID VERTICES
            XC(IVERT)=XGRID(I)
            YC(IVERT)=YGRID(J)
            ZC(IVERT)=ZGRID(K)
 130        CONTINUE
 120      CONTINUE
 100  CONTINUE
C
C++++++++++++++++ END OF USER AREA 5
++++++++++++++++++++++++++++++++
C
```

```
      RETURN
      END

C
C ******************* SUBROUTINES ******************
C

C
C ******************* SUBROUTINES ******************
C
          SUBROUTINE GEO1(SMALL,RLARGE,RL,FRAC,N)

C DATE: 19/10/98
C AUTHOR: JONATHAN TYLER, UNIV OF ALBERTA
C
C DESCRIPTION: SUBROUTINE TO CALCULATE APPROXIMATE
C  GEOMETRIC PROGRESSION BASED ON SIZE OF SMALLEST
C  RLARGE  LARGEST DIVISION
C  SMALL   SMALLEST DIVISION
C  RL  LENGTH TO SOLVE TO
C
C RETURNS: ZFRAC() THE STEP FRACTIONAL VALUES
C          N      THE INTEGER NUMBER OF GRIDS


C       AUTHOR:  JONATHAN TYLER
C       DATE:    NOVEMBER 15, 1998
C       REVISION: 000
C                 001  FEB 10, 1999 FINAL DO LOOP INDICES
C                      INCREASED TO RANGE FROM 3 TO N+2


       DIMENSION FRAC(100)

       PLENGTH=0.0
          LENGTH=RL
          BIG=RLARGE
          ALPHA=0.0
          N=0
          FLAG=0
       TEMP=0.0

          DO J=1,100
          ALPHA=(SMALL/BIG)**(1.0/FLOAT(J))
                PLENGTH=BIG*(1.0-(ALPHA)**FLOAT(J))/(1.0-
ALPHA)
```

```
                ERROR=PLENGTH-LENGTH

                IF (ERROR .GE. 0.0 .AND. FLAG .NE. 1) THEN
               RALPHA=ALPHA
                        N=J+1
                        FLAG=1
          END IF
          END DO

C          N=N+2
          N=N+1
          DO J=1,N
                FRAC(J)=SMALL*RALPHA**(1.0-FLOAT(J))
          END DO

         END

C ****************************************
      SUBROUTINE US_GEO(RSEED,RLNGTH,RDELTA,NUMB,ZFRAC)
C
C AUTHOR: JONATHAN TYLER, UNIVERSITY OF ALBERTA
C DATE:   AUGUST 16, 1998
C DESC:   SUBROUTINE WILL DETERMINE THE GRID SPACING VALUES
FOR A
C         GEOMETRIC PROGRESSION BASED ON THE NUMBER OF
GRIDS, THE
C         SIZE THAT THE FINAL GRID WILL BE EQUAL TO.
C VARIABLES:
C     RSEED    INITIAL GUESS VALUE FOR NEWTON'S METHOD (USU
1.15)
C     RLNGTH   LENGTH OVER WHICH TO GRID
C     RDELTA   VALUE THAT LAST GEOMETRIC GRID SHOULD MAP TO
C     NUMB     NUMBER OF GRID SPACES
C     ZFRAC     RETURNED ARRAY OF STEP VALUES
C
      DIMENSION ZFRAC(100)

      RALPHA=RSEED
      RL=RLNGTH
      RB=RDELTA
      N=NUMB
C IMPLEMENTATION OF NEWTON'S METHOD FOR SOLVING FOR ALPHA
      DO 30 J=1,30
         TEMP1=(RB*RALPHA**(-N)-RB)/(1.0-RALPHA)-RL
         TEMP2=-N*RB*RALPHA**(-N-1)/(1.0-RALPHA)
         TEMP3=(1.0-RALPHA)**(-2)*(RB*RALPHA**(-N)-RB)
         RALPHA2=RALPHA-TEMP1/(TEMP2+TEMP3)
         RALPHA=RALPHA2
30       CONTINUE

C DETERMINE THE SIZE OF THE FIRST GRID
         H1=RB/RALPHA**N

C DETERMINE THE SIZE OF EACH AND STORE IN ZFRAC ARRAY
      DO 40 J=1,N+2
         ZFRAC(J)=H1*RALPHA**(J-1)
40    CONTINUE

700   FORMAT ('ALPHA = ',F12.8)
      END



     SUBROUTINE DISPLAY(GRID,NUMB,STRING)
     DIMENSION GRID(100)
     CHARACTER *5 STRING

     DO 10 J=1,NUMB
          PRINT 8,STRING,J,GRID(J)
10   CONTINUE
8    FORMAT(A5,'(',I3,')=',F12.6)

     END



      SUBROUTINE USRTPL(NBLOCK,NPATCH,NGLUE
     +
,NDBLK,CBLK,INFPCH,CPATCH,INFGLU,IBBPP,IBBPD
     +                       ,WORK,IWORK,CWORK)
C
      CHARACTER*(*) CBLK,CPATCH,CWORK
C
C++++++++++++++++ USER AREA 1
+++++++++++++++++++++++++++++++++++++++++
C---- AREA FOR USERS EXPLICITLY DECLARED VARIABLES
C
C     THESE FOLLOWING CHARACTER VARIABLES ARE USED IN THE
USER EXAMPLES
       CHARACTER*32
CNAME,CNAME1,CNAME2,CLIST1,CLIST2,CBLOCK
       CHARACTER*6 CTYPE
C
```

```
C++++++++++++++++ END OF USER AREA 1
++++++++++++++++++++++++++++++++++
C
      COMMON
     + /ALLWRK/ NRWS,NIWS,NCWS,IWRFRE,IWIFRE,IWCFRE
     + /BBCYCL/ XCYCLE(3)
     + /BBDIM/  MBB, MBBPAT, MBBNOD, MBBNBR,
     +          MBB1, MBB2, MBB3, MBB4, MBB5,
     +          MBB6, MBB7, MBB8, MBB9, MBB10,
     +          MBB11, MBB12, MBB13, MBB14, MBB15,
     +          MBB16, MBB17, MBB18, MBB19, MBB20
     + /CHKUSR/ IVERS,IUCALL,IUSED
     + /DEVICE/ NREAD,NWRITE,NRDISK,NWDISK
     + /LIMTPL/ NBLMAX,NPCMAX,NGLMAX
     + /SGLDBL/ IFLGPR,ICHKPR
C
        COMMON /UCGRID/ XGRID(200),YGRID(200),ZGRID(200),
     +         NI,NJ,NK,NNOZUP,NNOZDP

        COMMON /UCBLOK/ YNOZUP,YWIDTH,FINES,BDHGHT,NTOP,
     +          BDWDTH,BDDPTH,
     +          ZWIDTH,NUMZ,
     +          FACTOR,DIAM,
     +          RNSERT,WALL,
     +          NOZDEN


C
      DIMENSION WORK(NRWS),IWORK(NIWS),CWORK(NCWS)

+,NDBLK(3,*),CBLK(*),INFPCH(9,*),CPATCH(2,*),INFGLU(5,*)
     +,IBBPP(MBB1,MBB2),IBBPD(MBB3)
C
          DIMENSION FRAC(100),RTEMP(200)
C
      IVERS=3
      ICHKPR = 1
C
       IUSED=1
C
C++++++++++++++++ END OF USER AREA 4
++++++++++++++++++++++++++++++++++
C
       IF (IUSED.EQ.0) RETURN
C
C---- FRONTEND CHECKING OF USER ROUTINE
```

```
       IF (IUCALL.EQ.0) RETURN
C
C++++++++++++++++ USER AREA 5
+++++++++++++++++++++++++++++++++++++++++

C ****************************************************
C **                                                **
C **      ADJUST DIMENSION VARIABLES                **
C **                                                **
C ****************************************************
C THIS IS NECESSARY TO ENSURE PROPER NUMERICAL ACCURACY
C WHEN USING NEWTON'S METHOD TO DETERMINE SOME OF THE
C GRID PARAMETERS

       YNOZUP=YNOZUP*10.0
       YWIDTH=YWIDTH*10.0
       FINES=FINES*10.0

       INSERT=INSERT*10.0
       WALL=WALL*10.0
       RNSERT=RNSERT*10.0

       BDHGHT=BDHGHT*10.0
       BDWDTH=BDWDTH*10.0

       BDDPTH=BDDPTH*100.0
       ZWIDTH=ZWIDTH*100.0


C ****************************************************
C **                                                **
C **      Y GRIDDING SECTION                        **
C **                                                **
C ****************************************************

C JUNE 16, 1999
C MODIFICATION B
        DY = YWIDTH/(NOZDEN+1)
        WALL=DY

        DELTA=(BDHGHT-(FINES+YWIDTH+YNOZUP+2.0*WALL))/NTOP
C         CALCULATE THE FIRST LINEAR DELTA FOR FREEBOARD

     CALL GEO1(WALL,DELTA,YNOZUP+WALL,FRAC,NNOZUP)
C         DETERMINE GEOMETRIC GRID SPACING BASED ON
SMALLEST
C         UNIT (WALL) TO LARGEST (DELTA) OVER A DISTANCE
```

```
C          YNOZUP+WALL


     YGRID(NNOZUP+1)=YNOZUP+WALL
        YGRID(NNOZUP+2)=YNOZUP+WALL+YWIDTH
     YGRID(NNOZUP)=YNOZUP
     YGRID(1)=0.0
C SET THE VALUES THAT ARE SPECIFIED


     DO 10 J=NNOZUP-1,1,-1
          TEMP=YGRID(J+2)
          YGRID(J+1)=TEMP-FRAC(NNOZUP-J)
10   CONTINUE


        DO 11 J=1,NNOZUP-1
              TEMP=YGRID(NNOZUP+J+1)
              YGRID(NNOZUP+J+2)=TEMP+FRAC(J)
11      CONTINUE


     N1=NNOZUP+1


     DELTA=(BDHGHT-YGRID(2*NNOZUP))/NTOP
C         NEW DELTA VALUE ENSURES THAT THE TOTAL REACTOR
C         HEIGHT IS CORRECT

     DO 15 J=1,NTOP+1
          YGRID(J+2*NNOZUP)=YGRID(2*NNOZUP)+FLOAT(J)*DELTA
15   CONTINUE
C         FINISH LINEAR GRIDDING IN THE FREEBOARD


C INCREASE THE DENSITY OF THE GRIDDING IN THE Y DIRECTION
FOR NOZZLE

        DY = (YGRID(NNOZUP+2)-YGRID(NNOZUP+1))/(NOZDEN+1)
C THIS IS THE DELTA Y VALUE FOR INCREASED GRID DENSITY

C TEMPORARILY HOLD YGRID(NNOZUP+2) TO
YGRID(2*NNOZUP+NTOP+1)
        DO 16 J=NNOZUP+2,2*NNOZUP+NTOP+1
          RTEMP(J)=YGRID(J)
16      CONTINUE
```

```
        DO 17 J=1,NOZDEN
           YGRID(NNOZUP+1+J)=YGRID(NNOZUP+1)+J*DY
17      CONTINUE

        DO 18 J=NNOZUP+2,2*NNOZUP+NTOP+1
           YGRID(J+NOZDEN)=RTEMP(J)
18      CONTINUE
        NTOP=NTOP+NOZDEN


     DO 20 J=1,2*NNOZUP+NTOP+1
          YGRID(J)=YGRID(J)/10.0
20   CONTINUE
C         DIVIDE THE Y DIMENSIONS BY 10 TO GET PROPER
C         PHYSICAL DIMENSIONS

C REVISION: CORRECT IF YGRID(2) IS GREATER THAN
C           YGRID(3)-YGRID(2)

        IF (YGRID(2).GT.(YGRID(3)-YGRID(2))) THEN
            YGRID(1)=YGRID(2)/2.0
            NTOP=NTOP+1

            DO 22 J=2*NNOZUP+NTOP+1,2,-1
               YGRID(J)=YGRID(J-1)
22          CONTINUE
            YGRID(1)=0.0
        ENDIF


        NJ=2*NNOZUP+NTOP


C ***************************************************
C **                                               **
C **        X GRIDDING SECTION                     **
C **                                               **
C ***************************************************

         XGRID(1)=0.0
         CALL MERRY(RL,0.0029245,1.2,1450.0,0.000374,250.0)

      XGRID(1)=0.0
      NXTOP=NINT((BDWDTH-RNSERT)/DELTA)

C          THE NUMBER OF X DIVISIONS IS EQUAL TO
```

```
C         BEDWITH-RNSERT  DIVIDED BY THE LINEAR STEP IN
C         THE Y DIRECTION
     XDELTA=(BDWDTH-RNSERT)/NXTOP

        IJ=1

        DO WHILE(RNSERT/IJ .GT. XDELTA)
           IJ=IJ+1
        END DO


C GRID THE NOZZLE SECTION
        DO 24 J=1,IJ+1
              XGRID(J+1)=XGRID(J)+RNSERT/IJ
24      CONTINUE



     DO 30 J=1,NXTOP+1
          XGRID(J+IJ+1)=RNSERT+XDELTA*FLOAT(J)
30   CONTINUE

     DO 32 J=1,NXTOP+2+IJ
          XGRID(J)=XGRID(J)/10.0
32   CONTINUE
C         DIVIDE THE X DIMENSIONS BY 10 TO GET
C         THE PROPER PHYSICAL DIMENSIONS

        NI=NXTOP+1+IJ


C ***************************************************
C **                                               **
C **      Z GRIDDING SECTION                       **
C **                                               **
C ***************************************************


     INHALF=(NUMZ-1)/2
     DHALF=(BDDPTH-ZWIDTH)/2.0

     ZGRID(1)=0.0
     ZGRID(INHALF+1)=DHALF
     ZGRID(INHALF+2)=DHALF+ZWIDTH

C JUNE 16, 1999
        DZ=ZWIDTH/(NOZDEN+1.0)
```

```
      CALL US_GEO(0.85,DHALF,DZ,INHALF,FRAC)

C        CALL US_GEO(0.85,DHALF,ZWIDTH,INHALF,FRAC)

      DO 35 J=1,INHALF
           ZGRID(J+1)=ZGRID(J)+FRAC(J)
           ZGRID(INHALF+J+2)=ZGRID(INHALF+J+1)+
     +                FRAC(INHALF+1-J)
35    CONTINUE

      ZGRID(2*INHALF+2)=DHALF*2.0+ZWIDTH

C CHECK NOZDEN VARIABLE TO SEE IF THE NOZZLE INLET
C PATCH MUST BE DENSIFIED FOR IMPLEMENTATION.

         NK=NUMZ+NOZDEN
         NNOZDP=INHALF+1


         DZ= (ZGRID(NNOZDP+1) - ZGRID(NNOZDP) ) / (NOZDEN+1)
C DELTA Z FOR INCREASING DENSITY OF THE NOZZLE GRID

C TEMPORARILY HOLD NNOZDP+1 TO NUMZ+1 FOR INSERTION
         DO 36 J=NNOZDP+1,NUMZ+1
            RTEMP(J)=ZGRID(J)
36       CONTINUE

         DO 37 J=1,NOZDEN
            ZGRID(NNOZDP+J)=ZGRID(NNOZDP)+J*DZ
37       CONTINUE

         DO 38 J=NNOZDP+1,NUMZ+1
            ZGRID(J+NOZDEN)=RTEMP(J)
38       CONTINUE


      DO 40 J=1,NK+1
           ZGRID(J)=ZGRID(J)/100.0
40    CONTINUE
C          DIVIDE THE Z DIMENSIONS BY 100 TO GET
C          THE PROPER PHYSICAL DIMENSIONS

C
C++++++++++++++++ END OF USER AREA 5
++++++++++++++++++++++++++++++++++
C
```

```
C++++++++++++++++ USER AREA 6
+++++++++++++++++++++++++++++++++++++++++
C
C *****************************************************
C **                                                 **
C **    TOPOLOGY SECTION                             **
C **                                                 **
C *****************************************************

        CBLOCK='BLOCK-1'
        CALL BLOCK(CBLOCK,NI,NJ,NK,NBLOCK,NDBLK,CBLK)
C CREATE THE SINGLE BLOCK IN THIS USER FORTRAN ROUTINE

        LABEL=1
        CTYPE='INLET '
        CNAME='DISTRIBUTOR'

        CALL PATCH (CTYPE,CNAME,CBLOCK,LABEL,
     +            1,NI,1,1,1,NK,5,
     +            NBLOCK,NPATCH,NDBLK,CBLK,INFPCH,CPATCH)
C CREATE THE DISTRIBUTOR PATCH

C MARCH 11, 1999 ADDITIONS HERE

        CTYPE='SOLID '
        CNAME='PIPE'

        NPI1=1
        NPI2=IJ
        NPJ1=NNOZUP+1
        NPJ2=NNOZUP+3+NOZDEN
        NPK1=NNOZDP-1
        NPK2=NNOZDP+1+NOZDEN

        CALL PATCH (CTYPE,CNAME,CBLOCK,LABEL,
     +            NPI1,NPI2,NPJ1,NPJ2,NPK1,NPK2,0,
     +            NBLOCK,NPATCH,NDBLK,CBLK,INFPCH,CPATCH)


        CTYPE='INLET '
        CNAME='NOZZLE'

     NI1=IJ+1
        NI2=IJ+1
        NJ1=NNOZUP+2
        NJ2=NNOZUP+2+NOZDEN
        NK1=NNOZDP
        NK2=NNOZDP+NOZDEN

        CALL PATCH (CTYPE,CNAME,CBLOCK,LABEL,
     +             NI1,NI2,NJ1,NJ2,NK1,NK2,4,
     +             NBLOCK,NPATCH,NDBLK,CBLK,INFPCH,CPATCH)


        CTYPE='PRESS '
        CNAME='OUTLET'

        CALL PATCH (CTYPE,CNAME,CBLOCK,LABEL,
     +             1,NI,NJ,NJ,1,NK,2,
     +             NBLOCK,NPATCH,NDBLK,CBLK,INFPCH,CPATCH)
C CREATE THE PRESSURE OUTLET PATCH


       YWIDTH=YWIDTH/10.0
       FINES=FINES/10.0

       BDHGHT=BDHGHT/10.0
       BDWDTH=BDWDTH/10.0

       BDDPTH=BDDPTH/100.0
       ZWIDTH=ZWIDTH/100.0

C **************************************************
C **                                              **
C **    GEOMETRY FILE SECTION                     **
C **                                              **
C **************************************************

        OPEN (UNIT=1,FILE='GEOMETRY',FORM='FORMATTED',
     +      ACCESS='SEQUENTIAL',STATUS='NEW')

        DO 45 J=1,INHALF
           WRITE(UNIT=1,FMT=800)J,FRAC(J)
45       CONTINUE
           WRITE(UNIT=1,FMT=801)'OVERALL DATA',1

           WRITE(UNIT=1,FMT=801)'YNOZUP=',YNOZUP
           WRITE(UNIT=1,FMT=801)'MERRY=',RL
           WRITE(UNIT=1,FMT=804)'NI=',NI
           WRITE(UNIT=1,FMT=804)'NJ=',NJ
           WRITE(UNIT=1,FMT=804)'NK=',NK
           WRITE(UNIT=1,FMT=805)'IJ=',IJ

           WRITE(UNIT=1,FMT=805)'++++++++',5
```

```
            WRITE(UNIT=1,FMT=805)'PIPE I1:',NPI1
            WRITE(UNIT=1,FMT=805)'PIPE I2:',NPI2
            WRITE(UNIT=1,FMT=805)'PIPE J1:',NPJ1
            WRITE(UNIT=1,FMT=805)'PIPE J2:',NPJ2
            WRITE(UNIT=1,FMT=805)'PIPE K1:',NPK1
            WRITE(UNIT=1,FMT=805)'PIPE K2:',NPK2
            WRITE(UNIT=1,FMT=805)'++++++++',5
            WRITE(UNIT=1,FMT=805)'NOZZLE I1:',NI1
            WRITE(UNIT=1,FMT=805)'NOZZLE I2:',NI2
            WRITE(UNIT=1,FMT=805)'NOZZLE J1:',NJ1
            WRITE(UNIT=1,FMT=805)'NOZZLE J2:',NJ2
            WRITE(UNIT=1,FMT=805)'NOZZLE K1:',NK1
            WRITE(UNIT=1,FMT=805)'NOZZLE K2:',NK2
            WRITE(UNIT=1,FMT=805)'++++++++',5
            WRITE(UNIT=1,FMT=801)'DZ = ',DZ


         DO 50 J=1,NJ

            WRITE(UNIT=1,FMT=802)'YGRID',J,YGRID(J)
50       CONTINUE

         DO 55 J=1,NI
            WRITE(UNIT=1,FMT=802)'XGRID',J,XGRID(J)
55       CONTINUE

         DO 56 J=1,NK
            WRITE(UNIT=1,FMT=802)'ZGRID',J,ZGRID(J)
56       CONTINUE


         KHOLD=0
         FLAG=.TRUE.

         DO 60 J=NJ,1,-1
            IF( (FACTOR .GT. YGRID(J)) .AND. (FLAG .EQ.
.TRUE.) ) THEN
                  KHOLD=J+1
                  FLAG=.FALSE.
            END IF
60       CONTINUE

         WRITE(UNIT=1,FMT=803)KHOLD,YGRID(KHOLD),FACTOR


800      FORMAT('FRAC(',I3,')= ',F12.8)
801      FORMAT(A,F12.8)
```

```
802      FORMAT(A,'('I3,') = ',F12.8)
803      FORMAT('AT ',I3,' YGRID=',F12.8' CLOSE TO ',F12.8)
804      FORMAT(A,I3)
805      FORMAT(A,I3)
         END FILE(UNIT=1)
         CLOSE(UNIT=3)
C
      RETURN
      END

      SUBROUTINE MERRY(RL,D0,RHOG,RHOP,DP,U0)

      RA=(RHOG/RHOP)**0.2
      RB=(DP/D0)**0.2
      RC=5.25*((RHOG*U0**2)/(0.45*9.81*DP))**0.4

      RL=D0*(RA*RB*RC-4.5)
      END
```